Controlled Growth and Characterization of Lead-free Halide Double Perovskites for Optoelectronic Applications

A Thesis Submitted to
Indian Institute of Technology Guwahati
for the Degree of
Doctor of Philosophy

By
Ravinder

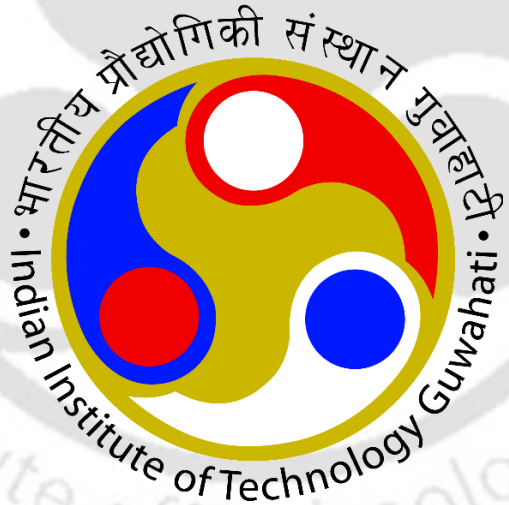

Department of Physics
Indian Institute of Technology Guwahati
Guwahati-781039, India

September 2025

Dedicated to

My late father

Whose courage and sacrifices built the foundation

Department of Physics
Indian Institute of Technology Guwahati
Guwahati-781039, India

STATEMENT

The work presented in the thesis entitled "**Controlled Growth and Characterization of Lead-free Halide Double Perovskites for Optoelectronic Applications**" has been carried out by me at Indian Institute of Technology Guwahati under the Supervision of Prof. P. K. Giri, Professor, Department of Physics, Indian Institute of Technology Guwahati. This work has not been submitted elsewhere for the award of any other degree.

Ravinder
Roll No. – 196121024
Senior Research Fellow
Department of Physics
Indian Institute of Technology Guwahati
Guwahati-781039, India

Prof. P. K. Giri
Professor
Department of Physics
Indian Institute of Technology Guwahati
Guwahati-781039, India
Phone: ***+91 3612582703, Fax: +91 361 2690762***
Email: ***giri@iitg.ac.in***

CERTIFICATE

This is to certify that the work contained in the thesis entitled "**Controlled Growth and Characterization of Lead-free Halide Double Perovskites for Optoelectronic Applications"** has been carried out by **Mr. Ravinder** at Indian Institute of Technology Guwahati under my supervision. This work has not been submitted elsewhere for the award of any degree.

Prof. P. K. Giri
Thesis supervisor

Acknowledgements

It is with deep gratitude and heartfelt appreciation that I acknowledge the people who have guided and supported me throughout the journey of my thesis.

First and foremost, I would like to express my sincere thanks to **Prof. P. K. Giri**, Department of Physics, for being an exceptional mentor. His unwavering support, insightful feedback, and inspiring guidance have been instrumental in shaping both my research and academic outlook. I am deeply thankful for his patience, encouragement, and the trust he placed in me during challenging times.

I would like to thank my **Doctoral Committee** members, **Prof. D. Pamu**, **Prof. M. Qureshi**, and **Dr. C. Kadolkar,** for their regular review of my work, constructive criticism, and valuable suggestions throughout my academic growth.

I would also like to thank the **Ministry of Human Resources Development (MHRD),** Government of India, for providing the financial support that enabled me to pursue this work. I would also like to thank the **Department of Physics**, IIT Guwahati, for providing a nurturing and stimulating research environment and facilitating my academic growth over the years. I would like to express my sincere appreciation to the **Central Instrument Facility** and the **Centre for Nanotechnology**, IIT Guwahati, for granting access to the state-of-the-art instruments that were crucial for the successful execution of my research throughout the course of this study.

To my **seniors**, Dr. Larionett PL Mawlong, Dr. Abhilasha Bora, Dr. Somorjit Singh, Dr. Joydip Ghosh, Dr. Sumaiya Praveen, Dr. Ruma Das, Dr. Tarik Hossain, Dr. Sumana Paul, thank you for the endless discussions, encouragement, and moments of laughter that made this journey lighter and more fulfilling. You have been an important part of this experience. To my **labmates**, Dr. Koushik Ghosh, Dr. Abdul Kaim Mia, and Dr. Tadasha Jena, thank you for your constant support inside and outside the lab. I would also like to thank all my lab **juniors**, Shipra Aswal, Sirsendu Ghosal, Sanju Nandi, Subhankar Debnath, Debabrata Sahu, Sanjoy Sur, Sourav Dey, Garima Chowdhary, and Shantnu Dhara, for being the best juniors throughout the journey.

I would also like to thank the **Sports Board**, IIT Guwahati, for providing the necessary facilities that contributed to maintaining both my physical and mental well-being. I am especially grateful to the **Cricket Club**, IIT Guwahati, for offering a relaxing and rejuvenating

space that helped me unwind after long and demanding days. I would like to express my heartfelt gratitude to my dear friends **Sourav Kumar**, **Dr. Abhay Pratap Singh**, **Nedup Sherpa**, **Dr. Esha Bhatia** and **Pragatisheel Tiwari** for their constant support, encouragement, and companionship throughout this journey. The laughter, meaningful conversations, and countless moments of joy we shared on campus made this period truly memorable. Your friendship added warmth and balance to my academic life, and I am deeply thankful for the wonderful memories we created together.

I express my deepest gratitude to my **mother**, whose unconditional love, sacrifices, and constant encouragement have been the guiding light of my life. Her strength, patience, and faith have always inspired me to persevere through every challenge. My heartfelt thanks also go to my **sisters (Anju and Manju)** and **brother (Sanjay Chahal)** for their endless love, motivation, and understanding. Their unwavering support and belief in me have been a source of strength and comfort throughout this journey. Your support carried me through every high and low of this journey.

I dedicate this work to the loving memory of my **late father**, whose values and sacrifices continue to guide every step of my life. He taught me to be honest, brave, and to face every challenge with integrity and determination. His unwavering dedication and the countless sacrifices he made laid the foundation for all that I have achieved today. Though he departed from this world before witnessing the outcome of his hard work and dreams, his presence is deeply felt in every success I accomplish. I will forever remain grateful for his love, wisdom, and the strength he instilled in me.

This thesis is a result of the contributions and blessings of many, and I feel incredibly grateful to each one of you.

Ravinder
IIT Guwahati

SYNOPSIS **11**
List of Publications **17**
List of Abbreviations **18**
Chapter 1 Introduction **20**
1.1 Introduction of Double Perovskites 20
1.2 Metal Halide Double Perovskites 21
1.3 Crystal Structure of Double Perovskite 21
1.4 Band Structure of Double Perovskites 23
1.5 Key Features of Double Perovskites 24
1.5.1 Bandgap Engineering 25
1.5.2 Charge Carrier Dynamics 26
1.5.3 Defect Tolerance 28
1.6 Fabrication of Double Perovskite Thin Films 30
1.6.1 Solution Process 31
1.6.2 Vacuum Deposition 33
1.7 Fabrication of $Cs_2AgBiBr_6$ Nanostructures 35
1.8 Optoelectronic Applications of $Cs_2AgBiBr_6$ Double Perovskites 37
1.8.1 Solar Cell 38
1.8.2 X-ray Detection 40
1.8.3 Photodetection 41
1.9 Other Applications of Double Perovskites 44
1.10 Challenges in Fabrication and Application of Double Perovskites 47
1.11 Focus of the Present Thesis 48
1.12 Organization of the Thesis 48
References 51
Chapter 2 Chemical Vapor Deposition Growth of Highly Stable $Cs_2AgBiBr_6$ Double Perovskite Thin Films and Their Ultralow Thermal Conductivity and Fast Photoresponse **58**
2.1 Introduction 58
2.2 Experimental Details 60
2.2.1 Chemicals 60
2.2.2 Seed Layer Preparation 61
2.2.3 CVD Deposition of $Cs_2AgBiBr_6$ DP Thin Film 61
2.3. Measurement and Characterizations 62
2.4 Results and discussion 63
2.4.1 Growth Mechanism of $Cs_2AgBiBr_6$ DP Thin Film 63

2.4.2 Structural and Crystalline Properties of $Cs_2AgBiBr_6$ DP Thin Film 65
2.4.2.1 XRD Analysis: 65
2.4.2.2 Raman Analysis: 71
2.4.2.3 XPS Analysis 73
2.4.3 Morphology and Compositional Analysis of $Cs_2AgBiBr_6$ Thin Film 75
2.4.4 Optoelectronic Properties of $Cs_2AgBiBr_6$ DP Thin Film 78
2.4.6 Low-temperature Raman Studies 82
2.4.6.1 Spectral Shift 82
2.4.6.2 Raman Linewidth 85
2.4.6.3 Raman Intensity 86
2.4.7 Thermal Conductivity 87
2.4.8 Thermal and Environmental Stability 91
2.4.9 Application as a Photodetector 93
2.5 Conclusions 94
References 96
Chapter 3 Facile In-situ Synthesis of Double Perovskite $Cs_2AgBiBr_6/WS_2$ Heterostructure and Interfacial Charge Transfer Mediated High-Performance Ultraviolet Photodetection 101
3.1 Introduction 101
3.2 Experimental Details 103
3.2.1 Materials Used 103
3.2.2 $Cs_2AgBiBr_6$ Double Perovskite Nanosheets Synthesis 103
3.2.3 WS_2 Nanosheets Synthesis 103
3.2.4 $Cs_2AgBiBr_6/WS_2$ Heterostructure Synthesis 104
3.2.5 Device Fabrication 104
3.3 Characterization Techniques 104
3.4 Results and Discussion 105
3.4.1 Morphology, Structure, and Phase Analysis 105
3.4.2 Optical Analysis 111
3.4.3 Carrier Dynamics 113
3.4.4 Photodetector Application 115
3.5 Conclusions 122
References 124
Chapter 4 Lead-free Halide Double Perovskites Nanoflakes as High-Performance SERS Substrates for Detection of Trace Organic Pollutants: Chemical Enhancement versus Field Enhancement Effects 128

4.1 Introduction 128
4.2 Experimental Section 130
4.2.1 Chemicals 130
4.2.2 Preparation of $Cs_2AgBiBr_6$ DP SERS substrate 130
4.3 Characterization Tools 131
4.4 Computational Details 131
4.5 FEM Simulations 132
4.6 Results and Discussions 132
4.6.1 Morphology Analysis 132
4.6.2 Structural Analysis 135
4.6.3 Optical Properties 139
4.6.4 SERS performance of $Cs_2AgBiBr_6$ DP 142
4.6.5 SERS Mechanism 153
4.7 Conclusion 159
References 160
Chapter 5 All Inorganic Lead-free $Cs_2AgBiBr_6$ Double Perovskite Single Crystal / $Cs_3Bi_2I_9$ Nanocrystals Heterojunction for High-Performance Photodetector Application 164
5.1 Introduction 164
5.2 Materials and Methods 166
5.2.1 Materials 166
5.2.2 Synthesis of $Cs_2AgBiBr_6$ Single Crystal 167
5.2.3 Synthesis of $Cs_3Bi_2I_9$ Nanocrystals 167
5.2.4 Device Fabrication 167
5.2.5 DFT Calculations 168
5.3 Characterization Techniques 168
5.3 Results and Discussions 169
5.3.1 Characterization of $Cs_2AgBiBr_6$ SC 169
5.3.2 Characterization of $Cs_3Bi_2I_9$ NCs 173
5.3.3 Characterization of the $Cs_2AgBiBr_6$ SC/$Cs_3Bi_2I_9$ NCs Heterostructure 177
5.3.4 Photodetector Performance 180
5.3.5 UPS Study 186
5.3.6 DFT Calculations 188
5.4 Conclusion 189
References 191
Chapter 6 Summary and Outlooks 194

6.1 Highlights and summary of the Thesis contributions.....194
6.2 Scope of the Future Work.....200

SYNOPSIS

Metal halide perovskites have emerged as prominent materials in the field of optoelectronics over the past few decades. Their exceptional optical and electronic properties, combined with tunable morphologies, have garnered significant interest, surpassing that of conventional semiconductors. Notably, the power conversion efficiency (PCE) of perovskite-based solar cells has exceeded 25% in recent years. Beyond photovoltaic applications, these materials are being actively investigated for use in light-emitting diodes (LEDs), sensors, photodetectors, and various electrochemical systems. However, despite their promising performance and adaptability for optoelectronic devices, the commercial scalability of halide perovskites remains limited due to concerns regarding their intrinsic toxicity and environmental instability. To address the challenges associated with toxicity and instability, the scientific community is actively exploring lead-free, non-toxic, and environmentally stable alternatives to conventional perovskites. A promising approach to addressing the toxicity issue in lead-based perovskites involves the homovalent substitution of Pb^{2+} with Sn^{2+} ions. However, this strategy is hindered by the inherent instability of Sn^{2+}, which readily oxidizes to Sn^{4+}, leading to rapid degradation of device performance even under inert atmospheres. To circumvent this limitation, recent research has shifted towards heterovalent substitution, replacing Pb^{2+} with trivalent metal cations (M^{3+}) in the conventional ABX_3 perovskite framework. Among these, Bi^{3+} has garnered significant attention due to its low toxicity and electronic configuration analogous to Pb^{2+}. Nevertheless, the incorporation of Bi^{3+} into the hybrid perovskite structure is nontrivial due to charge imbalance. In 2016, Volonakis et al. proposed a solution to this issue by suggesting the replacement of Pb^{2+} with a combination of monovalent (M^{+}) and trivalent (M^{3+}) cations, giving rise to a double perovskite (DP) or 'elpasolite' structure. While alkali metal-based double perovskites generally exhibit wide bandgaps (~3–4 eV), which limit their absorption in the visible spectrum, certain thallium (Tl)-based compounds offer narrower bandgaps (~2.1 eV). However, the high toxicity of thallium severely restricts its use as a viable alternative to lead. In this context, halide double perovskites have attracted considerable attention owing to their structural similarity and comparable optoelectronic properties to lead-based perovskites. Additionally, double perovskites exhibit intriguing optical characteristics and diverse morphological tunability, making them promising candidates for next-generation optoelectronic applications.

It is important to emphasize that not all halide double perovskite (HDP) candidates exhibit stable crystal structures. The formation and stability of a perovskite structure are primarily governed by two geometrical parameters: (1) the octahedral factor (μ) and (2) the tolerance factor (t). The Goldschmidt tolerance factor (GTF) is widely employed to assess the structural stability of HDPs using these parameters. For an HDP to form a stable perovskite structure, the tolerance factor must fall within the range $0.81 < t < 1.11$, and the octahedral factor within $0.41 < \mu < 0.90$. For instance, in the case of Cs2AgBiBr6, the calculated tolerance factor is $t = 0.890$, and the octahedral factor for the $[AgBr_6]^{5-}$ octahedron is $\mu = 0.587$, indicating structural feasibility. In addition to geometric factors, the thermodynamic stability of a perovskite is influenced by its decomposition energy (ΔH). A positive ΔH value suggests higher thermodynamic stability, while a negative value indicates instability. Notably, compounds such as CsBr, AgBr, Cs_2AgBr_3, $CsAgBr_2$, and Cs_3Bi2Br_9 exhibit positive decomposition energies, exceeding that of $MAPbI_3$, and thus imply enhanced stability. Specifically, in $Cs_2AgBiBr_6$, Pb^{2+} ions are substituted by Ag^+ and Bi^{3+} ions, which increase the Coulombic interaction energy and result in a more positive decomposition energy of +0.38 eV. On the contrary, Cs_2AgBiI_6 is unstable due to a negative decomposition energy ($\Delta H = -0.41$ eV).

Among halide double perovskites (DPs), $Cs_2AgBiBr_6$ has emerged as the most extensively studied and synthesized material, primarily due to its favourable optoelectronic properties-including a relatively narrow bandgap of approximately 2.19 eV, long charge carrier lifetimes on the order of hundreds of nanoseconds, and superior thermal and environmental stability. $Cs_2AgBiBr_6$ is closely followed by Cs_2SnI_6 in terms of research interest. Thin film deposition of DPs is typically achieved through two primary techniques: solution processing and vapor deposition. Solution-processed $Cs_2AgBiBr_6$ films often suffer from suboptimal film morphology, high surface roughness, and elevated defect densities. These issues stem from the high sensitivity of the process to several parameters, including annealing temperature, solvent selection, precursor ratios, and solution concentration. While sequential vapor deposition methods are more commonly employed for DP thin films, the high-vacuum evaporation of individual precursors, such as CsBr, AgBr, and BiBr3, is both technically challenging and complex. Moreover, achieving the correct stoichiometry in the final film is highly dependent on the deposition sequence and precise control of component ratios. Thus, an alternative route for the fabrication of high-quality, stoichiometrically controlled $Cs_2AgBiBr_6$ thin films is necessary.

Incorporating 2D materials with robust light absorption layers is an efficient way of enhancing the functionality of perovskite-based optoelectronic devices. Owing to their large surface-to-volume ratio, ultrathin thickness, and quantum confinement effect, 2D-transition metal dichalcogenides (TMDs) exhibit exceptional properties in electronics and optoelectronics. In recent times, researchers have incorporated 2D materials with metal halide perovskite crystals to achieve enhanced optoelectronic properties. Some of the examples include $CsPbBr_3$/black phosphorus nanosheet-based heterostructure for photodetector applications, $CH_3NH_3PbI_3$/ black phosphorus/MoS_2 composite photodiode, $CH_3NH_3PbI_3$/ reduced graphene oxide for photocatalysis, etc. The heterostructure of DP with TMDs can enhance the durability and performance of the optoelectronic devices.

Further, owing to the high charge carrier population and long diffusion lengths, $Cs_2AgBiBr_6$ DPs are significantly employed in applications other than optoelectronics, like Surface-enhanced Raman spectroscopy (SERS), electrochemical and Hydrogen evolution reactions (HER), chemical and biological sensing, environmental sensing, and memory devices. The large area growth of DP nanoflakes provides uniform adsorption of environmental pollutants. The self-trapped excitons (STE) play a vital role in supporting additional charge transfer pathways and enhancing the performance of the devices. These defects can be manipulated by post-growth annealing treatment of the DP. The in-depth analysis of photoluminescence (PL) and STE emission provides substantial evidence that STEs can directly affect the SERS performance of the DP substrate.

This thesis presents a systematic study on the controlled growth of bulk and 2D $Cs_2AgBiBr_6$ DPs. The study includes chemical vapor deposition (CVD) growth of DP thin films on various substrates, type-II heterojunction with the few-layer WS_2 for improved photoconductive application. Furthermore, we delve into the STE-assisted charge transfer pathways for improved SERS enhancement using DP as a substrate. We believe that these studies are very significant to understand the fundamentals of light emission and pave the way to cope with the current challenges of energy and multifunctional optoelectronic applications of DP materials. The complete thesis work has been organized into six chapters as detailed below:

Chapter 1 presents a brief introduction to the challenges of lead-based perovskites in the field of optoelectronics and the emergence of lead-free halide double perovskites (LFHDP) as an alternate solution. Geometrically and thermally stable alternatives for lead-based perovskites and the potential for future applications are discussed. This chapter covers the important aspects

of LFHDP required for different applications such as solar cells, photodetectors, LEDs, SERS, HER, and memory devices. We discuss the major challenges related to the synthesis processes and present a brief account of the experimental techniques used. Recent advancements in the fabrication of $Cs_2AgBiBr_6$ DP and hybrids for photodetection are presented. Then, the focus of the thesis is briefly outlined. The significant aspects of DP-based HSs and their possible applications are highlighted in this chapter. The problems and challenges of employing DP-based HSs in the various hybrid systems and the key parameters to overcome them are addressed, and the motivation of the present work is presented at the end of the chapter.

Chapter 2 presents a systematic study for the optimization of synthesis protocols for $Cs_2AgBiBr_6$ DP thin film on different substrates, as well as the phase change at higher temperature growth by chemical vapour deposition (CVD) technique. We have utilized the BiBr3 seed layer for the nucleation of larger grains inside the CVD setup. Our results demonstrate the formation of highly crystalline and uniform thin film growth over different substrates. We observed the phase change at higher substrate temperatures. In case of CVD grown DP, it is noted that by tuning factors such as the growth temperature, time, carrier gas flow, and thickness, the phase purity of the DP film can be controlled. The substrate temperature plays an important role in structural stability and phase composition. Further, low-temperature and power-dependent Raman studies were utilized to investigate the electron-phonon coupling of the CVD-grown DP thin film. We have estimated ultralow thermal conductivities as $\sim$1.97 $\pm$ 0.48 and $\sim$16.14 $\pm$ 1.58 W/m-K for suspended and supported films of Cs2AgBiBr6 DP, respectively, which are close to the theoretical predictions. The difference in thermal conductivity values for suspended and supported films is mainly because of the larger heat dissipation to the substrate in the latter case. Thermal and environmental stability experiments on the $Cs_2AgBiBr_6$ thin film are carried out utilizing high-temperature Raman and XRD measurements. Further, we have demonstrated the potential of a CVD-grown $Cs_2AgBiBr_6$ DP thin film for optoelectronic applications by fabricating a planar photodetector device using the DP thin film.

Chapter 3 presents the in-situ growth of $Cs_2AgBiBr_6$-WS_2 HS by using a planetary ball milling system. We have introduced a successful way to fabricate $Cs_2AgBiBr_6/WS_2$ local heterostructures via a low-cost mechanochemical approach to improve the optoelectronic properties, including the photodetection performance of a planar photodetector device. In the $Cs_2AgBiBr_6/WS_2$ heterostructure, the noticeable shift in the Raman A_{1g} and E_{2g} modes of WS_2 indicates the charge transfer and milling-induced strain, respectively. As compared to the bare

$Cs_2AgBiBr_6$, the heterostructure exhibits an improved current on/off ratio of 5.9×10^3, a high responsivity of 2.01 A W^{-1}, and a high specific detectivity of 3.6×10^{13} Jones under 405 nm light illumination. The high light-to-dark current ratio and efficient charge transfer are credited to enhanced charge carrier generation and collection of the photocarriers within the $Cs_2AgBiBr_6/WS_2$ heterostructure. This is supported by enhanced absorbance, photoluminescence (PL) quenching, and shortened photocarrier lifetime (from 3.65 ns to 0.82 ns). The $Cs_2AgBiBr_6/WS_2$ heterostructure is believed to form a local p-n junction at the interface, enhancing carrier separation. The resulting heterostructure exhibits a significant photocurrent even at 0 V bias, making the device self-powered in nature. The high linear dynamic range (LDR) (75 dB), fast photoresponse speed (80 ms/120 ms), and self-powered behavior signify promising prospects for low-power consumption optoelectronic devices in the future.

Chapter 4 explored the SERS performance of $Cs_2AgBiBr_6$ DP nanoflakes grown by the space confinement method. The self-trapped exciton (STE) defects were controlled by post-growth annealing of the sample under an argon (Ar) atmosphere, minimizing the Ag_{Bi} and Bi_{Ag} anti-site disorder. The sample with the highest STE defects demonstrates the highest SERS performance owing to the defect-assisted charge transfer process. We successfully identified methylene blue (MB) and rhodamine 6G (R6G) at concentrations as low as $\sim 10^{-10}$ M, achieving a remarkable SERS enhancement factor (EF) of 5.04×10^7 and 1.37×10^7, respectively, which is highly significant for a semiconductor-based SERS substrate. Additionally, notable amplification was observed for other cationic dyes, including crystal violet (CV), rhodamine B (RhB), and malachite green (MG). By varying the annealing temperature and the deconvolution of the photoluminescence spectra, we demonstrate a direct correlation between the defect density and the SERS signal intensity. To further understand the underlying enhancement mechanisms, we analyzed the individual contributions of chemical and electromagnetic enhancements to the overall SERS amplification. This analysis was conducted using finite element method (FEM) simulations and density functional theory (DFT) computations. These insights provide a foundational basis for designing highly efficient metal-free SERS substrates, opening new possibilities for advanced detection technologies.

Chapter 5 presents the heterostructure photodetector based on the $Cs_2AgBiBr_6$ single crystal (SC) and $Cs_3Bi_2I_9$ nanocrystals (NCs) to enhance the matrices of the device. $Cs_2AgBiBr_6$ DP SC was grown using the inverse temperature crystallization process. The mm-sized SC were synthesized using the above method. $Cs_3Bi_2I_9$ NCs were synthesized by a mechanical ball

milling system. The successful incorporation of $Cs_3Bi_2I_9$ NCs on top of the DP SC results in the reduction of the dark current, as well as enhancing the photocurrent of the device. Compared to the pristine $Cs_2AgBiBr_6$ SC device, the heterojunction configuration yielded a ~30-fold improvement in the on/off current ratio and an approximate six-fold enhancement in responsivity, reflecting superior photodetection performance. Ultraviolet photoelectron spectroscopy (UPS) revealed a type-II band alignment at the heterointerface, favouring charge separation and transport across the junction. Complementary density functional theory (DFT) calculations further corroborated significant electron transfer from the CBI NCs to the $Cs_2AgBiBr_6$ SC, in agreement with the observed device characteristics.

Chapter 6 summarizes the work done in the thesis and highlights its contributions to the study of $Cs_2AgBiBr_6$ DP and their HSs with other materials for various optoelectronic applications. The future scope of the work on LFHDP is presented at the end.

List of Publications

Journal Papers:

1. Ravinder Chahal, Abhilasha Bora, and P. K. Giri, Chemical Vapor Deposition Growth of Highly Stable Cs2AgBiBr6 Double Perovskite Thin Films and Their Ultralow Thermal Conductivity and Fast Photoresponse**, ACS Appl. Energy Mater., 2023, 6, 8794-8807.**
2. Ravinder Chahal, Abdul Kaium Mia, Abhilasha Bora, and P. K. Giri, Facile in situ synthesis of double perovskite Cs2AgBiBr6/WS2 heterostructure and interfacial charge transfer mediated high-performance ultraviolet photodetection, **J. Mater. Chem. C, 2024, 12, 12835.**
3. Ravinder Chahal, Sirsendu Ghosal, Joydip Ghosh, and P. K. Giri, Lead-free halide double perovskite nanoflakes as high-performance SERS substrate for detection of trace organic pollutants: chemical enhancement vs electromagnetic enhancement, **Nanoscale, 2025, 17, 9401-9417.**
4. Shipra Aswal, Shipra Aswal, Sirsendu Ghosal, Himanshu Murari, Ravinder Chahal, Viliam Vretenár, Ravi K Biroju, Ľubomír Vančo, Subhradip Ghosh, PK Giri, Anisotropic in-plane thermal transport in monolayer $ReSe_2$ and its modulation through layer control and selenium vacancies: experiment vs. theory, **Nanoscale, 2026, 18, 974-989.**
5. Ravinder Chahal, Koushik Ghosh, Shipra Aswal, Joydip Ghosh, and P. K. Giri, Low dark current and Type-II band Alignment in Double Perovskite Single Crystal $Cs_2AgBiBr_6/Cs_3Bi_2I_9$ Nanocrystals Heterojunction Enable High-Performance Photodetection. **J. Mater. Chem. C, 2026, DOI: 10.1039/D6TC00044D**.

Conference/Workshops attended:

1. Ravinder Chahal, and P. K. Giri, '*Lead-free halide double perovskite nanoflakes as high-performance SERS substrate for detection of Trace organic pollutants: chemical enhancement vs electromagnetic enhancement*', **Scientifique: Poster Presentation at RIC Integration'24**, 2024, IIT Guwahati. (Best Poster Award)
2. Ravinder Chahal, and P. K. Giri, '*Facile In-situ growth of double perovskite Cs2AgBiBr6/WS2 heterostructure and interfacial mediated charge transfer mediated high performance ultraviolet photodetection*, **ICANN 2023**, IIT Guwahati, 2023.
3. Ravinder Chahal, Abhilasha Bora, and P. K. Giri, '*Temperature dependent Raman studies and Thermal conductivity of CVD grown Cs2AgBiBr6 double perovskite thin film*' (**IUMRS-ICA**), IIT Jodhpur, 2022.
4. Ravinder Chahal, **'DAE BRNS National Workshop on Materials Chemistry (NWMC-2019)**, Manipal University, Rajasthan, 2019.

List of Abbreviations

Abbreviation	Description
1-L	Monolayer
2D	Two Dimensional
CVD	Chemical Vapor Deposition
CL	Cathodoluminescence
DRS	Diffuse Reflectance Spectroscopy
EDS	Energy Dispersive X-ray Spectroscopy
ETL	Electron Transport Layer
EQE	External Quantum Efficiency
FESEM	Field Emission Scanning Electron Microscopy
FETEM	Field Emission Transmission Electron Microscopy
FWHM	Full Width at Half Maxima
HRTEM	High Resolution Transmission Electron Microscopy
HTL	Hole Transport Layer
KPFM	Kelvin Probe Force Microscopy
LED	Light Emitting Diode
MACE	Metal-assisted Chemical Etching
NC	Nanocrystal
NIR	Near Infrared
NP	Nanoparticle
NW	Nanowire
PD	Photodetector
PCE	Power Conversion Efficiency
PL	Photoluminescence
QC	Quantum Confinement
QD	Quantum Dot
QY	Quantum Yield
STEM	Scanning Transmission Electron Microscopy
TEM	Transmission Electron Microscopy

TRPL	Time Resolved Photoluminescence
UV-Vis	Ultraviolet Visible
XPS	X-ray Photoelectron Spectroscopy
XRD	X-ray Diffraction

Chapter 1 Introduction

1.1 Introduction of Double Perovskites

In recent decades, significant advancements have been made in the synthesis, processing, and characterization of semiconductor nanostructures and thin films. These developments are largely motivated by the wide range of potential technological applications. Such applications include energy conversion and storage devices, integrated optoelectronic and photonic systems, and biosensors, among others. Since 2009, metal-halide perovskites have garnered considerable attention as a promising class of semiconducting materials.[1] This interest stems from their exceptional performance in solar cells and other optoelectronic devices. Key attributes contributing to their potential include a tunable optical bandgap, long electron-hole diffusion lengths, and high carrier mobility. Additionally, they offer the benefits of low-cost manufacturing and compatibility with low-temperature processing techniques.

Despite promising advances in lead-based three-dimensional (3D) hybrid perovskites for photoelectronic applications, their practical commercialization is still limited by several drawbacks. One is that they contain lead in their chemical composition, leading to severe toxicity problems. The environmental concerns related to lead have created serious questions about the practical uses of such materials. Pervasive use of lead-based perovskites would cause substantial environmental pollution, limiting their potential contribution to large-scale applications. To address this problem, several types of designs have been proposed. Among them, the most highlighted strategy is replacing lead with less cytotoxic or nontoxic metals. This alternative approach to the replacement strategy aims to identify new, environmentally safe, lead-free perovskites that retain their optoelectronic properties while minimizing their impact on both health and the environment. Substituting lead with other Group IVA metals, such as tin (Sn) and germanium (Ge), is perhaps the simplest strategy for the removal of lead from hybrid perovskites. This approach has led to the discovery of new lead-free compounds, such as $CH_3NH_3SnI_3$ and $CH_3NH_3GeI_3$.[2] The photovoltaic properties of these replacements, however, have not been equivalent to those of their lead-based analogues. One of the main drawbacks of these tin- and germanium-based perovskites is their poor resistance against oxidation. The 2^+ oxidation states of Sn and Ge oxidize easily to the 4^+ oxidation states, respectively. This oxidation process is responsible for the long-term phase instability observed in the material. Consequently, there is a growing research emphasis on identifying and developing novel lead-free perovskite alternatives. The goal is to resolve the toxicity challenges

while retaining the unique optoelectronic properties that make lead-based perovskites so promising for photovoltaic and related applications.

1.2 Metal Halide Double Perovskites

Metal Halide Perovskites (MHPs) generally follow the chemical formula ABX3, where A represents a monovalent cation (such as Cs^+, MA^+, FA^+, etc.), B is a divalent cation (e.g., Pb^{2+}, Sn^{2+}, Eu^{2+}, etc.), and X denotes a halide anion (Cl^-, Br^-, I^-). Although extensive research has been devoted to mitigating the toxicity and stability issues associated with lead-based perovskite solar cells, alternative B-site substitutions often introduce new challenges. For instance, Sn-based perovskites exhibit limited stability due to rapid oxidation, and Bi-based counterparts suffer from dimensional instability. To address these limitations, Slavney et al. pioneered the synthesis of a lead-free double perovskite by substituting lead with a combination of Bi^{3+} and Ag^+, resulting in a structurally stable elpasolite-type double perovskite with improved optoelectronic properties.[3] The halide double perovskites are generally represented by the chemical formula $A_2BB'X_6$, where A denotes a monovalent heavy metal cation, B is a monovalent cation, B' is a trivalent cation, and X is a halide anion. The tunability in composition through the selection of different A, B, B', and X ions enables the synthesis of a wide range of double perovskite materials exhibiting diverse optical properties. These compositional variations play a crucial role in tailoring the materials for specific optoelectronic applications. Building on recent advancements, $Cs_2AgBiBr_6$ double perovskite (DP) has emerged as a promising candidate for optoelectronic applications, offering excellent stability along with performance metrics that are relatively comparable to those of conventional perovskite materials.[3]

1.3 Crystal Structure of Double Perovskite

The heterovalent substitution strategy commonly employed in double perovskites involves replacing lead (Pb) with a combination of monovalent and trivalent metal cations, while preserving the three-dimensional connectivity of the perovskite lattice. At room temperature, $Cs_2AgBiBr_6$ adopts a cubic double perovskite structure with a space group of $Fm\bar{3}m$ and a lattice parameter of 11.27 Å.[4] This structure is characterized by a rock-salt-type ordering of corner-sharing $[AgBr_6]^{5-}$ and $[BiBr_6]^{3-}$ octahedra extending along all three crystallographic directions, with Cs^+ ions occupying the interstitial cavities of the framework. The spatial arrangements of these octahedra, including factors such as volumetric variation and distortion or tilting (primarily governed by bond lengths and bond angles), play a crucial role in

influencing the electronic structure, thereby dictating the optoelectronic properties of the material. In the ordered structure of $Cs_2AgBiBr_6$, the Ag-Br and Bi-Br bonds within the $[AgBr_6]^{5-}$ and $[BiBr_6]^{3-}$ octahedra maintain ideal bond angles of 90° or 180°, and the corresponding bond lengths are relatively similar, ranging from 2.804 Å to 2.828 Å.[5] Compared to $MAPbI_3$, the $Cs_2AgBiBr_6$ framework exhibits shorter bond lengths, indicating strong metal halide bonding and greater lattice stiffness, as the bonding electrons are more tightly bound to the constituent elements. The volume and distortions of these octahedra are influenced by several factors, including the ionic radii of the metal cations (1.15 Å for Ag^+ and 1.03 Å for Bi^{3+}), their respective electronegativities (1.93 for Ag^+ and 2.02 for Bi^{3+}), and the interactions with neighbouring octahedra. These parameters collectively contribute to a complex structural behaviour involving octahedral expansion or contraction, ultimately affecting the overall structural dynamics of the material.[5]

At room temperature, $Cs_2AgBiBr_6$ generally crystallizes in the $Fm\bar{3}m$ space group, adopting a face-centred cubic structure, as shown in **Fig. 1.1**. However, this high-symmetry phase is susceptible to phase transition under certain external conditions, such as temperature reduction, application of high pressure, or compositional modifications. Structural transformation into tetragonal, monoclinic, or triclinic phases has been observed under such perturbations. For instance, when the temperature is lowered to approximately 122K or a pressure of ~2.3 GPa is applied, the ambient cubic phase transitions to a tetragonal phase with the *I4/m* space group **(Fig. 1.1)**.[6–8] Similarly, substitution of Bi^{3+} with a specific fraction of Fe^{3+} induces a reduction in octahedral symmetry, thereby triggering a comparable phase transformation. [9]

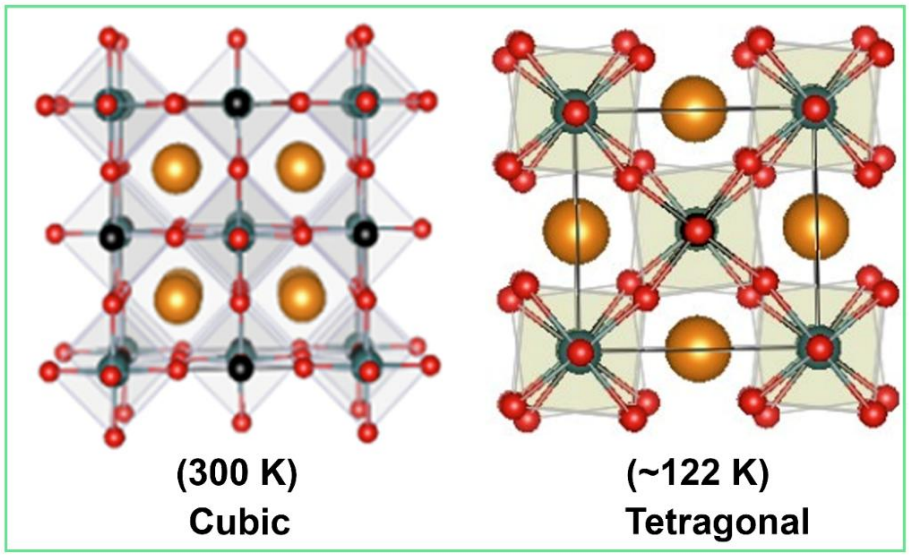

Fig. 1.1: Crystal structure of $Cs_2AgBiBr_6$ at 300 K and 122 K. Adapted from ref. [7].

The structural stability of these perovskites is often assessed using the octahedral factor and goldsmith tolerance factor, which provide theoretical guidelines for predicting the feasibility and robustness of the ABX_3 perovskite framework. The octahedral factor (μ) and tolerance factor (τ), both of which offer high predictive accuracy for structural stability, are defined based on the ionic radii and oxidation states of the constituent ions.[10]

$$\tau = \frac{r_A}{r_B} - n_A\left(n_A - \frac{\frac{r_A}{r_B}}{\ln\left(\frac{r_A}{r_B}\right)}\right) \qquad (i)$$

$$\mu = \frac{r_B}{r_X} \qquad (ii)$$

Specifically, r_i denotes the ionic radius of ion i, and n_i represents its oxidation state, with the condition $r_A > r_B$. A perovskite structure is generally considered stable when $\tau < 4.18$ and $0.44 < \mu > 0.90$. In the case of a double perovskite, such as Cs_2AgBiX_6 (X = Br, Cl), the effective radius r_B is approximated as the average of the radii of Ag+ and Bi3+. Accordingly, the calculated values of (μ, τ) for Cs_2AgBiX_6 fall within the stability range of 0.56 to 0.60 for μ and 4.07 to 4.21 for τ.[11] Additionally, the decomposition enthalpies (ΔH) for various possible degradation pathways, including CsBr, AgBr, Cs_2AgBr_3, $CsAgBr_2$, and $Cs_3Bi_2Br_9$, are found to be positive and notably higher than $MAPbI_3$. This implies that $Cs_2AgBiBr_6$ exhibits superior thermodynamic stability, making it a promising candidate for long-term optoelectronic applications.[12]

1.4 Band Structure of Double Perovskites

Investigating the electronic properties of the $Cs_2AgBiBr_6$ double perovskite is crucial for its application in optoelectronics. **Fig. 1.2(a)** represents the crystal structure of ordered and disordered $Cs_2AgBiBr_6$ double perovskite. The double perovskite materials generally exhibit an indirect bandgap due to high electron-phonon coupling and spin-orbit coupling. However, the bandgap values may show a slight variation depending on the computational methods (e.g., DFT with HSE06, GGA, or GW corrections).[13,14] To induce a direct bandgap in $Cs_2AgBiBr_6$, atomic substitutions were introduced within the supercell structure. Specifically, two face-centred Ag atoms were exchanged with Bi atoms, while the body-centred Bi atoms in the ordered supercell were replaced by an Ag atom. In the ordered structure, the conduction band minimum (CBM) appears at the L-point above the Fermi level. In contrast, the valence band maximum (VBM) is located at the Γ-point on the Fermi level, indicating an indirect band. The

calculated bandgap for the ordered $Cs_2AgBiBr_6$ double perovskite is found to be 2.04 eV. In the disordered $Cs_2AgBiBr_6$ structure, the Bi 6p orbitals notably influence the CBM from the L-point to the Γ-point. This transition converts the material from an indirect to a direct band gap semiconductor.[15] Additionally, a substantial reduction in the bandgap is observed, decreasing from 2.04 eV in the ordered phase to 1.59 eV in the disordered phase, as shown in **Fig. 1.2(b)**. This order-to-disorder transformation fundamentally alters the electronic band structure of $Cs_2AgbiBr_6$, thereby modifying its optoelectronic properties. A similar approach was used by Yang et al. to reduce the bandgap from 1.93 eV to 0.44 eV in a fully ordered $Cs_2AgBiBr_6$ double perovskite to a randomly oriented $Cs_2AgBiBr_6$ structure, respectively.[16]

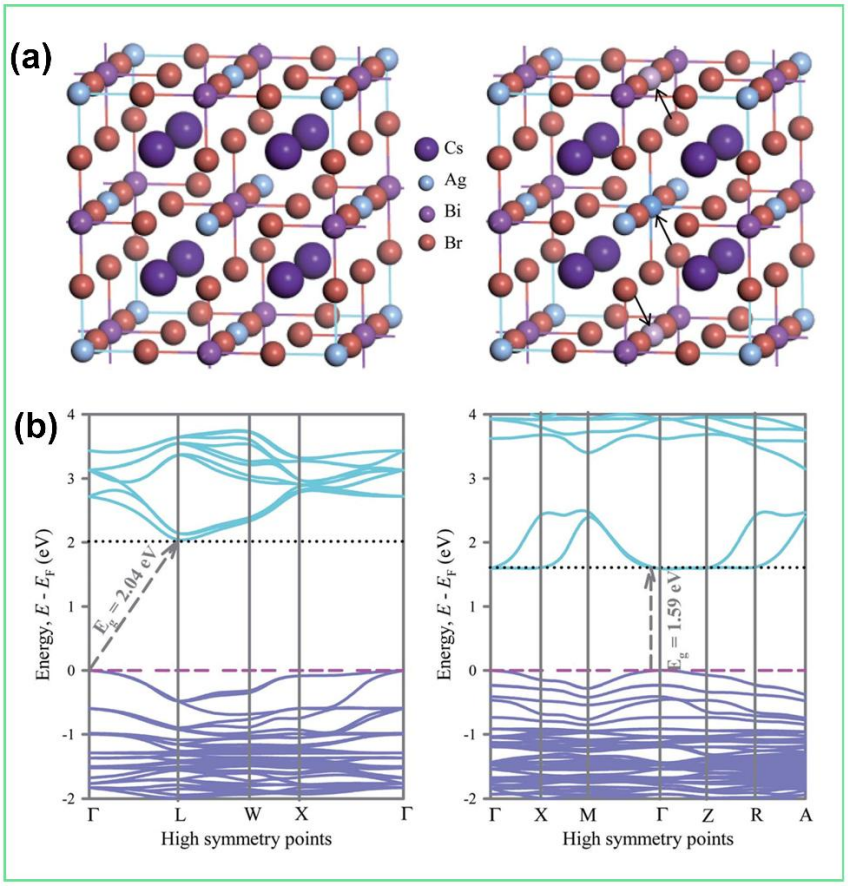

Fig. 1.2: (a) Ordered and disordered crystal structure of the $Cs_2AgBiBr_6$ double perovskite, respectively. **(b)** Corresponding band alignment of ordered and disordered $Cs_2AgBiBr_6$ Double perovskite. Adapted from ref. [14].

1.5 Key Features of Double Perovskites

Some of the important key features of double perovskite materials for optoelectronic applications are summarized below.

1.5.1 Bandgap Engineering

Owing to its relatively wide and suitable bandgap, $Cs_2AgBiBr_6$ double perovskite has emerged as a promising candidate for tandem solar cell applications. Recent developments in PSCs utilizing $Cs_2AgBiBr_6$-based double perovskites have achieved power conversion efficiencies (PSCs) exceeding 6%, underscoring the growing interest in further optimizing this material, particularly through bandgap engineering.[17] The material's light absorption ability, inherently linked to its electronic structure, is constrained by its bandgap, reported to be around 2.2 eV. Consequently, efforts to transform the material from an indirect to a direct bandgap semiconductor have shown promise in enhancing its optical absorption, thereby contributing to short circuit current density (Jsc) in solar cell performances.[16,18–20]

To modify the structure of $Cs_2AgBiBr_6$ and enhance its potential for improved PSCs, both physical and chemical strategies are commonly employed. Among physical methods, thermal and pressure treatments are particularly effective. These treatments can induce an order-disorder transition, leading to a narrowing of the bandgap in $Cs_2AgBiBr_6$-based double perovskites. Under high-pressure conditions, the applied pressure resulted in a significant bandgap reduction of 22.3%, shifting it from 2.2 eV to 1.7 eV. Notably, even after the pressure was released, the material retained a bandgap reduction of 8.2%, highlighting the partial reversibility and potential stability of the structural changes.[21] Moreover, it has been demonstrated that the degree of cation ordering in $Cs_2AgBiBr_6$ double perovskite is dependent on the temperature. At temperatures below 1200 K, partially disordered $Cs_2AgBiBr_6$ phases begin to form, with the extent of disorder progressively increasing as the temperature rises. A fully disordered phase is achieved at temperatures exceeding 3000 K.[16] These findings indicate that both temperature and pressure play critical roles in promoting structural disorder, which in turn leads to a reduction in the band gap of $Cs_2AgBiBr_6$.

Through a crystal engineering strategy, $Cs_2AgBiBr_6$ double perovskites have achieved the narrowest reported band gap of 1.72 eV. Single crystals were synthesized by carefully controlling the evaporation rate of the precursor solution at varying temperatures. Notably, crystals grown at a higher evaporation temperature (150 °C) exhibited a significant band gap reduction of approximately 0.26 eV compared to those formed at lower temperatures (60 °C), despite the crystal structure remaining largely unchanged. Theoretical studies attribute this band gap narrowing at elevated temperatures to an increased degree of Ag–Bi cation disorder, which introduces isolated defect states within the band structure, thereby reducing the effective band gap.[22]

Published studies have demonstrated that the band gap of $Cs_2AgBiBr_6$ crystals can be effectively tuned through functional doping, wherein partial substitution of Bi^{3+} with other trivalent cations such as In^{3+}, Sb^{3+}, and Ti^{3+} is employed to enhance the material's optoelectronic properties.[23] Experimental results reveal that the band gap may either increase or decrease depending on the specific dopant introduced. For instance, Sb doping leads to band gap reduction, while In doping results in an increase. In particular, $Cs_2AgBi_{0.625}Sb_{0.375}Br_6$ exhibits a reduced band gap of approximately 1.86 eV, whereas $Cs_2AgBi_{0.25}In_{0.75}Br_6$ shows an increased band gap of about 2.27 eV.[24] This band gap modulation directly influences the material's color, thereby enabling absorption across different spectral ranges and expanding its potential for application in optoelectronic devices.

1.5.2 Charge Carrier Dynamics

Key parameters such as carrier lifetime, mobility, and the rate of non-radiative electron–hole recombination play a crucial role in determining the photovoltaic efficiency of perovskite solar cells (PSCs). Time-resolved photoluminescence (TRPL) measurements on $Cs_2AgBiBr_6$ single crystals reveal an initial rapid decay followed by a slower tail, indicative of long-lived charge carriers. The room-temperature TRPL decay time reaches up to ~660 ns.[25] Complementary transient absorption spectroscopy studies estimate the charge carrier lifetime to be approximately 1.4 μs, which is notably longer than that observed in conventional lead-based halide perovskites. This prolonged microsecond-scale lifetime enhances charge extraction and transport, making $Cs_2AgBiBr_6$ a highly promising lead-free light absorber for next-generation PSCs. Despite promising results, the charge carrier dynamics in $Cs_2AgBiBr_6$ remain under investigation and are subject to ongoing debate. Bartesaghi et al. employed time-resolved microwave conductance measurements to explore charge carrier generation and recombination mechanisms at both the bulk and surface levels.[26] They proposed a comprehensive kinetic model for charge carrier recombination in $Cs_2AgBiBr_6$. Upon laser excitation (process 1), photoinduced electrons and holes are generated in the conduction band (CB) and valence band (VB), respectively. Recombination may occur via two primary pathways: band-to-band recombination (process 2) and surface-state-mediated recombination (process 3). Additionally, trap states present within the bulk can capture charge carriers (process 4), which may subsequently be thermally released back to the band edges (process 5). For convenience, the self-trapped exciton (STE) emission may be denoted as Process 5 (**Fig. 1.3(a)**). The recombination pathways associated with Processes 2, 3, and 5 collectively account for the experimentally observed photoluminescence (PL) spectra of $Cs_2AgBiBr_6$. Simultaneously,

competitive non-radiative recombination can occur through deep-level bandgap defects and surface or interface trap states and can be represented as Process 6.[26] This model highlights the complex interplay between various recombination pathways and the role of trap states in influencing charge carrier behaviour in $Cs_2AgBiBr_6$.

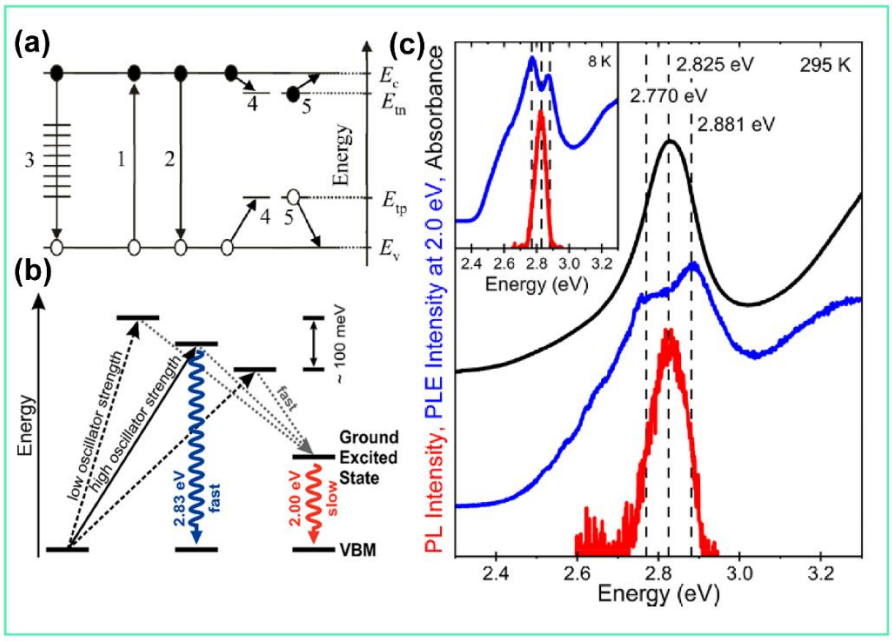

Fig. 1.3: (a) Band structure schematic of $Cs_2AgBiBr_6$ illustrating a comprehensive kinetic model for charge carrier recombination. **(b)** Schematic illustration of relaxation and recombination of charge carriers excited at resonant energy in $Cs_2AgBiBr_6$. **(c)** Energetic substructure of the resonant absorption feature at room temperature. Main panel: Absorbance (black), high-energy photoluminescence spectrum (red), and photoluminescence excitation spectrum (blue) recorded at an emission energy of 2.0 eV at room temperature. Inset: High-energy photoluminescence spectrum (red) and photoluminescence excitation spectrum (blue) of the same sample at 8 K. Adopted from ref. [25, 26].

Bartesaghi et al. proposed that trap-assisted recombination at surface states occurs rapidly and dominates as the primary recombination mechanism in thin-film $Cs_2AgBiBr_6$, whereas in the bulk, electron and hole trap states are relatively shallow, leading to a slower recombination rate. In contrast, Kentsch et al. employed femtosecond UV–vis–NIR transient absorption spectroscopy to investigate the photophysical behaviour of $Cs_2AgBiBr_6$ and provided evidence for the presence of excitons, along with strong electron–phonon coupling mediated by Fröhlich interactions (**Fig. 1.3(b)**). This behaviour is similar to that observed in other Bi-based materials, such as Cs_3Bi_2Br9 and $BiBr_3$. However, the study also indicated that these electron–phonon interactions, along with the presence of excitons, could contribute to unwanted charge carrier recombination, potentially affecting the overall photovoltaic performance of the material.[27] A

temperature-dependent analysis of the emission line width revealed a Fröhlich coupling constant of approximately 230 meV for $Cs_2AgBiBr_6$, which is significantly higher than that of traditional lead-based halide perovskites (typically 40–60 meV).[28] The pronounced absorption peak at 2.83 eV in $Cs_2AgBiBr_6$ consists of multiple electronic transitions (**Fig. 1.3(c)**), exhibiting a well-resolved energetic splitting exceeding 100 meV.[29] Additionally, the material exhibits temperature-dependent charge carrier mobility, following a T^{-p} relationship ($p \approx 1.5$), and the mobility is comparatively lower than that observed in lead-based counterparts.[30] This trend indicates that phonon scattering is the dominant factor limiting mobility, aligning with behaviours observed in Pb-based perovskites. Nonetheless, the extended charge carrier lifetime in $Cs_2AgBiBr_6$ compensates for the lower mobility, offering favourable conditions for efficient charge carrier transport.

Nevertheless, several factors–such as the formation of excitons and strong electron–phonon interactions–facilitate charge carrier recombination in $Cs_2AgBiBr_6$. Despite recent advancements, the charge carrier dynamics of this material remain not fully understood and continue to be a subject of scientific debate, warranting further in-depth investigation to clarify the underlying mechanisms.

1.5.3 Defect Tolerance

Ideally, all atoms in a semiconductor crystal lattice should occupy their designated positions without any imperfections or impurities. However, in practice, various types of defects inevitably form during material synthesis and processing. These defects are generally categorized as point defects (e.g., vacancies, interstitials, and antisite defects), line defects (e.g., dislocations), plane defects (e.g., surfaces and grain boundaries), and bulk defects (e.g., voids and precipitates). A thorough understanding of such defects at the fundamental level is essential for the development of high-performance optoelectronic devices, as they play a critical role in influencing charge carrier transport and recombination dynamics within perovskite materials and device architectures. Lead-based perovskites are known for their exceptional defect tolerance, primarily because most of the defects introduced during synthesis are shallow-level states, located just above the valence band maximum (VBM) or just below the conduction band minimum (CBM).[31–33] As a result, these defects exert only a minimal influence on key optoelectronic properties, such as charge carrier mobility and lifetime. This remarkable tolerance is attributed to several intrinsic features of lead-based perovskites, including the strong antibonding interactions involving Pb^{2+} lone-pair orbitals, crystallographic symmetry,

high ionic character, and a large lattice constant, all of which help mitigate the detrimental effects typically associated with structural defects.[34]

In contrast to lead-free perovskites, $Cs_2AgBiBr_6$ exhibits a markedly different defect landscape, primarily due to the presence of two distinct B-site cations (Ag^+ and Bi^{3+}).[35–37] **Fig. 1.4 (a, b)** illustrate the formation enthalpies of common point defects in $Cs_2AgBiBr_6$ under Br-rich and Br-poor conditions, respectively, while **Fig. 1.4 (c, d)** summarize the thermodynamic transition energy levels of these defects. To obtain these insights, density functional theory (DFT) calculations were performed using the Heyd-Scuseria-Ernzerhof (HSE) hybrid functional with spin–orbit coupling (SOC), based on Perdew-Burke-Ernzerhof (PBE) optimized geometries.[35,38–40] A comprehensive set of twenty distinct point defects was analyzed, including vacancies, interstitials, cation-on-anion antisites, and anion-on-cation antisites, to understand their energetic behavior and impact on the material's defect chemistry. Based on the computational analysis of $Cs_2AgBiBr_6$, several key conclusions can be drawn regarding its defect chemistry: (i) Among all point defects, Ag vacancies (V_{Ag}) are the most readily formed, even under Ag-rich conditions, due to their lowest formation enthalpy. These defects act as shallow acceptors, contributing to the material's intrinsic p-type conductivity without significantly degrading its optoelectronic properties.[40] (ii) In contrast, certain defects–such as Br vacancies (V_{Br}), Bi vacancies (V_{Bi}), Bi-on-Ag (Bi_{Ag}), and Ag-on-Bi (Ag_{Bi}) antisites–are identified as deep-level acceptor defects, typically located within the middle third of the bandgap. Although they may also have relatively low formation energies, these deep traps are not thermally ionized; instead, they serve as non-radiative recombination centers, governed by Shockley-Read-Hall (SRH) recombination. These centers critically reduce carrier lifetimes and ultimately degrade device performance by eliminating photogenerated charge carriers.[41] (iii) Unlike lead-based perovskites, $Cs_2AgBiBr_6$ demonstrates a relatively low defect tolerance, primarily due to the presence of a greater number of deep-level defects. However, this does not necessarily indicate a higher density of trap states. Reported trap densities for $Cs_2AgBiBr_6$ are moderate, with values around 1.7×10^9 cm^{-3} for single crystals and approximately 10^{16}–10^{17} cm^{-3} in thin films or devices.[42–44] Beyond isolated point defects, many of these deep-level states are associated with higher-dimensional defects, such as those located at surfaces or grain boundaries. Therefore, careful control over the crystal growth conditions is essential to suppress the formation of such detrimental deep-level traps. Moreover, discrepancies in the reported literature may stem from the fact that defect formation energies and types are highly

sensitive to variations in the chemical environment and the computational methodologies employed.

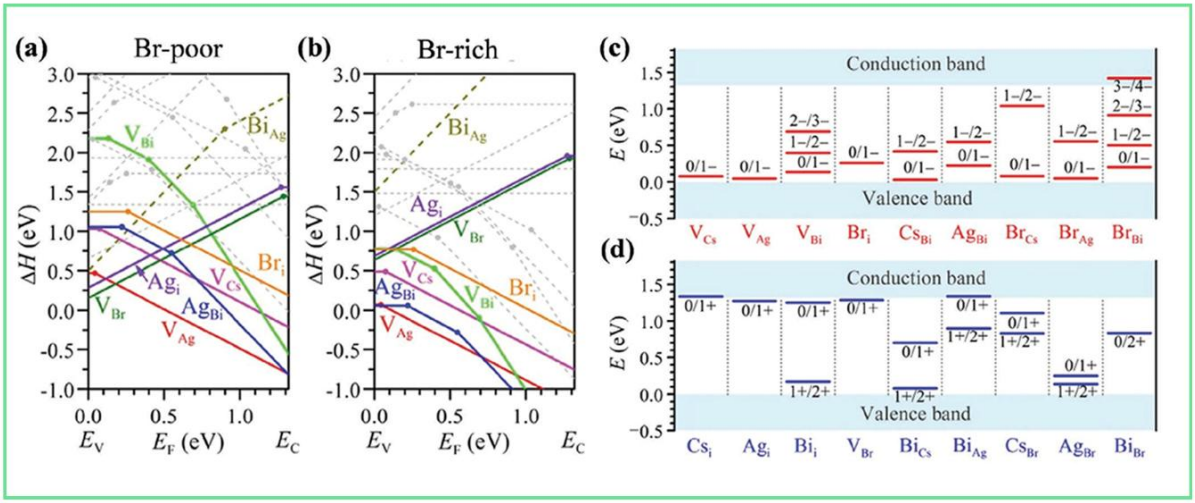

Fig. 1.4: The formation enthalpies (ΔH) of intrinsic defects in $Cs_2AgBiBr_6$ calculated under **(a)** Br-poor and **(b)** Br-rich conditions as a function of the Fermi level (E_F), with dashed lines representing defects exhibiting exceptionally high ΔH values. The transition energy levels E(eV) calculated for **(c)** intrinsic donor and **(d)** intrinsic acceptor defects. Adapted from ref. [34].

1.6 Fabrication of Double Perovskite Thin Films

The synthesis of $Cs_2AgBiBr_6$ in various morphologies–including single crystals, thin films, nanocrystals, and quantum dots–can be achieved through relatively straightforward methods. Bulk single crystals of this double perovskite have been successfully grown using several techniques, such as cooling-induced crystallization, inverse temperature crystallization, antisolvent vapor crystallization, and delayed solvent evaporation.[25,45,46] High-quality $Cs_2AgBiBr_6$ thin films can also be fabricated through one-step solution-based deposition methods like spin-coating or spray-coating, provided that the precursor stoichiometry is carefully optimized. However, thin films prepared via vacuum evaporation may suffer from halogen deficiencies, potentially leading to the formation of additional point defects. Furthermore, nanocrystals and quantum dots of $Cs_2AgBiBr_6$ with high phase purity, uniform morphology, and excellent crystallinity have been synthesized using hot-injection and ligand-assisted reprecipitation approaches. Here, we summarize some of the commonly used synthesis approaches for $Cs_2AgBiBr_6$ double perovskite.

1.6.1 Solution Process

Chemical solution deposition is a widely employed technique for fabricating thin films, wherein electrochemical or chemical reactions facilitate the formation of a uniform layer on the substrate surface. This method is characterized by its efficient material utilization, low energy requirements, and the capability to produce films with excellent compositional homogeneity and controlled stoichiometry. Additionally, it offers advantages in tailoring the particle size, morphology, and crystallographic orientation of the resulting materials.[47–49] The technique has been extensively adapted for the fabrication of hybrid perovskite films. Common approaches under this category include the scraping method, soaking method, two-step, and one-step deposition processes. Among these, the one-step method is predominantly used for synthesizing $A_2BB'X_6$-type double perovskites, primarily due to its simplicity and compatibility with diverse precursor solubilities.[49] Nevertheless, the exploration and refinement of alternative methods remain an important area of ongoing research.

The fabrication and integration of $Cs_2AgBiBr_6$ thin films into functional devices was first reported in 2017.[50] In this pioneering study, a heated precursor solution was spin-coated onto the electron transport layer at 2000 rpm, followed by thermal annealing at 285 °C for five minutes to achieve a pure-phase film. Motivated by the promising outcomes of earlier efforts, researchers have continued to explore and optimize thin film preparation techniques. For instance, Wang et al. prepared a perovskite precursor solution by dissolving CsBr, AgBr, and $BiBr_3$ in dimethyl sulfoxide (DMSO). Using a one-step spin-coating process, the precursor was uniformly deposited onto the electron transport layer, and subsequent annealing yielded films with well-defined morphology and phase purity.[51] In another approach, films were also formed by soaking the substrate in an indole dye solution, followed by a drying step.

Recent studies have highlighted anti-solvent-assisted crystallization as an effective strategy for synthesizing high-quality double perovskite crystals with significantly reduced root mean square (RMS) surface roughness (**Fig. 1.5(a)**).[52] However, the fabrication of such crystals remains challenging due to the relatively high processing temperatures required—approximately 500 °C for solid-state reactions and 110 °C for solution-based preparations. Furthermore, thermal annealing at around 285 °C is generally necessary to achieve optimal crystallinity and film quality. Lei et al. developed a one-step spin-coating technique combined with low-pressure drying to deposit $Cs_2AgBiBr_6$ thin films on Au electrodes (**Fig. 1.5(b)**).[53] In this method, precursor salts—CsBr, AgBr, and $BiBr_3$—were dissolved in dimethyl sulfoxide

(DMSO) at a concentration of 0.5 mol/L. The resulting films exhibited an average particle size of approximately 100 nm but also showed relatively high surface roughness.[54]

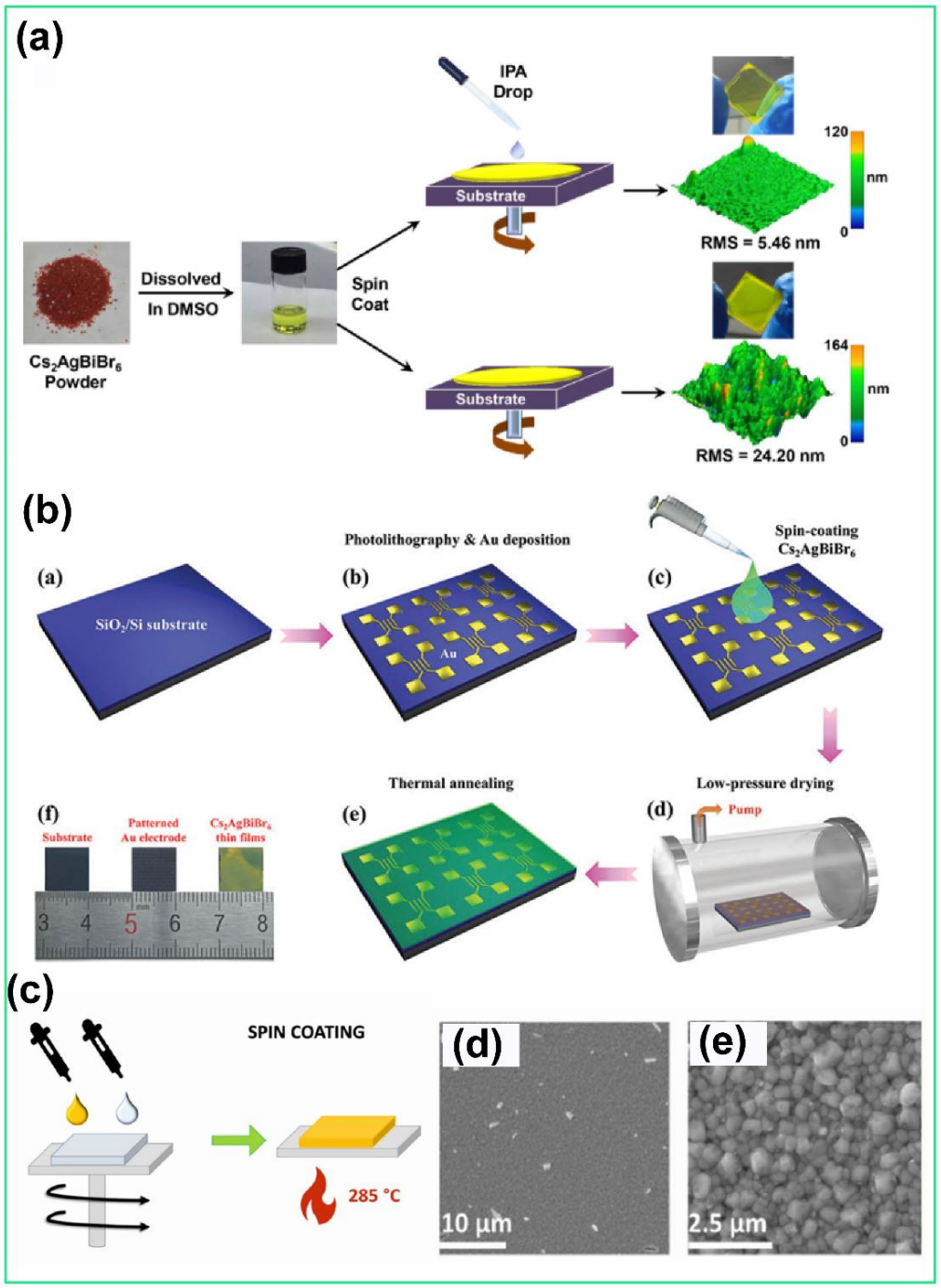

Fig. 1.5: (a) Schematic of the antisolvent-assisted crystallization spin coating process for deposition of $Cs_2AgBiBr_6$ double perovskite thin film. **(b)** Schematic of the low-pressure assisted vacuum drying spin coating, thin film deposition process. **(c)** Schematic representation of the blade coating technique for the thin film deposition of $Cs_2AgBiBr_6$ double perovskite. **(d, e)** Low and high-magnification SEM images of the thin film deposited by the blade coating technique. Adapted from ref. [52], [53] and [54].

Scanning electron microscopy (SEM) images revealed the presence of pinholes, indicating suboptimal film quality, which was attributed to the rapid solvent evaporation induced by the low-pressure drying process.

To enhance device performance and ensure reproducibility, the focus was placed on deposition techniques capable of producing uniform perovskite layers. In this context, blade coating was identified as a promising alternative to conventional spin-coating, offering advantages such as material efficiency and scalability.[55] Although spin-coating remains the most employed method for fabricating thin perovskite films, it is not without limitations—many of which arise inherently from the technique itself. In the blade-coating deposition method, reported by Barichello et al., a wet thin film is formed by uniformly spreading the precursor solution across the substrate using a blade. Several parameters critically influence the resulting film thickness, including the blade-to-substrate distance, substrate temperature, air-jet presence and intensity, and the velocity of the blade movement.[56] Notably, unlike certain other techniques, blade-coating does not require the use of an anti-solvent (**Fig. 1.5 (c)**); instead, film formation is facilitated through the combined effects of substrate heating and air-jet-assisted drying. **Fig. 1.5(d, e)** displays the SEM images of the compact thin films fabricated using the blade-coating technique.

1.6.2 Vacuum Deposition

Vapor deposition is a widely adopted method for thin film fabrication; however, it necessitates operation under vacuum conditions, thereby increasing equipment complexity and cost.[57] While effective, the development of double perovskite thin films via vapor deposition has progressed slowly, primarily due to the involvement of multiple material components and the technological challenges associated with the process.[58]

In 2018, Wang et al. reported the first successful fabrication of $Cs_2AgBiBr_6$ thin films using a successive vapor deposition approach.[59] The sequential deposition order of AgBr, $BiBr_3$, and CsBr onto the substrate plays a critical role, as the post-deposition annealing step facilitates the necessary diffusion-driven reactions. Notably, $BiBr_3$ contributes significantly to crystal growth and the suppression of impurity phases. To achieve high-quality films, the molar ratio of $BiBr_3$:AgBr:CsBr is carefully optimized within the range of 1:1:2 to 1.5:1:2. During the vacuum-assisted process, the substrate is positioned approximately 27 cm above the evaporation source and is rotated at a speed of 9 r/min to ensure uniform film formation (**Fig. 1.6(a)**). As reported by Wang et al., sequential vapor deposition of $Cs_2AgBiCl_6$ involves the

successive layering of CsCl, $BiCl_3$, and AgCl under high-vacuum conditions, specifically at pressures below 1×10^{-3} Pa.[60] This method can yield film thicknesses of up to 110 nm in a single deposition cycle. Upon annealing at 180 °C, a phase-pure $Cs_2AgBiCl_6$ film with well-oriented crystallization was obtained. Although the process is more complex and time-intensive compared to spin-coating, it results in superior crystallinity and phase purity.

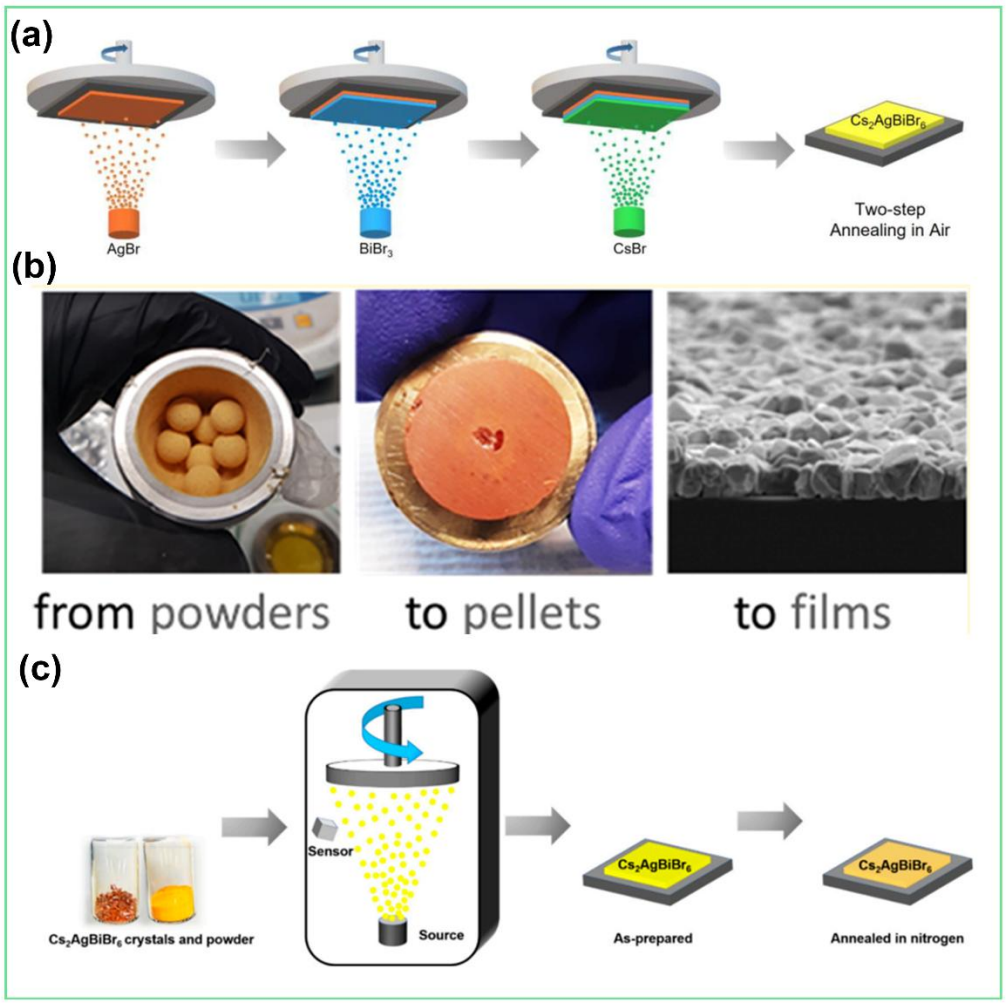

Fig. 1.6: (a) Schematic illustration of the sequential vapor deposition technique for the growth of $Cs_2AgBiBr_6$ double perovskite thin film. **(b)** Schematic illustration of the thin film deposition route of $Cs_2AgBiBr_6$ double perovskite by pulsed laser deposition technique. **(c)** Schematic representation of one-step vapor deposition growth of $Cs_2AgBiBr_6$ double perovskite thin film. Adapted from ref. [59], [61], and [62].

In 2021, researchers employed a ball milling method to synthesize $Cs_2AgBiBr_6$ powder and proposed pulsed laser deposition (PLD) as a viable approach for thin film fabrication.[61] The milled powder was compacted into a disk-shaped target under a uniaxial pressure of 600 MPa and subsequently subjected to laser ablation in an argon atmosphere (**Fig. 1.6(b)**). Film

deposition at 200 °C resulted in the formation of a continuous coating with a thickness ranging from 200 to 300 nm. This technique is particularly advantageous for multicomponent systems, as it enables near-stoichiometric material transfer—an essential factor in promoting high-quality thin film growth.

Fan et al. successfully fabricated high-quality $Cs_2AgBiBr_6$ double perovskite thin films using the single-source vapor deposition method. Initially, $Cs_2AgBiBr_6$ crystals were synthesized through a modified crystallization process in which a 2:1:1 molar ratio of CsBr, AgBr, and $BiBr_3$ was sequentially dissolved in 12 mL of 48% hydrobromic acid (HBr) within a clear glass vial. The resulting crystals were subsequently ground into fine powder to serve as the deposition source. For film deposition, the $Cs_2AgBiBr_6$ powder was placed in a tungsten boat, while pre-cleaned fluorine-doped tin oxide (FTO) substrates were mounted on a movable holder positioned above the evaporation source.[62] In the single-source vapor deposition setup shown in **Fig. 1.6(c)**, the distance between the evaporation source and the substrate was maintained at approximately 20 cm. The perovskite powder was gradually evaporated by increasing the heating current from 0 A to 120 A at a controlled rate of 20 A/min, once the vacuum chamber pressure reached 5.0×10^{-4} Pa. During the deposition process, the substrate holder was continuously rotated at 20 rpm to ensure uniform film coverage. Complete evaporation of the $Cs_2AgBiBr_6$ powder occurred within a few minutes, resulting in film formation. The performance of the resulting perovskite solar cells (PSCs) was optimized by systematically varying the post-annealing temperature (150 °C, 250 °C, 300 °C, and 350 °C), annealing duration (5, 15, 30, and 65 minutes), and film thickness (167 nm, 238 nm, and 297 nm). Post-annealing at 300 °C was found to yield high-quality $Cs_2AgBiBr_6$ thin films with optimal crystallinity and phase purity.[62] However, annealing at temperatures above 300 °C led to the emergence of impurity phases. Within this optimal temperature, the ideal annealing duration was identified to be between 15 and 30 minutes. Extended annealing beyond this time frame resulted in the appearance of secondary diffraction peaks, indicating the onset of phase decomposition or the formation of secondary phases.

1.7 Fabrication of $Cs_2AgBiBr_6$ Nanostructures

The commonly used techniques for synthesizing nanostructures of $Cs_2AgBiBr_6$ double perovskite are hot injection and the antisolvent method.[63–70] **Fig. 1.7(a)** illustrates the colloidal synthesis of lead-free halide double perovskite nanocrystals (NCs). $Cs_2AgBiBr_6$ NCs were synthesized under inert conditions using the hot-injection method with a standard Schlenk line

apparatus. Initially, 1 mmol of $AgNO_3$ was dissolved in 1 mL of trioctylphosphine (TOP) inside a nitrogen-filled glove box by stirring overnight at room temperature, resulting in a clear and transparent solution. The strong coordination between silver ions and TOP leads to the formation of a stable Ag–TOP complex, accounting for the high solubility of $AgNO_3$ in TOP—an interaction similar to that previously observed with indium and lead precursors. In the next step, a mixture containing bismuth neodecanoate and caesium carbonate, along with oleic acid, oleylamine, and octadecene, was degassed at 110 °C under continuous argon flow to ensure an oxygen- and moisture-free environment for subsequent reactions. Once the bismuth and caesium precursors were fully dissolved in the reaction mixture, the pre-prepared Ag–TOP complex was swiftly injected into the heated solution. Subsequently, benzoyl bromide was rapidly introduced into the reaction mixture, triggering an immediate colour change from pale yellow to orange. This distinct colour transition indicated the successful formation of $Cs_2AgBiBr_6$ NCs.[71]

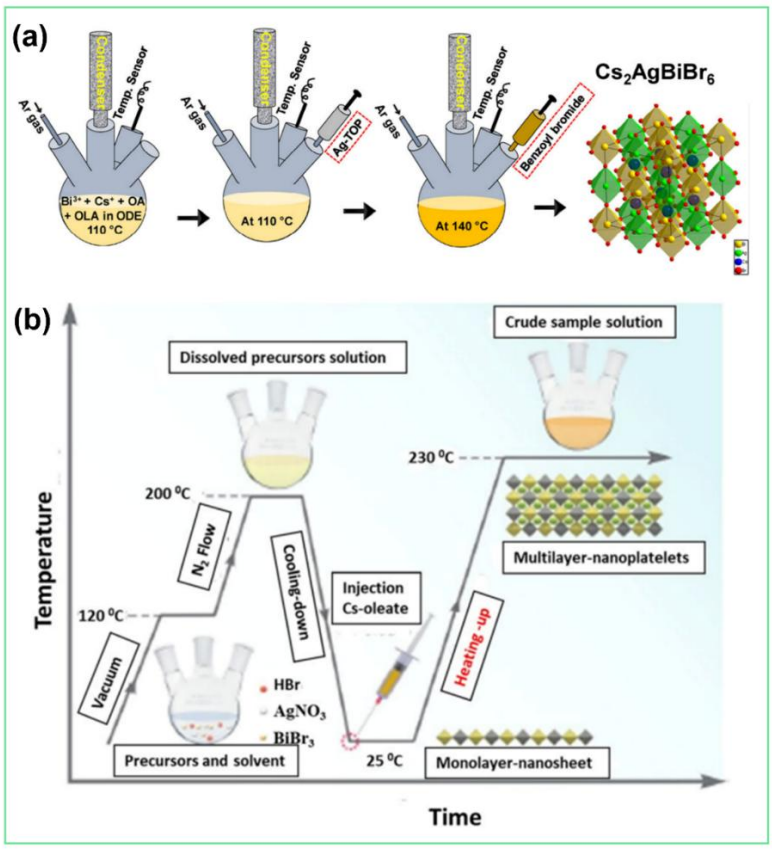

Fig. 1.7: (a) Schematic illustration of colloidal synthesis of $Cs_2AgBiBr_6$ double perovskite NCs using the hot-injection technique. **(b)** Schematic illustration of $Cs_2AgBiBr_6$ double perovskite nanoplatelets using the hot-injection technique. Adopted from ref. [71] and [72].

Fig. 1.7(b) illustrates the synthetic pathway for lead-free Cs_2AgBiX_6 double perovskite nanoplatelets (NPLs). In a typical synthesis of $Cs_2AgBiBr_6$ NPLs, $BiBr_3$, $AgNO_3$, HBr, oleic acid, oleylamine, and 1-octadecene were combined in a reaction flask, followed by degassing at 120 °C. The mixture was then heated to 200 °C under a nitrogen atmosphere to form a homogeneous solution. After allowing the reaction mixture to cool to room temperature, a pre-prepared Cs-oleate precursor solution was injected to initiate the nucleation of $Cs_2AgBiBr_6$ cluster-based nanosheets. Subsequent heating of the mixture to 230 °C for 10 minutes led to the formation of multilayer NPLs.[72] The second approach, recrystallization, entails dissolving the precursor in DMSO, followed by the addition of isopropanol under vigorous stirring. The resulting mixture is then subjected to centrifugation to isolate $Cs_2AgBiBr_6$ NCs. In contrast to the products obtained via previous synthesis methods, this technique yields quasi-spherical NCs. However, the underlying mechanism governing the morphological evolution of these nanocrystals remains unclear.

1.8 Optoelectronic Applications of $Cs_2AgBiBr_6$ Double Perovskites

$Cs_2AgBiBr_6$ has emerged as a promising lead-free double perovskite material due to its exceptional stability, non-toxic nature, notable optoelectronic properties, and multifunctional applicability, positioning it as a viable alternative to conventional lead-based perovskites.[73] **Fig. 1.8** shows the multidisciplinary applications of $Cs_2AgBiBr_6$ double perovskites.

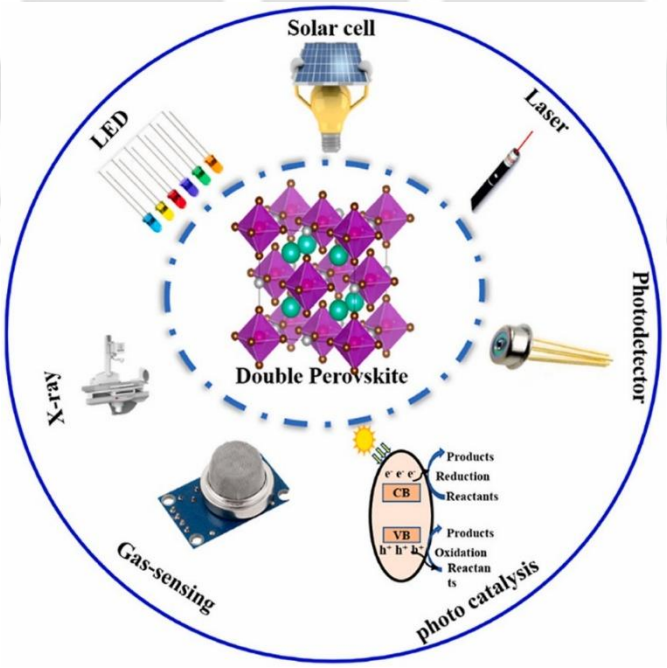

Fig. 1.8: Schematic illustration of the multifunctional applications of double perovskites. Adopted from ref. [73].

Some of the important optoelectronic applications of $Cs_2AgBiBr_6$ double perovskites are summarized below.

1.8.1 Solar Cell

The initial synthesis of $Cs_2AgBiBr_6$ showcased its potential for photovoltaic applications, highlighted by an electron–hole pair lifetime of approximately 660 ns and an optical bandgap of around 1.95 eV.[3] In the realm of lead-free photovoltaics, theoretical studies have predicted a power conversion efficiency (PCE) of nearly 16% for solar cells based on $Cs_2AgBiBr_6$ double halide perovskites.[74–76] Early research efforts primarily centered on Ag–Bi-based double perovskites, such as Cs_2AgBiX_6 (X= Br, Cl), due to their distinct excitonic behavior and indirect bandgap in the range of 2.0–2.3 eV. Furthermore, Islam et al. explored a non-toxic, fully inorganic photovoltaic device architecture through simulation studies, employing $Cs_2AgBiBr_6$ as the active layer and Cu_2O as the hole transport layer (HTL). At an optimized perovskite layer thickness of 600 nm, a maximum power conversion efficiency (PCE) of 7.25% was achieved[74], corresponding to an open-circuit voltage (VOC) of 1.5 V, short-circuit current density (JSC) of 11.45 mA/cm^2, and a fill factor (FF) of 42.1%. Further performance enhancement was demonstrated through numerical simulations using the Solar Cell Capacitance Simulator in one dimension (SCAPS-1D), applied to the lead-free double perovskite composition $Cs_2AgBi_{0.75}Sb_{0.25}Br_6$, a mixed bismuth–antimony halide system. By optimizing the perovskite absorber layer thickness along with the hole and electron transport layers (HTL and ETL), a theoretical PCE of 18% was reported.[77] The simulated optimal photovoltaic parameters were VOC = 1.39 V, JSC = 16.04 mA/cm^2, and FF = 78.34%, indicating that $Cs_2AgBi_{0.75}Sb_{0.25}Br_6$ is an auspicious absorber material for the development of efficient lead-free double halide perovskite solar cells.

Greul et al. conducted the first investigation into $Cs_2AgBiBr_6$-based double halide PSCs employing a mesostructured architecture, where large agglomerates were observed within the perovskite film.[48] **Fig. 1.9(a)** represents the I-V curve and the corresponding band alignment of the resulting device. Their study reported abnormal hysteresis behaviour in the device. Upon optimization, an inverted planar heterojunction solar cell incorporating $Cs_2AgBiBr_6$ achieved a power conversion efficiency (PCE) of 2.23%, with a V_{OC} of 1.01 V, J_{SC} of 3.19 mA/cm², and a fill factor (FF) of 69.2%.[50] **Fig. 1.9(b)** shows the I-V curve and the corresponding device architecture of $Cs_2AgBiBr_6$ double perovskite with the ETL and HTL. Notably, the device demonstrated excellent operational stability and minimal hysteresis. The enhanced performance observed in planar-structured $Cs_2AgBiBr_6$-based PSCs is largely attributed to the

significantly longer electron diffusion length relative to that of holes. To further investigate the photovoltaic performance of $Cs_2AgBiBr_6$ double perovskites, a planar n–i–p structured solar cell was fabricated using SnO_2 and poly(3-hexylthiophene-2,5-diyl) (P3HT) as the electron transport layer (ETL) and hole transport material (HTM), respectively, with the device configuration ITO/SnO_2/$Cs_2AgBiBr_6$/P3HT/Au. An increase in the annealing temperature from 150°C to 250°C resulted in a corresponding enhancement in device performance.

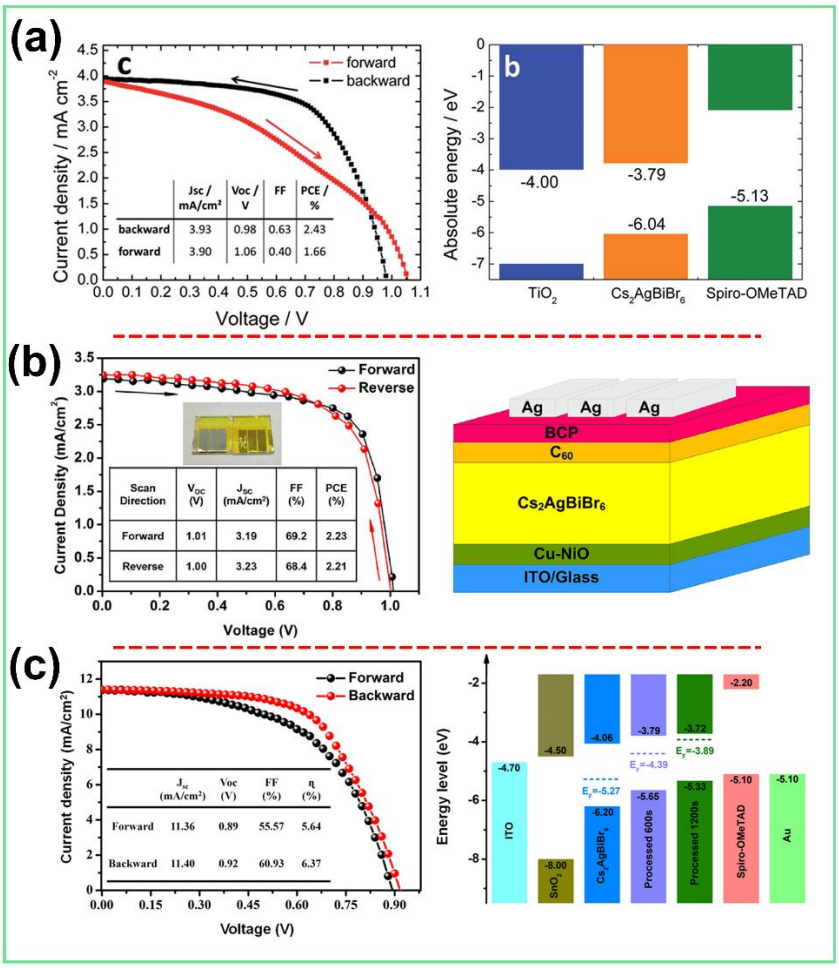

Fig. 1.9: (a) I-V curve of the $Cs_2AgBiBr_6$ double perovskite solar cell device in forward and reverse direction and the corresponding band alignment. The inset shows the table highlighting the PCE of the device. **(b)** I-V curve of the $Cs_2AgBiBr_6$ double perovskite with the corresponding device architecture. The inset shows the device image and the PCE table. **(c)** I-V curve of the hydrogenated $Cs_2AgBiBr_6$ device and the corresponding band alignment. The inset shows the PCE table. Adopted from ref. [48], [50] and [17].

Specifically, the PCE improved from 0.57% to 1.37%, the fill factor (FF) increased from 0.67 to 0.72, the J_{SC} rose from 0.78 to 1.78 mA/cm^2, and the V_{OC} increased from 1.03 V to 1.07 V.[52] Furthermore, additional strategies—such as incorporating dye interlayers or utilizing photo-

sensitive ETL/HTL materials—have been explored to enhance the efficiency of double perovskite solar cells.[78] Zhang et al. achieved the highest reported PCE for $Cs_2AgBiBr_6$-based double perovskite solar cells through interstitial hydrogen doping.[17] This hydrogenation strategy effectively reduced the material's bandgap from 2.18 eV to 1.64 eV, thereby extending the absorption range to cover the entire visible spectrum. The corresponding current–voltage (I–V) characteristics, along with the device architecture, are illustrated in **Fig. 1.9(c)**. Nevertheless, the experimentally achieved PCEs remain below the theoretically predicted values, indicating significant scope for further optimization and the exploration of new strategies to enhance device efficiency.

1.8.2 X-ray Detection

Recently, solution-processed $Cs_2AgBiBr_6$ single crystals have been employed in the fabrication of highly sensitive X-ray detectors. X-ray detection is of significant interest across a broad range of applications, including scientific research, medical diagnostics, safety protection, industrial material inspection, security screening, and environmental monitoring.[79–83] Solid-state detectors operate by utilizing semiconductor materials to directly register incoming X-ray photons. In direct digital detectors, the X-ray photons are converted directly into electrical charges, which are then processed into a digital image. In contrast, indirect detection systems first convert the X-ray photons into ultraviolet or visible light, which is subsequently transformed into an electrical signal. $Cs_2AgBiBr_6$ perovskites have emerged as promising candidates for X-ray detection applications, primarily due to their high stopping power.[84] An essential requirement for effective X-ray detection is a large $\mu\tau$ product, which governs charge carrier transport efficiency. Alongside this, key performance metrics include sensitivity—reflecting the detector's response speed—and the X-ray detectivity limit. $Cs_2AgBiBr_6$ perovskite films demonstrate excellent detector characteristics, attributed to their high $\mu\tau$ product and intrinsic resistivity. The material exhibits a low detection limit of 59.7 nGy air and a minimal dark current density of 0.1 nA/cm^2 at an applied bias of 5 V.[85] For an X-ray detector to function efficiently, it must exhibit both high sensitivity and long-term stability. Additional critical parameters influencing detector performance include low noise current, a low detection limit, and a rapid response time. Although $Cs_2AgBiBr_6$-based X-ray detectors demonstrate favourable attributes such as a low detection threshold, good stability, and fast response, their sensitivity and detection limits still fall short compared to those of lead-halide perovskites.[43,86,87] To enhance the X-ray detection capabilities of $Cs_2AgBiBr_6$ perovskite systems, it is essential to increase the $\mu\tau$ product, reduce trap state density, and suppress ion

migration. Moreover, surface and interface passivation play a crucial role in enhancing both the sensitivity and detection limit of $Cs_2AgBiBr_6$-based X-ray detectors. Considering these critical parameters—such as μτ product, trap state density, ion migration, and interfacial quality—continued research and development are necessary to further advance the performance of $Cs_2AgBiBr_6$ as a next-generation, lead-free X-ray detection material.

1.8.3 Photodetection

Photodetectors, in their simplest form, are photosensors designed to detect electromagnetic radiation, most commonly light.[88] They are typically classified based on their detection mechanisms or key performance metrics. In semiconductor-based photodetectors, a p–n junction is employed to convert incident sunlight into electrical energy. Among the most widely used technologies today are photodetectors such as photodiodes and phototransistors, fabricated from conventional bulk semiconductors including silicon, III–V, and II–VI compounds; however, their manufacturing costs remain relatively high.[89] Owing to its exceptional stability and high resistivity, $Cs_2AgBiBr_6$ has emerged as one of the most promising double halide perovskites for optoelectronic applications.[90–92] Furthermore, these perovskites display notable optoelectronic characteristics, including low to moderate exciton binding energies and a tunable bandgap.[93–96] To evaluate and compare photodetector performance, a range of critical parameters is commonly employed. Key optoelectronic properties of a photodetector include its spectral sensitivity and specific detectivity, both of which are critical for determining its application range. Equally important are device stability and response time, which directly influence operational reliability and performance. Broadly, photodetector architectures can be classified into three primary types: photodiodes, photoconductors, and phototransistors. In 2018, $Cs_2AgBiBr_6$ double perovskite films fabricated via a one-step spin-coating method were first utilized in photoconductive photodetectors, demonstrating promising optoelectronic performance. The devices exhibited a high responsivity of 7.01 A/W, a specific detectivity of 5.66×10^{11} Jones, an on/off photocurrent ratio of 2.16×10^4, and rapid response and recovery times of 956 μs and 995 μs, respectively.[51] These findings highlight the potential of $Cs_2AgBiBr_6$ as a lead-free perovskite material for photoelectric detection applications. To further enhance device performance—particularly in achieving broader spectral response, higher responsivity, and improved detectivity—it is essential to precisely tailor the perovskite bandgap and optimize the interface between the perovskite absorber and the electron/hole transport layers (ETL/HTL). In 2020, Mai et al.[97] successfully developed ultrathin metal oxide (MO_x) interlayers via atomic layer deposition (ALD), including ALD-TiO_2, ALD-Al_2O_3, and

ALD-NiO_x, by sequentially depositing titanium tetrachloride ($TiCl_4$), trimethylaluminum, and nickelene on fluorine-doped tin oxide (FTO) glass substrates. Water vapor was used as the oxygen source, while high-purity nitrogen served as the carrier gas. These ALD-fabricated layers were then employed as HTLs in the construction of weak-light photodetectors with the device architecture FTO/ALD-MO_x interlayer/$Cs_2AgBiBr_6$/ETL/Au. A schematic representation of the interfacial Bi–O bond formation between the $Cs_2AgBiBr_6$ film and the ALD-Al_2O_3-modified substrate is illustrated in **Fig. 1.10(a)**. Compared to the unmodified photodetector devices, those incorporating ALD-MO_x interlayers exhibited a tenfold enhancement in the switching ratio, with the detectivity increasing from 3.3×10^{11} Jones to 1.2×10^{13} Jones, and the minimum detectable radiation decreasing from 9.7×10^{-8} W cm^{-2} to 1.9×10^{-9} W cm^{-2} (**Fig 1.10(b, c)**). These performance improvements are attributed to the formation of Bi–O or Ag–O bonds at the interface between the MO_x substrate and the $Cs_2AgBiBr_6$ perovskite layer. This interfacial bonding promotes the formation of high-quality perovskite films with larger grain sizes and reduced pinhole density. Furthermore, it is well established that the selection of suitable ETL and HTL plays a vital role in enhancing photocarrier transport efficiency and refining perovskite film morphology, both of which are essential for realizing high-performance photodetectors.

Inorganic copper thiocyanate (CuSCN) has attracted significant attention as a hole transport layer (HTL) in perovskite-based devices due to its intrinsic p-type semiconducting nature, high hole mobility (1.2×10^{-3} cm^2 V^{-1}s^{-1}), favourable energy level alignment, and excellent thermal stability.[98–100] In 2020, CuSCN was introduced as the HTL in a self-powered $Cs_2AgBiBr_6$ photodetector system. The device architecture is shown in **Fig. 1.10(d)**. Incorporation of the CuSCN layer significantly improved the photodetector's weak-light imaging capability, as evidenced by the reduction in the light detection limit from approximately 7×10^{-9} W cm^{-2} to 1×10^{-2} W cm^{-2} compared to devices lacking the CuSCN HTL.[99] In the device operation, photo-generated carriers are separated into electrons and holes, with electrons migrating toward the FTO layer and holes moving toward the Au electrode. This directional transport reduces carrier recombination and facilitates efficient electrical signal generation. However, the work function of the Au electrode lies between the valence band maximum and the conduction band minimum of $Cs_2AgBiBr_6$. This energy level alignment enables both electrons and holes to flow toward the Au electrode, resulting in unwanted carrier recombination and consequent energy losses. The work function of the Au electrode lies between the valence band maximum and conduction band minimum of $Cs_2AgBiBr_6$, enabling both electrons and holes to migrate toward the Au

electrode, thereby inducing energy losses through unwanted recombination (**Fig. 1.10(e, f)**). The introduction of a CuSCN HTL significantly enhances device performance by effectively blocking electron transport to the Au electrode, while simultaneously facilitating more efficient hole collection.

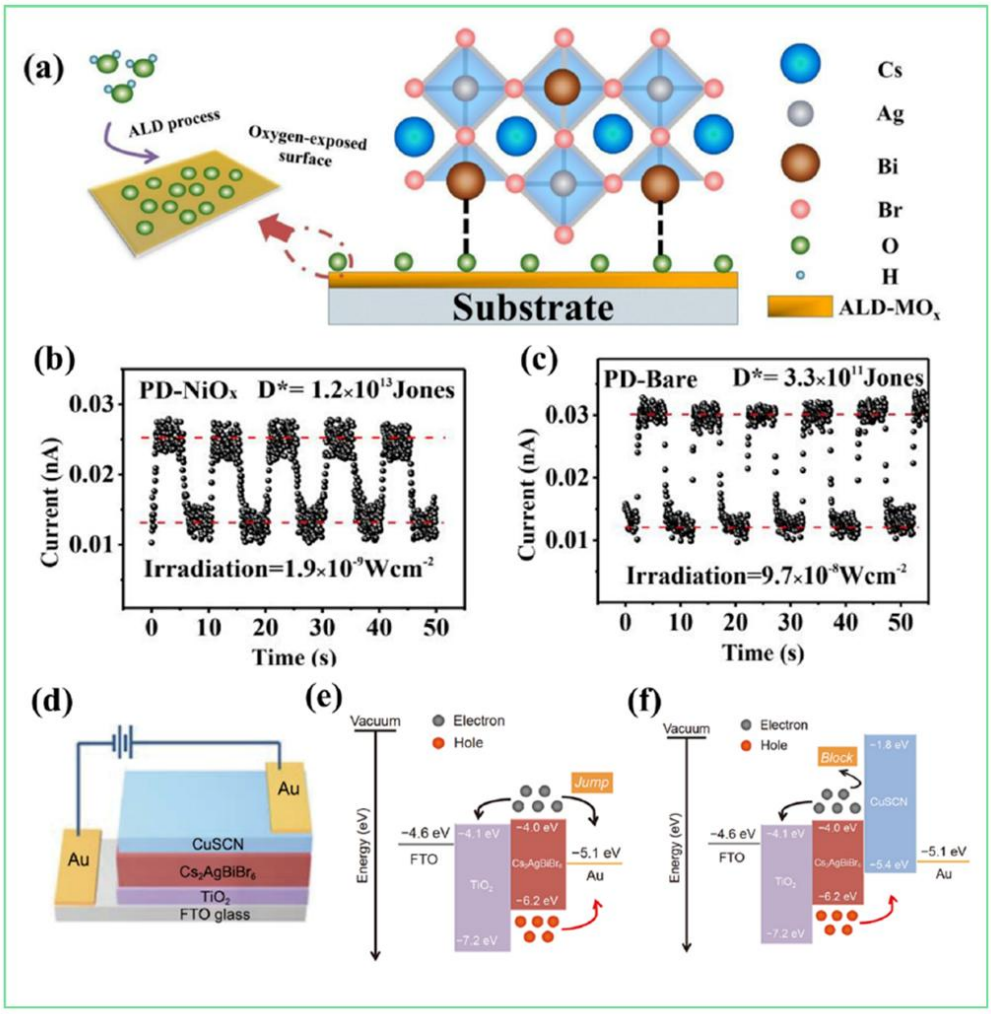

Fig. 1.10: (a) Schematic illustration of the Bi–O interfacial interaction at the interface between $Cs_2AgBiBr_6$ and the ALD-MO_x layer-modified substrate. **(b, c)** Typical photoresponse curves of PD–NiO_x and PD–Bare devices at their lowest measured irradiation levels. **(d)** Schematic diagram of a photodetector based on $Cs_2AgBiBr_6$. **(e)** and **(f)** Device energy band diagrams for configurations with and without the CuSCN hole transport layer (HTL). Adapted from ref. [97].

In 2022, Shen et al. enhanced the performance of $Cs_2AgBiBr_6$-based photodetectors by incorporating a ZnO/SnO_2 double ETL. The device fabrication process comprised five key steps. First, a ZnO seed layer was spin-coated onto the fluorine-doped tin oxide (FTO) substrate and annealed at 300 °C for 10 minutes; this deposition cycle was repeated three times. Second, ZnO nanorods were grown by immersing the FTO substrates in a zinc nitrate hydrate solution

for three hours. Third, a SnO_2 layer was deposited via spin-coating, followed by annealing at 150 °C for 30 minutes. Fourth, the $Cs_2AgBiBr_6$ absorber layer was deposited using a low-pressure-assisted technique. Finally, an Au electrode was deposited via thermal evaporation to complete the device structure. At a wavelength of 450 nm, the response rate and specific detectivity of the SnO_2/ZnO double-ETL-based photodetector were 12.7 and 16.5 times higher, respectively, compared to devices employing only a ZnO ETL.[101] This substantial improvement is attributed to the introduction of the SnO_2 layer, which reduces interfacial energy losses, enhances electron transport and extraction, and effectively mitigates the energy-level mismatch between the ZnO ETL and the $Cs_2AgBiBr_6$ perovskite absorber.[102,103] Additionally, the inherently hydrophobic surface of ZnO often hinders the formation of high-quality perovskite films.[104,105] The incorporation of the SnO_2/ZnO double ETL improves interfacial wettability, enabling the growth of smooth, pinhole-free perovskite films with superior morphological quality.[106] An additional strategy to improve photodetection performance is ultraviolet (UV) irradiation treatment. In 2022, Yuan et al. applied UV immersion to a series of $Cs_2AgBiBr_6$-based photodetectors with different device architectures. A xenon lamp (365 nm, 250 W) served as the UV light source, positioned directly in front of the photodetector samples.[107] To mitigate potential heating effects from UV exposure, the samples were allowed to equilibrate under ambient conditions before subsequent measurements. The results revealed that UV treatment significantly enhanced device performance, reducing the response time from 30.1 s to 340 ns and increasing the photocurrent from approximately 1.0×10^{-5} A to 1.5×10^{-4} A. To elucidate the mechanism underlying the observed performance enhancement, space-charge-limited current (SCLC) measurements were performed. The analysis revealed that the defect density in UV-treated devices was significantly reduced to 3.33×10^{16} cm^{-3}, compared to 8.97×10^{16} cm^{-3} in untreated devices. These results suggest that continuous UV irradiation effectively passivates both bulk and interfacial defects in the perovskite layer, thereby improving carrier concentration and/or mobility.[108–112] Such defect passivation strategies provide a compelling pathway for advancing the performance of double perovskite-based photodetectors.

1.9 Other Applications of Double Perovskites

Double perovskites have been widely utilized in various other applications, such as light-emitting diodes (LEDs)[113,114] and artificial synapses[115,116]. LED applications of double perovskites are limited due to the indirect band gap nature of these materials. However, the use of vacancy-ordered double perovskites resolves this issue. It is reported that vacancy-ordered perovskites ($A_2M^{4+}X_6$) exhibit high photoluminescence quantum yield (PLQY) and much

higher stability than lead-based perovskites.[117] It was observed that 2.75% Bi doping exhibits the highest PLQY compared to other lead-free perovskite materials, which is 78.9%. To demonstrate the potential application of Bi-doped Cs_2SnCl_6 perovskites in solid-state lighting, a W-LED was fabricated by combining Cs_2SnCl_6:2.75%Bi, which exhibits blue emission, with yellow phosphors—namely $Ba_2Sr_2SiO_4:Eu^{2+}$ and $GaAlSiN_3:Eu^{2+}$. The blue-emitting perovskite and yellow phosphors were mixed with a curable resin, applied onto a commercially available 365 nm LED chip, and subsequently cured to form a uniform composite layer.

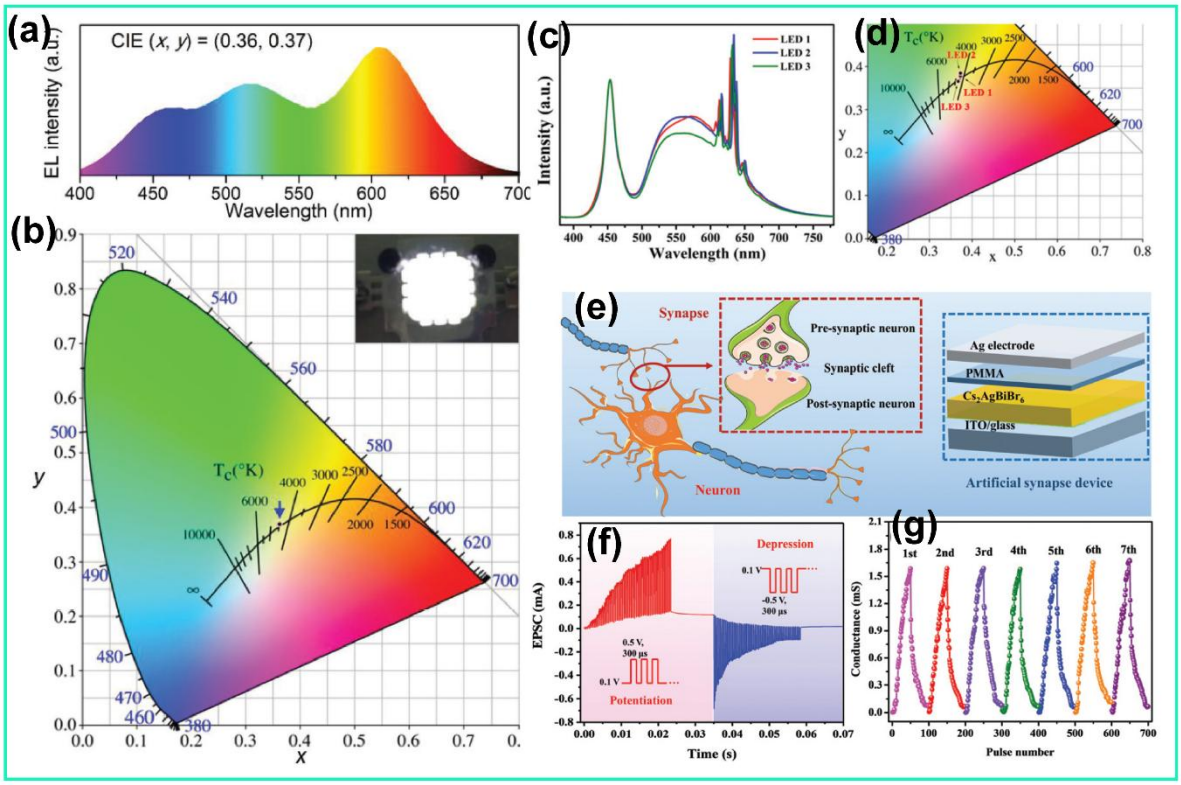

Fig. 1.11: (a) Electroluminescent spectra from Cs_2SnCl_6:2.75%Bi-based LEDs with warm white emission. **(b)** CIE colour coordinates corresponding to the white-LED device and (inset) photo of operating LED. **(c, d)** EL spectra and CIE chromaticity diagram of $Rb_2KAlF_6:Mn^{4+}$ (LED1), $Cs_2KAlF_6:Mn^{4+}$ (LED2), and $Cs_2RbAlF_6:Mn^{4+}$ (LED3), respectively. **(e)** Schematic illustration of biological neurons and $Cs_2AgBiBr_6$-based synaptic device. **(f)** The potentiation and depression mimicking behaviour of the device triggered by 50 positive and negative pulses, respectively. **(g)** Conductance evolution of potentiation and depression in 7 continuous cycles. Adapted from ref. [117], [118], and [119].

The electroluminescent (EL) spectrum of the fabricated W-LED, shown in **Fig. 1.11(a)**, exhibits a broad and balanced emission across the visible range. The CIE chromaticity coordinates of the device were determined to be (0.36, 0.37), corresponding to a warm white

light with a correlated colour temperature (CCT) of 4486 K, as illustrated in **Fig. 1.11(b)**. The inset image displays the operational LED device, which emitted bright white light under UV excitation. Additionally, Deng et. al. tailored the PL stability in $A_2BAlF_6:Mn^{4+}$ double perovskites (A= Rb, Cs; B= K, Rb) via neighbouring-cation modulation. To regulate the structural rigidity and PL stability of Mn^{4+}-doped double perovskite phosphors, the study introduced the innovative concept of "neighbouring-cation modulation," wherein the A-site and B-site cations (Rb/Cs and K/Rb) were selectively substituted. The incorporation of smaller A-site or larger B-site cations led to a chemical pressure effect, compressing the $[AlF_6]$ octahedra, thereby enhancing the crystal field strength and reinforcing the Mn^{4+}–F bonding, which collectively resulted in tunable PL emission characteristics.[118] Among the synthesized compounds, $Cs_2KAlF_6:Mn^{4+}$ exhibited excellent moisture resistance, maintaining 65% of its initial emission intensity after 72 hours under conditions of 85% relative humidity and 85 °C. However, it demonstrated relatively poor thermal stability, retaining only 59.8% emission intensity at 423 K. In contrast, $Rb_2KAlF_6:Mn^{4+}$ and $Cs_2RbAlF_6:Mn^{4+}$ displayed slightly reduced moisture tolerance but significantly improved thermal stability, with emission losses of merely 3.2% and 27.9%, respectively, at 423 K. **Fig. 1.11(c, d)** shows the EL spectra and CIE chromaticity diagram of the warm W-LEDs. These findings indicate that while water resistance primarily depends on the structural stability of the host matrix, the thermal stability is strongly correlated with the rigidity of the Mn^{4+} coordination environment. Furthermore, these optimized phosphors were successfully employed as red-emitting components in the fabrication of warm W-LEDs, demonstrating their practical potential for high-efficiency and thermally stable solid-state lighting applications.

A double perovskite $Cs_2AgBiBr_6$ thin film with a vertical Ag/PMMA/$Cs_2AgBiBr_6$/ITO structure was utilized to demonstrate an artificial synapse.[119] The device effectively exhibited typical synaptic behaviours, where the bipolar I–V response and synaptic simulation originated from the formation and rupture of conductive filaments in the $Cs_2AgBiBr_6$ layer due to Br^- and Ag^+ ion migration. The synaptic device also showed excellent environmental stability, maintaining consistent performance after 20 days of exposure. Based on LTP/LTD experimental data using the MNIST handwritten digit dataset, the device achieved a recognition accuracy of 91.3%, confirming its reliable synaptic functionality. Learning and memory rely on biological synapses, which serve as the pathways for information transmission between neurons.[119] A biological synapse consists of a pre-synaptic neuron, a post-synaptic neuron, and a synaptic cleft (**Fig. 1.11(e)**). In the present system, the top Ag electrode, the

PMMA/Cs2AgBiBr6 layers, and the grounded bottom ITO glass electrode correspond to the pre-synaptic neuron, synaptic cleft, and post-synaptic neuron, respectively (**Fig. 1.11(e)**). To evaluate tunable synaptic plasticity, the device was subjected to 50 consecutive positive voltage pulses (+0.5 V, 300 ms) for potentiation and 50 consecutive negative voltage pulses (−0.5 V, 300 ms) for depression (**Fig. 1.11(f)**). The application of positive pulses increased the excitatory postsynaptic current (EPSC), while negative pulses led to its reduction. These behaviours are analogous to the LTP and LTD characteristics of biological synapses. The conductance values, measured at 0.1 V over seven consecutive cycles of potentiation and depression, are presented in **Fig. 1.11(g)**, clearly demonstrating the excellent reproducibility and stability of the device's response to repeated voltage pulse stimuli.

1.10 Challenges in Fabrication and Application of Double Perovskites

The widespread application of $Cs_2AgBiBr_6$ double perovskites is hindered by several interconnected challenges in their synthesis and processing. A major limitation arises from the poor solubility of precursor salts in conventional solvents, which complicates the fabrication of homogeneous, phase-pure thin films. Large-scale production is further constrained by the need for specialized solvents—such as hot dimethyl sulfoxide (DMSO)—and high annealing temperatures, typically exceeding 250 °C. Additionally, the material often exhibits high defect densities, originating both from extrinsic impurities introduced during fabrication and from intrinsic structural characteristics, such as antisite disorder between Ag and Bi cations. These structural imperfections critically impair device performance by inducing short carrier diffusion lengths and elevated non-radiative recombination rates. Achieving precise control over film morphology remains a significant challenge; while dense, high-quality crystalline structures are essential for optimal optoelectronic properties, conventional fabrication approaches often yield incomplete phase conversion and pronounced grain boundary formation. Furthermore, the intrinsically wide indirect bandgap of $Cs_2AgBiBr_6$ (1.9–2.2 eV) limits its light-harvesting efficiency in photovoltaic applications. Although alloying and doping strategies offer potential pathways to enhance carrier mobility and tailor the bandgap, their successful implementation demands meticulous process optimization and precise compositional control. Despite exhibiting excellent stability against moisture, heat, and light, along with non-toxicity, $Cs_2AgBiBr_6$ suffers from limited light absorption and suboptimal charge transport, resulting in substantially lower power conversion efficiencies in solar cells compared to lead-based perovskites. While its high atomic number renders it a promising candidate for X-ray detection, its sensitivity remains inferior to that of lead-containing

materials, underscoring the need for further device optimization. Realizing the full potential of this stable and environmentally benign perovskite will depend on progress in defect passivation, interface engineering, innovative fabrication techniques, and the design of advanced device architectures.

1.11 Focus of the Present Thesis

Although substantial progress has been made in the fabrication and application of lead-free $Cs_2AgBiBr_6$ double perovskites, several challenges remain. These include the development of high-quality thin films, the design of heterostructures with other materials to enhance light absorption, and the exploration of their potential for surface-enhanced Raman spectroscopy (SERS). In this thesis, we have focused on the controlled growth of $Cs_2AgBiBr_6$ double perovskites in diverse morphologies—from single crystals to nanoflakes—and explored their functional applications.

The main objectives of the present work are:

- Optimization of $Cs_2AgBiBr_6$ thin film growth via chemical vapor deposition (CVD), including investigation of phase transitions at elevated growth temperatures and evaluation of the device's fast photoresponse.
- Determination of the ultra-low thermal conductivity of $Cs_2AgBiBr_6$ using low-temperature and power-dependent Raman spectroscopy.
- Fabrication and characterization of a solvent-free, in situ $Cs_2AgBiBr_6/WS_2$ nanosheet heterostructure, aimed at improving the specific responsivity and detectivity of the $Cs_2AgBiBr_6/WS_2$-based photodetector.
- Investigation of the SERS mechanism in $Cs_2AgBiBr_6$ nanoflakes for the detection of trace organic pollutants.
- Development of an all-inorganic, lead-free $Cs_2AgBiBr_6/Cs_3Bi_2I_9$ 3D/0D heterostructure for enhanced photodetection performance.

1.12 Organization of the Thesis

This thesis is systematically organized into six chapters, each addressing a critical aspect of the design, synthesis, characterization, and application of lead-free $Cs_2AgBiBr_6$ double perovskites and their heterostructures for advanced optoelectronic and photonic devices.

Chapter 1 provides a comprehensive overview of growth techniques employed for $Cs_2AgBiBr_6$ double perovskites and related halide materials. It discusses in detail their crystal

chemistry, electronic band structures, and optical properties, along with strategies for bandgap tuning through compositional and dimensional modifications. The chapter also reviews recent research developments in the field, highlighting the growing significance of lead-free double perovskites as sustainable alternatives to lead-based systems. Furthermore, it outlines their potential applications in photodetectors, light-emitting diodes (LEDs), solar cells, and X-ray detectors, establishing the motivation and scope of the present work.

Chapter 2 focuses on the growth mechanism and structural optimization of high-quality $Cs_2AgBiBr_6$ thin films. It details the chemical vapor deposition (CVD) process parameters and the role of substrate temperature in achieving phase-pure and uniform thin films. Using low-temperature and power-dependent Raman spectroscopy, the ultralow thermal conductivity of these films is quantitatively analyzed, revealing their phonon transport characteristics. The optimized films are subsequently integrated into planar photodetector devices, which demonstrate rapid photoresponse, low dark current, and excellent operational stability, underscoring their potential for practical optoelectronic applications.

Chapter 3 presents a surfactant- and solvent-free mechanochemical synthesis approach for the fabrication of $Cs_2AgBiBr_6/WS_2$ heterostructures. The chapter investigates their structural integrity, interfacial coupling, and enhanced ultraviolet photodetection performance. The synergistic combination of the perovskite's strong absorption and WS_2's high carrier mobility is shown to significantly improve responsivity, detectivity, and response speed. These findings highlight the importance of perovskite-2D material hybridization in tailoring interfacial charge dynamics for high-performance photodetectors.

Chapter 4 explores the space-confined growth of $Cs_2AgBiBr_6$ nanoflakes and their application in the surface-enhanced Raman scattering (SERS) detection of trace organic pollutants. Through systematic experimental and density functional theory (DFT) analyses, the study elucidates the chemical enhancement mechanism driven by self-trapped excitons (STEs) and interfacial charge transfer between the analyte molecules and the perovskite surface. The results establish $Cs_2AgBiBr_6$ as a robust and reusable SERS substrate, combining high sensitivity with environmental stability.

Chapter 5 discusses the growth of $Cs_2AgBiBr_6$ single crystals and $Cs_3Bi_2I_9$ nanocrystals, followed by the fabrication of a heterojunction photodetector based on these materials. The heterostructure exhibits type-II band alignment, enabling efficient carrier separation and drift-assisted charge transport across the interface. The resulting Au/$Cs_2AgBiBr_6$ SC/$Cs_3Bi_2I_9$

NC/Au device demonstrates enhanced photoresponsivity, high specific detectivity, and fast temporal response, confirming the effectiveness of the heterojunction design for broad-spectrum photodetection.

Chapter 6 summarizes the major findings and scientific contributions of the research, highlighting the interplay between material design, structural modulation, and device functionality. It also outlines the future perspectives of this work, including the integration of $Cs_2AgBiBr_6$-based materials into large-area optoelectronic systems, neuromorphic devices, and sustainable energy technologies. The chapter concludes by emphasizing the broader impact of this study in advancing the field of lead-free double perovskites, paving the way for environmentally benign, stable, and multifunctional materials for next-generation electronic and photonic applications.

References

1 S. Soltani, M. Hjiri, N. I. A. Ahmed, A. Jbeli, A. M. Aldukhayel and N. A. Althumairi, *Royal Society of Chemistry*, 2025, preprint, DOI: 10.1039/d5ra02730f.

2 A. Aftab and R. Murshed, *Elsevier Ltd*, 2025, preprint, DOI: 10.1016/j.solener.2025.113866.

3 A. H. Slavney, T. Hu, A. M. Lindenberg and H. I. Karunadasa, *J Am Chem Soc*, 2016, **138**, 2138–2141.

4 Z. Xiao, W. Meng, J. Wang and Y. Yan, DOI:10.1002/cssc.v9.18/issuetoc.

5 L. Dong, S. Sun, Z. Deng, W. Li, F. Wei, Y. Qi, Y. Li, X. Li, P. Lu and U. Ramamurty, *Comput Mater Sci*, 2018, **141**, 49–58.

6 R. Fu, Y. Chen, X. Yong, Z. Ma, L. Wang, P. Lv, S. Lu, G. Xiao and B. Zou, *Nanoscale*, 2019, **11**, 17004–17009.

7 T. Bellakhdar, Z. Nabi, B. Bouabdallah, B. Benichou and H. Saci, *Appl Phys A Mater Sci Process*, DOI:10.1007/s00339-022-05276-8.

8 L. Schade, A. D. Wright, R. D. Johnson, M. Dollmann, B. Wenger, P. K. Nayak, D. Prabhakaran, L. M. Herz, R. Nicholas, H. J. Snaith and P. G. Radaelli, *ACS Energy Lett*, 2019, **4**, 299–305.

9 Y. Puttisong, F. Moro, S. L. Chen, P. Höjer, W. Ning, F. Gao, I. A. Buyanova and W. M. Chen, *Journal of Physical Chemistry Letters*, 2020, **11**, 4873–4878.

10 C. J. Bartel, C. Sutton, B. R. Goldsmith, R. Ouyang, C. B. Musgrave, L. M. Ghiringhelli and M. Scheffler, *New tolerance factor to predict the stability of perovskite oxides and halides*, 2019.

11 C. J. Bartel, C. Sutton, B. R. Goldsmith, R. Ouyang, C. B. Musgrave, L. M. Ghiringhelli and M. Scheffler, *New tolerance factor to predict the stability of perovskite oxides and halides*, 2019.

12 X. G. Zhao, J. H. Yang, Y. Fu, D. Yang, Q. Xu, L. Yu, S. H. Wei and L. Zhang, *J Am Chem Soc*, 2017, **139**, 2630–2638.

13 C. N. Savory, A. Walsh and D. O. Scanlon, *ACS Energy Lett*, 2016, **1**, 949–955.

14 L. Moulaoui, A. Najim, M. Archi, M. Al-Hattab, O. Bajjou, A. Bakour, Y. Lachtioui, K. Rahmani and B. Manaut, *Results Chem*, DOI:10.1016/j.rechem.2025.102025.

15 M. A. Hadi, M. N. Islam and J. Podder, *RSC Adv*, 2022, **12**, 15461–15469.

16 J. Yang, P. Zhang and S. H. Wei, *Journal of Physical Chemistry Letters*, 2018, **9**, 31–35.

17 Z. Zhang, Q. Sun, Y. Lu, F. Lu, X. Mu, S. H. Wei and M. Sui, *Nat Commun*, DOI:10.1038/s41467-022-31016-w.

18 L. Schade, A. D. Wright, R. D. Johnson, M. Dollmann, B. Wenger, P. K. Nayak, D. Prabhakaran, L. M. Herz, R. Nicholas, H. J. Snaith and P. G. Radaelli, *ACS Energy Lett*, 2019, **4**, 299–305.

19 W. Meng, X. Wang, Z. Xiao, J. Wang, D. B. Mitzi and Y. Yan, *Journal of Physical Chemistry Letters*, 2017, **8**, 2999–3007.

20 G. Volonakis, M. R. Filip, A. A. Haghighirad, N. Sakai, B. Wenger, H. J. Snaith and F. Giustino, *Journal of Physical Chemistry Letters*, 2016, **7**, 1254–1259.

21 Q. Li, Y. Wang, W. Pan, W. Yang, B. Zou, J. Tang and Z. Quan, *Angewandte Chemie*, 2017, **129**, 16185–16189.

22 F. Ji, J. Klarbring, F. Wang, W. Ning, L. Wang, C. Yin, J. S. M. Figueroa, C. K. Christensen, M. Etter, T. Ederth, L. Sun, S. I. Simak, I. A. Abrikosov and F. Gao, *Angewandte Chemie - International Edition*, 2020, **59**, 15191–15194.

23 A. H. Slavney, L. Leppert, D. Bartesaghi, A. Gold-Parker, M. F. Toney, T. J. Savenije, J. B. Neaton and H. I. Karunadasa, *J Am Chem Soc*, 2017, **139**, 5015–5018.

24 K. Du, W. Meng, X. Wang, Y. Yan and D. B. Mitzi, *Angewandte Chemie*, 2017, **129**, 8270–8274.

25 A. H. Slavney, T. Hu, A. M. Lindenberg and H. I. Karunadasa, *J Am Chem Soc*, 2016, **138**, 2138–2141.

26 D. Bartesaghi, A. H. Slavney, M. C. Gélvez-Rueda, B. A. Connor, F. C. Grozema, H. I. Karunadasa and T. J. Savenije, *Journal of Physical Chemistry C*, 2018, **122**, 4809–4816.

27 R. Kentsch, M. Scholz, J. Horn, D. Schlettwein, K. Oum and T. Lenzer, *Journal of Physical Chemistry C*, 2018, **122**, 25940–25947.

28 J. A. Steele, P. Puech, M. Keshavarz, R. Yang, S. Banerjee, E. Debroye, C. W. Kim, H. Yuan, N. H. Heo, J. Vanacken, A. Walsh, J. Hofkens and M. B. J. Roeffaers, *ACS Nano*, 2018, **12**, 8081–8090.

29 A. Schmitz, L. Leander Schaberg, S. Sirotinskaya, M. Pantaler, D. C. Lupascu, N. Benson and G. Bacher, *ACS Energy Lett*, 2020, **5**, 559–565.

30 E. M. Hutter, M. C. Gélvez-Rueda, D. Bartesaghi, F. C. Grozema and T. J. Savenije, *ACS Omega*, 2018, **3**, 11655–11662.

31 Z. Guo, M. Yuan, G. Chen, F. Liu, R. Lu and W. J. Yin, *Advanced Science*, DOI:10.1002/advs.202305799.

32 J. Kim, C. H. Chung and K. H. Hong, *Physical Chemistry Chemical Physics*, 2016, **18**, 27143–27147.

33 X. Liu, Y. Cheng, B. Tang, Z. G. Yu, M. Li, F. Lin, S. Zhang, Y. W. Zhang, J. Ouyang and H. Gong, *Nano Energy*, DOI:10.1016/j.nanoen.2020.104556.

34 Y. Yuan, G. Yan, C. Dreessen, T. Rudolph, M. Hülsbeck, B. Klingebiel, J. Ye, U. Rau and T. Kirchartz, *Nat Mater*, 2024, **23**, 391–397.

35 Z. Xiao, W. Meng, J. Wang and Y. Yan, *ChemSusChem*, 2016, **9**, 2628–2633.

36 I. C. Ri, C. S. Ri, S. H. Yu, S. H. Jo, S. H. Choe and C. J. Yu, *Chemical Communications*, 2025, **61**, 3896–3899.

37 A. Frebel, S. Yoon, S. Meles Neguse, D. M. Jöckel, M. Widenmeyer, S. Lange, V. Naumann, A. Rosspeintner, S. G. Ebbinghaus, B. Balke and A. Weidenkaff, *Adv Photonics Res*, DOI:10.1002/adpr.202200061.

38 J. P. Perdew, K. Burke and M. Ernzerhof, *Generalized Gradient Approximation Made Simple*, 1996.

39 J. Paier, M. Marsman, K. Hummer, G. Kresse, I. C. Gerber and J. G. Angyán, 2006, preprint, DOI: 10.1063/1.2403866.

40 T. Li, X. Zhao, D. Yang, M. H. Du and L. Zhang, *Phys Rev Appl*, DOI:10.1103/PhysRevApplied.10.041001.

41 C. Freysoldt, B. Grabowski, T. Hickel, J. Neugebauer, G. Kresse, A. Janotti and C. G. Van De Walle, *Rev Mod Phys*, 2014, **86**, 253–305.

42 W. Gao, C. Ran, J. Xi, B. Jiao, W. Zhang, M. Wu, X. Hou and Z. Wu, *ChemPhysChem*, 2018, **19**, 1696–1700.

43 J. Yang, C. Bao, W. Ning, B. Wu, F. Ji, Z. Yan, Y. Tao, J. M. Liu, T. C. Sum, S. Bai, J. Wang, W. Huang, W. Zhang and F. Gao, *Adv Opt Mater*, DOI:10.1002/adom.201801732.

44 J. A. Steele, W. Pan, C. Martin, M. Keshavarz, E. Debroye, H. Yuan, S. Banerjee, E. Fron, D. Jonckheere, C. W. Kim, W. Baekelant, G. Niu, J. Tang, J. Vanacken, M. Van der Auweraer, J. Hofkens and M. B. J. Roeffaers, *Advanced Materials*, DOI:10.1002/adma.201804450.

45 L. Yin, H. Wu, W. Pan, B. Yang, P. Li, J. Luo, G. Niu and J. Tang, *Adv Opt Mater*, DOI:10.1002/adom.201900491.

46 W. Zhang, H. Zhu, S. Pan, H. Li, J. Zhang, Z. Gong, Y. Zhang and J. Pan, *J Cryst Growth*, DOI:10.1016/j.jcrysgro.2019.125440.

47 F. Zeng, Y. Tan, W. Hu, X. Tang, H. Yin, T. Jing, L. Huang, Y. Yang, J. Liao and C. Zhou, *Appl Phys Lett*, DOI:10.1063/5.0199584.

48 N. Daem, J. Dewalque, F. Lang, A. Maho, G. Spronck, C. Henrist, P. Colson, S. D. Stranks and R. Cloots, *Solar RRL*, DOI:10.1002/solr.202100422.

49 S. Umer, M. I. Khan, A. Ullah, Ihtisham-ul-haq, M. Asad, Imen kebaili, W. Mnif, Z. Algarni and M. I. Saleem, *Opt Mater (Amst)*, DOI:10.1016/j.optmat.2024.115896.

50 E. Greul, M. L. Petrus, A. Binek, P. Docampo and T. Bein, *J Mater Chem A Mater*, 2017, **5**, 19972–19981.

51 B. Wang, N. Li, L. Yang, C. Dall'Agnese, A. K. Jena, T. Miyasaka and X. F. Wang, *J Am Chem Soc*, 2021, **143**, 14877–14883.

52 W. Gao, C. Ran, J. Xi, B. Jiao, W. Zhang, M. Wu, X. Hou and Z. Wu, *ChemPhysChem*, 2018, **19**, 1696–1700.

53 L. Z. Lei, Z. F. Shi, Y. Li, Z. Z. Ma, F. Zhang, T. T. Xu, Y. T. Tian, D. Wu, X. J. Li and G. T. Du, *J Mater Chem C Mater*, 2018, **6**, 7982–7988.

54 C. Wu, Q. Zhang, Y. Liu, W. Luo, X. Guo, Z. Huang, H. Ting, W. Sun, X. Zhong, S. Wei, S. Wang, Z. Chen and L. Xiao, *Advanced Science*, DOI:10.1002/advs.201700759.

55 W. Minjie, C. Teng, C. Xuedan, W. Maoxue, L. V. Chen, M. Kai and Y. Shuanglong, *Chemistry - A European Journal*, DOI:10.1002/chem.202403716.

56 J. Barichello, G. Shankar, P. Mariani, A. Di Carlo and F. Matteocci, *Mater Today Energy*, DOI:10.1016/j.mtener.2024.101725.

57 I. Biswas, A. Dey, A. Dalal, S. Saha, J. M. Nunzi and A. Mondal, *J Alloys Compd*, DOI:10.1016/j.jallcom.2023.172903.

58 P. Jain, M. N. Tran, I. J. Cleveland, Y. Liu, S. Sarp and E. S. Aydil, *Journal of Physical Chemistry C*, 2025, **129**, 5301–5311.

59 M. Wang, P. Zeng, S. Bai, J. Gu, F. Li, Z. Yang and M. Liu, *Solar RRL*, DOI:10.1002/solr.201800217.

60 M. Wang, P. Zeng, Z. Wang and M. Liu, *Advanced Science*, DOI:10.1002/advs.201903662.

61 N. Rodkey, S. Kaal, P. Sebastia-Luna, Y. A. Birkhölzer, M. Ledinsky, F. Palazon, H. J. Bolink and M. Morales-Masis, *Chemistry of Materials*, 2021, **33**, 7417–7422.

62 P. Fan, H. X. Peng, Z. H. Zheng, Z. H. Chen, S. J. Tan, X. Y. Chen, Y. Di Luo, Z. H. Su, J. T. Luo and G. X. Liang, *Nanomaterials*, DOI:10.3390/nano9121760.

63 Y. Bekenstein, J. C. Dahl, J. Huang, W. T. Osowiecki, J. K. Swabeck, E. M. Chan, P. Yang and A. P. Alivisatos, *Nano Lett*, 2018, **18**, 3502–3508.

64 Y. Liu, Y. Jing, J. Zhao, Q. Liu and Z. Xia, *Chemistry of Materials*, 2019, **31**, 3333–3339.

65 W. Lee, S. Hong and S. Kim, *Journal of Physical Chemistry C*, 2019, **123**, 2665–2672.

66 J. C. Dahl, W. T. Osowiecki, Y. Cai, J. K. Swabeck, Y. Bekenstein, M. Asta, E. M. Chan and A. P. Alivisatos, *Chemistry of Materials*, 2019, **31**, 3134–3143.

67 L. Zhou, Y. F. Xu, B. X. Chen, D. Bin Kuang and C. Y. Su, *Small*, DOI:10.1002/smll.201703762.

68 B. Yang, F. Hong, J. Chen, Y. Tang, L. Yang, Y. Sang, X. Xia, J. Guo, H. He, S. Yang, W. Deng and K. Han, *Angewandte Chemie*, 2019, **131**, 2300–2305.

69 S. E. Creutz, E. N. Crites, M. C. De Siena and D. R. Gamelin, *Nano Lett*, 2018, **18**, 1118–1123.

70 F. Locardi, M. Cirignano, D. Baranov, Z. Dang, M. Prato, F. Drago, M. Ferretti, V. Pinchetti, M. Fanciulli, S. Brovelli, L. De Trizio and L. Manna, *J Am Chem Soc*, 2018, **140**, 12989–12995.

71 R. Ahmad, G. V. Nutan, D. Singh, G. Gupta, U. Soni, S. Sapra and R. Srivastava, *Nano Res*, 2021, **14**, 1126–1134.

72 Z. Liu, H. Yang, J. Wang, Y. Yuan, K. Hills-Kimball, T. Cai, P. Wang, A. Tang and O. Chen, *Nano Lett*, 2021, **21**, 1620–1627.

73 S. Chand Yadav, A. Srivastava, V. Manjunath, A. Kanwade, R. S. Devan and P. M. Shirage, *Elsevier Ltd*, 2022, preprint, DOI: 10.1016/j.mtphys.2022.100731.

74 M. T. Islam, M. R. Jani, S. M. Al Amin, M. S. U. Sami, K. M. Shorowordi, M. I. Hossain, M. Devgun, S. Chowdhury, S. Banerje and S. Ahmed, *Opt Mater (Amst)*, DOI:10.1016/j.optmat.2020.109957.

75 S. Rai, B. K. Pandey, A. Garg and D. K. Dwivedi, *Opt Mater (Amst)*, DOI:10.1016/j.optmat.2021.111645.

76 S. Sharma, R. Pandey, J. Madan and R. Sharma, *Opt Mater (Amst)*, DOI:10.1016/j.optmat.2020.110644.

77 V. Pecunia, L. G. Occhipinti, A. Chakraborty, Y. Pan and Y. Peng, *American Institute of Physics Inc.*, 2020, preprint, DOI: 10.1063/5.0022271.

78 I. Alam, R. Mollick and M. A. Ashraf, *Physica B Condens Matter*, DOI:10.1016/j.physb.2021.413187.

79 S. Kasap, J. B. Frey, G. Belev, O. Tousignant, H. Mani, J. Greenspan, L. Laperriere, O. Bubon, A. Reznik, G. DeCrescenzo, K. S. Karim and J. A. Rowlands, 2011, preprint, DOI: 10.3390/s110505112.

80 A. Sakdinawat and D. Attwood, 2010, preprint, DOI: 10.1038/nphoton.2010.267.

81 S. I. Parkera, C. J. Kenneya and J. Segalb, *ELSEVIER Secton A 3D-A proposed new architecture for solid-state radiation detectors'*, 1997, vol. 395.

82 M. J. Yaffe and J. A. Rowlands, *X-ray detectors for digital radiography*, 1997, vol. 42.

83 P. N. Luke, C. S. Rossington and M. F. Wesela, *Low Energy X-ray Response of Ge Detectors with Amorphous Ge Entrance Contacts*, 1994, vol. 41.

84 H. Wei, Y. Fang, P. Mulligan, W. Chuirazzi, H. H. Fang, C. Wang, B. R. Ecker, Y. Gao, M. A. Loi, L. Cao and J. Huang, *Nat Photonics*, 2016, **10**, 333–339.

85 B. Yang, W. Pan, H. Wu, G. Niu, J. H. Yuan, K. H. Xue, L. Yin, X. Du, X. S. Miao, X. Yang, Q. Xie and J. Tang, *Nat Commun*, DOI:10.1038/s41467-019-09968-3.

86 J. A. Steele, W. Pan, C. Martin, M. Keshavarz, E. Debroye, H. Yuan, S. Banerjee, E. Fron, D. Jonckheere, C. W. Kim, W. Baekelant, G. Niu, J. Tang, J. Vanacken, M. Van der Auweraer, J. Hofkens and M. B. J. Roeffaers, *Advanced Materials*, DOI:10.1002/adma.201804450.

87 Z. Xu, X. Liu, Y. Li, X. Liu, T. Yang, C. Ji, S. Han, Y. Xu, J. Luo and Z. Sun, *Angewandte Chemie*, 2019, **131**, 15904–15908.

88 H. J. Haugan, S. Elhamri, F. Szmulowicz, B. Ullrich, G. J. Brown and W. C. Mitchel, *Appl Phys Lett*, DOI:10.1063/1.2884264.

89 F. Wang, X. Zou, M. Xu, H. Wang, H. Wang, H. Guo, J. Guo, P. Wang, M. Peng, Z. Wang, Y. Wang, J. Miao, F. Chen, J. Wang, X. Chen, A. Pan, C. Shan, L. Liao and W. Hu, *John Wiley and Sons Inc*, 2021, preprint, DOI: 10.1002/advs.202100569.

90 W. Zhang, Z. Gong, S. Pan, Y. Zhang, D. Chen and J. Pan, *J Cryst Growth*, DOI:10.1016/j.jcrysgro.2020.125922.

91 C. Wu, B. Du, W. Luo, Y. Liu, T. Li, D. Wang, X. Guo, H. Ting, Z. Fang, S. Wang, Z. Chen, Y. Chen and L. Xiao, *Adv Opt Mater*, DOI:10.1002/adom.201800811.

92 Y. Li, Z. Shi, L. Lei, S. Li, D. Yang, D. Wu, T. Xu, Y. Tian, Y. Lu, Y. Wang, L. Zhang, X. Li, Y. Zhang, G. Du and C. Shan, *Adv Mater Interfaces*, DOI:10.1002/admi.201900188.

93 C. Bao, W. Xu, J. Yang, S. Bai, P. Teng, Y. Yang, J. Wang, N. Zhao, W. Zhang, W. Huang and F. Gao, *Nat Electron*, 2020, **3**, 156–164.

94 N. Li, Z. Lan, L. Cai and F. Zhu, *Royal Society of Chemistry*, 2019, preprint, DOI: 10.1039/C8TC06078A.

95 M. Ahmadi, T. Wu and B. Hu, *Wiley-VCH Verlag*, 2017, preprint, DOI: 10.1002/adma.201605242.

96 F. P. García De Arquer, A. Armin, P. Meredith and E. H. Sargent, *Nature Publishing Group*, 2017, preprint, DOI: 10.1038/natrevmats.2016.100.

97 G. Yan, B. Jiang, Y. Yuan, M. Kuang, X. Liu, Z. Zeng, C. Zhao, J. H. He and W. Mai, *ACS Appl Mater Interfaces*, 2020, **12**, 6064–6073.

98 P. Qin, S. Tanaka, S. Ito, N. Tetreault, K. Manabe, H. Nishino, M. K. Nazeeruddin and M. Grätzel, *Nat Commun*, DOI:10.1038/ncomms4834.

99 G. Yan, Z. Ji, Z. Li, B. Jiang, M. Kuang, X. Cai, Y. Yuan and W. Mai, *Sci China Mater*, 2021, **64**, 198–208.

100 N. Arora, M. I. Dar, † Alexander Hinderhofer, N. Pellet, F. Schreiber, S. M. Zakeeruddin and M. Grätzel, *Perovskite solar cells with CuSCN hole extraction layers yield stabilized efficiencies greater than 20%*, .

101 W. Shen, U. Jung, Z. Xian, B. Jung and J. Park, *J Alloys Compd*, DOI:10.1016/j.jallcom.2022.167329.

102 P. Ruankham, D. Wongratanaphisan, A. Gardchareon, S. Phadungdhitidhada, S. Choopun and T. Sagawa, *Appl Surf Sci*, 2017, **410**, 393–400.

103 G. Liu, Y. Zhong, H. Mao, J. Yang, R. Dai, X. Hu, Z. Xing, W. Sheng, L. Tan and Y. Chen, *Chemical Engineering Journal*, DOI:10.1016/j.cej.2021.134235.

104 Z. Yang, B. H. Babu, S. Wu, T. Liu, S. Fang, Z. Xiong, L. Han and W. Chen, *Wiley-VCH Verlag*, 2020, preprint, DOI: 10.1002/solr.201900257.

105 K. Sivashanmugan, C. H. Lin, S. H. Hsu, T. F. Guo and T. C. Wen, *Mater Chem Phys*, 2018, **219**, 90–95.

106 H. Niu, C. Fang, X. Wei, H. Wang, L. Wan, Y. Li, X. Mao, J. Xu and R. Zhou, *Dalton Transactions*, 2021, **50**, 6477–6487.

107 Y. Yuan, G. Yan, Z. Li, B. Jiang, Z. Liang, H. J. Fan and W. Mai, *Sci China Mater*, 2022, **65**, 442–450.

108 Y. Tian, M. Peter, E. Unger, M. Abdellah, K. Zheng, T. Pullerits, A. Yartsev, V. Sundström and I. G. Scheblykin, *Physical Chemistry Chemical Physics*, 2015, **17**, 24978–24987.

109 W. Tress, M. Yavari, K. Domanski, P. Yadav, B. Niesen, J. P. Correa Baena, A. Hagfeldt and M. Graetzel, *Energy Environ Sci*, 2018, **11**, 151–165.

110 Y. Tian, A. Merdasa, E. Unger, M. Abdellah, K. Zheng, S. Mckibbin, A. Mikkelsen, T. Pullerits, A. Yartsev, V. Sundström and I. G. Scheblykin, *Journal of Physical Chemistry Letters*, 2015, **6**, 4171–4177.

111 Y. Yamada, M. Endo, A. Wakamiya and Y. Kanemitsu, *Journal of Physical Chemistry Letters*, 2015, **6**, 482–486.

112 S. Chen, X. Wen, S. Huang, F. Huang, Y. B. Cheng, M. Green and A. Ho-Baillie, *Solar RRL*, DOI:10.1002/solr.201600001.

113 L. Chu, W. Ahmad, W. Liu, J. Yang, R. Zhang, Y. Sun, J. Yang and X. Li, *SpringerOpen*, 2019, preprint, DOI: 10.1007/s40820-019-0244-6.

114 X. Zheng, A. Du, Y. Ye, E. Chen, S. Xu and T. Guo, *Ceram Int*, 2024, **50**, 1474–1487.

115 W. Y. Huang, W. M. Zhong, J. Y. Chen, Q. X. Liu, Y. P. Jiang, L. H. Nie and X. G. Tang, *Colloids Surf A Physicochem Eng Asp*, DOI:10.1016/j.colsurfa.2024.134629.

116 F. Zeng, Y. Tan, B. Sun, W. Hu, H. Yin, X. Tang, L. Huang, J. Liao and M. Tang, *ACS Omega*, DOI:10.1021/acsomega.5c04702.

117 Z. Tan, J. Li, C. Zhang, Z. Li, Q. Hu, Z. Xiao, T. Kamiya, H. Hosono, G. Niu, E. Lifshitz, Y. Cheng and J. Tang, *Adv Funct Mater*, DOI:10.1002/adfm.201801131.

118 T. T. Deng, E. H. Song, Y. Y. Zhou, L. Y. Wang and Q. Y. Zhang, *J Mater Chem C Mater*, 2017, **5**, 12422–12429.

119 A. Mallik, N. Chakraborty, S. Goswami, M. Saha, S. M. Nawaz, B. Das, A. Biswas and K. K. Chattopadhyay, *ACS Appl Electron Mater*, 2025, **7**, 4783–4792.

Chapter 2 Chemical Vapor Deposition Growth of Highly Stable $Cs_2AgBiBr_6$ Double Perovskite Thin Films and Their Ultralow Thermal Conductivity and Fast Photoresponse

The lead-free double perovskite $Cs_2AgBiBr_6$ is a promising alternative to toxic lead-based perovskites due to its high stability and excellent optoelectronic properties. We report the direct growth of uniform, highly crystalline $Cs_2AgBiBr_6$ thin films via chemical vapor deposition (CVD). Structural and compositional uniformity was confirmed by XRD, Raman, and XPS analyses, while temperature- and power-dependent Raman studies revealed a temperature coefficient of -0.01431 ± 0.0039 $cm^{-1}K^{-1}$ and thermal conductivity of $\sim 1.97 \pm 0.48$ W/m-K. The films, when integrated into a self-powered planar photodetector, exhibited ultrafast response times of ~170/177 µs, surpassing previously reported $Cs_2AgBiBr_6$ devices. These results highlight CVD-grown $Cs_2AgBiBr_6$ as a highly stable and efficient candidate for next-generation lead-free optoelectronic applications.

2.1 Introduction

In recent years, the perovskite family of materials has garnered considerable attention for its optoelectronic applications. In less than a decade, lead-based perovskite solar cells (PSCs) have achieved > 25% power conversion efficiencies (PCEs) for planar solar cells and more than 32.5% PCE for monolithic tandem solar cells[1]. Besides solar cells, lead-based perovskites also show excellent potential for other optoelectronic applications like light-emitting diodes (LEDs)[2,3], photodetectors [PDs][4–7], X-ray detectors[8,9], etc. However, various practical challenges hinder the commercialization of lead-based perovskite devices. Further, the pronounced toxicity of lead and poor stability of lead-based devices create issues for practical applications. Therefore, the search for lead-free perovskites has become a prime goal for researchers worldwide. Various combinations of Tin (Sn^{2+}), Silver (Ag^{+}), and Bismuth (Bi) based perovskites have been attempted to replace lead (Pb^{2+}). Nevertheless, due to the facile oxidation of Sn^{2+} to Sn^{4+} in air, its feasibility for photovoltaic applications has been hindered[10,11]. Bi^{3+} is a promising substitute due to its non-toxicity and isoelectronic nature with Pb^{2+}, but the charge inequality and resulting low-dimensional structures are less feasible for optoelectronic applications than their Pb^{2+}-based counterparts[12-16].

Among the DPs, $Cs_2AgBiBr_6$ has shown great potential, both theoretically and experimentally, towards optoelectronic applications owing to its exceptional properties of non-toxicity, environmental stability, long carrier lifetime (of the order of hundreds of nanoseconds), long

diffusion lengths, and high carrier mobility[17–19]. However, synthesizing the highly pure and crystalline thin film of these perovskites is challenging for optoelectronic applications. Because of low precursor solubility and the quaternary nature of this double perovskite, it is much more complex to synthesize this material than Pb-based perovskites. Solution processing and vapor deposition are the most widely used synthesis approaches for double perovskite thin films. Solution-aided synthesis routes widely use one- or two-step spin coating processes. Greul et al. developed mesostructured $Cs_2AgBiBr_6$ solar cells using a straightforward one-step spin coating technique.[20] Bismuth bromide ($BiBr_3$), silver bromide (AgBr), and cesium bromide (CsBr) precursors were simply spin-coated on the porous TiO_2 to create the absorber layer. The surface morphology of the resulting $Cs_2AgBiBr_6$ films seemed to be poor, with significant roughness and defect density.[20] In particular, pinhole defect-containing perovskite films resulted in direct contact between electron and hole transport layers, causing losses due to photogenerated carrier recombination. This is primarily because the solution-processed perovskite films are extremely sensitive to several conditions, including annealing temperature, solution concentration, precursor composition, and solvent choice.[21] By using anti-solvent and low-pressure assisted techniques, *Gao et* al. and *Wu et* al. obtained flat $Cs_2AgBiBr_6$ films. However, the low solubility (less than 0.6 mol/L) of DP precursors in typical solvents restricts the preparation of high-quality films as well as their commercial applications.[22,23] Furthermore, $Cs_2AgBiBr_6$ solar cells were made by successive vapor deposition by *Wang et al*.[24] However, ensuring the sequential evaporation of AgBr, $BiBr_3$, and CsBr powders under high vacuum and determining their suitable composition ratio posed complications. The composition ratios of the as-prepared $Cs_2AgBiBr_6$ films deviated significantly from the ideal stoichiometry, which proved detrimental to the fabrication of high-efficiency solar cells.[24] Thus, we believe that chemical vapor deposition (CVD) would be the alternative solution to the challenges faced in solution-processed synthesis techniques. To our knowledge, there is no report on the CVD growth of DP thin films with large grain size and high stability, despite their crucial application in cutting-edge areas of optoelectronics.

Additionally, the thermal conductivity of materials has a direct impact on the performance of electronic systems. It is a unique tool for interpreting complex systems and planning heat transfer in a wide range of technical applications. Thermal wall coverings, thermoelectric energy harvesting, and solid-state cooling are just a few of the applications that need materials with extremely low thermal conductivity.[25] Likewise, a material with excellent thermal conductivity may disperse heat quickly, preventing gadget damage.[26] Owing to their lattice

dynamical instability and extraordinarily high anharmonicity, Pb-free halide DP is predicted to have ultralow thermal conductivity, which is important for thermoelectric applications.[27,28] Klarbring et al. reported an ultralow thermal conductivity of ~0.33 W/(m-K) for $Cs_2AgBiBr_6$ DP[29], and Haque et al. predicted an ultralow lattice thermal conductivity of 0.0065 W/m-K at 300 K for $Cs_2BiAgCl_6$, attributed to its low phonon group velocity and large phonon scattering.[30] However, to the best of our knowledge, there are no reports that have proved these theoretical estimations experimentally. Biswas et al. reported a low lattice thermal conductivity of 0.37-0.22 W/m-K in various halide perovskites.[31–33] Sajjad et al. predicted ultra-low thermal conductivity (0.15 W/m-K at 300 K) of Cs_2PtI_6 double perovskite.[34] Raman spectroscopy is a non-destructive method that allows us to understand the electron-phonon and phonon-phonon interactions in complex and highly anharmonic systems such as $Cs_2AgBiBr_6$ DPs, and is a powerful tool to determine attributes like thermal conductivity of these systems.

Here, we have successfully synthesized a highly crystalline and smooth thin film of $Cs_2AgBiBr_6$ DP by a CVD method on different substrates, Silicon (Si), quartz, and Silicon dioxide (SiO_2). We observed high-quality film growth on SiO_2 substrates with minimal pinhole defects and minimum film roughness. We discuss the growth mechanism of the DP film with the help of controlled experiments on the intermediate products. By analyzing the low temperature and power-dependent Raman spectra, we have measured a low thermal conductivity of ~1.97 W/(m-K) for lead-free $Cs_2AgBiBr_6$ DP thin film for the first time. High-temperature Raman study is utilized to understand the thermal stability of the $Cs_2AgBiBr_6$ DP thin film, which is stable up to 220 °C. X-ray diffraction pattern confirmed the phase stability of $Cs_2AgBiBr_6$ DP thin film for more than three months. We utilized the as-grown $Cs_2AgBiBr_6$ film on a SiO_2 substrate to fabricate a photodetector that exhibited a fast photoresponse of ~170/177 µs, which is far improved as compared to previously reported $Cs_2AgBiBr_6$-based photodetectors. Furthermore, the device exhibited photoconduction at zero bias as well, making it self-powered in nature. Note that no charge-transporting layer was used in the $Cs_2AgBiBr_6$ photodetector device reported here.

2.2 Experimental Details

2.2.1 Chemicals

Cesium bromide (CsBr, 99.99%, Sigma Aldrich), silver bromide (AgBr, 99.99%, Sigma Aldrich), bismuth bromide ($BiBr_3$, >99%, Alfa Asar), and toluene (>99%, Merck) were used for the synthesis of $Cs_2AgBiBr_6$ DP thin film without any further purification.

2.2.2 Seed Layer Preparation

0.125 mmol of bismuth bromide was dissolved in 5mL of toluene at 75°C for 15 minutes with continuous stirring at 800 rpm. All the substrates (SiO_2, quartz, and Si) were cleaned by bath ultrasonication in acetone and propanol for 30 minutes, followed by nitrogen treatment, and dried for 20 minutes at 90°C. Then, 30 µL of the $BiBr_3$ solution was drop-cast on each substrate and dried for 10 minutes at 75°C. All substrates were then transferred to the furnace for the CVD process. The schematic illustration of seed layer preparation is shown in **Fig. 2.1(a)**.

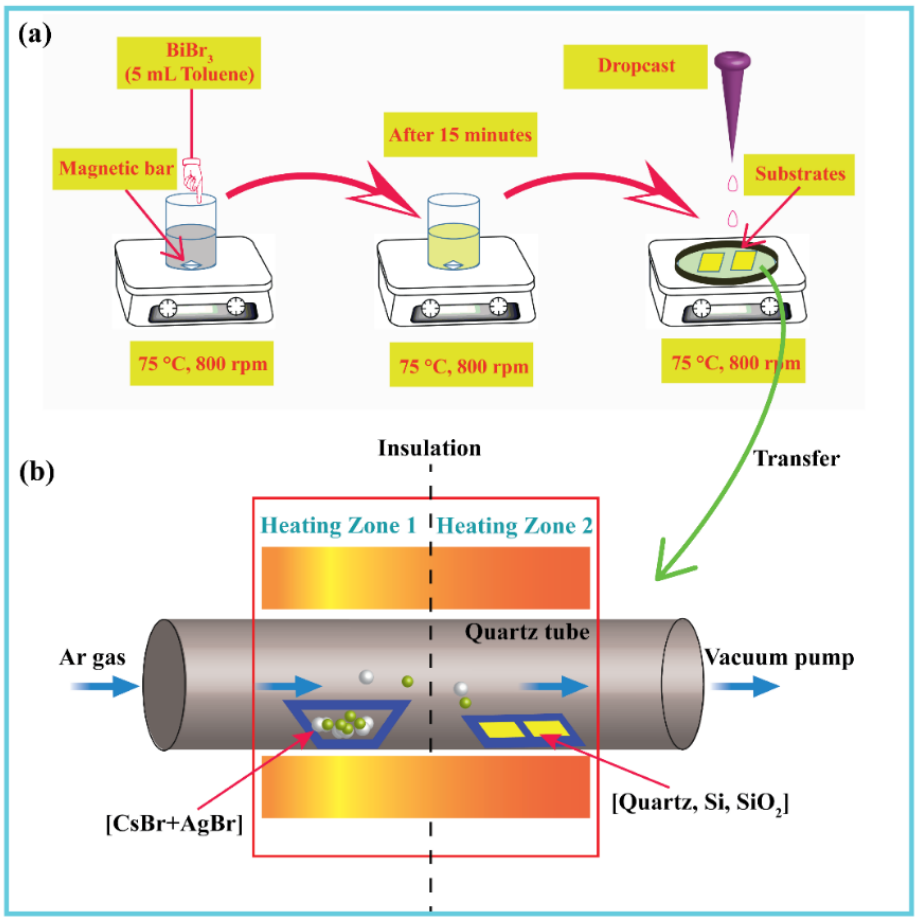

Fig. 2.1: (a) Schematic illustration of the preparation of the $BiBr_3$ seed layer. **(b)** Chemical vapor deposition setup used for the deposition of the $Cs_2AgBiBr_6$ DP thin film.

2.2.3 CVD Deposition of $Cs_2AgBiBr_6$ DP Thin Film

We used a homemade CVD system consisting of a two-zone muffle furnace and controlled gas flow to grow $Cs_2AgBiBr_6$ DP thin film. A mixture of 0.5 mmol of CsBr and 0.25 mmol of AgBr was placed in a quartz boat and heated to 800°C in zone 1 within a 2-inch quartz tube. The substrates were kept downstream in the second zone at a distance of 23 cm from the source materials (**Fig. 2.1(b)**). The detailed temperature profile and growth parameters for Zone 1 and

Zone 2 are shown in **Fig. 2.2.** At first, 200 sccm Ar was purged into the quartz tube for 20 minutes to remove any gaseous residues or surface-adsorbed impurities. Subsequently, a constant flow rate of 100 sccm of Ar gas was maintained throughout the experiment. A ramping rate of 17°/minute was set for the first zone. The growth time and substrate temperature for deposition were optimized to be 30 minutes and 130°C, respectively. After deposition, the system was allowed to cool down naturally. We successfully synthesized high-quality $Cs_2AgBiBr_6$ DP thin film on various substrates following this procedure.

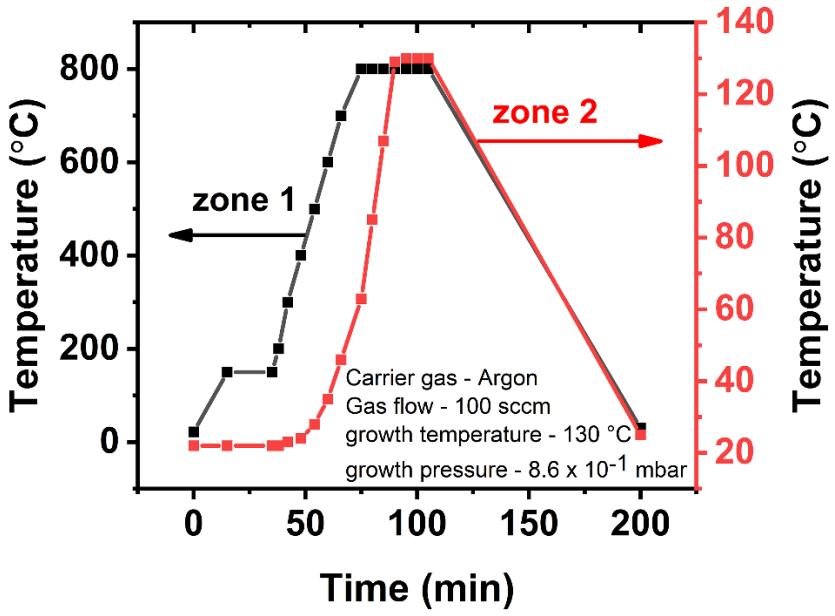

Fig. 2.2: Growth parameters and temperature profile of zone-1 and zone-2 of the CVD system for the growth of $Cs_2AgBiBr_6$ DP thin film.

2.3. Measurement and Characterizations

X-ray diffraction (XRD) (Rigaku RINT 2500 TTRAX-III, Cu K radiation) has been used to determine the crystal structure of the $Cs_2AgBiBr_6$ DP thin film. By using high-resolution micro-Raman spectroscopy (LabRam HR800, Jobin Yvon) with an excitation wavelength (λ_{ex}) of 532 nm (Ar ion laser), the crystalline phase of the $Cs_2AgBiBr_6$ DP thin film has been investigated. The laser was focused with a 100x objective lens to a spot size of 1 µm, and an excitation power of 140 µW was used. The generated signal was then collected by a charge-coupled device (CCD) in a backscattering geometry and transmitted through a multimode fibre grating with 1800-mm^{-1} grooves. Raman spectra were acquired for a fixed constant acquisition time. A field emission scanning electron microscope (FESEM, SIGMA 300, Ziess) running at 200 kV was used to examine the surface morphology, thickness, and elemental mapping of the as-

grown $Cs_2AgBiBr_6$ DP thin film. The average film roughness of the $Cs_2AgBiBr_6$ DP thin film was studied using atomic force microscopy (AFM) (Cypher, Oxford Instruments). To investigate the chemical composition, X-ray photoelectron spectroscopy (XPS) measurements were carried out using a PHI 5000 VersaProbe III photoelectron spectrometer (ULVAC-PHI, INC.) with an Al Kα X-ray beam (1486.6 eV) at a beam current of 20 mA. The absorption spectra in the UV-Vis range were recorded using a PerkinElmer Lambda 950 commercial spectrometer. Additionally, the steady-state photoluminescence spectra were recorded at room temperature utilizing a Horiba Jobin Yvon Fluromax-4 commercial fluorimeter with a 405 nm excitation laser source. Time-resolved PL measurements were carried out at room temperature using a 405 nm pulsed laser excitation source with <50 ps instrument response time (Lifespec II, Edinburgh Instruments). The temperature-dependent Raman spectra were acquired using liquid nitrogen as the coolant and a temperature stage with a remote operating span of 50x objective. By using different powers of a 532 nm laser power source and a 50x objective with NA = 0.9, power-dependent Raman spectra were obtained at ambient temperature. The I-V measurements and photoresponse of the device were measured using a homemade setup with a source meter (Keithley 2400, Germany), a Xenon lamp with a monochromator (Newport, USA), and a probe station (Ecopia, S. Korea). All the measurements were done in an ambient environment (without a glovebox) with relatively high humidity.

2.4 Results and discussion

2.4.1 Growth Mechanism of $Cs_2AgBiBr_6$ DP Thin Film

CVD is a relatively new yet versatile technique for producing high-quality, uniform two-dimensional crystalline films. Characteristics such as growth temperature, carrier gas, precursors, and substrate position play a dynamic role in film growth. We synthesized highly crystalline $Cs_2AgBiBr_6$ DP thin films on different substrates by varying the substrate temperature and keeping all other parameters constant. We used a two-step approach to deposit the $Cs_2AgBiBr_6$ DP thin film: (i) the creation of a $BiBr_3$ seed layer on the growth substrates, aiding nucleation, and (ii) chemical reaction of the seed layer with CsBr and AgBr for the growth of the $Cs_2AgBiBr_6$ DP thin film. The XRD pattern of the $BiBr_3$ seed layer drop-cast on the SiO_2 substrate is collected and shown in **Fig. 2.3(a)** to understand the growth mechanism. The obtained diffraction pattern matches the standard diffraction pattern of $BiBr_3$ (JCPDS: 01-083-1427). The quality of the $Cs_2AgBiBr_6$ DP thin film depends upon the quality of the seed layer, as this is the primary source of the Bi content and nucleation. We have obtained very

large grains of $BiBr_3$, as confirmed by the FESEM image in **Fig. 2.3(b)**, which will act as the nucleation sites for the growth of high-quality $Cs_2AgBiBr_6$ DP thin film with larger grain size. Note that the larger grain size particles of the seed layers are not compact, but at the time of growth, the higher substrate temperature helps in the formation of a highly compact $Cs_2AgBiBr_6$ DP thin film. The AFM image estimated the thickness of the seed layer as ~55 nm (**Fig. 2.3(c)**), which is kept constant for all further experiments.

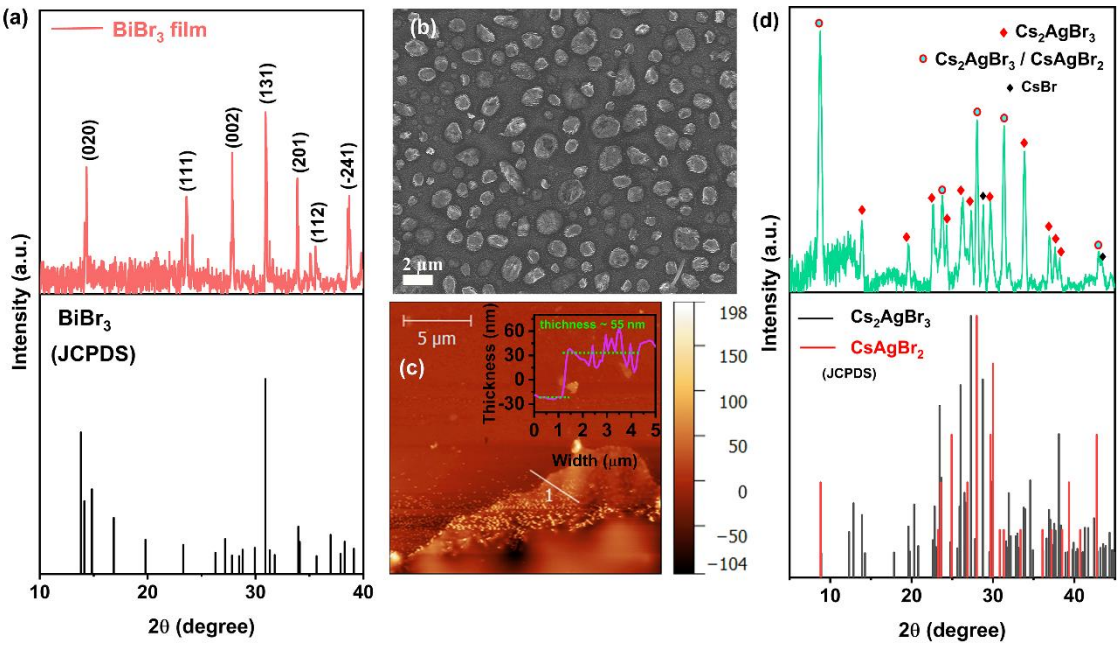

Fig. 2.3: (a) XRD pattern of $BiBr_3$ seed layer drop cast on SiO_2 substrate (above) and JCPDS data (below). **(b)** Top view FESEM image of $BiBr_3$ seed layer. **(c)** AFM image of the $BiBr_3$ layer. The inset image shows the height profile of the seed layer. **(d)** XRD pattern of the intermediate phase formed without the seed layer, confirming the formation of the Cs_2AgBr_3 phase.

There are four possible pathways for the nucleation, followed by the reaction of the precursors: (i) Independent evaporation of CsBr and AgBr and reaction with the $BiBr_3$ layer to form $Cs_2AgBiBr_6$ DP. (ii) Primary evaporation of AgBr owing to its low melting point (~430 °C) and formation of $AgBiBr_4$, followed by further reaction with CsBr to form $Cs_2AgBiBr_6$ DP. (iii-iv) Simultaneous evaporation of AgBr and CsBr leading to the formation of the Cs_2AgBr_3 and/or $CsAgBr_2$ phases, which can then react with AgBr and $Cs_3Bi_2Br_9$ to form $Cs_2AgBiBr_6$ DP. The chemical reactions for the above different pathways are as follows:

Pathway 1: $2CsBr + AgBr + BiBr_3 \rightarrow Cs_2AgBiBr_6$ (2.1)

Pathway 2: $2CsBr + AgBiBr_4 \rightarrow Cs_2AgBiBr_6$ (2.2)

Pathway 3: $2CsBr + AgBr \rightarrow Cs_2AgBr_3$

$$3CsBr + 2BiBr_3 \rightarrow Cs_3Bi_2Br_9$$

$$Cs_2AgBr_3 + 3AgBr + 2Cs_3Bi_2Br_9 \rightarrow 4Cs_2AgBiBr_6 \quad (2.3)$$

Pathway 4: $CsBr + AgBr \rightarrow CsAgBr_2$

$$CsAgBr_2 + 2AgBr + 2Cs_3Bi_2Br_9 \rightarrow 4Cs_2AgBiBr_6 \quad (2.4)$$

As a mixture of CsBr and AgBr was used, the possibility of reaction pathways (3) and (4) is assumed to be higher than (1) or (2). The enthalpy of the formation of Cs_2AgBr_3 is more negative than the enthalpy of the formation of $CsAgBr_2$[35]. To further confirm the growth reaction, we monitored the intermediate growth phases by evaporating CsBr and AgBr together on a bare SiO_2 substrate (without the seed layer), keeping all the parameters unchanged. The XRD pattern confirmed the formation of the Cs_2AgBr_3 phase, as shown in **Fig. 2.3(d)**, which matches well with the JCPDS data shown in Figure S2. It may be noted that some of the peaks of the Cs_2AgBr_3 phase coincide with the peaks of $CsAgBr_2$, and the corresponding peak intensities are higher. Due to the larger number of peaks for Cs_2AgBr_3 in the XRD pattern, we believe that equation (3) is more probable than equation (4) in our experiment. Thus, the formation of $Cs_2AgBiBr_6$ film primarily follows the equation (3). As there is no seed layer over the substrate, most of the precursors reacted together to form the Cs_2AgBr_3 phase. However, a few peaks of unreacted CsBr were also observed in the XRD pattern (**Fig. 2.3**(d)), which further confirms that pathway (3) is mainly responsible for the growth of $Cs_2AgBiBr_6$ DP thin film. We have carried out the growth of $Cs_2AgBiBr_6$ DP thin film using three different substrate temperatures: 130 °C, 150 °C, and 180 °C. The ramping rate of the second zone is adjusted such that the growth temperature is attained in 15 minutes. Further analysis of temperature and substrate-dependent growth is discussed in later sections.

2.4.2 Structural and Crystalline Properties of $Cs_2AgBiBr_6$ DP Thin Film

2.4.2.1 XRD Analysis:

$Cs_2AgBiBr_6$ DP has a fundamental perovskite structure of a 3D framework with a corner-sharing octahedral, as depicted in **Fig. 2.4**. Ag and Bi alternately occupy the centers of the octahedron in all three directions, whereas Cs^+ occupies the middle position of the cuboctahedral cavity. XRD measurements were carried out to study the phase purity of the $Cs_2AgBiBr_6$ thin film. **Fig. 2.5(a)** displays the indexed XRD patterns of our films, which demonstrate the formation of a pure DP phase for a 130 °C substrate temperature.

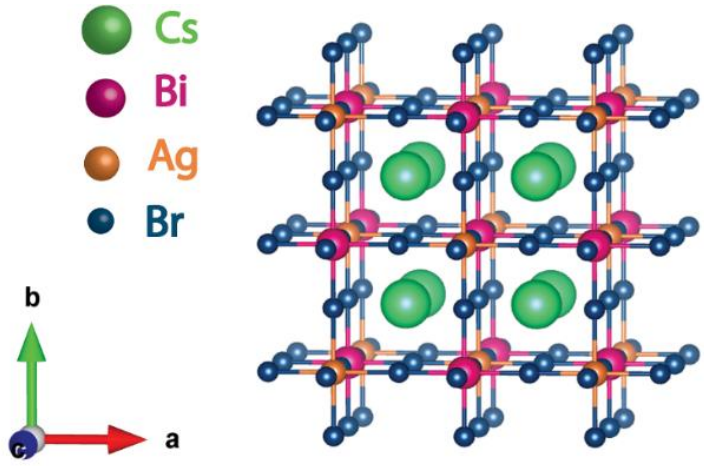

Fig. 2.4: Cubic crystal structure of $Cs_2AgBiBr_6$ DP.

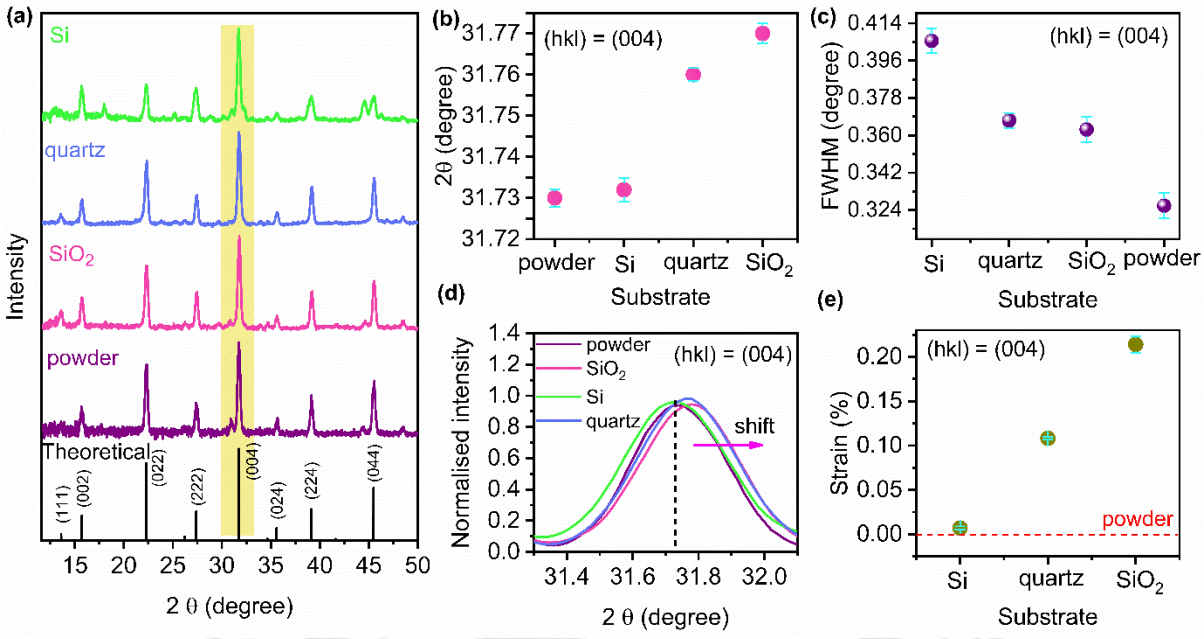

Fig. 2.5: (a) XRD pattern of $Cs_2AgBiBr_6$ DP powder and thin film over Si, quartz, and SiO_2 substrates. **(b,d)** The substrate-dependent shift in the 2θ of (004) peak in $Cs_2AgBiBr_6$ DP with respect to the powder sample. **(c)** The variation of FWHM of the (004) peak of $Cs_2AgBiBr_6$ DP powder and thin film deposited on different substrates, and **(e)** the corresponding compressive strain of $Cs_2AgBiBr_6$ DP thin film deposited on different substrates.

The lattice constant of the $Cs_2AgBiBr_6$ DP is around 11.25 Å with space group $Fm\bar{3}m$, revealing a cubic structure. The diffraction peaks situated at 13.6, 15.7, 22.3, 27.4, 31.8, 35.6, 39.2, and 45.5° correspond to (111), (002), (022), (222), (004), (024), (244), and (044) planes of $Cs_2AgBiBr_6$ DP phase, respectively.[22] We have recorded the XRD patterns for samples grown at 150 and 180 °C substrate temperatures, as shown in **Fig. 2.6(a)**.

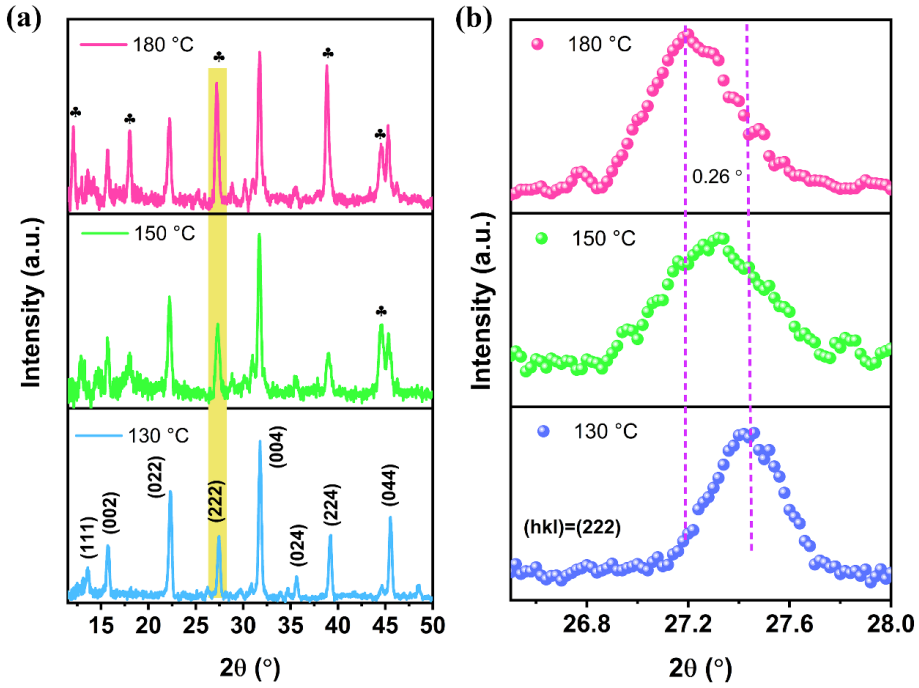

Fig. 2.6: (a) XRD pattern of $Cs_2AgBiBr_6$ DP thin film on SiO_2 substrate for growth temperatures 130°C, 150°C, and 180°C, respectively. Symbol ♣ indicated the peak positions corresponding to the secondary phase $Cs_3Bi_2Br_9$. **(b)** Comparison of the (222) peak for different substrate temperatures. A downshift in the XRD peak position at higher temperatures is obvious.

We have observed some extra diffraction peaks at 18.1° and 44.5°, which are attributed to the most common secondary phase of DP, $Cs_3Bi_2Br_9$.[36] Furthermore, we observed that there is a clear shift in the peak positions corresponding to (222) and (224) planes, indicating the formation of $Cs_3Bi_2Br_9$ at higher substrate temperatures (**Fig. 2.6(b)**).[36] These peaks matched well with standard JCPDS data (JCPDS: 00-044-0714) (**Fig. 2.7**). Rodkey et al. observed similar growth at low pressure and high substrate temperatures.[37] The group reported the migration of Ag particles on the surface of the thin film at high substrate temperatures. Due to the use of relatively high temperatures during the growth, there is a possibility of migration of Ag atoms from the film lattice to the surface, which may favor the formation of the secondary phase. We believe this leads to a resultant vacancy of Ag atoms in the film lattice, which might act as a catalyst for the phase change of $Cs_2AgBiBr_6$ DP to $Cs_3Bi_2Br_9$. **Fig. 2.5(a)** shows the XRD patterns of $Cs_2AgBiBr_6$ DP powder and thin films deposited on Si, quartz, and SiO_2 substrates. The XRD patterns confirmed highly crystalline growth over all substrates. However, the film deposited on the Si substrate shows some peaks of the secondary phase as well. These peaks are associated with the secondary phase $Cs_3Bi_2Br_9$, as confirmed by the JCPDs file in

Fig. 2.7. Since Si is a better thermal conductor than SiO_2 or quartz, secondary phases may be forming on the Si substrate due to higher heat flow.

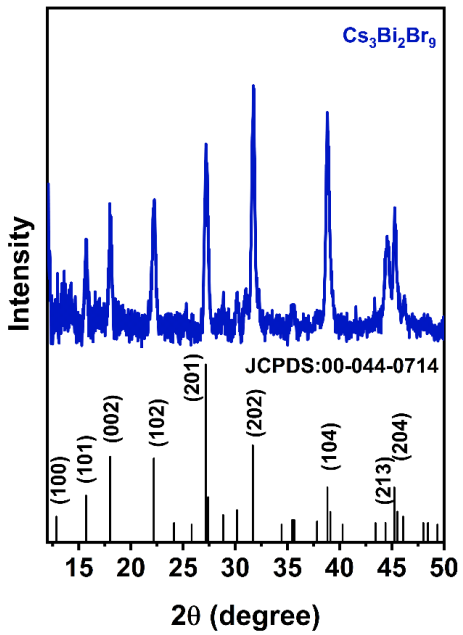

Fig. 2.7: XRD pattern of $Cs_3Bi_2Br_9$ DP deposited at a substrate temperature of 180 ºC and the corresponding JCPDS data.

Perovskites typically have two distinct sources of strain: local lattice strain and external condition-induced strain. Local lattice strain is mainly caused by the ionic size mismatch or local lattice mismatch[38]. The external factor-induced strain arises primarily from two types of mismatches: the lattice mismatch between the perovskite and substrate, categorized as biaxial strain[39], and the thermal expansion mismatch[40]. Perovskites usually possess high thermal expansion coefficients (α) in the range of 3.3 to 8.4×10^{-5} K^{-1}.[41] A significant difference in α between the perovskite film and the growth substrate, thus, leads to thermally induced strain in perovskite films. In particular, a perovskite film grown at a high temperature would compress as it cooled down to room temperature because of the positive thermal expansion coefficient. Moreover, to obtain a high-quality $Cs_2AgBiBr_6$ thin film, we need to anneal the film at temperatures of around 250 °C.[21] Therefore, during the growth or annealing process, the contact made between the perovskite and a growth substrate with a lower α prevents the perovskite from contracting naturally when it cools back to room temperature, causing tensile strain in the in-plane direction. Simultaneously, there is a compressive strain in the out-of-plane direction.

The strain calculations for different substrates are discussed below.

$$\varepsilon = \frac{(d_{powder(004)} - d_{strained(004)})}{d_{powder(004)}}$$

Where $d_{strained(004)}$ and $d_{powder(004)}$ are the plane spacing of the (004) plane of $Cs_2AgBiBr_6$ DP thin film with or without strain, respectively. Then, the corresponding lattice constant was calculated.

$$\varepsilon = \frac{|a' - a|}{a'}$$

Where a is the lattice constant of the (004) plane calculated from the (004) plane diffraction of the XRD pattern, and a′ is the lattice constant calculated from the powder $Cs_2AgBiBr_6$ DP. The respective strain induced in the perovskite film for different substrates is listed in **Table 2.1**.

Table 2.1 Strain calculation of the (004) plane of $Cs_2AgBiBr_6$ DP film deposited on different substrates.

Substrate	a′ (Å) (Powder)	a (Å) (Calculated)	Δa (a-a′) (Å)	Strain [Δa/a′] (%)	Strain type
Si	11.2710	11.2702	-0.0008	-0.007	compressive
SiO_2	11.2710	11.2468	-0.0242	-0.214	compressive
quartz	11.2710	11.2588	-0.0122	-0.108	compressive

As the thermal expansion coefficient of Si is larger than that of quartz and SiO_2 substrates, the corresponding strain is less in $Cs_2AgBiBr_6$ DP thin film over a Si substrate (**Fig. 2.5(e)**, **Table 2.1**).

Table 2.2. XRD peak position and corresponding FWHM of (004) plane of $Cs_2AgBiBr_6$ DP film deposited on different substrates.

Substrate	2θ (degree)	Std. Error (degree)	FWHM (degree)	Std. Error (degree)
Powder	31.7300	0.002	0.3262	0.006
Silicon	31.7324	0.003	0.4055	0.005
SiO_2	31.7746	0.002	0.3628	0.006
Quartz	31.7652	0.002	0.3672	0.004

The corresponding shift in the (004) plane towards a higher angle for the SiO_2 substrate further confirms the larger compressive strain in the as-grown $Cs_2AgBiBr_6$ DP film (see **Fig. 2.5(b,d)**). The dashed line in **Fig. 2.5(d)** shows the peak position of the strain-free powder DP phase, which matches well with the JCPDS: 01-084-9972 data file.

Table 2.3 Mean crystallite sizes of $Cs_2AgBiBr_6$ DP films for different substrates.

Substrate	2θ (degree)	Crystallite size (nm)	Average crystallite size (nm)
Si	15.7	32	36
	22.3	40	
	27.3	33	
	31.7	38	
	39.1	38	
	45.5	36	
Quartz	15.7	38	45
	22.3	43	
	27.4	49	
	31.8	45	
	39.2	49	
	45.5	48	
SiO_2	15.7	43	47
	22.3	42	
	27.4	47	
	31.8	42	
	39.2	67	
	45.5	43	

The full width at half maximum (FWHM) measures the film's quality and crystallinity. We have extracted the FWHM by fitting all the major diffraction peaks using Gaussian deconvolution. We observed that we get the best quality $Cs_2AgBiBr_6$ DP thin film over SiO_2 substrate with a minimum FWHM of 0.36° corresponding to (004) plane (**Fig. 2.5(c)** and **Table 2.1**). We calculated the average crystallite size for all substrates using Scherrer's equation (2.5). We have calculated the average crystallite size of $Cs_2AgBiBr_6$ DP thin film deposited on Si, Quartz, and SiO_2 substrates by using Scherrer's equation, as follows:

$$D = \frac{K\lambda}{\beta \cos\theta} \quad (2.5)$$

Where D is the crystallite size and K is the Scherrer's constant. K is a variable Scherr's constant that relies on the crystal's form. For a cubic structure, K is 0.94. $\lambda = 1.5406$ Å is the wavelength of the X-ray used. θ is the Bragg angle of the diffraction peak. β is the line broadening at full-width half maximum (FWHM). We estimated the average crystallite sizes of the deposited $Cs_2AgBiBr_6$ DP thin films to be ~36 nm, 45 nm, and 47 nm on Si, quartz, and SiO_2 substrates, respectively (**Table 2.3**).

2.4.2.2 Raman Analysis:

Fig. 2.8(a-c) depicts the micro-Raman spectrum of as-grown DP thin film on Si, quartz, and SiO_2 substrates, respectively. A laser excitation of 532 nm was used for the measurement. **Fig. 2.9** depicts a pictorial representation of various Raman modes in $Cs_2AgBiBr_6$. The primary mode (A_{1g}) is a breathing mode in which the six Br atoms move towards and away from the central Ag atom. The E_g mode is similar, but with three Br atoms traveling towards and three away from the Ag atom at the same time. The $T_{2g}^{(1)}$ vibrational mode corresponds to the vibration of the Cs atoms in addition to Br, whereas, in the case of the $T_{2g}^{(2)}$ mode, all the atoms participate in the vibration. The major Raman modes of the cubic phase have been determined to be approximately 73 cm^{-1}, 133 cm^{-1}, and 177 cm^{-1}, and they are T_g (anharmonic breathing) and E_g and A_g (both stretching) modes of either $(BiBr_6)^{3-}$ or $(AgBr_6)^{5-}$ octahedra.[36] The Raman spectra of thin films at various growth temperatures are shown in **Fig. 2.10**. We have observed a systematic phase change of $Cs_2AgBiBr_6$ DP to $Cs_3Bi_2Br_9$ as the substrate temperature increased. These results are in good correlation with our XRD results. The crystal symmetries also permit Raman scattering of low-frequency lattice modes of $Cs_2AgBiBr_6$ DP, as was discovered in elpasolites, in addition to the three characteristic Raman modes of the $BiBr_6$ octahedra.[42,43] We have fitted the Raman spectra for all three substrates with a Lorentzian line shape, which reveals the FWHM of the A_{1g} mode as 10.74 cm^{-1}, 10.23 cm^{-1}, and 9.80 cm^{-1} for Si, quartz, and SiO2 substrates, respectively. This suggests that the highly crystalline growth of $Cs_2AgBiBr_6$ DP is deposited on the SiO_2 substrate. Raman shifts of all the modes with respective FWHM are tabulated in **Table 2.4**. The change in vibrational frequency brought about by the variation in chemical bond length caused by compressive or tensile strain may be easily identified by Raman spectral analysis.

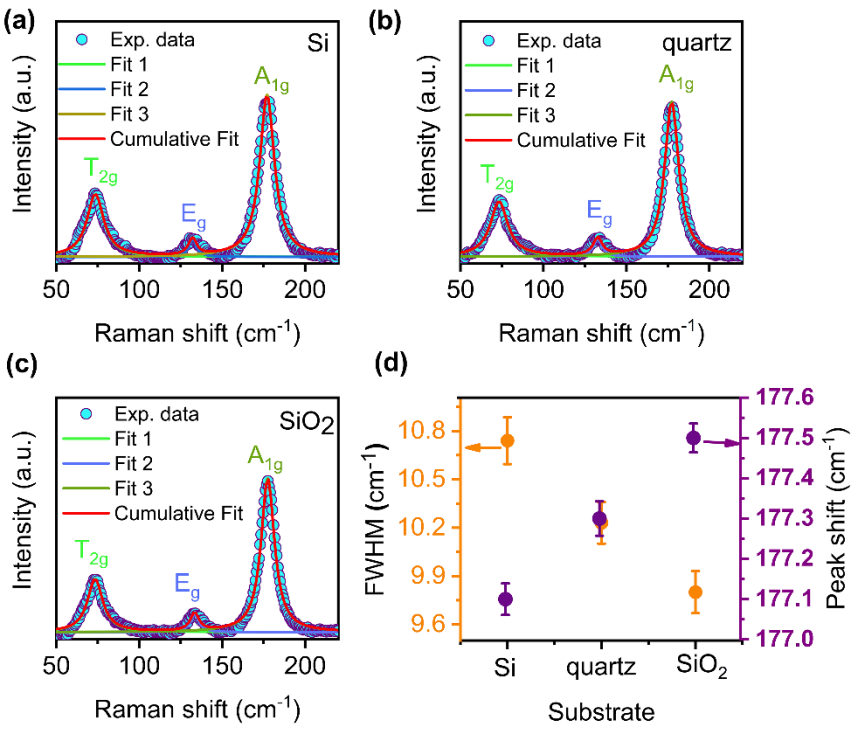

Fig. 2.8: (a-c) Raman spectra of $Cs_2AgBiBr_6$ DP thin film on different substrates (Si, quartz, and SiO_2) using a 532 nm laser excitation source. **(d)** Variation of FWHM and peak shift in the A_{1g} Raman mode of double perovskite thin films for different substrates.

Table 2.4 Raman shifts and corresponding FWHM of all Raman active modes of $Cs_2AgBiBr_6$ DP film deposited on different substrates.

Substrate	**T_{2g}**			**E_g**			**A_{1g}**		
	Raman Shift (cm^{-1})	FWHM (cm^{-1})	Std. Error (cm^{-1})	Raman shift (cm^{-1})	FWHM (cm^{-1})	Std. Error (cm^{-1})	Raman Shift (cm^{-1})	FWHM (cm^{-1})	Std. Error (cm^{-1})
Si	73.5	12.3	0.07	132.2	5.8	0.19	177.1	10.7	0.02
Quartz	73.3	12.6	0.07	132.7	6.4	0.16	177.3	10.2	0.02
SiO_2	73.4	11.0	0.06	133.4	6.3	0.15	177.5	9.8	0.02

Spectroscopic methods may also be used to identify strain in the case of perovskites since various perovskite phases have varying Raman activity. Strain can result in a blue shift of Raman modes as well as changes in peak broadening, splitting, and bond stiffness.[39] Figure 3d shows the variation of Raman peak shift as well as FWHM for different substrates. The blue shift in the A_{1g} mode of $Cs_2AgBiBr_6$ DP thin film on SiO_2 substrate, concerning the Si substrate, indicated larger compressive strain in the former case.

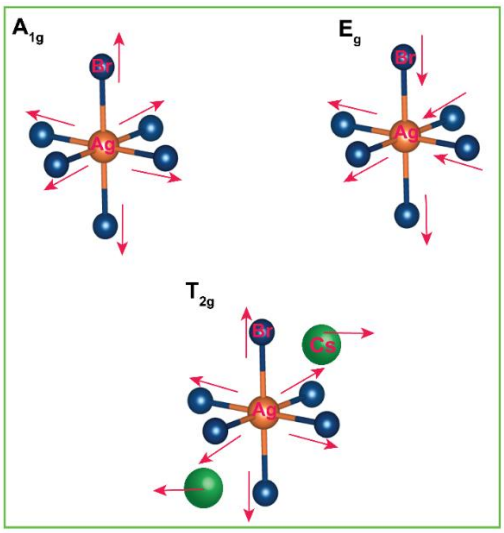

Fig. 2.9: Schematic of the Raman active modes of $Cs_2AgBiBr_6$ DP.

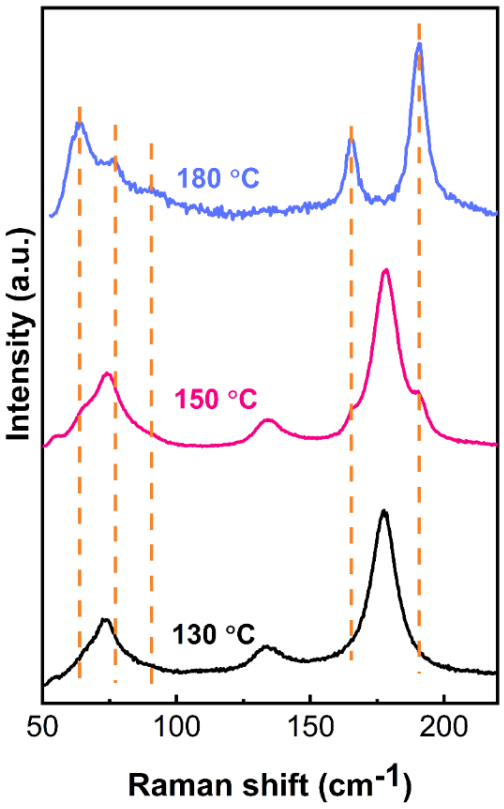

Fig. 2.10: Comparison of the Raman spectra of $Cs_2AgBiBr_6$ DP thin film synthesized at different substrate temperatures.

2.4.2.3 XPS Analysis

X-ray Photoelectron Spectroscopy (XPS) analysis was performed to examine both the crystallinity and the elemental composition of the $Cs_2AgBiBr_6$ double perovskite (DP) thin

films synthesized via the chemical vapor deposition (CVD) technique. XPS is a powerful characterization tool that provides insight into the chemical environment and electronic states of the constituent elements, thereby enabling a precise evaluation of the film's phase purity and stoichiometry. **Fig. 2.11(a)** illustrates the wide survey scan obtained from the as-grown $Cs_2AgBiBr_6$ thin film. This scan clearly reveals the characteristic peaks corresponding to cesium (Cs), silver (Ag), bismuth (Bi), and bromine (Br), thus confirming the successful incorporation of all the required elements in the expected stoichiometric ratios. Furthermore, **Fig. 2.11(b–f)** depicts the high-resolution core-level spectra of individual elements, including C 1s, Cs 3d, Ag 3d, Bi 4f, and Br 3d. These spectra provide detailed information regarding the binding energies and electronic states of the constituent atoms, which is essential for understanding the film's chemical composition and bonding nature. The corresponding binding energy values for the identified states are summarized in **Table 2.5**. Notably, the observed peak positions align closely with those reported in previously published studies, which serves as strong evidence that the film exhibits the correct crystalline phase and chemical configuration. This agreement with literature values further validates the high quality and phase purity of the $Cs_2AgBiBr_6$ double perovskite thin film synthesized through the CVD method. Such confirmation is crucial because even minor deviations in chemical states or stoichiometry could lead to significant changes in the film's optoelectronic performance.

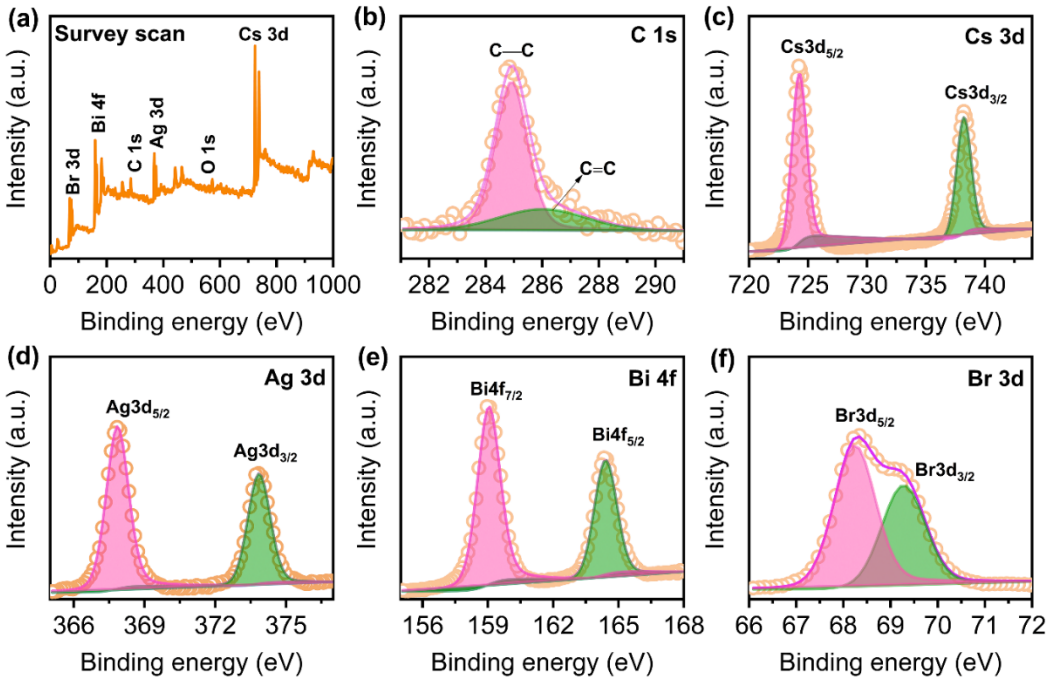

Fig. 2.11: (a) Survey scan XPS spectrum of $Cs_2AgBiBr_6$ DP thin film deposited on SiO_2 substrate. **(b-f)** High-resolution XPS spectra with fitting for C, Cs, Ag, Bi, and Br core levels, respectively.

Table 2.5. Summary of the binding energies of different elements present in CVD-grown $Cs_2AgBiBr_6$ DP thin film.

Elements		Binding energy (eV)
Cs	$3d_{3/2}$	738.22
	$3d_{5/2}$	724.26
Ag	$3d_{3/2}$	373.85
	$3d_{5/2}$	367.85
Bi	$4f_{5/2}$	164.46
	$4f_{7/2}$	159.04
Br	$3d_{3/2}$	69.28
	$3d_{5/2}$	68.24

2.4.3 Morphology and Compositional Analysis of $Cs_2AgBiBr_6$ Thin Film

The morphology of the as-synthesized $Cs_2AgBiBr_6$ DP thin film (substrate temperature~130 °C) was investigated by FESEM imaging. A highly compact, uniform, and smooth film was grown (**Fig. 2.12**). In the case of higher substrate temperatures, we have observed a non-smooth film because of grain agglomeration over the film surface. This is most likely caused by the fast crystallization process during CVD growth. The increased substrate temperature enhances the nucleation growth of the perovskite film, which results in nucleation at random sites, causing fast crystallization and growth of a non-uniform thin film. We believe that this fast crystallization process impedes homogeneous crystal growth, leading to agglomerates on the film surface. **Fig. 2.12(a-c)** shows FESEM images of $Cs_2AgBiBr_6$ DP thin film on SiO_2, Si, and quartz substrates, respectively. A dense and smooth film of $Cs_2AgBiBr_6$ DP is deposited on the SiO_2 substrate without any noticeable pinhole defects. The grain size was measured to be ~300 nm. The larger grain size of $Cs_2AgBiBr_6$ DP is attributed to the larger grain size of the seed layer, which acts as a nucleation site for the DP. The inset shows the magnified view of **Fig. 2.13(a)**. In contrast, many pinhole and line defects can be seen clearly on the films over Si and quartz substrates, suggesting an inferior film on these substrates.

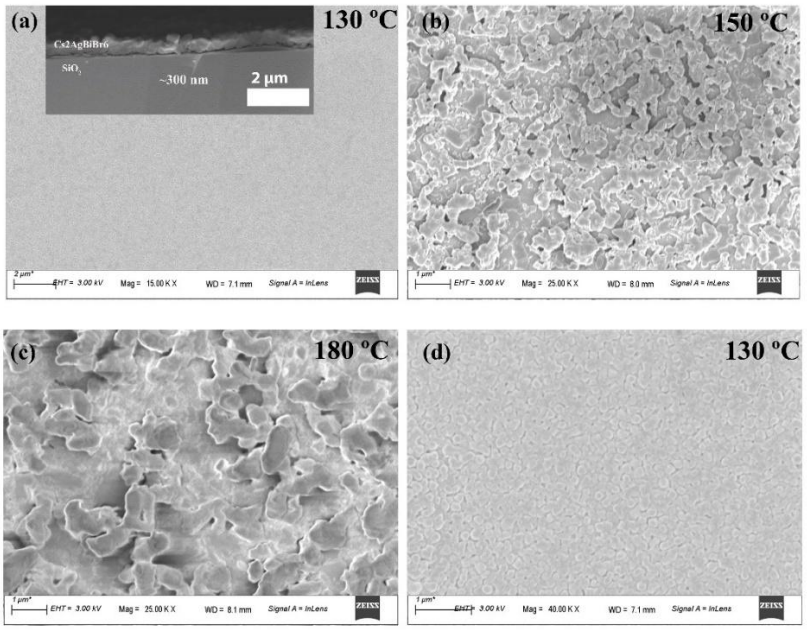

Fig. 2.12: Top-view FESEM image of $Cs_2AgBiBr_6$ DP thin film deposited at substrate temperatures **(a)** 130, **(b)** 150, and **(c)** 180°C. The inset in **(a)** shows the cross-section FESEM image of the DP film on the SiO_2 substrate. **(d)** Magnified image of $Cs_2AgBiBr_6$ DP deposited at 130°C substrate temperature.

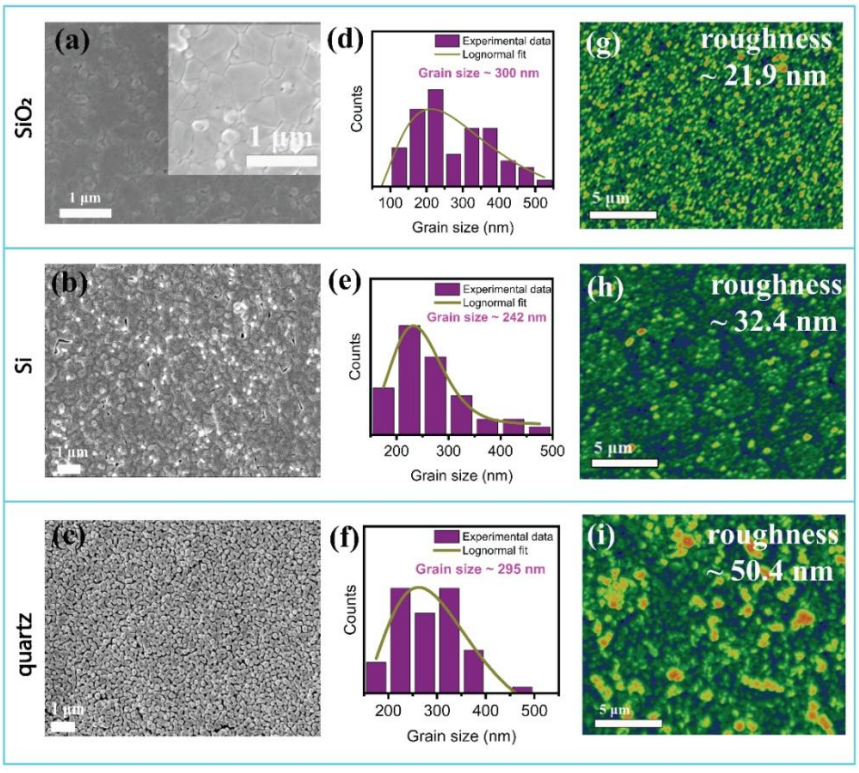

Fig. 2.13: Top-view FESEM images of $Cs_2AgBiBr_6$ films deposited on **(a)** SiO_2, **(b)** Si, and **(c)** quartz substrates. The inset of **(a)** shows the magnified view of the film with a large grain size. **(d-f)** Grain size distribution of $Cs_2AgBiBr_6$ films deposited on SiO_2, Si, and quartz substrates, respectively. **(g-i)** AFM images of $Cs_2AgBiBr_6$ films deposited on SiO_2, Si, and quartz substrates, respectively.

Grain size distribution for all substrates is shown in **Fig. 2.13(d-f)**. The variation in the grain size over different substrates can be explained by the hydrophilic or hydrophobic nature of the substrate. The slow and fast diffusion of the atoms over the specific substrates can affect the nucleation of the film.[45] To analyse the surface roughness of $Cs_2AgBiBr_6$ DP thin film, AFM imaging was carried out. The as-grown $Cs_2AgBiBr_6$ shows a minimum root-mean-square (RMS) roughness of 21.9 nm on the SiO_2 substrate, as shown in **Fig. 2.13(g)**. The film roughness that we have acquired by the CVD method is significantly lower than most solution-processed as well as vapor-deposited thin films of $Cs_2AgBiBr_6$ DP.[20,46] Films on Si and quartz substrates exhibit high surface roughness of ~ 32.4 nm and ~50.4 nm, respectively (**Fig. 2.13(h, i)**). Isolated gaps and pinhole defects cause higher film roughness, as confirmed by the FESEM images. The roughness of the substrate itself plays a vital role in the growth of the film, as it can affect the nucleation and growth of the thin film during deposition. The roughness can influence the distribution of defects in the thin film, which can, in turn, affect its mechanical and electrical properties. The roughness of all the substrates is studied using AFM (see **Fig. 2.14**). The surface roughness of SiO_2, Si, and quartz substrates is 0.96 nm, 1.43 nm, and 1.87 nm, respectively. We have observed a minimum roughness of the film deposited on the SiO_2 substrate due to the minimum substrate roughness.

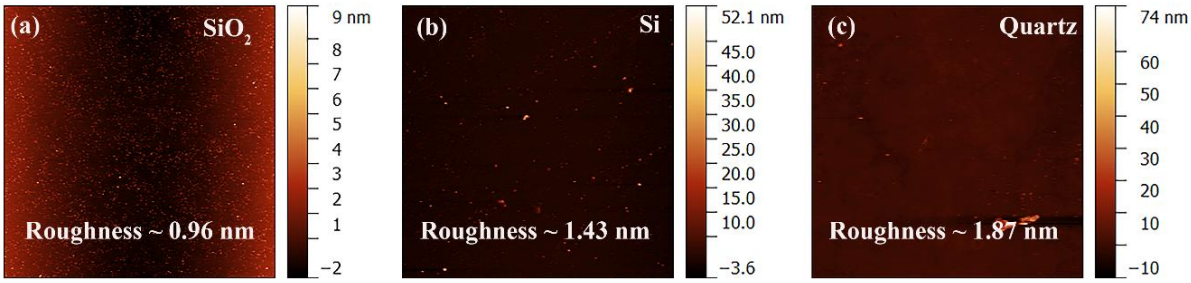

Fig. 2.14: (a-c) AFM images of SiO_2, Si, and quartz substrates, respectively. The scale of the images is 30 × 30 μm.

Next, energy-dispersive spectroscopy (EDS) measurements were done to look into the distribution and chemical composition of the $Cs_2AgBiBr_6$ DP thin film deposited on the SiO_2 substrate. The elements Cs, Ag, Bi, and Br were evenly distributed across the chosen region (depicted in **Fig. 2.15**). No other chemical impurities were found in the sample besides the known compositions. The incorporated Cs, Ag, Bi, and Br elements have an atomic percentage that is very close to the nominal ratio predicted by the stoichiometry of the precursor solutions. **Fig. 2.15(f)** displays the corresponding EDS spectrum with the atomic percentage. However, a

small peak near 2 keV emerges, which corresponds to Au from the top coating, which is essential for the measurement.

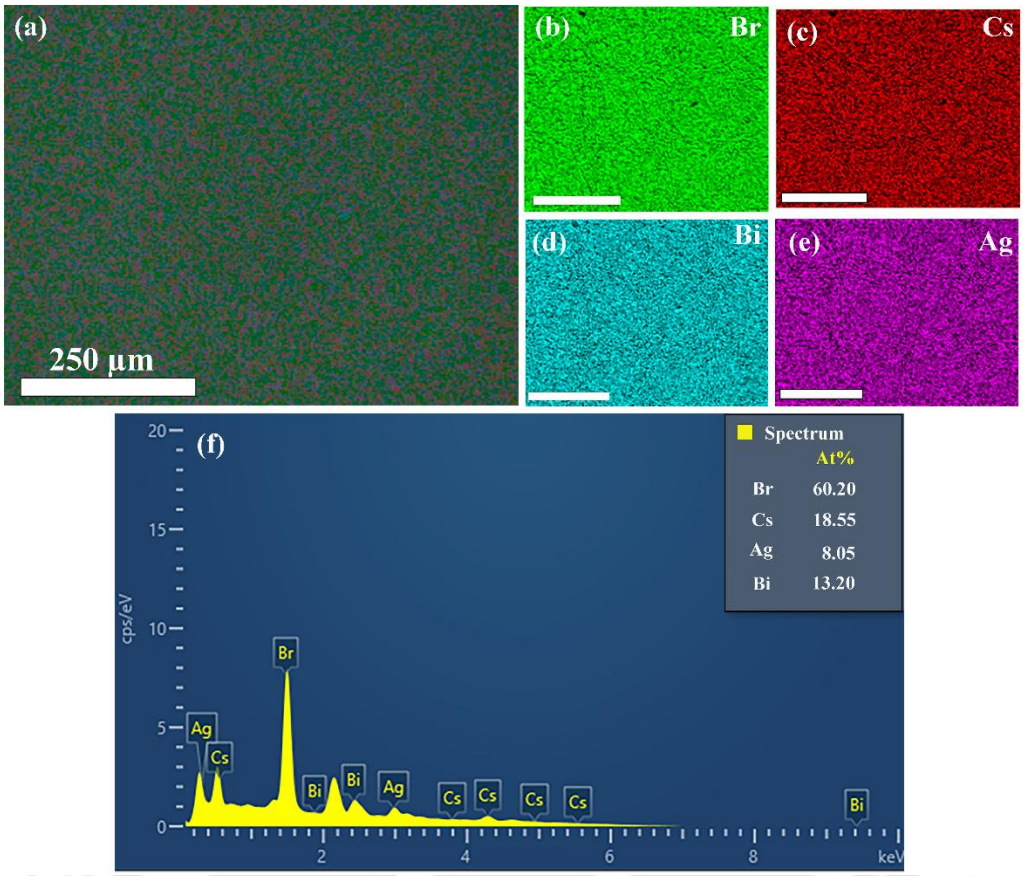

Fig. 2.15: (a) SEM image of $Cs_2AgBiBr_6$ film on SiO_2 substrate showing the elemental distribution of all elements over a large thin film area. **(b-e)** Elemental mapping of Cs, Br, Bi, and Ag, respectively, is present in the film. The scale bar in all images is 250 µm. **(f)** EDS spectrum of $Cs_2AgBiBr_6$ film showing the atomic percentage of different elements.

2.4.4 Optoelectronic Properties of $Cs_2AgBiBr_6$ DP Thin Film

The optical analysis of $Cs_2AgBiBr_6$ DP thin film was carried out using steady-state PL and absorption spectroscopy. **Fig. 2.16(a)** displays the absorption spectra of the thin film, exhibiting a strong absorption peak at ~422 nm, which is attributed to the Bi direct s-p transition[47]. However, the broad absorption tail indicates the indirect nature of the $Cs_2AgBiBr_6$ DP thin film. The Tauc plot was employed to determine the optical band gap of the DP thin films on different substrates (**Fig. 2.17**). Considering the indirect nature, we estimated optical band gaps of ~ 2.15 eV, 2.03 eV, and 1.80 eV for films on quartz, SiO_2, and Si substrates (**Table 2.6**), respectively, which are similar to the values reported for the bulk $Cs_2AgBiBr_6$ DP thin films.[21,22] The strain on the perovskite lattice significantly impacts the electronic band structure, particularly the

bandgap and the electronic states of the conduction band (CB) and valence band (VB) edges. This is because the electronic configuration of the crystal is strongly related to its lattice structure.[48] Generally, VB appears to be more sensitive to lattice strain than CB in the electrical band structure of perovskite materials. Chen et[43] showed the dependence of the bandgap on the strain induced in the system during growth. In the presence of compressive strain, the bandgap decreased in perovskite films, whereas in the presence of tensile strain, the bandgap showed an increasing trend. This correlates well with our results.

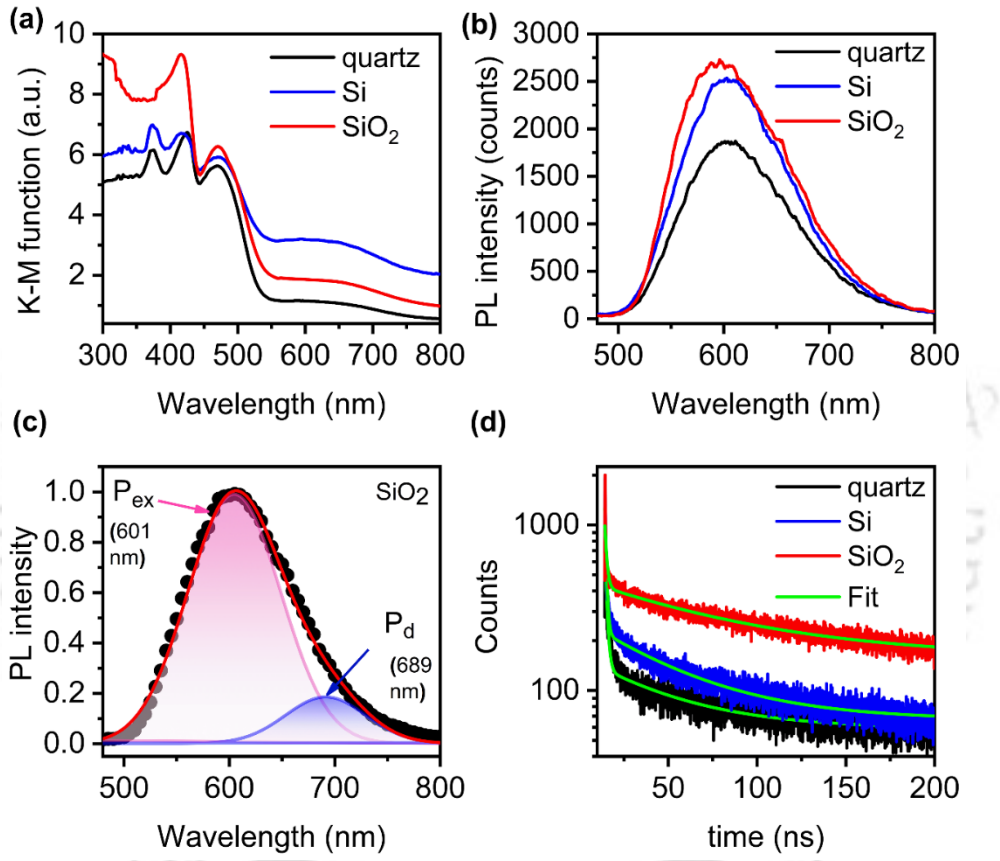

Fig. 2.16: (a) K-M plot of $Cs_2AgBiBr_6$ DP film deposited on different substrates. **(b)** PL emission spectra of $Cs_2AgBiBr_6$ DP film deposited on different substrates. **(c)** The Gaussian fit of the PL emission spectrum of $Cs_2AgBiBr_6$ film deposited on SiO_2 substrate. **(d)** Time-resolved PL decay profile of $Cs_2AgBiBr_6$ film deposited on different substrates.

Indirect bandgap and electron-phonon coupling are considered to be the causes of the relatively weak, broad, and Stokes-shifted PL peak of $Cs_2AgBiBr_6$ DP at room temperature. The nature of the PL emission of $Cs_2AgBiBr_6$ is still under debate. A broad red PL emission (typically between 600 and 700 nm) is observed at RT (**Fig. 2.16(b)**). Two PL peaks are revealed when deconvoluted with Gaussian fitting (**Fig. 2.16(c)**). The higher energy peak (P_{ex}) is attributed to band edge emission from the indirect bandgap, and the other lower energy emission (P_d) is

attributed to defect states in the band structure or self-trapped excitons (STEs).[49,50] Several studies contend that the PL emission is due to spatially localized color centers, which may represent defects or inherent self-trapping of excitons or carriers.[51,52] Conversely, Lei et[53] recently it was shown that band-to-band emission is primarily responsible for the PL emission of $Cs_2AgBiBr_6$ DP. The PL deconvolution parameters are tabulated in **Table 2.6**.

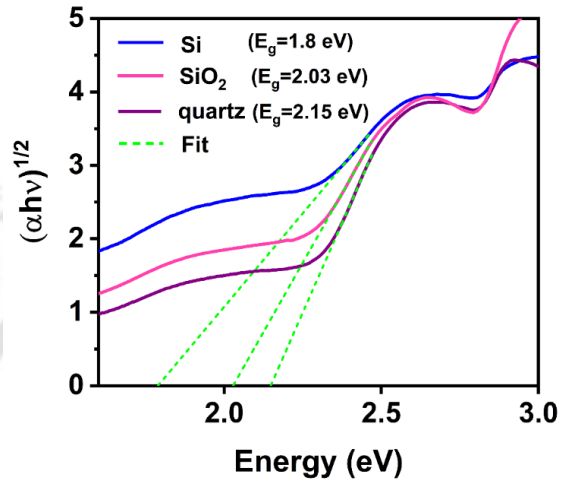

Fig. 2.17: Tauc plot of $Cs_2AgBiBr_6$ DP thin film deposited on Si (blue), quartz (purple), and SiO_2 (pink) substrates. The respective band gaps are calculated from the extrapolated lines (fitted).

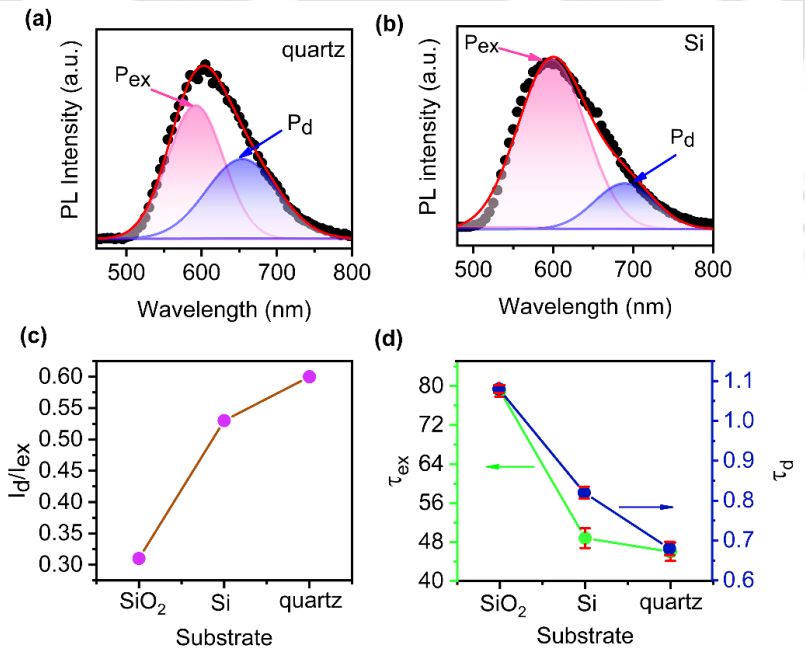

Fig. 2.18: Gaussian fitted PL spectra of $Cs_2AgBiBr_6$ DP thin film deposited on **(a)** quartz, and **(b)** Si substrates. **(c)** Variation of the intensity ratio of defect to excitonic peak in $Cs_2AgBiBr_6$ DP thin film deposited on different substrates. **(d)** Variation of decay components of $Cs_2AgBiBr_6$ DP thin film deposited on SiO_2, Si, and Quartz substrates.

To quantify the defects present in $Cs_2AgBiBr_6$ DP thin film for different substrates, we have calculated the ratio of the intensity of the defect peaks (I_d) to the intensity of the excitonic emission peak (I_{ex}) (see **Fig. 2.18 (a-c)**). We observed that the film deposited over the SiO_2 substrate has a minimum I_d/I_{ex} ratio, indicating the formation of a high-quality thin film with fewer defects. We found that Si creates a less strained sample. However, from FESEM images, we have observed a large number of pinholes in the thin film deposited on the Si substrate, which can act as the trapping sites for the charge carriers. In contrast, such pinholes are far fewer in the case of the SiO_2 substrate, leading to fewer trap states and thus relatively lower intensity of defect peak contribution. The apparent mismatch of the PL peak position with the bandgap data is due to the interference of the defect peak (P_d) with the excitonic peak (P_{ex}). Due to the higher contribution of the defect-related peak in the quartz, the mean position of the peak is right-shifted in the PL spectra. However, the excitonic peak positions are consistent with the bandgap data shown in **Table 2.6**.

Table 2.6. Bandgap, excitonic and defect peak positions, and the ratio of the intensities of defect peak to excitonic peak (I_d/I_{ex}) of $Cs_2AgBiBr_6$ DP for different substrates.

Substrate	**E_g (eV)**	**P_{ex} (nm)**	**P_d (nm)**	**I_d/I_{ex}**
Si	1.80±0.03	595.7	663	0.18
SiO_2	2.03±0.03	598.8	684	0.24
Quartz	2.15±0.02	603.2	688	0.27

The time-resolved PL measurement was performed to get a deeper understanding of the carrier recombination kinetics of the $Cs_2AgBiBr_6$ thin films. A bi-exponential fitting was used to fit the PL decay curve, as depicted in **Fig. 2.16(d)**. The first and second components are recombination lifetimes due to the defect component (τ_d) and excitonic component (τ_{ex}), respectively. A low concentration of trap states at the surface and/or interior of the $Cs_2AgBiBr_6$ thin films is implied by their comparatively long radiative lifetime[54], allowing the photodetector to capture and transfer photogenerated carriers. Using time-correlated single-photon counting (TCSPC), we looked into the PL decay periods of the DP films. The variation of τ_{ex} and τ_d for different substrates is depicted in **Fig. 2.18(d)**. The fitted parameters are listed in **Table 2.7**, where τ_1 and τ_2 correspond to τ_d and τ_{ex}, respectively. A long carrier lifetime of τ_{ex}~79 ns was observed for $Cs_2AgBiBr_6$ DP thin film over the SiO_2 substrate, which points

towards the growth of a film with negligible defects. The variation of the τ_d for different substrates is essentially due to the involvement of more trap or surface state emissions, which concurs with the reported literature.[55]

Table 2.7: Details of the fitting parameters of TRPL data of $Cs_2AgBiBr_6$ DP film deposited on different substrates.

Substrate	A_1(%)	τ_1 (ns)	$\Delta\tau$ (ns)	A_2 (%)	τ_2 (ns)	$\Delta\tau$ (ns)
SiO_2	5.054	1.089	0.04	94.94	79.05	0.0003
Si	31.848	0.82	0.03	68.152	48.82	0.0009
quartz	34.95	0.68	0.03	65.04	46.03	0.0005

The change in the decay time follows the same trend as that of the PL emission due to defect states. The increased I_d/I_{ex} ratio of $Cs_2AgBiBr_6$ DP thin film over quartz substrate indicates more trap states, resulting in a shorter decay time. The film deposited by the CVD method exhibits extended PL decay periods in the range of hundreds of nanoseconds, suggesting the possibility of fabricating a device with superior performance.

2.4.6 Low-temperature Raman Studies

2.4.6.1 Spectral Shift

To examine the variation of the dominant Raman modes with temperature, we carried out a low-temperature Raman study of the CVD-grown $Cs_2AgBiBr_6$ DP thin film on SiO_2 substrate over temperatures ranging from 153 K to 294 K. **Fig. 2.19(a)** displays the temperature-dependent Raman spectra. At room temperature, all three characteristic Raman modes are apparent: T_{2g} ~74 cm^{-1}, E_g ~132 cm^{-1}, and A_{1g} ~ 178 cm^{-1} of $Cs_2AgBiBr_6$ DP thin film. We observe a clear blue shift in the E_g and A_{1g} modes from 132.1 to 138.4 cm^{-1} and 178 to 180 cm^{-1}, respectively, whereas there is a red shift in the T_{2g} mode of $Cs_2AgBiBr_6$ DP with decreasing temperature. The T_{2g} mode exhibits mode softening (~74 cm^{-1} to ~71.8 cm^{-1}) with a decrease in temperature, contrasting with the mode stiffening exhibited by E_g and A_{1g} modes, which arises from the shortening of lattice constants following cooling.[56] Due to the symmetric shrinking of the lattice parameters, an overall increase in the total energy of the symmetric octahedral vibrational modes is expected. The anomalous mode softening behavior exhibited by T_{2g} is in accordance with previous literature.[56] The change in the Raman spectra with temperature is due to the highly anharmonic nature of the $Cs_2AgBiBr_6$ DP lattice.[29]

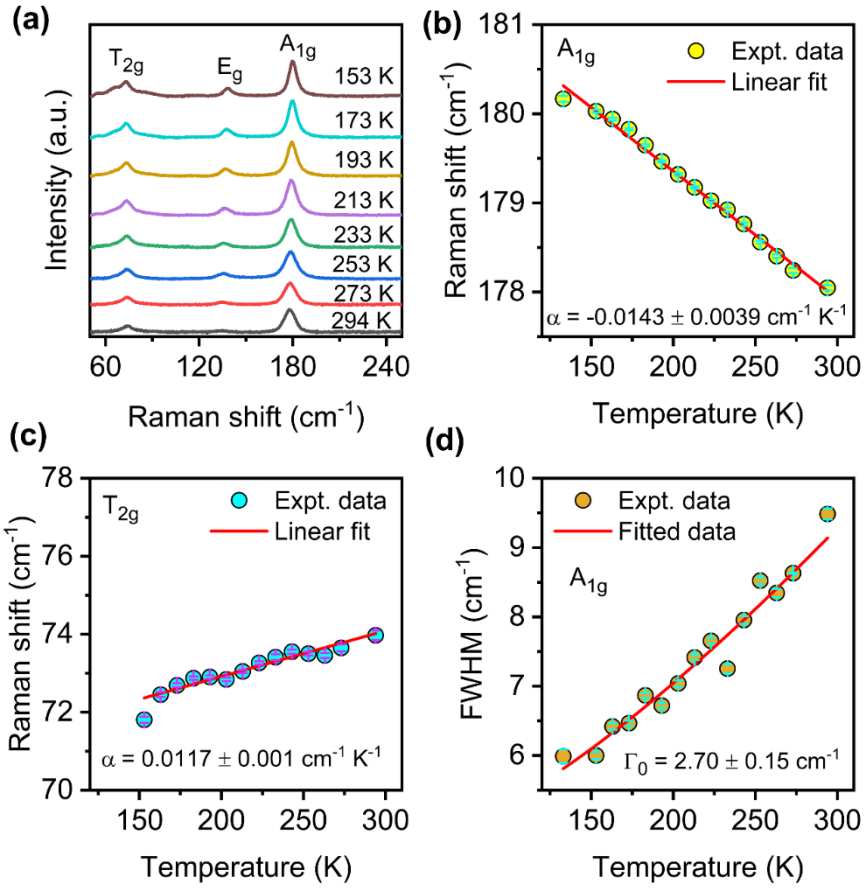

Fig. 2.19: (a) Low-temperature Raman spectra of $Cs_2AgBiBr_6$ double perovskite film at different temperatures, and **(b, c)** corresponding Raman shift in the A_{1g} and T_{2g} modes as a function of temperature. **(d)** Change in FWHM with the measurement temperature of $Cs_2AgBiBr_6$ double perovskite film. The symbols indicate the experimental data, and solid lines represent the fitted data.

Parameters such as the Raman peak's temperature coefficient and FWHM were extracted by fitting the Raman spectra with a Lorentzian line shape. To estimate the temperature coefficient (α), we have used the following equation,

$$\omega = \omega_0 + \alpha T \qquad (2.5)$$

Here, ω_0 represents the frequency of the Raman mode of $Cs_2AgBiBr_6$ DP at T= 0K, and α stands for its first-order temperature coefficient. Hence, the value of the temperature coefficient is determined from the slope obtained from the linear fitting of the experimental data points (**Fig. 2.19(b, c)** and **Fig. 2.20 (a)**. We have estimated the values of the first-order temperature coefficient (α) as -0.01431 ± 0.0039 cm^{-1} K^{-1}, -0.029 ± 0.001 cm^{-1} K^{-1}, and +0.0117 ± 0.001 cm^{-1} K^{-1} for A_{1g}, E_g, and T_{2g} modes of $Cs_2AgBiBr_6$ DP, respectively. Notably, we have neglected

the effect of higher-order temperature coefficients since these factors are significant only at high temperatures. The variation of Raman modes with temperature is listed in **Table 2.8**.

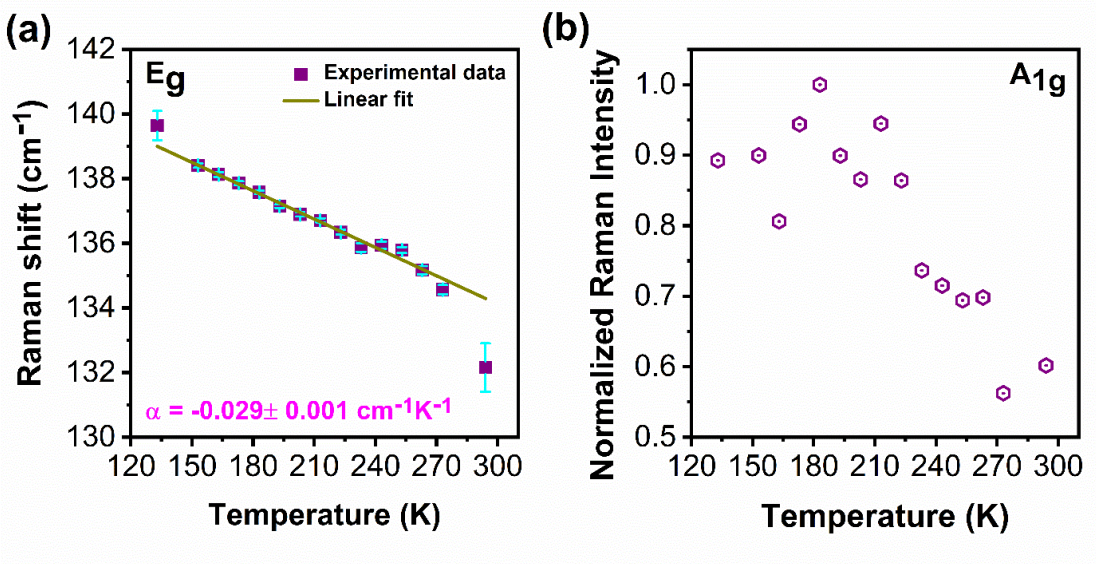

Fig. 2.20: (a) Variation of E_g Raman mode in $Cs_2AgBiBr_6$ DP as a function of temperature. **(b)** The intensity variation of the A_{1g} mode in $Cs_2AgBiBr_6$ DP with temperature change.

Table 2.8. Temperature-dependent Raman peak shift of all Raman active modes of $Cs_2AgBiBr_6$ DP thin film.

Temperature (K)	A_{1g}		E_g		T_{2g}	
	Raman shift(cm^{-1})	**Std. Error (cm^{-1})**	**Raman Shift(cm^{-1})**	**Std. Error (cm^{-1})**	**Raman shift(cm^{-1})**	**Std. Error (cm^{-1})**
294	178.0	0.03	132.1	0.74	73.9	0.12
273	178.2	0.03	134.5	0.14	73.6	0.09
263	178.4	0.02	135.1	0.13	73.4	0.06
253	178.5	0.02	135.7	0.09	73.5	0.05
243	178.7	0.02	135.9	0.11	73.5	0.06
233	178.9	0.02	135.8	0.13	73.4	0.08
223	179.0	0.01	136.3	0.07	73.2	0.04
213	179.1	0.01	136.7	0.06	73.0	0.04
203	179.3	0.01	136.8	0.07	72.8	0.05
193	179.4	0.01	137.1	0.06	72.9	0.04
183	179.6	0.01	137.5	0.05	72.8	0.04
173	179.8	0.01	137.8	0.06	72.6	0.05
163	179.9	0.02	138.1	0.07	72.4	0.06
153	180.0	0.02	138.4	0.07	71.8	0.08

2.4.6.2 Raman Linewidth

Fig. 2.19(d) depicts the variation of linewidth (FWHM) of the A_{1g} mode of $Cs_2AgBiBr_6$ DP with temperature. The linewidth of the A_{1g} mode monotonically decreased from ~9.4 cm^{-1} to ~6.0 cm^{-1} (**Table 2.9**). The narrowing of the A_{1g} mode with a decrease in the temperature is attributed to the reduced contribution of the thermal bath. We have carried out an in-depth analysis of the A1g mode to understand the broadening of the linewidth with temperature. The contribution of the pure temperature effect primarily considers the anharmonic effects of three- and four-phonon processes.[57]

Table 2.9. Variation of FWHM of A_{1g} mode in $Cs_2AgBiBr_6$ DP with temperature.

Temperature (K)	FWHM of A_{1g} mode (cm^{-1})	Standard Error (cm^{-1})
294	9.4	0.08
273	8.6	0.01
263	8.3	0.06
253	8.5	0.05
243	7.9	0.05
233	7.2	0.06
223	7.6	0.04
213	7.4	0.04
203	7.0	0.04
193	6.7	0.03
183	6.8	0.04
173	6.4	0.04
163	6.4	0.04
153	6	0.05

The light scattering process may be seen as involving the absorption of a photon, the emission of a photon, and the generation of an optical phonon, which subsequently decays anharmonically into two phonons, three phonons, etc.[57] Three-phonon and four-phonon processes are used to describe the creation of two and three phonons, respectively. A semi-quantitative simple model may adequately capture the pure temperature effect, including three- and four-phonon processes, given by the following equation[58]

$$\Gamma(T) = \Gamma 0 + a\left[1 + \frac{2}{\exp\left(\frac{2c}{T}\right) - 1}\right] + b\left[1 + \frac{3}{\exp\left(\frac{3c}{T}\right) - 1} + \frac{3}{\left(\exp\left(\frac{3c}{T}\right) - 1\right)^2}\right] \quad (2.6)$$

where $c = \frac{\hbar\omega}{k_B}$, Γ0 represents the FWHM of the A_{1g} mode of $Cs_2AgBiBr_6$ DP at absolute zero temperature, and a and b represent second-order and third-order anharmonic constants, respectively. The variation in the FWHM as a function of temperature for a three-phonon decay is well explained by the aforementioned equation (2.6). From the fitting, the FWHM of the A_{1g} Raman signal obtained at absolute zero temperature is 2.70 ± 0.15 cm^{-1}, indicating that $Cs_2AgBiBr_6$ DP crystallinity rises and phonon dispersion reduces at low temperatures. From the best fit of our data, we obtain a=2.00 and b=0.163. The relationship between Raman FWHM (Γ_0) and the phonon lifetime (T) is given by $T = 1/\pi * \Gamma_0$, where the Γ_0 is in cm^{-1}.[59] Thus, the phonon lifespan is estimated as ~ 0.12 ps at absolute zero temperature.

2.4.6.3 Raman Intensity

Fig. 2.20(b) depicts the temperature-dependent change in the Raman intensity of the A_{1g} mode. The intensity of the A_{1g} mode gradually increases as the temperature drops. According to Su et al., the Bose-Einstein distribution function determines the temperature-dependent hot-stimulated phonon population of the vibrational state[60], given by

$$\eta(\omega, T) = \frac{1}{[e^x - 1]} \quad (2.7)$$

where $x = \frac{\hbar\omega}{k_B T}$. As mentioned before, the core phonon splits into two, three, or more phonons as the temperature drops. The temperature-dependent Raman spectra show that as the temperature drops, there is a blueshift of the A_{1g} mode, which causes the value of "x" in the above equation to rise. This further suggests that the value of the Bose-Einstein distribution function will drop, along with the number of stimulated phonons of the vibrational state in $Cs_2AgBiBr_6$ DP. Reduced phonon stimulation at lower temperatures results in larger cumulative scattered photons of the same frequency, particularly over longer periods, and higher Raman signal strength.[61] Similarly, when the temperature rises, stimulated phonon intensifies, and the total number of scattered photons with the same frequency in a defined time decreases. At lower temperatures, the molecules in the sample have lower thermal energy. So, if the photon interacts with a molecule, the interaction time may be longer, leading to a larger Raman scattering cross section and, therefore, a higher Raman intensity. However, as the

temperature is further lowered, the vibration of atoms is constricted, leading to a decrease in the intensity (T<180 K).

2.4.7 Thermal Conductivity

As we have discussed, the dominant A_{1g} mode of $Cs_2AgBiBr_6$ DP is extremely sensitive to temperature change. Additionally, the power-dependent analysis suggests that long-term laser exposure contributes to generating a large amount of heat locally on the sample. As a result, it is critical to employ optimum laser power throughout the micro-Raman investigations. The schematic illustration for power-dependent Raman measurements is shown in **Fig. 2.21 (a).** For power-dependent analysis of the Raman spectra of the DP, using a supported $Cs_2AgBiBr_6$ DP film is futile since a change in laser power has a negligible effect on the Raman spectra due to the rapid dissipation of local heat energy to the substrate. We suspended our as-grown DP thin film by transferring it to a Cu grid to reduce heat loss through the substrate. The optical microscope picture of the suspended $Cs_2AgBiBr_6$ DP film on the Cu grid is shown in **Fig. 2.21(b)**. To compare the power dependence of $Cs_2AgBiBr_6$ DP film with or without substrate effect, we have carried out the power-dependent measurement in both cases.

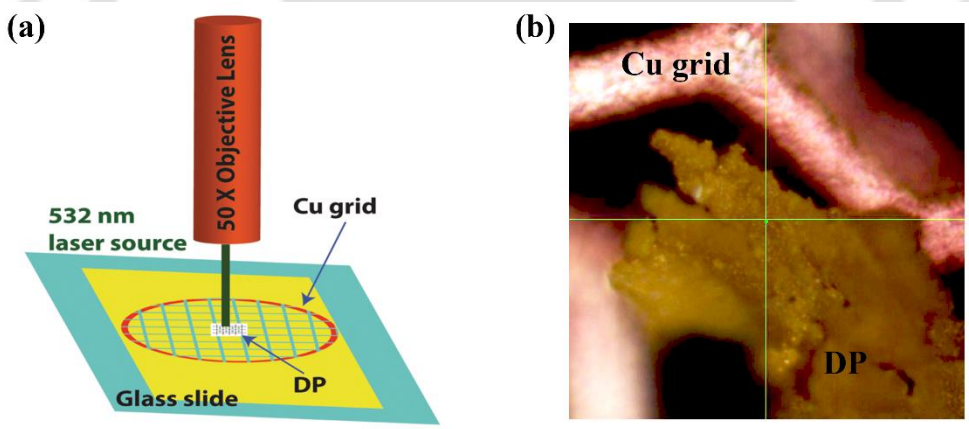

Fig. 2.21: (a) Schematic Illustration of the power-dependent measurements setup for the suspended $Cs_2AgBiBr_6$ DP thin film. **(b)** Optical image of the $Cs_2AgBiBr_6$ DP on a copper grid.

Fig. 2.22(a) displays a stacked plot of the power-dependent Raman spectra of $Cs_2AgBiBr_6$ DP on a Cu grid. In an attempt to quantify the change in thermal transport upon optical irradiation, we estimate the change in thermal conductivity based on our results from Raman thermometry. The equation $\frac{\partial Q}{\partial t} = -K \oint (\nabla T . dS)$ may be used to calculate the heat conduction over a surface with the cross-sectional area S, where Q is the amount of heat transmitted during the period t and T is the absolute temperature. The thermal conductivity is given by $K = \gamma . (\frac{Q}{\nabla T})$,[62] where

$\gamma = \frac{1}{2\pi d}$. A circular heat front moving radially outward in a circular geometry is considered. The thermal conductivity is given by $K = (\frac{1}{2\pi d})(\frac{\nabla P}{\nabla T})$, for uniform radial heat flow from the two laser excitation powers P_1 and P_2, which correspond to the two hot spot temperatures T_1 and T_2, respectively. Here, d denotes the thickness. Thus, ∇T denotes the local temperature rise caused by the difference in heating power $\nabla P = P_2 - P_1$. The peak shifts linearly with sample temperature at low excitation powers given by the equation: $\omega = \omega_0 + \alpha T$. In the radial heat wave example, the thermal conductivity can be expressed as

$$K = \alpha\left(\frac{1}{2\pi d}\right)\left(\frac{d\omega}{dP}\right)^{-1} \tag{2.8}$$

Where $d\omega$ is the shift in the Raman peak position of the A_{1g} mode concerning the change in incident laser power dP on the material surface, α is the first-order temperature coefficient, and d is the thickness of the material. Shen et al. and many other researchers demonstrated that the thermal conductivity of perovskite materials is independent of the thickness (d) in the range of 90 to 400 nm.[62,63] As a result, the influence of thickness " d " on thermal conductivity (K) may be considered to be insignificant. Thus, the only quantities to examine are α and ($d\omega/dP$).

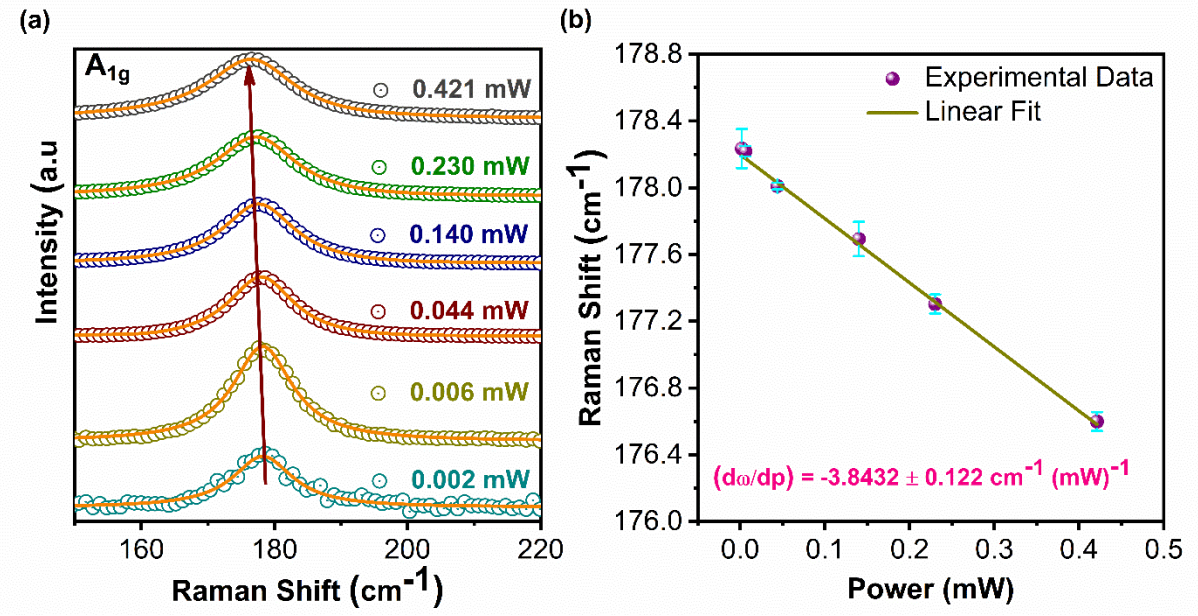

Fig. 2.22: (a) Incident laser power-dependent Raman spectra of the A_{1g} mode of $Cs_2AgBiBr_6$ film suspended on a Cu grid, and **(b)** the corresponding Raman shift of the A_{1g} mode with the laser power. The symbols represent experimental data, and the solid line indicates a linear fit.

The fitting parameters of the A_{1g} mode of $Cs_2AgBiBr_6$ DP film for various incident laser powers are shown in **Fig. 2.23**. We observed a gradual redshift in the distinctive A_{1g} Raman peak

location, accompanied by linewidth broadening, when the laser power was increased. The broadening of the Raman peak suggests that the laser beam causes localized heating. The increase in the excitation power results in an increase in the intensity and a redshift of the A_{1g} mode.

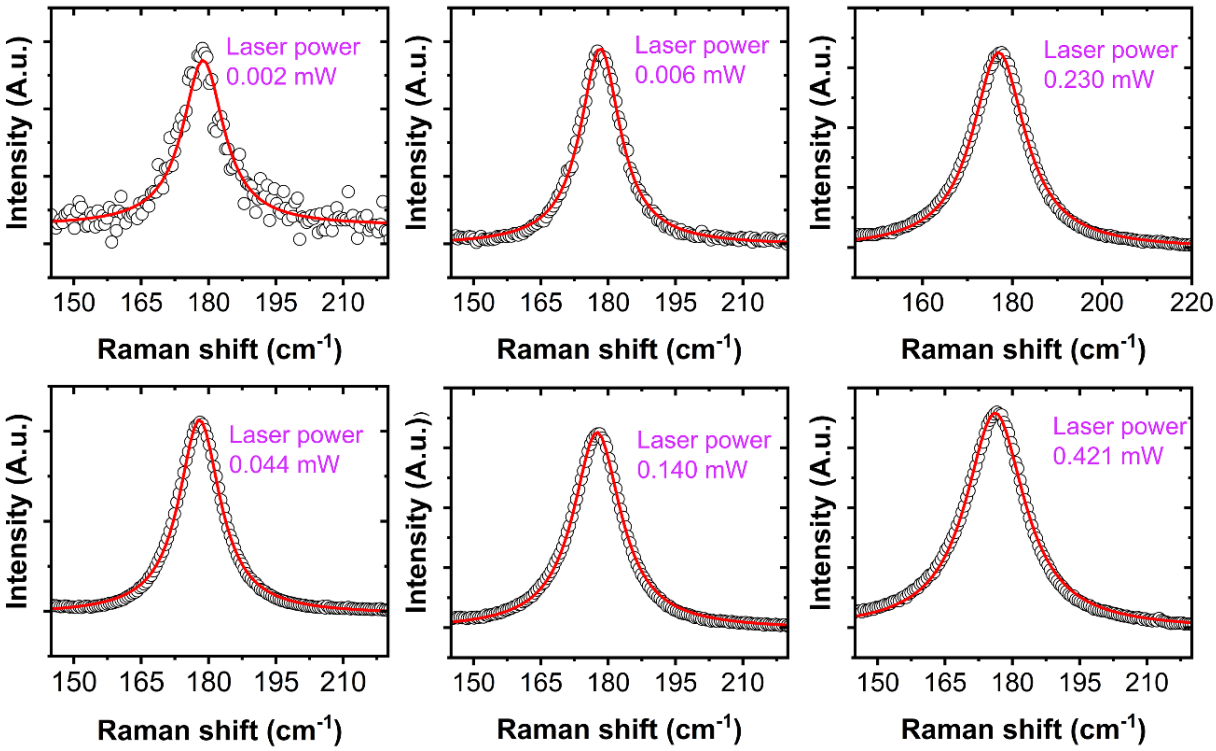

Fig. 2.23: Power-dependent Raman spectra of the A_{1g} mode of $Cs_2AgBiBr_6$ DP film suspended over a Cu grid with different incident laser powers. The symbol represents the experimental data, and the solid line represents the Lorentzian fit.

The increased intensity of the first-order Raman mode is due to the increased number of incoming photons associated with the increased laser power, which results in more phonons participating in the scattering. **Fig. 2.22(b)** depicts the change in the Raman peak position with incident laser power. The consistent red shift in peak location with the increase in the power points toward an increase in the local temperature of the suspended $Cs_2AgBiBr_6$ DP film.

The slope, $\frac{d\omega}{dP}$ of the corresponding plot, is estimated as -3.8432 $\pm$ 0.122 cm^{-1} $(mW)^{-1}$ for the suspended $Cs_2AgBiBr_6$ DP film. Power-dependent Raman measurements were also carried out on the supported $Cs_2AgBiBr_6$ DP film, as shown in **Fig. 2.24(a)**. We have observed the same behavior of A_{1g} mode for the supported film as expected, but the shift in the Raman peak position is less severe compared to the suspended film. This is mainly due to heat dissipation through the film to the substrate. The variation of the Raman spectra, particularly the A_{1g} mode

with incident laser power, is presented in **Fig. 2.24 (b)**. It is noted that for incident power less than 0.006mW, we do not observe this mode for the supported $Cs_2AgBiBr_6$ DP film, whereas we observe the significant intensity of the A_{1g} mode for the suspended film. The linear fitting of the data yields the slope, $\frac{d\omega}{dP}$, to be -0.4704 ± 0.083 cm^{-1} $(mW)^{-1}$ for the supported $Cs_2AgBiBr_6$ DP film. It is important to note that at high powers (>1.13 mW), we observed substantial sample damage (**Fig. 2.25**).

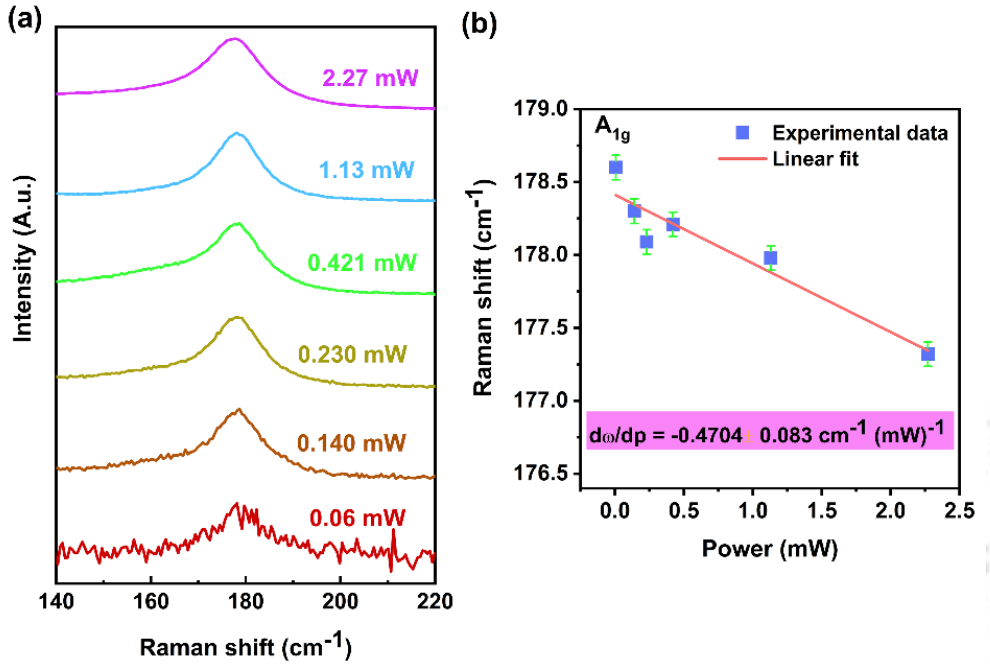

Fig. 2.24: (a) Power-dependent Raman spectra of the A_{1g} mode of $Cs_2AgBiBr_6$ DP thin film supported on SiO_2 substrate. **(b)** The corresponding Raman peak position as a function of incident laser power.

By using equation (2.8), we can estimate the value of thermal conductivity (K) for the supported and suspended $Cs_2AgBiBr_6$ DP thin film. Now, 'd' is the thickness of the $Cs_2AgBiBr_6$ DP thin film, which we have estimated as ~300 nm. The first-order temperature coefficient α is -0.01431 ± 0.0039 cm^{-1} K^{-1}. The value of $d\omega/dp$ is estimated as -3.8432 ± 0.122 cm^{-1} $(mW)^{-1}$ and -0.4704 ± 0.083 cm^{-1} $(mW)^{-1}$ for suspended and supported $Cs_2AgBiBr_6$ DP thin film, respectively. Thus, the thermal conductivity of $Cs_2AgBiBr_6$ DP thin film for supported and suspended film is estimated as ~16.14 ± 1.58 W/m-K and ~1.97 ± 0.48 W/m-K, respectively. Note that our estimated value of thermal conductivity K for the suspended film is about 6 times that of the theoretically predicted value (0.3 W/m-K) for $Cs_2AgBiBr_6$ DP.[29] The higher thermal conductivity may be primarily due to the higher value of the Raman temperature coefficient (α) of the film grown on the SiO_2 substrate. Note that the calculation of K involves the use of α of the film, which was not suspended for the α measurement, and thus, it is on the higher

side. Further, the film is grown at elevated temperatures, and it induces compressive strain in the film, which can lead to increased thermal conductivity.

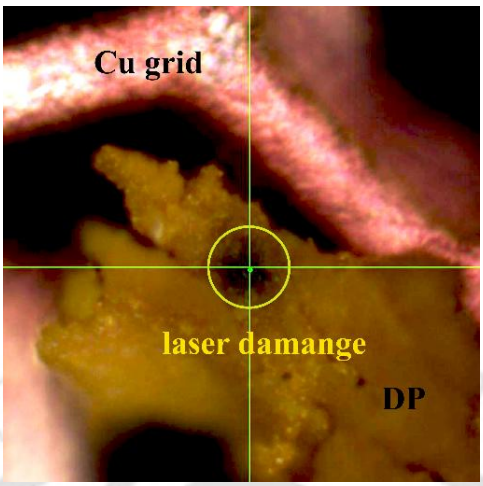

Fig. 2.25: Laser-induced damage on suspended $Cs_2AgBiBr_6$ DP film with laser power >1.13 mW.

To the best of our knowledge, there have been no reports on the experimental determination of the thermal conductivity of $Cs_2AgBiBr_6$ DP. Few studies have estimated the thermal conductivity of this material by theoretical simulations. However, theory estimates vary in a wide range of 0.065 W/m-K for $Cs_2BiAgCl_6$[30] to 0.3 W/m-K for $Cs_2AgBiBr_6$.[29] Due to the highly anharmonic nature of $Cs_2AgBiBr_6$ DP, approximating its thermal conductivity and thermal coefficient would be immensely important to describe the nature of the anharmonic lattice vibrations in these systems. It is worth mentioning that we used a simpler method to calculate the *K* value in $Cs_2AgBiBr_6$ DP thin film here. CVD is a highly advantageous synthesis technique for industrial applications since it is easy, inexpensive, and environmentally benign. CVD is a powerful tool to produce high-quality crystals of large domain sizes, exhibiting chemical homogeneity and structural uniformity. As a result, CVD-grown $Cs_2AgBiBr_6$ DP thin film opens the door to be used as one of the low thermally conductive and highly crystalline materials for thermoelectric and optoelectronic applications.

2.4.8 Thermal and Environmental Stability

The Raman spectra obtained at various temperatures may be used to directly infer the thermal stability of the $Cs_2AgBiBr_6$ DP thin film and laser-induced impacts on the structure. The Raman spectra for different temperatures were recorded with a 633 nm laser excitation source. The Raman modes observable at all temperatures indicate the strong structural stability of $Cs_2AgBiBr_6$ DP thin film. There is a dramatic increase in the broadening of the vibrational modes with an increase in temperature due to higher anharmonicities in the atomic vibrations

at elevated temperatures. Most importantly, the fact that the cubic structure of the $Cs_2AgBiBr_6$ is preserved at high temperatures shows that the compound is highly stable and does not experience thermal deterioration. This is in agreement with the findings published by Dakshinamurthy et al.[64], who used XRD and Raman measurements to show that the cubic polymorph of the $Cs_2AgBiBr_6$ structure is identifiable and stable up to 300 °C. **Fig. 2.26(a)** shows the recorded Raman spectra for a temperature range of 25 °C to 220 °C. The $Cs_2AgBiBr_6$ DP thin film exhibits excellent thermal stability up to 220 °C, and it shows no disintegration up to 220°C. There is no evidence of the presence of any other phases.

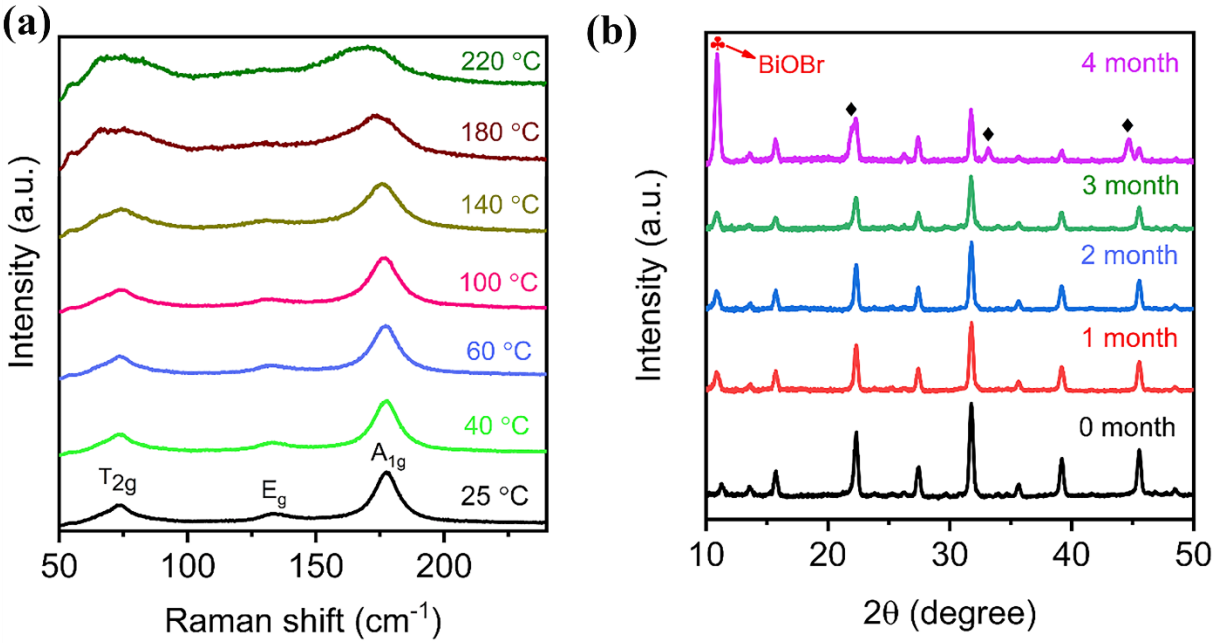

Fig. 2.26: (a) High-temperature Raman spectra of $Cs_2AgBiBr_6$ film in the range 25-220 °C. **(b)** XRD patterns of $Cs_2AgBiBr_6$ double perovskite film of freshly prepared sample and after 1, 2, 3, and 4 months, respectively.

Moreover, environmental stability is a key factor when considering the possible usage of perovskite materials for optoelectronic applications. We employed XRD measurements to look into the environmental stability of the $Cs_2AgBiBr_6$ DP thin film. The XRD tests (**Fig. 2.26(b)**) reveal that freshly manufactured $Cs_2AgBiBr_6$ DP thin film shows no evidence of decomposition in the ambient environment for up to 3 months. However, we observed extra peaks at ~33.1° and 44.6°. Also, the intensity of the peak corresponding to the (004) plane decreased significantly, indicating the degradation of the as-grown thin film after four months of exposure to the ambient environment. Moreover, the increased intensity of the peak located at ~10.8° is ascribed to the BiOBr side phase, which suggests that after long exposure of the $Cs_2AgBiBr_6$

DP thin film to the environment, oxygen reacts with Bi and hydrolyses into BiOBr in the presence of humidity.[21] The extra peaks at 33.1° and 44.6° and the splitting of the (022) plane indicate further decomposition of $Cs_2AgBiBr_6$ DP into a more stable secondary phase- $Cs_3Bi_2Br_9$. These results further substantiate the origin of extra peaks and justify the assignment to the decomposition by-products.

2.4.9 Application as a Photodetector

We have fabricated a $C_2AgBiBr_6$ DP thin film in optoelectronic device applications to verify the potential of CVD-grown $Cs_2AgBiBr_6$ DP photodetectors with planar geometry. The schematic of the device is shown in **Fig. 2.27(a)**. The device was fabricated using a simple silver paste as electrodes on top of the as-synthesized $Cs_2AgBiBr_6$ DP thin film on a SiO_2 substrate. A laser source of 405 nm was used to illuminate the device, as it had a high absorption at this wavelength. The I-V characteristics of the device under dark and light conditions are shown in **Fig. 2.27(b)**.

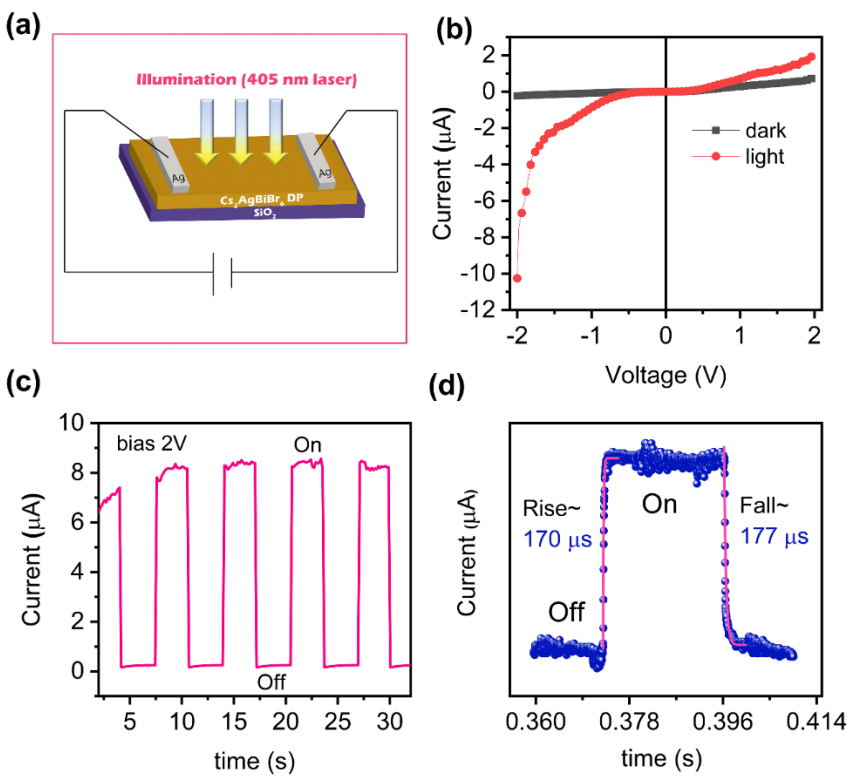

Fig. 2.27: (a) The schematic of photodetection measurement on CVD-grown $Cs_2AgBiBr_6$ DP thin film. **(b)** I-V characteristics of $Cs_2AgBiBr_6$ DP photodetector under light and dark conditions. **(c)** Temporal response of the photocurrent on $Cs_2AgBiBr_6$ DP photodetector at a bias voltage of -2 V. **(d)** The rise and fall time of the $Cs_2AgBiBr_6$ DP thin film photodetector under pulsed light.

The device, under an incident laser power of 5.21 mW/cm^2, showed a reasonably high on/off (I_{light}/I_{dark}) ratio of ~ 44 and a high photocurrent of 10.1 µA under the negative bias of 2 V (**Fig. 2.27(c)**). However, the obtained I_{ON}/I_{OFF} ratio is relatively low in our case compared to the reported literature[65], primarily due to the use of Silver (Ag) paste as a contact electrode in ambient conditions (without the use of any glovebox) for demonstration purposes. Here, the interface between the Ag and perovskite film may not be sufficiently clean, and it may contain defects, which trap the charge carriers and reduce the overall I_{ON}/I_{OFF} ratio. Note that Fang et al.[65] have used the Au/2D $Cs_2AgBiBr_6$ DP Schottky heterojunction for photodetection. They reported the highest I_{ON}/I_{OFF} ratio for 505 nm wavelength, which suggested the contribution of both Au and 2D $Cs_2AgBiBr_6$ DP in obtaining the higher I_{ON}/I_{OFF} ratio. We believe that vacuum deposition of Au electrodes on $Cs_2AgBiBr_6$ DP thin film may improve the I_{ON}/I_{OFF} ratio.

Nevertheless, our device exhibited fast rise and fall times of ~ 170 µs and ~ 177 µs, respectively (see **Fig. 2.27(d)**), which is almost three orders of magnitude faster than the solution-processed $Cs_2AgBiBr_6$ DP thin film photodetector[66]. Our device also showed photoresponse at 0 V bias (**Fig. 2.28**), thus, behaving as a self-powered device with significant photocurrent without any electron/hole transport layers, which authenticates our CVD method to grow a high-quality thin film of $Cs_2AgBiBr_6$ DP for practical optoelectronic device applications.

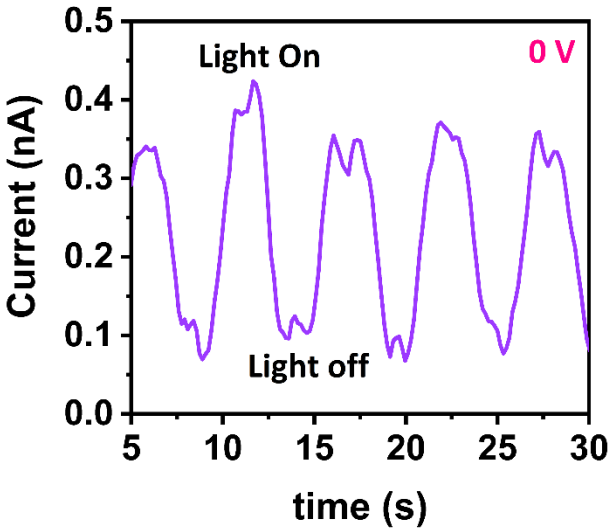

Fig. 2.28: Photoresponse of CVD-grown DP thin film device at 0V bias.

2.5 Conclusions

Herein, we successfully synthesized $Cs_2AgBiBr_6$ double perovskite thin film using a CVD technique for the first time. We have used the $BiBr_3$ seed layer to grow highly crystalline and

uniform thin films on various substrates. The optimization of thin film quality is achieved simply by varying the substrate temperature. Raman and XRD results indicated the phase change of $Cs_2AgBiBr_6$ DP to $Cs_3Bi_2Br_9$ at higher substrate temperatures, suggesting the growth of the pure phase of $Cs_2AgBiBr_6$ at a substrate temperature of 130°C. With the help of controlled experiments on the intermediate products, we discussed the growth mechanism of the DP film. It is important to note that the thin film quality deteriorates at higher substrate temperatures because of grain accumulation on the film's top surface. We have optimized the growth over different substrates to study the strain-induced effect on different properties of $Cs_2AgBiBr_6$ DP thin film. Based on our findings, the optimized $Cs_2AgBiBr_6$ DP thin film on the SiO_2 substrate showed high crystallinity, fewer pinhole defects, surface uniformity, and minimum film roughness. Low-temperature and power-dependent Raman studies were carried out on a SiO_2 substrate to estimate the thermal conductivity of the suspended $Cs_2AgBiBr_6$ DP thin film. We have estimated ultralow thermal conductivity as ~1.97 ± 0.48 W/m-K and ~16.14 ± 1.58 W/m-K for suspended and supported film of $Cs_2AgBiBr_6$ DP, respectively, which are close to the theoretical predictions. The difference in thermal conductivity values for suspended and supported film is mainly because of the larger heat dissipation to the substrate in the latter case. Thermal and environmental stability experiments on the $Cs_2AgBiBr_6$ thin film are carried out utilizing high-temperature Raman and XRD measurements. Our results show that the $Cs_2AgBiBr_6$ film is thermally stable up to 220°C. The as-grown $Cs_2AgBiBr_6$ DP maintains its phase purity for up to 3 months in the ambient environment with high humidity, which proves its high stability. Further, we have demonstrated the potential of CVD-grown $Cs_2AgBiBr_6$ DP thin film for optoelectronic applications. A planar photodetector device showed a high on/off ratio of ~44 and a high photocurrent of 10.1 µA even at a low bias (2 V). Our device also exhibited self-powered behavior and fast rise and fall times of 170 µs and 177 µs, respectively. We believe such a study on this novel compound is the first of its kind and will be of great utility to effectively integrate $Cs_2AgBiBr_6$ into various optoelectronic devices.

References

(1) National Renewable Energy Laboratory. Best Research-Cell Efficiency chart, https://www.nrel.gov/pv/assets/pdfs/best-research-cell-efficiencies-rev220126.pdf (2022).

(2) Stranks, S. D.; Snaith, H. J. Metal-Halide Perovskites for Photovoltaic and Light-Emitting Devices. Nat. Nanotechnol. Nature Publishing Group May 7, 2015, pp 391–402.

(3) Cho, H.; Jeong, S. H.; Park, M. H.; Kim, Y. H.; Wolf, C.; Lee, C. L.; Hyuck Heo, J.; Sadhanala, A.; Myoung, N.; Yoo, S.; Im, S. H.; Friend, R. H.; Lee, T. W. Overcoming the Electroluminescence Efficiency Limitations of Perovskite Light-Emitting Diodes. Science 2015; 350(6265): 1222-1225.

(4) Fang, Y.; Dong, Q.; Shao, Y.; Yuan, Y.; Huang, J. Highly Narrowband Perovskite Single-Crystal Photodetectors Enabled by Surface-Charge Recombination. Nat. Photonics 2015, *9* (10), 679–686.

(5) Ramasamy, P.; Lim, D. H.; Kim, B.; Lee, S. H.; Lee, M. S.; Lee, J. S. All-Inorganic Cesium Lead Halide Perovskite Nanocrystals for Photodetector Applications. Chem. Comm. 2016, *52* (10), 2067–2070.

(6) Dou, L.; Yang, Y. M.; You, J.; Hong, Z.; Chang, W. H.; Li, G.; Yang, Y. Solution-Processed Hybrid Perovskite Photodetectors with High Detectivity. Nat. Commun. 2014, *5*.

(7) Alamri, A. M.; Leung, S.; Vaseem, M.; Shamim, A.; He, J. H. Fully Inkjet-Printed Photodetector Using a Graphene/Perovskite/Graphene Heterostructure. IEEE Trans Electron Devices 2019, *66* (6), 2657–2661.

(8) Sytnyk, M.; Deumel, S.; Tedde, S. F.; Matt, G. J.; Heiss, W. A Perspective on the Bright Future of Metal Halide Perovskites for X-Ray Detection. *Appl. Phys. Lett.* 2019, *115* (19).

(9) Wei, H.; Fang, Y.; Mulligan, P.; Chuirazzi, W.; Fang, H. H.; Wang, C.; Ecker, B. R.; Gao, Y.; Loi, M. A.; Cao, L.; Huang, J. Sensitive X-Ray Detectors Made of Methylammonium Lead Tribromide Perovskite Single Crystals. Nat. Photonics 2016, *10* (5), 333–339.

(10) Chung, I.; Song, J. H.; Im, J.; Androulakis, J.; Malliakas, C. D.; Li, H.; Freeman, A. J.; Kenney, J. T.; Kanatzidis, M. G. $CsSnI_3$: Semiconductor or Metal? High Electrical Conductivity and Strong Near-Infrared Photoluminescence from a Single Material. High Hole Mobility and Phase-Transitions. J. Am. Chem. Soc. 2012, *134* (20), 8579–8587.

(11) Chen, J.; Luo, Z.; Fu, Y.; Wang, X.; Czech, K. J.; Shen, S.; Guo, L.; Wright, J. C.; Pan, A.; Jin, S. Tin (IV)-Tolerant Vapor-Phase Growth and Photophysical Properties of Aligned Cesium Tin Halide Perovskite ($CsSnX_3$; X = Br, I) Nanowires. ACS Energy Lett. 2019, *4* (5), 1045–1052.

(12) Fan, Q.; Biesold-McGee, G. V.; Ma, J.; Xu, Q.; Pan, S.; Peng, J.; Lin, Z. Bleifreie Halogenid-Perowskit-Nanokristalle: Kristallstrukturen, Synthese, Stabilitäten Und Optische Eigenschaften. Angew. Chem. 2020, *132* (3), 1042–1059.

(13) Lyu, M.; Yun, J. H.; Chen, P.; Hao, M.; Wang, L. Addressing Toxicity of Lead: Progress and Applications of Low-Toxic Metal Halide Perovskites and Their Derivatives. Adv. Energy Mater. Wiley-VCH Verlag August 9, 2017.

(14) Slavney, A. H.; Hu, T.; Lindenberg, A. M.; Karunadasa, H. I. A Bismuth-Halide Double Perovskite with Long Carrier Recombination Lifetime for Photovoltaic Applications. J. Am. Chem. Soc. 2016, *138* (7), 2138–2141.

(15) Wei, F.; Deng, Z.; Sun, S.; Xie, F.; Kieslich, G.; Evans, D. M.; Carpenter, M. A.; Bristowe, P. D.; Cheetham, A. K. The Synthesis, Structure and Electronic Properties of a Lead-Free Hybrid Inorganic-Organic Double Perovskite $(MA)_2KBiCl_6$ (MA = Methylammonium). Mater. Horiz. 2016, *3* (4), 328–332.

(16) Deng, Z.; Wei, F.; Sun, S.; Kieslich, G.; Cheetham, A. K.; Bristowe, P. D. Exploring the Properties of Lead-Free Hybrid Double Perovskites Using a Combined Computational-Experimental Approach. J. Mater. Chem. A Mater. 2016, *4* (31), 12025–12029.

(17) Filip, M. R.; Hillman, S.; Haghighirad, A. A.; Snaith, H. J.; Giustino, F. Band Gaps of the Lead-Free Halide Double Perovskites $Cs_2BiAgCl_6$ and $Cs_2BiAgBr_6$ from Theory and Experiment. J. Phys. Chem. Lett. 2016, *7* (13), 2579–2585.

(18) Volonakis, G.; Filip, M. R.; Haghighirad, A. A.; Sakai, N.; Wenger, B.; Snaith, H. J.; Giustino, F. Lead-Free Halide Double Perovskites via Heterovalent Substitution of Noble Metals. J. Phys. Chem. Lett. 2016, *7* (7), 1254–1259.

(19) Li, H.; Pi, C.; Chen, W.; Zhou, M.; Wei, J.; Yi, J.; Song, P.; Alexey, Y.; Zhong, Y.; Yu, X.; Qiu, J.; Xu, X. A Highly Stable Photodetector Based on a Lead-Free Double Perovskite Operating at Different Temperatures. J. Phys. Chem. Lett. 2021, *12* (24), 5682–5688.

(20) Greul, E.; Petrus, M. L.; Binek, A.; Docampo, P.; Bein, T. Highly Stable, Phase Pure $Cs_2AgBiBr_6$ Double Perovskite Thin Films for Optoelectronic Applications. J. Mater. Chem. A Mater. 2017, *5* (37), 19972–19981.

(21) Fan, P.; Peng, H. X.; Zheng, Z. H.; Chen, Z. H.; Tan, S. J.; Chen, X. Y.; Luo, Y. Di; Su, Z. H.; Luo, J. T.; Liang, G. X. Single-Source Vapor-Deposited $Cs_2AgBiBr_6$ Thin Films for Lead-Free Perovskite Solar Cells. Nanomaterials 2019, *9* (12).

(22) Gao, W.; Ran, C.; Xi, J.; Jiao, B.; Zhang, W.; Wu, M.; Hou, X.; Wu, Z. High-Quality $Cs_2AgBiBr_6$ Double Perovskite Film for Lead-Free Inverted Planar Heterojunction Solar Cells with 2.2 % Efficiency. ChemPhysChem 2018, *19* (14), 1696–1700.

(23) Wu, C.; Zhang, Q.; Liu, Y.; Luo, W.; Guo, X.; Huang, Z.; Ting, H.; Sun, W.; Zhong, X.; Wei, S.; Wang, S.; Chen, Z.; Xiao, L. The Dawn of Lead-Free Perovskite Solar Cell: Highly Stable Double Perovskite $Cs_2AgBiBr_6$ Film. Adv. Sci. 2018, *5* (3).

(24) Wang, M.; Wang, W.; Ma, B.; Shen, W.; Liu, L.; Cao, K.; Chen, S.; Huang, W. Lead-Free Perovskite Materials for Solar Cells. Nano-Micro Lett. Springer Science and Business Media B.V. January 1, 2021.

(25) Sahoo, S.; Mallik, S. K.; Sahu, M. C.; Joseph, A.; Rout, B.; Pradhan, G. K.; Sahoo, S. Thermal Conductivity of Free-Standing Silicon Nanowire Using Raman Spectroscopy. Nanotechnology 2020 Dec 11;31(50):505701.

(26) Peimyoo, N.; Shang, J.; Yang, W.; Wang, Y.; Cong, C.; Yu, T. Thermal Conductivity Determination of Suspended Mono- and Bilayer WS_2 by Raman Spectroscopy. Nano Res. 2015, *8* (4), 1210–1221.

(27) Xie, H.; Hao, S.; Bao, J.; Slade, T. J.; Snyder, G. J.; Wolverton, C.; Kanatzidis, M. G. All-Inorganic Halide Perovskites as Potential Thermoelectric Materials: Dynamic Cation Off-Centering Induces Ultralow Thermal Conductivity. J. Am. Chem. Soc. 2020, *142* (20), 9553–9563.

(28) Acharyya, P.; Ghosh, T.; Pal, K.; Rana, K. S.; Dutta, M.; Swain, D.; Etter, M.; Soni, A.; Waghmare, U. V.; Biswas, K. Glassy Thermal Conductivity in $Cs_3Bi_2I_6Cl_3$ Single Crystal. Nat. Commun. 2022, *13* (1).

(29) Klarbring, J.; Hellman, O.; Abrikosov, I. A.; Simak, S. I. Anharmonicity and Ultralow Thermal Conductivity in Lead-Free Halide Double Perovskites. Phys. Rev. Lett. 2020, *125* (4).

(30) Haque, E.; Hossain, M. A. Origin of Ultra-Low Lattice Thermal Conductivity in Cs_2BiAgX_6 (X=Cl, Br) and Its Impact on Thermoelectric Performance. J. Alloys Compd. 2018, *748*, 63–72.

(31) Bhui, A.; Ghosh, T.; Pal, K.; Singh Rana, K.; Kundu, K.; Soni, A.; Biswas, K. Intrinsically Low Thermal Conductivity in the N-Type Vacancy-Ordered Double Perovskite Cs_2SnI_6: Octahedral Rotation and Anharmonic Rattling. Chem. Mater. 2022, *34* (7), 3301–3310.

(32) Das, A.; Pal, K.; Acharyya, P.; Das, S.; Maji, K.; Biswas, K. Strong Antibonding I (p)-Cu (d) States Lead to Intrinsically Low Thermal Conductivity in $CuBiI_4$. J. Am. Chem. Soc. 2023, *145* (2), 1349–1358.

(33) Acharyya, P.; Ghosh, T.; Pal, K.; Kundu, K.; Singh Rana, K.; Pandey, J.; Soni, A.; Waghmare, U. V.; Biswas, K. Intrinsically Ultralow Thermal Conductivity in Ruddlesden-Popper 2D Perovskite $Cs_2PbI_2Cl_2$: Localized Anharmonic Vibrations and Dynamic Octahedral Distortions. J. Am. Chem. Soc. 2020, *142* (36), 15595–15603.

(34) Sajjad, M.; Mahmood, Q.; Singh, N.; Andreas Larsson, J. Ultralow Lattice Thermal Conductivity in Double Perovskite Cs_2PTi_6: A Promising Thermoelectric Material. ACS Appl. Energy Mater. 2020, *3* (11), 11293–11299.

(35) Xiao, Z.; Meng, W.; Wang, J.; Yan, Y. Thermodynamic Stability and Defect Chemistry of Bismuth-Based Lead-Free Double Perovskites. ChemSusChem 2016 Sep 22;9(18):2628-2633.

(36) Pistor, P.; Meyns, M.; Guc, M.; Wang, H. C.; Marques, M. A. L.; Alcobé, X.; Cabot, A.; Izquierdo-Roca, V. Advanced Raman Spectroscopy of $Cs_2AgBiBr_6$ Double Perovskites and Identification of Cs_3Bi2Br_9 Secondary Phases. Scr. Mater. 2020, *184*, 24–29.

(37) Rodkey, N.; Kaal, S.; Sebastia-Luna, P.; Birkhölzer, Y. A.; Ledinsky, M.; Palazon, F.; Bolink, H. J.; Morales-Masis, M. Pulsed Laser Deposition of $Cs_2AgBiBr_6$: From Mechanochemically Synthesized Powders to Dry, Single-Step Deposition. Chem. Mater.2021, *33* (18), 7417–7422.

(38) Saidaminov, M. I.; Kim, J.; Jain, A.; Quintero-Bermudez, R.; Tan, H.; Long, G.; Tan, F.; Johnston, A.; Zhao, Y.; Voznyy, O.; Sargent, E. H. Suppression of Atomic Vacancies via Incorporation of Isovalent Small Ions to Increase the Stability of Halide Perovskite Solar Cells in Ambient Air. Nat. Energy 2018, *3* (8), 648–654.

(39) Chen, Y.; Lei, Y.; Li, Y.; Yu, Y.; Cai, J.; Chiu, M. H.; Rao, R.; Gu, Y.; Wang, C.; Choi, W.; Hu, H.; Wang, C.; Li, Y.; Song, J.; Zhang, J.; Qi, B.; Lin, M.; Zhang, Z.; Islam, A. E.; Maruyama, B.;

Dayeh, S.; Li, L. J.; Yang, K.; Lo, Y. H.; Xu, S. Strain Engineering and Epitaxial Stabilization of Halide Perovskites. Nature 2020, *577* (7789), 209–215.

(40) Rolston, N.; Bush, K. A.; Printz, A. D.; Gold-Parker, A.; Ding, Y.; Toney, M. F.; McGehee, M. D.; Dauskardt, R. H. Engineering Stress in Perovskite Solar Cells to Improve Stability. Adv. Energy Mater. 2018, *8* (29).

(41) Xue, D. J.; Hou, Y.; Liu, S. C.; Wei, M.; Chen, B.; Huang, Z.; Li, Z.; Sun, B.; Proppe, A. H.; Dong, Y.; Saidaminov, M. I.; Kelley, S. O.; Hu, J. S.; Sargent, E. H. Regulating Strain in Perovskite Thin Films through Charge-Transport Layers. Nat. Commun. 2020, *11* (1).

(42) Vtyurin, A.; Krylov, A.; Voronov, V.; Krylova, S. Raman Scattering and Phase Transitions in Fluorides with Elpasolite Structure. Ferroelectrics 2017, *512* (1), 58–64.

(43) Krylov, A. S.; Vtyurin, A. N.; Oreshonkov, A. S.; Voronov, V. N.; Krylova, S. N. Structural Transformations in a Single-Crystal Rb_2NaYF_6: Raman Scattering Study. J. Raman Spectrosc. 2013, *44* (5), 763–769.

(44) Igbari, F.; Wang, R.; Wang, Z. K.; Ma, X. J.; Wang, Q.; Wang, K. L.; Zhang, Y.; Liao, L. S.; Yang, Y. Composition Stoichiometry of $Cs_2AgBiBr_6$ Films for Highly Efficient Lead-Free Perovskite Solar Cells. Nano Lett. 2019, *19* (3), 2066–2073.

(45) Deng, Y. H.; Yang, Z. Q.; Ma, R. M. Growth of Centimeter-Scale Perovskite Single-Crystalline Thin Film via Surface Engineering. Nano Converg. 2020, *7* (1).

(46) Wang, M.; Zeng, P.; Bai, S.; Gu, J.; Li, F.; Yang, Z.; Liu, M. High-Quality Sequential-Vapor-Deposited $Cs_2AgBiBr_6$ Thin Films for Lead-Free Perovskite Solar Cells. Sol. RRL 2018, *2* (12).

(47) Bekenstein, Y.; Dahl, J. C.; Huang, J.; Osowiecki, W. T.; Swabeck, J. K.; Chan, E. M.; Yang, P.; Alivisatos, A. P. The Making and Breaking of Lead-Free Double Perovskite Nanocrystals of Cesium Silver-Bismuth Halide Compositions. Nano Lett. 2018, *18* (6), 3502–3508.

(48) Wu, J.; Liu, S. C.; Li, Z.; Wang, S.; Xue, D. J.; Lin, Y.; Hu, J. S. Strain in Perovskite Solar Cells: Origins, Impacts and Regulation. Natl. Sci. Rev. Oxford University Press August 1, 2021.

(49) Schmitz, A.; Leander Schaberg, L.; Sirotinskaya, S.; Pantaler, M.; Lupascu, D. C.; Benson, N.; Bacher, G. Fine Structure of the Optical Absorption Resonance in $Cs_2AgBiBr_6$ Double Perovskite Thin Films. ACS Energy Lett. 2020, *5* (2), 559–565.

(50) Du, K.; Meng, W.; Wang, X.; Yan, Y.; Mitzi, D. B. Bandgap Engineering of Lead-Free Double Perovskite $Cs_2AgBiBr_6$ through Trivalent Metal Alloying. Angew. Chem. 2017, *129* (28), 8270–8274.

(51) Wright, A. D.; Buizza, L. R. V.; Savill, K. J.; Longo, G.; Snaith, H. J.; Johnston, M. B.; Herz, L. M. Ultrafast Excited-State Localization in $Cs_2AgBiBr_6$ Double Perovskite. J. Phys. Chem. Lett. 2021, *12* (13), 3352–3360.

(52) Zelewski, S. J.; Urban, J. M.; Surrente, A.; Maude, D. K.; Kuc, A.; Schade, L.; Johnson, R. D.; Dollmann, M.; Nayak, P. K.; Snaith, H. J.; Radaelli, P.; Kudrawiec, R.; Nicholas, R. J.; Plochocka, P.; Baranowski, M. Revealing the Nature of Photoluminescence Emission in the Metal-Halide Double Perovskite $Cs_2AgBiBr_6$. J. Mater. Chem. C Mater. 2019, *7* (27), 8350–8356.

(53) Lei, H.; Hardy, D.; Gao, F. Lead-Free Double Perovskite $Cs_2AgBiBr_6$: Fundamentals, Applications, and Perspectives. Adv. Funct. Mater. John Wiley and Sons Inc December 1, 2021.

(54) Bartesaghi, D.; Slavney, A. H.; Gélvez-Rueda, M. C.; Connor, B. A.; Grozema, F. C.; Karunadasa, H. I.; Savenije, T. J. Charge Carrier Dynamics in $Cs_2AgBiBr_6$ Double Perovskite. J. Phys. Chem. *C* 2018, *122* (9), 4809–4816.

(55) Slavney, A. H.; Hu, T.; Lindenberg, A. M.; Karunadasa, H. I. A Bismuth-Halide Double Perovskite with Long Carrier Recombination Lifetime for Photovoltaic Applications. J. Am. Chem. Soc. 2016, *138* (7), 2138–2141.

(56) Puttisong, Y.; Moro, F.; Chen, S. L.; Höjer, P.; Ning, W.; Gao, F.; Buyanova, I. A.; Chen, W. M. Effect of Crystal Symmetry on the Spin States of $Fe^{3+}$and Vibration Modes in Lead-Free Double-Perovskite Cs_2AgBi (Fe)Br_6. J. Phys. Chem. Lett. 2020, *11* (12), 4873–4878.

(57) Balkanski, M.; Wallis, R. F.; Haro, E. *Anharmonic Effects in Light Scattering Due to Optical Phonons in Silicon*. Phys. Rev. B 28, 1928;15 Aug 1983: Vol. 8.

(58) Hossain, M. T.; Giri, P. K. Temperature-Dependent Raman Studies and Thermal Conductivity of Direct CVD Grown Non-van Der Waals Layered Bi2O2Se. J. Appl. Phys. 2021, *129* (17).

(59) Carnevali, V.; Mukherjee, S.; Voneshen, D. J.; Maji, K.; Guilmeau, E.; Powell, A. V.; Vaqueiro, P.; Fornari, M. Lone Pair Rotation and Bond Heterogeneity Leading to Ultralow Thermal Conductivity in Aikinite. J. Am. Chem. Soc. 2023,145,16, 9313-9325.

(60) Su, Z.; Sha, J.; Pan, G.; Liu, J.; Yang, D.; Dickinson, C.; Zhou, W. Temperature-Dependent Raman Scattering of Silicon Nanowires. J. Phys. Chem. B 2006, *110* (3), 1229–1234.

(61) Jena, T.; Hossain, M. T.; Giri, P. K. Temperature-Dependent Raman Study and Determination of Anisotropy Ratio and in-Plane Thermal Conductivity of Low-Temperature CVD-Grown PdSe2using Unpolarized Laser Excitation. J. Mater. Chem. C Mater. 2021, *9* (46), 16693–16708.

(62) Shen, C.; Du, W.; Wu, Z.; Xing, J.; Ha, S. T.; Shang, Q.; Xu, W.; Xiong, Q.; Liu, X.; Zhang, Q. Thermal Conductivity of Suspended Single Crystal $CH_3NH_3PbI_3$ Platelets at Room Temperature. Nanoscale 2017, *9* (24), 8281–8287.

(63) Halder, S.; Kessel, A.; Mazurski, N.; Levy, U. Thermal Transport in Engineered Hybrid Organic-Inorganic Perovskite Metasurfaces. J. Phys. Chem. C 2021, *125* (28), 15134–15144.

(64) C. Dakshinamurthy, A.; Sudakar, C. Photoinduced Degradation of Thermally Stable $Cs_2AgBiBr_6$ Double Perovskites by Micro-Raman Studies. Mater. Adv. 2022, *3* (14), 5813–5817.

(65) Fang, F.; Li, H.; Fang, S.; Zhou, B.; Huang, F.; Ma, C.; Wan, Y.; Jiang, S.; Wang, Y.; Tian, B.; Shi, Y. 2D $Cs_2AgBiBr_6$ with Boosted Light–Matter Interaction for High-Performance Photodetectors. Adv. Opt. Mater. 2021, *9* (9).

(66) Shen, W.; Jung, U.; Xian, Z.; Jung, B.; Park, J. Enhanced Device Performance of $Cs_2AgBiBr_6$ Double Perovskite Photodetector by SnO_2/ZnO Double Electron Transport Layer. J. Alloys Compd. 2022, *929*.

Chapter 3 Facile In-situ Synthesis of Double Perovskite $Cs_2AgBiBr_6/WS_2$ Heterostructure and Interfacial Charge Transfer Mediated High-Performance Ultraviolet Photodetection

Lead-free halide perovskites have emerged as promising alternatives to toxic Pb-based counterparts, offering high stability and strong UV–visible absorption. Meanwhile, 2D transition metal dichalcogenides (TMDCs) such as WS_2 provide exceptional light detection capability. In this work, $Cs_2AgBiBr_6/WS_2$ local heterostructures were fabricated via a simple mechanochemical route to enhance optoelectronic performance. Raman, XPS, and UPS analyses confirmed charge transfer and strain effects at the interface, suggesting the formation of a local p–n junction. The heterostructure-based photodetector shows remarkable improvements over pristine $Cs_2AgBiBr_6$, achieving a current on/off ratio of ~5.9×10^3, responsivity of 2.01 A W^{-1}, detectivity of 3.6×10^{13} Jones, and a reduced carrier lifetime (0.82 ns). The device also exhibits self-powered operation, with a significant photocurrent at 0 V, a fast response (80/120 ms), and a wide linear dynamic range (75 dB). These results demonstrate the potential of $Cs_2AgBiBr_6/WS_2$ heterostructures for efficient, low-power optoelectronic applications.

3.1 Introduction

The emergence of the perovskite family of materials, particularly those with lead composition $APbX_3$, has positioned them as promising candidates in cutting-edge areas of optoelectronics owing to their high absorption ability, long diffusion lengths, and good stability.[1,2] However, the extensively researched 3D metal halide perovskites, such as $Ch_3NH_3PBI_3$ ($MAPBI_3$), often exhibit poor stability and contain hazardous lead (Pb) atoms, significantly limiting their commercialization.[3] 2D-Ruddlesden-Popper perovskites recently gained much attention towards encrypted light communication devices.[4–6] Lead-free $Cs_3Cu_2I_5$ flexible fibrous photodetectors with a high on/off ratio and high responsivity provide new insights into flexible optoelectronic devices.[7] Recent studies suggest that metal halide double perovskites with a general formula $A_2BB'X_6$ ($A = Cs^+$; $B = Ag^+$, Na^+, K^+; $B' = Bi^{3+}$, Sb^{3+}, In^{3+}), could be the solution to these stability and toxicity concerns. These materials, being environmentally friendly and lead-free, hold significant potential in addressing the above challenges.[8,9] $Cs_2AgBiBr_6$ DP demonstrates relatively good air stability[10] and holds promise for various applications, such as solar cells[11], photodetectors[12], and X-ray detectors[13]. However, due to indirect bandgap[14] and significant electron-phonon coupling[15], $Cs_2AgBiBr_6$ DP exhibits poor

efficiency in light emission and charge transport. To address these limitations and expand its potential applications, $Cs_2AgBiBr_6$ DP has been integrated with other functional materials. [16]

Two-dimensional transition metal dichalcogenides (2D-TMDCs) have garnered significant interest in the field of optoelectronics due to their unique optical and electrical characteristics emanating from their 2D confinement.[17,18] However, the performance of these atomically thin layered devices in optoelectronics is hampered by the limited light absorption by the sub-nanometre films, thus restricting photocarrier generation.[19] As such, considerable research has been dedicated to improving the light-harvesting capabilities of TMDC-based optoelectronic devices. Incorporating TMDCs with robust light absorption layers is an efficient way of enhancing the functionality of perovskite-based optoelectronic devices.[20] Owing to their large surface-to-volume ratio, ultrathin thickness, and quantum confinement effect, 2D-TMDCs exhibit exceptional properties in electronics and optoelectronics.[21] In recent times, researchers have incorporated 2D materials with metal halide perovskite crystals to achieve enhanced optoelectronic properties.[22] Some of the examples include $CsPbBr_3$/black phosphorus nanosheet-based heterostructure for photodetector applications[23], $CH_3NH_3PbI_3$/ black phosphorus/MoS_2 composite photodiode[24], $CH_3NH_3PbI_3$/reduced graphene oxide for photocatalysis,[25] etc. Compared to Pb-based halide perovskites, $Cs_2AgBiBr_6$ DP exhibits higher resistivity, resulting in reduced dark current and high detectivity (D*).[26,27] For example, photodetectors based on $Cs_2AgBiBr_6$ DP thin films demonstrated a high D value of 5.66×10^{11} Jones and responsivity of 7.01 A/W.[28] Additionally, it was found that reduced dimensionality with optimized thickness of highly crystalline $Cs_2AgBiBr_6$ DP can enhance the detectivity and responsivity of an optoelectronic device.[27] A similar improvement in optoelectronic device performance was observed with another 2D perovskite-based device, where the ultrathin 2D structure reduced carrier recombination probability.[29,30] Moreover, due to the strong interface contact between their ultra-flat surfaces, the nanostructure facilitated the integration of perovskites with TMDC materials, further enhancing their utility.[31]

In this study, we have successfully synthesized $Cs_2AgBiBr_6$ DP nanosheets and their heterostructure with few-layer WS_2 by a surfactant-free mechanochemical ball milling method. XRD measurements validate the pure phase growth of $Cs_2AgBiBr_6$ DP, which was intact after the heterostructure formation. Field Emission Transmission Electron Microscopy (FETEM) and Selected Area Electron Diffraction (SAED) measurements indicated the successful in-situ growth of $Cs_2AgBiBr_6$ DP over larger-size WS_2 nanosheets. From the shift in Raman mode

accompanied by photoluminescence (PL) quenching, we show that there is a fast and effective charge transfer from $Cs_2AgBiBr_6$ DP to WS_2. Our claim is supported by the careful examination of XPS spectra of the resultant heterostructure (HS) as well. We demonstrate that the $Cs_2AgBiBr_6/WS_2$ heterostructure photodetector device possesses a high on/off ratio, a relatively high responsivity, and a high specific detectivity. Our device exhibits photoresponse even at 0V, making it a self-powered device. Our findings lay the groundwork for in-situ and surfactant/ligand-free growth of highly crystalline perovskite-TMDC heterostructures, potentially applicable across various fields of optoelectronics.

3.2 Experimental Details

3.2.1 Materials Used

Cesium bromide (>99.99%, Sigma Aldrich), Silver bromide (>99.99%, Sigma Aldrich), Bismuth bromide (>99%, Sigma Aldrich), IPA (>98%, Sigma Aldrich), Tungsten (>99.99%, Sigma Aldrich), Sulphur (>99.99%, Sigma Aldrich), Ethanol (>99%, Merck), NMP (>99.99%, Merck). All chemicals were used without any further purification or alteration.

3.2.2 $Cs_2AgBiBr_6$ Double Perovskite Nanosheets Synthesis

$Cs_2AgBiBr_6$ double perovskite nanosheets were synthesized using a surfactant/ligand-free ball milling technique. A mixture containing 0.5 mmol of CsBr, 0.25 mmol of AgBr, and 0.25 mmol of $BiBr_3$ was placed in a 50 mL zirconium vial along with 90 zirconium spherical balls, each with a diameter of 5 mm. This setup was then placed in a ball mill system (PM100, Retch, Germany) and milled for 1 hour at 500 rpm under gas-tight conditions. These parameters were found to be optimal for achieving well-crystallized nanosheets without any sintering. The resulting DP nanosheets were collected in isopropanol and stored under an inert environment.

3.2.3 WS_2 Nanosheets Synthesis

WS_2 nanosheets were synthesized separately using a simple top-down chemical exfoliation method, as previously reported by our group. In brief, bulk WS_2 powder was dissolved in 50 mL of NMP at a concentration of 1 mg mL^{-1}. The solution in a glass beaker underwent sonication in an ice-cooled environment using an ultrasonic homogenizer (Sonic Ruptor 250, Omni International) set to 40% output power and a frequency of 20,000 cycles per second for 5 hours. The resulting solution was then heated to 120ºC using a magnetic stirrer at 400 rpm until the solvent completely evaporated. The resultant product, with a known mass, was

centrifuged at 12000 rpm in ethanol at 4ºC for 30 minutes to separate the WS_2 nanosheets from the WS_2 quantum dots. The upper portion was discarded, and this process was repeated two times to get a few-layer WS_2 nanosheet.

3.2.4 $Cs_2AgBiBr_6/WS_2$ Heterostructure Synthesis

The in-situ growth of highly crystalline $Cs_2AgBiBr_6/WS_2$ heterostructure was carried out by simply milling 10 mg of WS_2 nanosheets (prepared by the method mentioned above) along with the precursor chemicals used for $Cs_2AgBiBr_6$ DP nanosheets. During the milling process, the kinetic energy of the balls is transferred to Cs, Ag, and Bi bromide precursors on WS_2 nanosheets to form $Cs_2AgBiBr_6$ double perovskite. This transfer facilitates the collision between the reactant molecules to form the $Cs_2AgBiBr_6/WS_2$ heterostructure. The $Cs_2AgBiBr_6$ is abbreviated as DP, and the $Cs_2AgBiBr_6/WS_2$ heterostructure as HS in this work.

3.2.5 Device Fabrication

The $Cs_2AgBiBr_6/WS_2$ heterojunction device was fabricated using interdigitated electrodes (IDEs) prepared by a conventional photolithography technique. Gold electrodes were deposited using electron beam evaporation. Each IDE featured 6 fingers, each with a channel width of ~6 µm and a channel length of 50 µm. The elimination of access metal from undesired areas was achieved through a lift-off process involving immersion of the device in acetone for 20 minutes. Subsequently, the device underwent a thermal treatment at 130ºC for 30 minutes to minimize contact resistance. After completion, the solution containing WS_2, $Cs_2AgBiBr_6$ DP, and $Cs_2AgBiBr_6/WS_2$ was drop-casted onto the device and dried before further measurements.

3.3 Characterization Techniques

The structural characterizations of the as-prepared samples were conducted using a Rigaku RINT 2500 TRAX-III diffractometer with Cu Kα radiation (λ= 1.5418 Å), employing the X-ray powder diffraction (XRD) technique within a 2θ range from 5º to 50º. Morphological and structural analysis of as-synthesized materials was conducted using field emission transmission electron microscopy (FETEM) and selected area electron diffraction (SAED) analysis utilizing (FETEM, JEOL-2100F). Raman measurements were performed using a high-resolution micro-Raman spectrometer (LabRam HR800, Jobin Yvon) with a 633 nm laser with a spot size of ~1µm with 1800 cm-1 grooves. A field scanning electron microscope (FESEM, SIGMA 300, Ziess runs at 200 kV) was utilized for elemental mapping analysis. Furthermore, steady-state PL measurements were conducted at room temperature utilizing a Horiba Jobin Yvon Fluoromax-4 fluorometer using a 405 nm excitation laser (external). Time-resolved PL

measurements were performed using time-correlated single photon counting (TCSPC), having an instrument response time <10 ps (Lifespec II, Edinburgh Instruments) with a 405 nm pulsed laser excitation. Elemental composition and chemical states of different elements were studied using a photoelectron spectrometer (PHI 5000 VersaProbe III, ULVAC-PHI, Inc.) using an Al K_α X-ray beam of current 20 mA operating at 1486.6 eV. The electrical characterization was conducted using a shielded DC probe station, which was equipped with an external laser source and function generator, in conjunction with a Keithley 4200 SCS system.

3.4 Results and Discussion

3.4.1 Morphology, Structure, and Phase Analysis

The $Cs_2AgBiBr_6$ DP nanosheets were successfully synthesized by surfactant/ligand-free mechanical ball milling of the precursor chemicals (**Fig. 3.1**). During milling, the high kinetic energy of the zirconium balls aids the initiation of the reaction process between the precursor chemicals of Cs, Ag, and Bi bromides, allowing them to produce $Cs_2AgBiBr_6$ nanosheets. The reaction process is shown below[32]

$$2CsBr + AgBr + BiBr_3 \rightarrow Cs_2AgBiBr_6 \qquad (3.1)$$

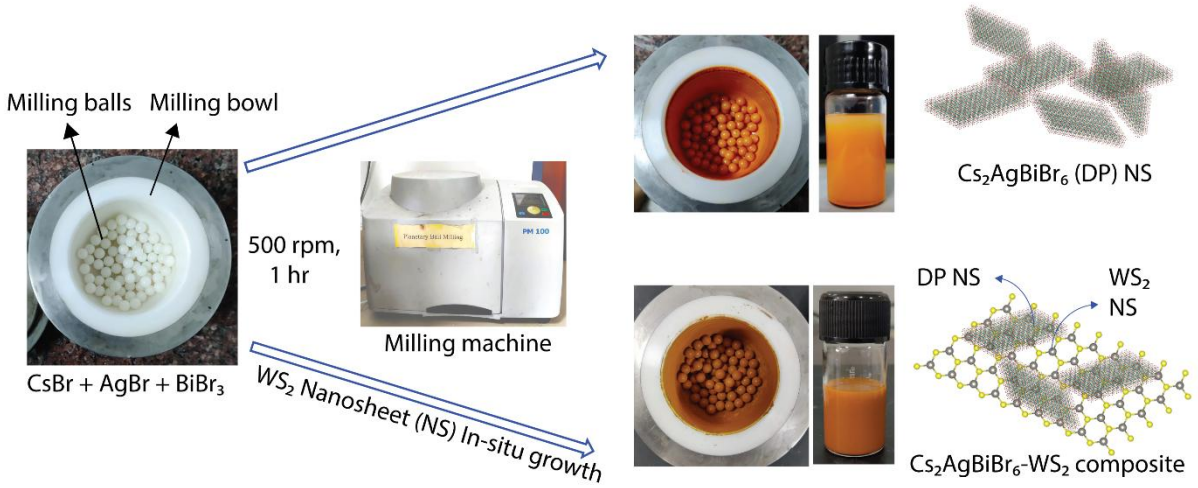

Fig. 3.1: Schematic illustration of the mechanochemical synthesis of $Cs_2AgBiBr_6$ DP nanosheets and in-situ growth of $Cs_2AgBiBr_6/WS_2$ heterostructure.

FETEM and HRTEM imaging were utilized to analyze the morphology and crystal structure of the as-prepared $Cs_2AgBiBr_6$ DP. The obtained $Cs_2AgBiBr_6$ DP nanosheets have lateral sizes ranging from a few hundred nm (**Fig. 3.2(a)**). HRTEM lattice fringes have an interplanar spacing of 0.38 nm, corresponding to the (220) plane of the $Cs_2AgBiBr_6$ phase (**Fig. 3.2(b)**).[33]

WS_2 nanosheets were prepared using the tip-sonication method reported previously by our group.[34] The lateral size of the WS_2 nanosheets is larger than $Cs_2AgBiBr_6$ DP (**Fig. 3.3(a)**).

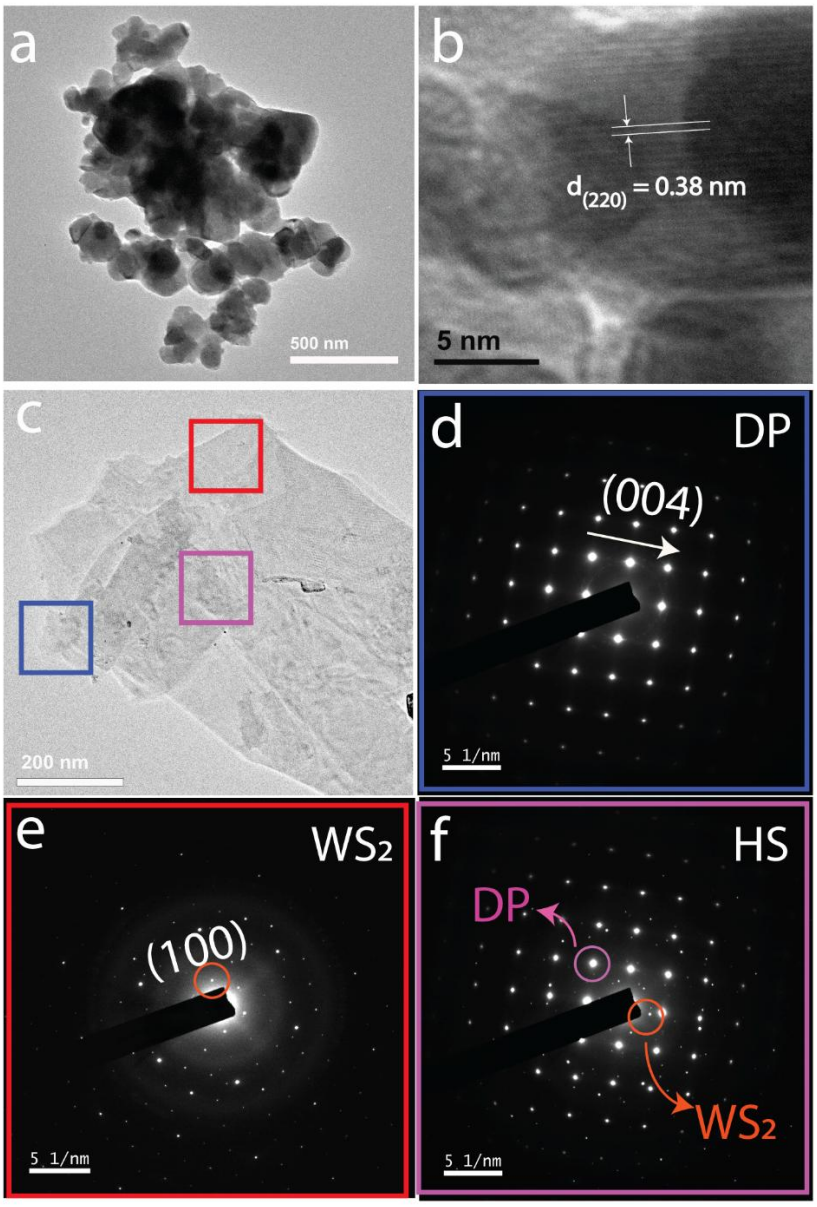

Fig. 3.2: (a-b) Low-resolution and high-resolution FETEM images of $Cs_2AgBiBr_6$ DP nanosheets synthesized mechanochemically**. (c)** FETEM image of $Cs_2AgBiBr_6/WS_2$ heterostructure. Three squares of different colours indicate the position of the SAED pattern. Blue square indicates the pure DP phase, red indicates pure WS_2, and violet indicates the presence of both DP and WS_2 in the heterostructure. **(d-f)** The SAED patterns of DP, WS_2, and DP/WS_2 heterostructure, respectively.

The high-resolution SAED pattern confirmed the synthesis of highly crystalline WS_2 nanosheets (**Fig. 3.3(b)**). The in-situ $Cs_2AgBiBr_6/WS_2$ heterostructure was formed by adding 10 mg of WS_2 nanosheets along with the precursor chemicals of DP before milling. After the

heterostructure formation, $Cs_2AgBiBr_6$ DP nanosheets appeared to be partially dispersed over large WS_2 nanosheets (**Fig. 3.2(c)**).

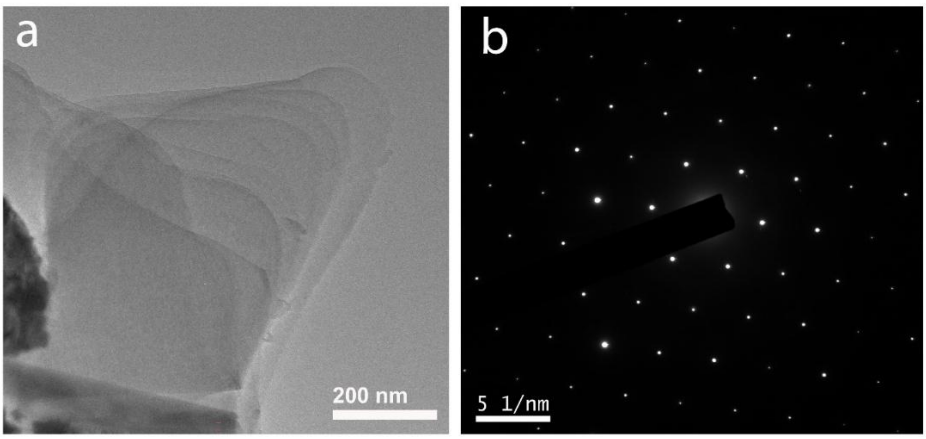

Fig. 3.3: (a) FETEM image of multi-layer WS_2 nanosheets prepared by the ultrasonication method. **(b)** The corresponding selected area electron diffraction pattern of WS_2 nanosheets.

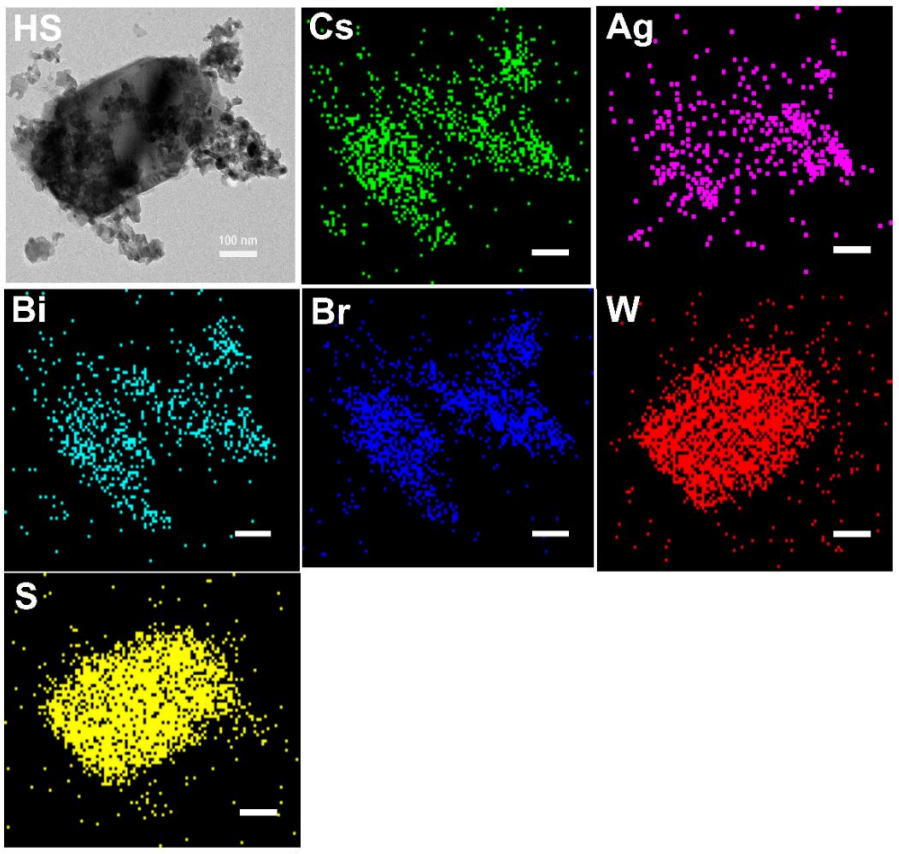

Fig. 3.4: (a) FETEM image of the $Cs_2AgBiBr_6/WS_2$ heterostructure. **(b-g)** Elemental mapping of Cs, Ag, Bi, Br, W, and S elements in $Cs_2AgBiBr_6/WS_2$ heterostructure, respectively. The scale bar in each image is 100 nm.

SAED measurement was conducted across multiple regions of the heterostructure demarcated by squares to differentiate between distinct phases. The SAED pattern is the Fourier-space projection of the real structure. The SAED pattern of the (004) plane of the highly crystalline $Cs_2AgBiBr_6$ DP is represented by the blue square (**Fig. 3.2(d)**). The red marking indicates the presence of the WS_2 nanosheets (**Fig. 3.2(e)**), and the purple marking highlights the formation of the heterostructure (**Fig. 3.2(f)**). Despite the presence of WS_2 planes in the heterostructure, their intensity appears diminished due to partial encapsulation by $Cs_2AgBiBr_6$ DP nanosheets. Field Emission Transmission Electron Microscopy with Energy Dispersive X-ray spectroscopy (FETEM-EDX) mapping confirms the homogeneous integration of WS_2 with DP within the resultant heterostructure (**Fig. 3.4**). The corresponding EDX spectra confirmed that the stoichiometry ratio of the elements matched the DP pure phase. However, less sulphur is observed than the ideal composition of WS_2, which suggests the formation of sulphur vacancies after heterostructure formation (**Fig. 3.5**).

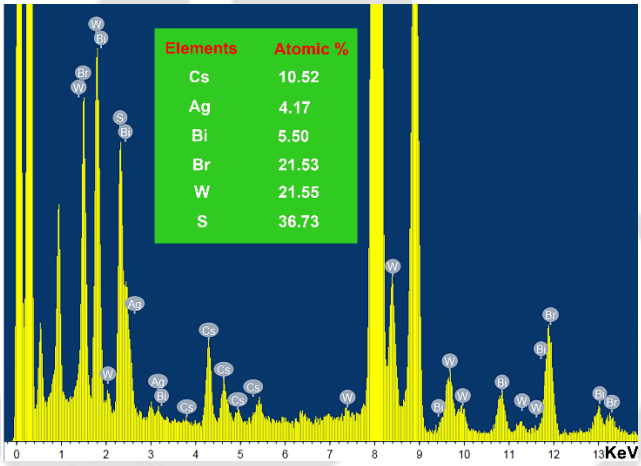

Fig. 3.5: The corresponding TEM-EDX spectra of the DP/WS_2 heterostructure.

XRD analyses were conducted to elucidate the structure of the $Cs_2AgBiBr_6$ DP samples, both before and after heterojunction formation (**Fig. 3.6(a)**). The XRD pattern reveals distinct peaks corresponding to (002), (022), (222), (004), (024), (224), and (044) planes, with 2θ values at 15.69º, 22.30º, 27.41º, 31.76º, 35.58º, 39.15º, and 45.53º respectively. The cubic structure of $Cs_2AgBiBr_6$ DP is confirmed, detailing the Bi/Ag arrangement resembling rock salt, with a lattice constant of a = 11.2811 Å and $Fm\bar{3}m$ space group symmetry, which is in agreement with our previous work.[35] The XRD pattern of both $Cs_2AgBiBr_6$ DP and heterostructure exhibits identical cubic crystal phases.

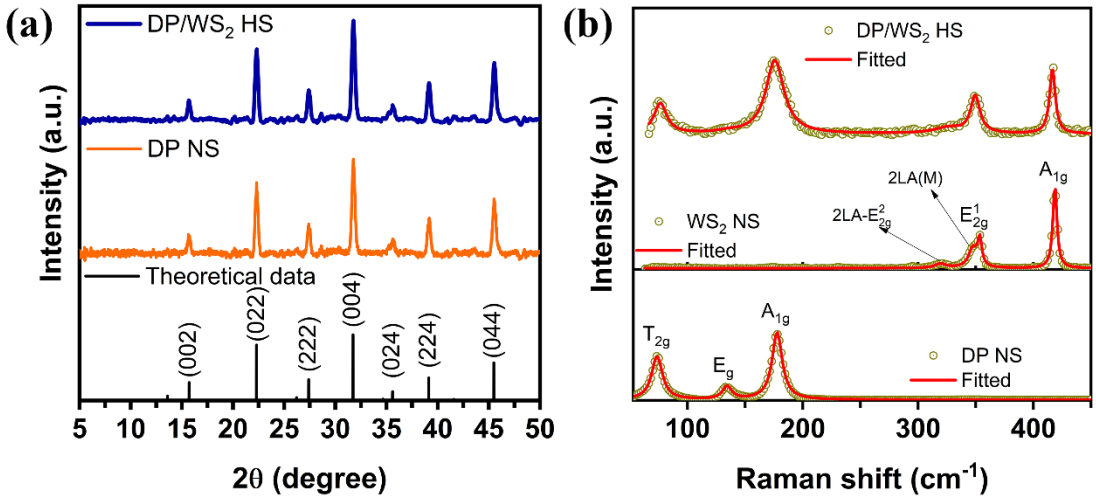

Fig. 3.6: (a) XRD pattern of pure $Cs_2AgBiBr_6$ DP (orange) and $Cs_2AgBiBr_6/WS_2$ heterostructure (blue) on the glass substrate. **(b)** Raman spectra of $Cs_2AgBiBr_6$ DP, few-layer WS_2 nanosheets, and $Cs_2AgBiBr_6/WS_2$ heterostructure.

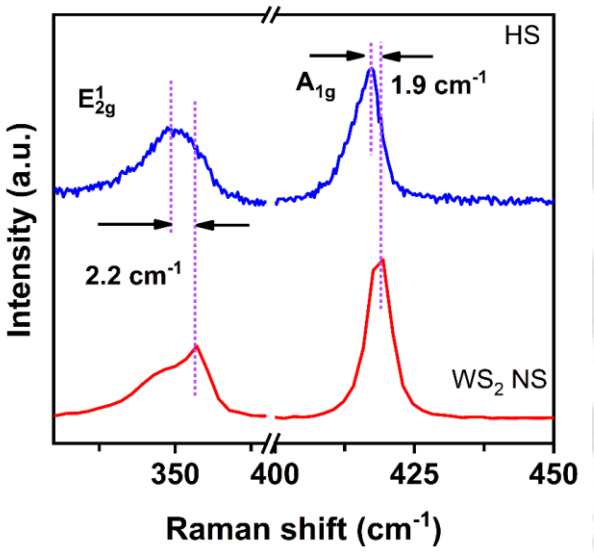

Fig. 3.7: Comparison of the Raman spectra of WS_2 (red) and $Cs_2AgBiBr_6/WS_2$ (blue) heterostructure.

This similarity indicates that including WS_2 does not modify the phase composition under the specific synthesis conditions employed. Additionally, Raman spectroscopy was used to determine the chemical structure and the number of layers in the WS_2 nanosheet. In **Fig. 3.6(b)**, the A_{1g} (peak at ~418.2 cm^{-1}) mode of WS_2 is stronger than the 2LA(M) (peak at ~347.5 cm^{-1}) mode. The frequency difference between the A_{1g} mode and E_{2g} mode (~352.4 cm^{-1}) of WS_2 is ~66 cm^{-1}. All these findings align well with the characteristics of the multilayer formation of WS_2.[36] Three distinct peaks at 73.5 cm^{-1}, 134.3 cm^{-1}, and 177.6 cm^{-1} correspond to T_{2g}, E_g, and A_{1g} modes of $Cs_2AgBiBr_6$ DP, respectively.[37] Importantly, the unique Raman signal of WS_2

remains intact in the heterostructure formation, indicating minimal structural damage to WS_2 during milling. However, we have observed a redshift of 1.9 cm^{-1} in the A_{1g} mode and 2.2 cm^{-1} in the E_{2g} mode of WS_2 in the heterostructure (**Fig. 3.7**). These observations suggest an electron-doping effect on multilayer WS_2 and the induction of strain during heterostructure formation.[38]

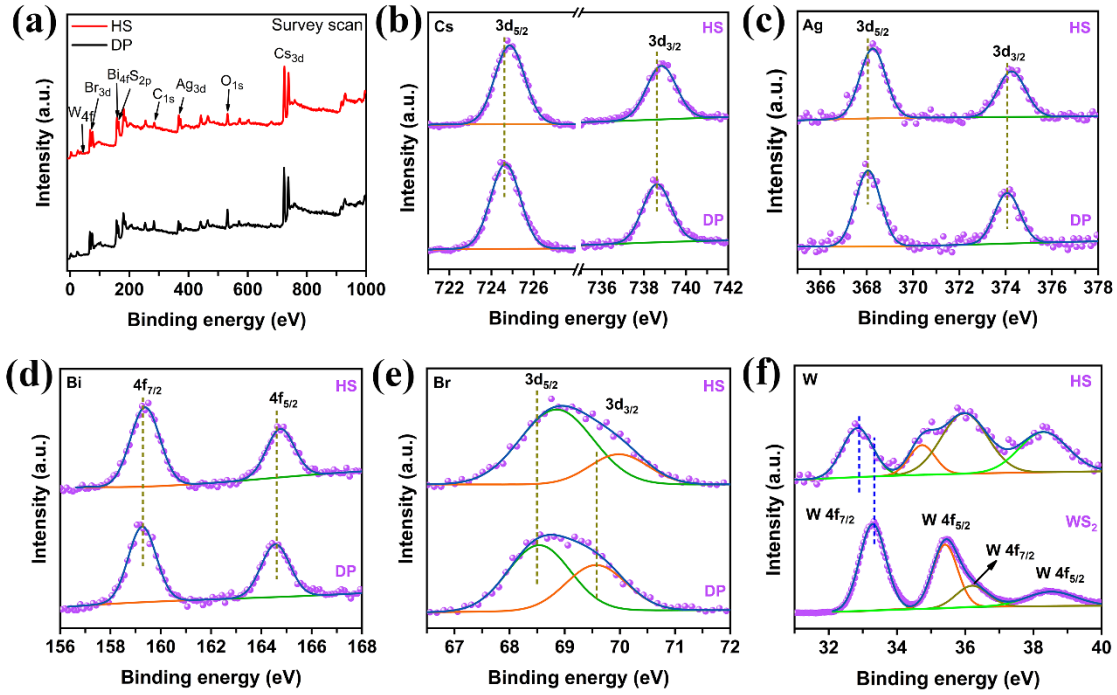

Fig. 3.8: (a) XPS survey scan spectra of $Cs_2AgBiBr_6$ DP (black) and $Cs_2AgBiBr_6/WS_2$ heterostructure (red). **(b-e)** High-resolution XPS spectra of Cs, Ag, Bi, and Br elements in $Cs_2AgBiBr_6$ DP and $Cs_2AgBiBr_6/WS_2$ heterostructure, respectively. The symbols display experimental data points, and the solid blue line represents cumulative fitting. **(f)** Comparison of high-resolution XPS spectra of tungsten (W) in WS_2 nanosheets and $Cs_2AgBiBr_6/WS_2$ heterostructure.

The effectiveness of a heterojunction in optoelectronic devices is widely recognized as being significantly dependent on the transfer of charge carriers across the interface. This transfer is closely linked to the alignment of the band energies and the strength of the electron coupling between the two components of the heterojunction. Consequently, to investigate the specific interaction at the interface between $Cs_2AgBiBr_6$ DP and WS_2 nanosheets in the heterostructure, we used X-ray photoelectron (XPS) and Ultraviolet photoelectron spectroscopy (UPS) measurements.

The survey scan XPS spectra of $Cs_2AgBiBr_6$ DP and $Cs_2AgBiBr_6/WS_2$ heterostructure are shown in **Fig. 3.8(a)**. The Br 3d spectrum of pure $Cs_2AgBiBr_6$ DP exhibits two distinct peaks

at 68.2 eV and 69.1 eV, corresponding to Br $3d_{5/2}$ and Br $3d_{3/2}$, respectively.[39] In the heterostructure, the binding energies of Br $3d_{5/2}$ and Br $3d_{3/2}$ experience a significant positive shift (~0.3 eV) compared to the pure $Cs_2AgBiBr_6$ DP system. This upshift suggests electron transfer from $Cs_2AgBiBr_6$ DP to WS_2.[40,41] Additionally, the peaks of Cs, Ag, and Bi in the heterostructure also exhibit a noticeable shift towards higher energies compared to those of pure $Cs_2AgBiBr_6$ DP (**Fig. 3.8(b-e)**). In pristine WS_2, W 4f displays two distinct peaks at 33.2 eV and 35.4 eV, corresponding to W $4f_{7/2}$ and W $4f_{5/2}$, respectively. These high-intensity peaks indicate the presence of a W^{4+} oxidation state in pure WS_2 nanosheets, indicative of the 2H semiconducting phase.[34] These peaks are notably shifted to the lower energies, approximately by 0.4 eV in the heterostructure system (**Fig. 3.8(f)**). This indicates that there is a transfer of electrons from $Cs_2AgBiBr_6$ DP to WS_2, resulting in the relocation of the Fermi energy level of WS_2 closer to the edge of the conduction band.[42,43]

3.4.2 Optical Analysis

Further, absorption spectra were collected to delve into the optical properties of $Cs_2AgBiBr_6$ DP and WS_2 heterojunction. In the visible range, the $Cs_2AgBiBr_6$ DP spectrum displays a broad absorption commencing at 600 nm (**Fig. 3.9(a)**), corresponding to an indirect bandgap of 2.04 eV (**Fig. 3.9(b)**). Two excitonic peaks were detected in the pure WS_2 spectra: one at 635 nm and the other at 528 nm. These peaks correspond to A and B excitons of WS_2, respectively.[44] The multilayer WS_2 material exhibits an indirect bandgap characterized by a bandgap energy of 1.8 eV (**Fig. 3.9(c)**). Upon forming a heterojunction, the absorption spectra remain akin to WS_2; however, with heightened absorption features. The persistence of WS_2 excitons in the absorption spectra of the heterostructure implies the continued presence of WS_2 post-heterojunction formation. Nevertheless, the collective bandgap of the heterostructure decreases upon integration with WS_2, suggesting that the incorporation of additional energy bands facilitated by WS_2 has occurred.

Steady-state PL and time-resolved PL spectroscopy are employed to investigate the optical characteristics and charge transfer dynamics in the heterostructure configuration. The $Cs_2AgBiBr_6$ DP manifests a broad PL spectrum indicative of an indirect transition and the presence of self-trapped exciton (STE) emission (**Fig. 3.9(d)**).[45] In contrast, the PL intensity of the heterojunction experiences substantial quenching, pointing towards efficient carrier relaxation pathways and charge transfer between the $Cs_2AgBiBr_6$ DP and WS_2 components.[46] To delve deeper into this phenomenon, the PL spectra of both the $Cs_2AgBiBr_6$ DP and

$Cs_2AgBiBr_6/WS_2$ heterostructure were deconvoluted. Within the DP spectrum, two distinct peaks emerge, one at approximately 608 nm and another at around 665 nm (**Fig. 3.9(e)**).

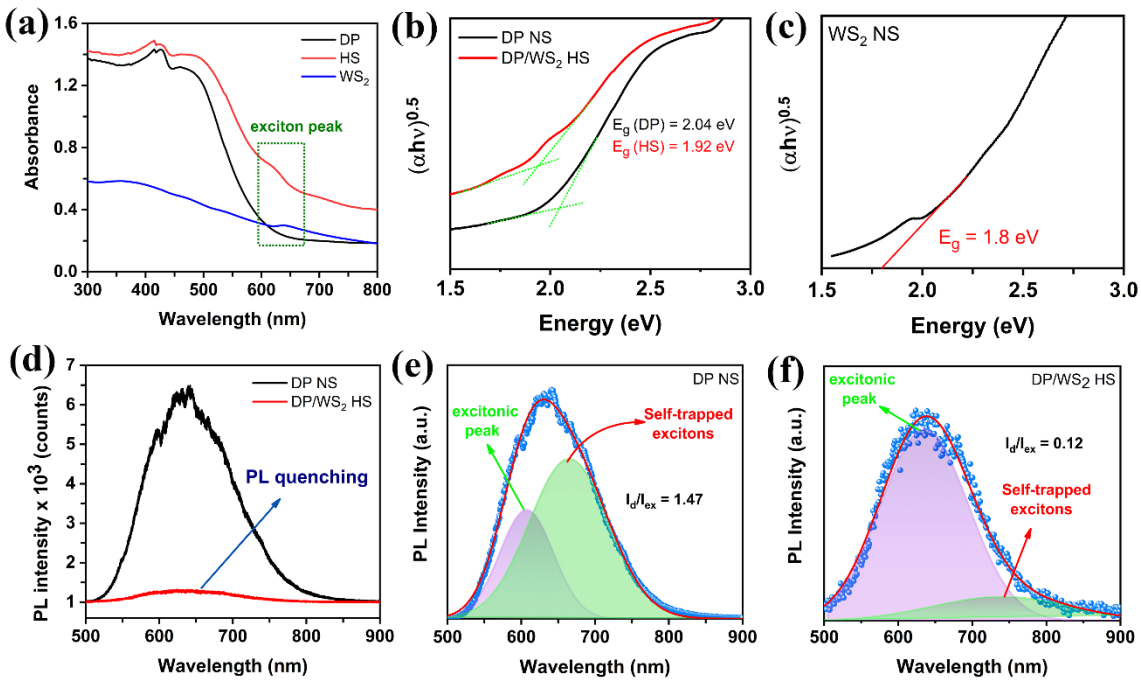

Fig. 3.9: (a) Absorption spectra of few-layer WS_2 nanosheets (blue), pure $Cs_2AgBiBr_6$ DP nanosheets (black), and $Cs_2AgBiBr_6/WS_2$ heterostructure (red). **(b)** Tauc plot of $Cs_2AgBiBr_6$ DP (black) and $Cs_2AgBiBr_6/WS_2$ heterostructure (red). The green dotted line displays the linear fitting of the graphs. **(c)** Tauc plot of the few-layer WS_2 nanosheets (black). The red line is the linear fitting of the graph. **(d)** PL spectra of $Cs_2AgBiBr_6$ DP (black) and $Cs_2AgBiBr_6/WS_2$ heterostructure (red). **(e, f)** Deconvoluted PL spectra of $Cs_2AgBiBr_6$ DP and $Cs_2AgBiBr_6/WS_2$ heterostructure, respectively.

The former, characterized by lower intensity, corresponds to the excitonic transition intrinsic to the DP system, linked to its bandgap. On the other hand, the latter peak at 665 nm is attributed to the transitions involving self-trapped excitons (STEs), reflecting the presence of defects within the DP lattice.[47] Similarly, the deconvoluted PL spectrum of the heterostructure reveals two peaks: one at 635 nm, corresponding to the excitonic transition associated with the bandgap of the HS, and another at 743 nm, attributed to the STE emission (**Fig. 3.9(f)**). Multilayer WS_2 does not have any PL emission. Also, it has an indirect band gap similar to the DP band gap. Because of the similar behavior of the bands, we did not observe any specific shape change in the PL spectra. In pristine DP, the photogenerated carriers recombine only through band-to-band and self-trapped states, but in HS, there are additional energy states of WS_2 as well. So, the photogenerated carriers recombine through additional WS_2 energy states and then through trap states, which leads to the significant Stokes shift in the case of HS. Some of the free carriers

recombine through WS_2 energy states, which do not contribute to PL due to their nonradiative nature. Self-trapped exciton emission can depend on various factors like the degree of electron-phonon interaction, fabrication methods, the dimensionality of the material, and also on the thickness of the material.[48,49] In general, the Stokes shift is a signature of defects in the system, and a smaller Stokes shift may indicate a lower defect density in the system, which is beneficial for efficient charge transfer at the interface and less recombination, resulting in a high photoresponse. Notably, the intensity of the STE emission is diminished compared to that of the excitonic emission peak. The reduced I_d/I_{ex} (from 1.42 to 0.12) ratio indicates that the incorporation of WS_2 in the heterostructure effectively suppresses STE emission while concurrently augmenting excitonic emission, where I_d and I_{ex} are the intensities of STE emission and excitonic emission, respectively. The schematic illustration of various recombination pathways of the $Cs_2AgBiBr_6$ DP and the $Cs_2AgBiBr_6/WS_2$ heterostructure is shown in **Fig. 3.10(a, b)**, respectively.

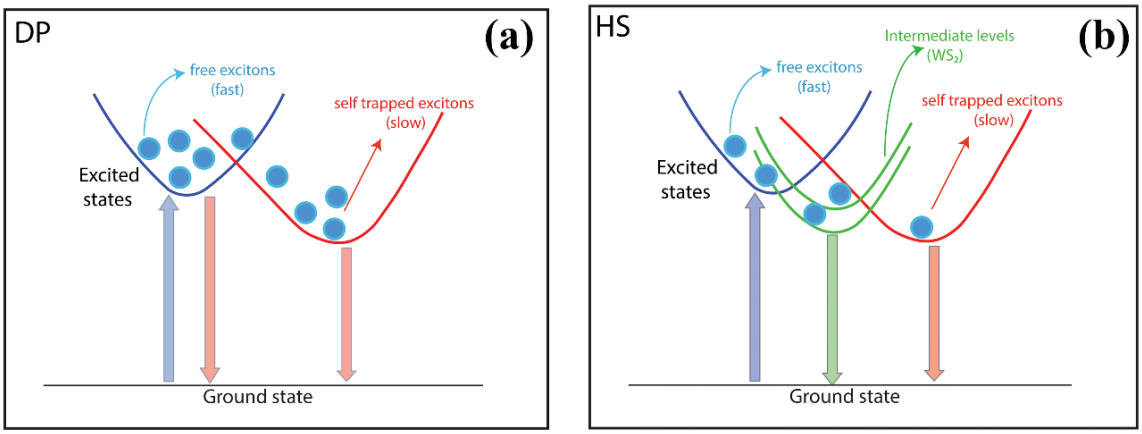

Fig. 3.10: (a, b) Schematic illustration of the photoexcited charge carrier dynamics in $Cs_2AgBiBr_6$ DP and $Cs_2AgBiBr_6/WS_2$ heterostructure, respectively. The blue circles represent the charge carriers.

3.4.3 Carrier Dynamics

The charge transport characteristics of $Cs_2AgBiBr_6$ DP and heterojunction were further investigated through time-resolved PL measurements. Analysis of the resulting decay curves, fitted using the bi-exponential function, aided in the estimation of the average lifetime (**Table 3.1**) of the charge carriers. The average PL lifetime (τ_{avg}) can be determined using the following equation:

$$\tau_{avg} = \frac{A_1\tau_1^2 + A_2\tau_2^2}{A_1\tau_1 + A_2\tau_2} \quad (2)$$

These two lifetimes revealed two distinct processes, including radiative relaxation attributed to the direct formation of free charge carriers and the self-trapped excitons (**Fig. 3.11**).[43] Note that both fast and slow components decay more rapidly in the heterostructure, suggesting efficient charge extraction across the interface. This is consistent with the reduced steady-state PL intensity.[50] The significant decrease in the decay time in the heterostructure (from 3.65 ns to 0.82 ns) suggests the emergence of additional energy levels following the inclusion of WS_2.

Table 3.1: TRPL decay parameters of $Cs_2AgBiBr_6$ DP and $Cs_2AgBiBr_6/WS_2$ HS.

Sample	A_1	τ_1 (ns)	A_2	τ_2 (ns)	τ_{avg} (ns)
$Cs_2AgBibr_6$ DP	2.4	0.16	7.3	3.7	3.65
$Cs_2AgBiBr_6$ DP/ WS_2 (HS)	3.5	0.14	2.8	0.95	0.82

The excited carriers in $Cs_2AgBiBr_6$ DP recombine radiatively through direct excitonic transition and trap states. The incorporation of non-radiative energy levels of WS_2 minimizes the radiative recombination through trap states, resulting in the quenching of the PL intensity of STE emission. These newly introduced levels play an important role in mitigating the emission due to self-trapped excitons, facilitating more efficient charge transport across the interface.

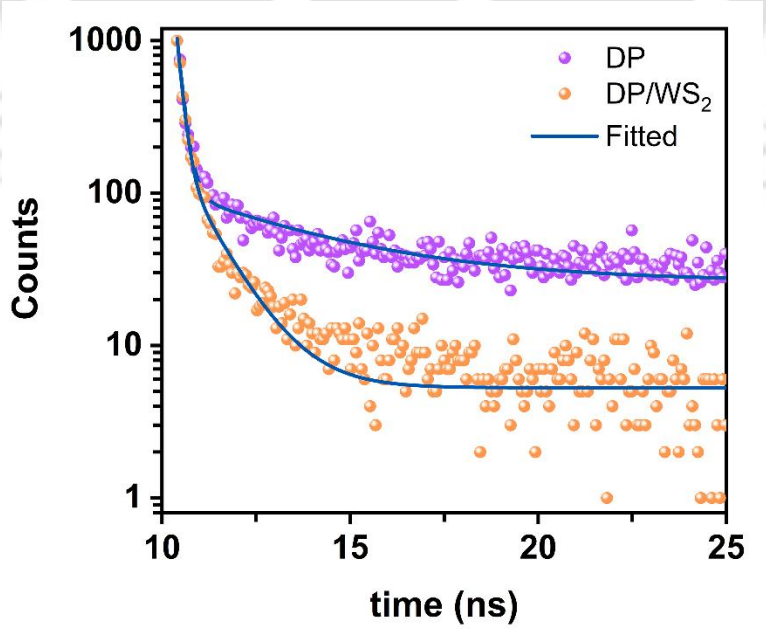

Fig. 3.11: Time-resolved PL spectra of $Cs_2AgBiBr_6$ DP (magenta) and $Cs_2AgBiBr_6/WS_2$ heterostructure (orange). The solid blue line represents exponential fitting.

UPS was employed to examine the band structure and Fermi levels of DP and WS_2 NS (**Fig. 3.12(a, b)**), respectively. The Fermi level (E_f) was estimated using the formula $E_f = 21.22 - E_{cutoff}$, where E_{cutoff} denotes the high binding energy cutoff.[51] Similarly, the position of the Valence band (E_{VB}) was determined using the formula $E_{VB} = E_f + E_0$, where E_0 stands for the low binding energy tail.[52] The values obtained for E_{VB} and E_F were 5.53 eV and 4.75 eV, respectively, for $Cs_2AgBiBr_6$ DP. Similarly, for WS_2, the values obtained for E_{VB} and E_F were 5.76 eV and 4.6 eV, respectively. The $Cs_2AgBiBr_6$ DP and WS_2 bandgap were determined to be 2.04 eV and 1.8 eV, respectively, using Tauc's plot. These obtained bandgap values were then employed to compute the conduction band position using the formula: $E_{CB} = E_{VB} + E_g$, where E_{CB} represents the conduction level and E_g represents the bandgap of the respective materials. The obtained values for E_{CB} were 3.49 eV and 3.91 eV for $Cs_2AgBiBr_6$ DP and WS_2, respectively. The effective band alignment and charge transfer mechanism in the $Cs_2AgBiBr_6/WS_2$ heterostructure will be discussed in later sections.

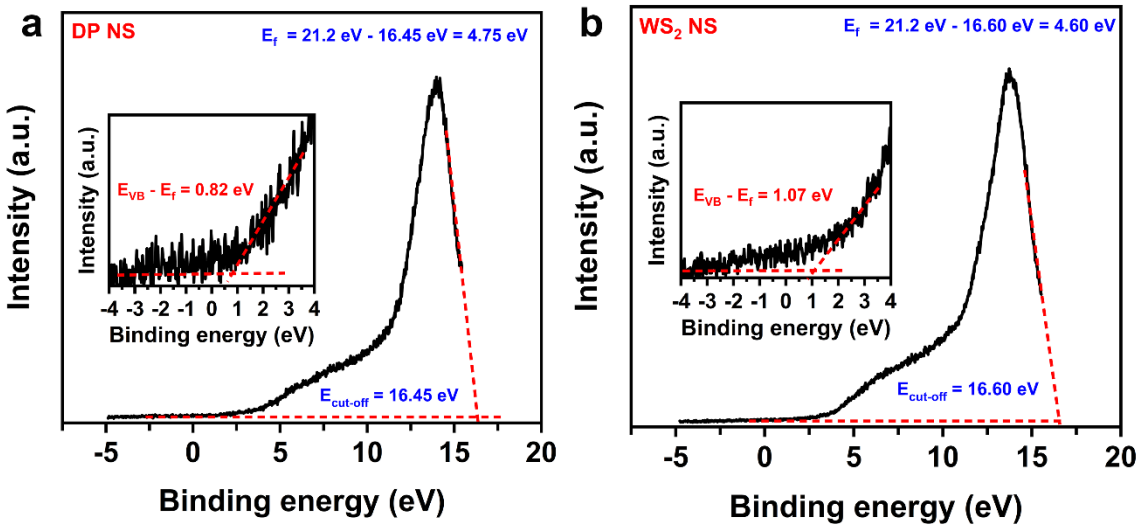

Fig. 3.12: UPS spectra of **(a)** $Cs_2AgBiBr_6$ DP, and **(b)** WS_2 nanosheets. The inset in each case shows the magnified view of the plot in the lower binding energy region.

3.4.4 Photodetector Application

As both $Cs_2AgBiBr_6$ DP and WS_2 exhibit strong light absorption in the UV region and effective charge transfer between them has been established, we have fabricated a UV photodetector device. To summarize, first, the photoresist (PR) S1813 (MICROPOSIT™) was coated using a spin coater, and then metal pads were patterned simultaneously by a direct UV laser writing. Next, Au contacts were deposited via an e-beam evaporation followed by lift-off. Finally, the devices were heated at 90 °C for 10 minutes to remove the residual solvents. Using this method,

the electrode separations can be well controlled by a few mm. The smaller separation will enhance the responsivity and response time. **Fig. 3.13(a)** illustrates the schematic representation of the device. Gold electrodes featuring an approximate channel width of 6 µm were deposited, and 405 nm laser illumination was used for all the measurements of the device. **Fig. 3.13(b)**displays the optical image of the device, with an active illuminated area estimated to be around 300 μm^2 using ImageJ software. The real-time optical image of the heterostructure device is depicted in **Fig. 3.13(c)**, with red circle markings denoting the active area of the device.

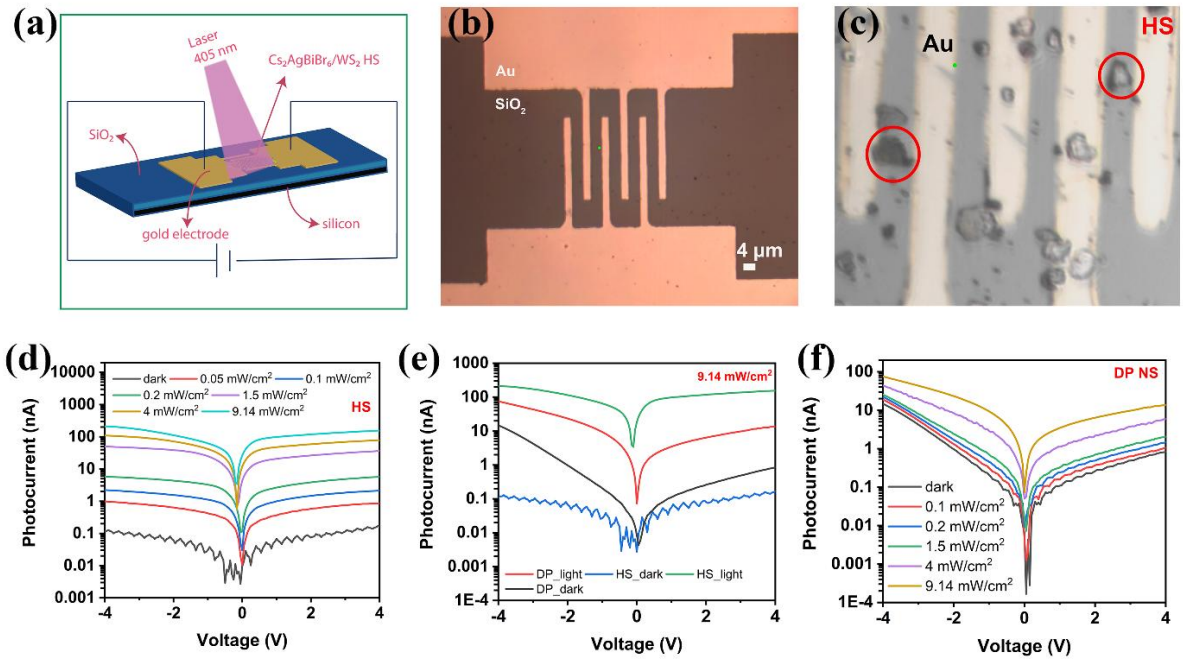

Fig. 3.13: (a) Schematic illustration of the photodetector device using $Cs_2AgBiBr_6/WS_2$ heterostructure. **(b)** Optical microscopy image of the device. **(c)** The real-time image of the $Cs_2AgBiBr_6/WS_2$ heterostructure photodetector. **(d)** I-V characteristics of $Cs_2AgBiBr_6/WS_2$ heterostructure with various incident laser power densities. **(e)** Comparison of I-V characteristics of $Cs_2AgBiBr_6/WS_2$ heterostructure with bare $Cs_2AgBiBr_6$ DP. **(f)** I-V characteristics of $Cs_2AgBiBr_6$ DP with varying incident laser power.

The current-voltage (I-V) characteristics of the heterostructure device were measured under dark conditions and with varying laser power densities, as illustrated in **Fig. 3.13(d)**. The photocurrent demonstrates a subsequent increase with the rise in laser power density. At 0V bias, the dark current of the heterostructure is ~2.5×10^{-12} A, while the photocurrent is 8.5×10^{-9} A, resulting in a current on/off ratio of 3.4×10^3 at a laser power density of 9.14 mW/cm^2. This high light-to-dark current ratio is a result of efficient charge transport and reduced carrier

recombination at the $Cs_2AgBiBr_6/WS_2$ heterostructure interface. A comparison with the bare $Cs_2AgBiBr_6$ DP device reveals that the dark current is significantly suppressed (by nearly 2 orders of magnitude), and the photocurrent is enhanced in the $Cs_2AgBiBr_6/WS_2$ heterostructure (**Fig. 3.13(e)**). The I-V characteristics of $Cs_2AgBiBr_6$ DP are shown in **Fig. 3.13(f)**.

Furthermore, while the $Cs_2AgBiBr_6$ DP device did not exhibit any response at 0V, the $Cs_2AgBiBr_6/WS_2$ heterostructure device demonstrated a substantial current of ~8.5 nA for 9.14 mW/cm^2 incident laser power, rendering it self-powered in nature (**Fig. 3.14(a)**).

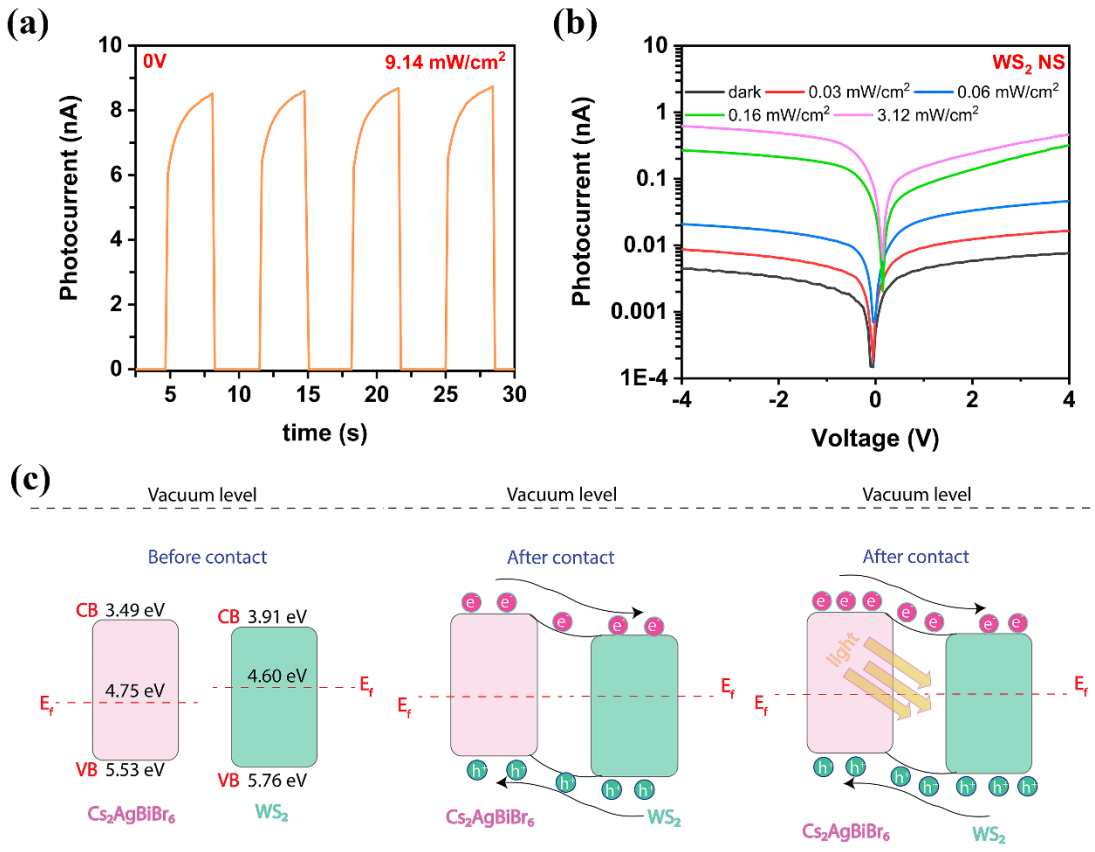

Fig. 3.14: (a) Photoresponse of $Cs_2AgBiBr_6/WS_2$ heterostructure at 0V bias under 9.14 mW/cm^2 intensity. **(b)** I-V characteristics of WS_2 nanosheets with different laser power illumination. **(c)** Schematic illustration of the band alignment of $Cs_2AgBiBr_6$ DP and WS_2 nanosheets before contact, after contact, and under light illumination.

It may be noted that the rise time is relatively slower than the fall time at zero bias conditions. At zero-bias conditions, where the electric field in the depletion layer is lower than the biased case, it can give rise to slow drift and corresponding slow response of the carriers. In general, the response time of a photodetector is determined by two factors: (i) drift of the electrons and holes that are photogenerated in the depletion layer, (ii) diffusion of the electrons and holes that

are photogenerated in the diffusion regions (outside the depletion region). The drift of the carriers across the depletion layer is a fast process– given by the transit times of the photogenerated electrons and holes across the depletion layer. Diffusion of the carriers is a slow process caused by the optical absorption in the diffusion regions outside of the high-field depletion region. Further, it may be noted that we have prepared the samples via the probe sonication method followed by ball milling; both processes create vacancies and defect sites in the HS. The presence of these defects slows down the flow of carriers via Auger recombination and trapping of photoelectrons by defects and trap sites at the interface.[53] **Fig. 3.14(b)** depicts the I-V characteristics of a WS_2 NS photodetector. The observed minimal photocurrent in WS_2 can be attributed to its inherently low light-absorbing capacity, low carrier mobility, small sheet size, and irregular shape resulting from exfoliation.[54] The primary factors driving the enhanced photocurrent in the hetero-junction include the exceptional light-absorbing capacity of the $Cs_2AgBiBr_6$ DP and the efficient charge transfer occurring at the interface of $Cs_2AgBiBr_6$ DP and WS_2.

The performance of the photodetector device hinges on achieving appropriate band alignment between electrodes, $Cs_2AgBiBr_6$ DP, and WS_2. To elucidate the efficient charge transfer within our materials, we constructed the energy band diagram of the $Cs_2AgBiBr_6/WS_2$ heterojunction based on the energy levels determined from the UPS measurement. In **Fig. 3.14(c)**, it's evident that the conduction band of WS_2 sits at ~0.42 eV lower than that of $Cs_2AgBiBr_6$ DP. This notable energy offset implies that photogenerated carriers (electrons) can transit from $Cs_2AgBiBr_6$ DP to WS_2. The equilibrium band alignment, representing a Type-II band alignment, of $Cs_2AgBiBr_6/WS_2$ heterojunction is illustrated in **Fig. 3.14(c)** (after contact). The diminished dark current is due to the formation of a depletion region and a Schottky barrier at the $Au/Cs_2AgBiBr_6/WS_2$ interface. When illuminated, electron-hole pairs are generated in the $Cs_2AgBiBr_6$ DP and separated efficiently at the $Cs_2AgBiBr_6/WS_2$ interface, leading to a high photocurrent (**Fig. 3.14(c)** (after illumination)).

The evaluation of photodetector performance commonly relies on two key parameters: responsivity (R) and specific detectivity (D). R reflects how effectively the photodetector converts incident light into electrical signals. D indicates the device's ability to discern weak signals from background noise. The R is expressed as[16]

$$R = \frac{I_{light} - I_{dark}}{P_{in} \times A} \quad (3)$$

Where I_{light} is the photocurrent, I_{dark} is the dark current, P_{in} is the incident light power density, and A is the active illuminated area of the device (~300 μm^2 for our device). Interestingly, the heterostructure device exhibits a high responsivity value of 2.04 A/W for the light power density of 0.03 mW/cm^2 (**Fig. 3.15(a)**). As seen in the figure, the responsivity of the device decreases with an increase in the light power density, owing to the increase in recombination with increased laser power.[55] We have studied the wavelength-dependent photoresponse of HS, and the corresponding responsivity at different wavelengths is shown in **Fig. 3.15(b)**. The photoresponse follows the absorption spectra.

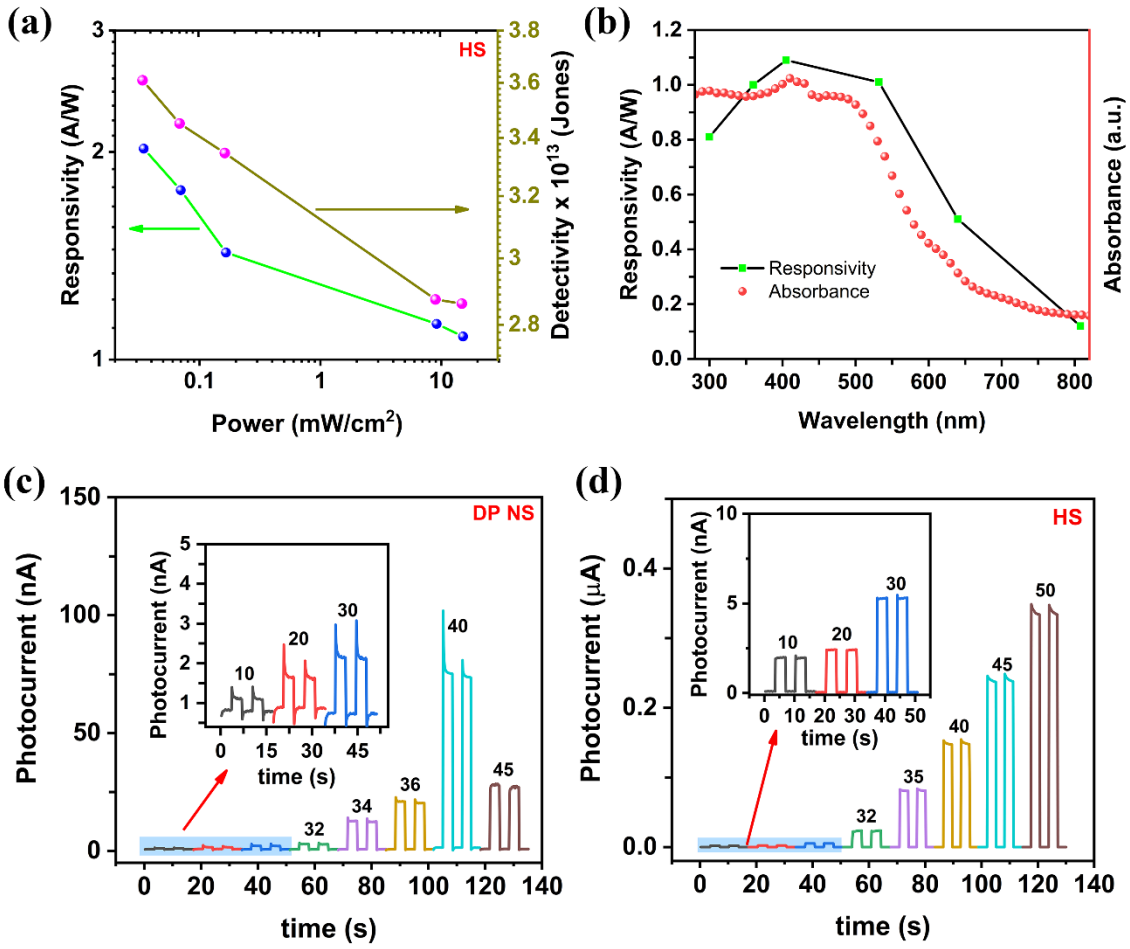

Fig. 3.15: (a) Responsivity (R) (left) and detectivity (D) (right) of $Cs_2AgBiBr_6/WS_2$ heterostructure for different incident power densities. **(b)** Wavelength-dependent Responsivity and absorption spectra of DP/WS_2 heterostructure. **(c, d)** Photocurrent response of $Cs_2AgBiBr_6$ DP NS and $Cs_2AgBiBr_6/WS_2$ heterostructure with varying incident laser powers for 405 nm diode laser, respectively.

The D is expressed as[50]

$$D = \frac{R}{\sqrt{2qI_{dark}}} \quad (4)$$

Where q is the electronic charge, and I_{dark} is the dark current of the device. We obtained a high detectivity value of 3.6×10^{13} Jones for a power density of 0.03 mW/cm^2 (**Fig. 3.15(a)**) for the $Cs_2AgBiBr_6/WS_2$ heterostructure. The comparison of the existing heterostructure photodetector devices based on $Cs_2AgBiBr_6$ DP is given in **Table 3.2**. The detectivity and on/off ratio values of our device are superior to other reported devices. To quantitatively analyze the relationship between photocurrent and illumination power density, **Fig. 3.15(c, d)** illustrates the photocurrent of $Cs_2AgBiBr_6$ DP and the $Cs_2AgBiBr_6/WS_2$ HS plotted against incident light power density, respectively, recorded at a bias voltage of -4V.

Table 3.2. Performance comparison of different heterostructures of perovskites with TMDCs.

Materials	On/off ratio	Responsivity (A/W)	Detectivity (Jones)	Rise and Fall time	LDR	Ref.
$Cs_2AgBiBr_6/BiOCl$	100	-	-	0.24/0.56 s	-	58
$CsPBBr_3/MoS_2$	342	6.7	1.02×10^{12}	5.48/24.05 µs	-	50
2D Cs2AgBiBr$_6$/WS$_2$/ graphene	~10^4	0.52	1.5×10^{13}	52.3/53.6 µs	60	16
$WS_2/C_2H_5C_2H_4NH_3PbI_4$/graphene	1.5×10^3	1.3×10^{-4}	-	200/200 ms	-	59
$Cs_2AgBiBr_6/WS_2$	5.9×10^3	2.01	3.6×10^{13}	80/120 ms	75	This work

The corresponding photoresponse of $Cs_2AgBiBr_6$ DP and $Cs_2AgBiBr_6/WS_2$ heterostructure with laser power density is displayed in **Fig. 3.16(a, b)**, respectively. The fitting of the variation of the photocurrent with laser power density was done using the basic power law equation[56]

$$I_{ph} = AP^{\theta} \quad (5)$$

Where θ represents the exponent, P denotes the laser power density, A is a scaling constant, and I_{ph} signifies the photocurrent. The obtained exponent (θ ~0.7 for $Cs_2AgBiBr_6$ and ~0.9 for $Cs_2AgBiBr_6/WS_2$ heterostructure) demonstrates a good fit for the power law equation (depicted by a red line) to the experimental data points (depicted by solid spheres). The photocurrent of $Cs_2AgBiBr_6$ DP decreased abruptly due to the laser-induced damage to the DP at higher power density. This fitting suggests that the saturation in HS is attributed to the kinetics of photo-

generated carriers, involving both carrier-carrier interaction and recombination states.[56] The value of the exponent for the ideal photodetector is 1.0. Since our device exhibits an exponent value of 0.9, which is close to the ideal value, these findings suggest the potential use of $Cs_2AgBiBr_6/WS_2$ heterostructure in future optoelectronic devices with minimum losses due to recombination.

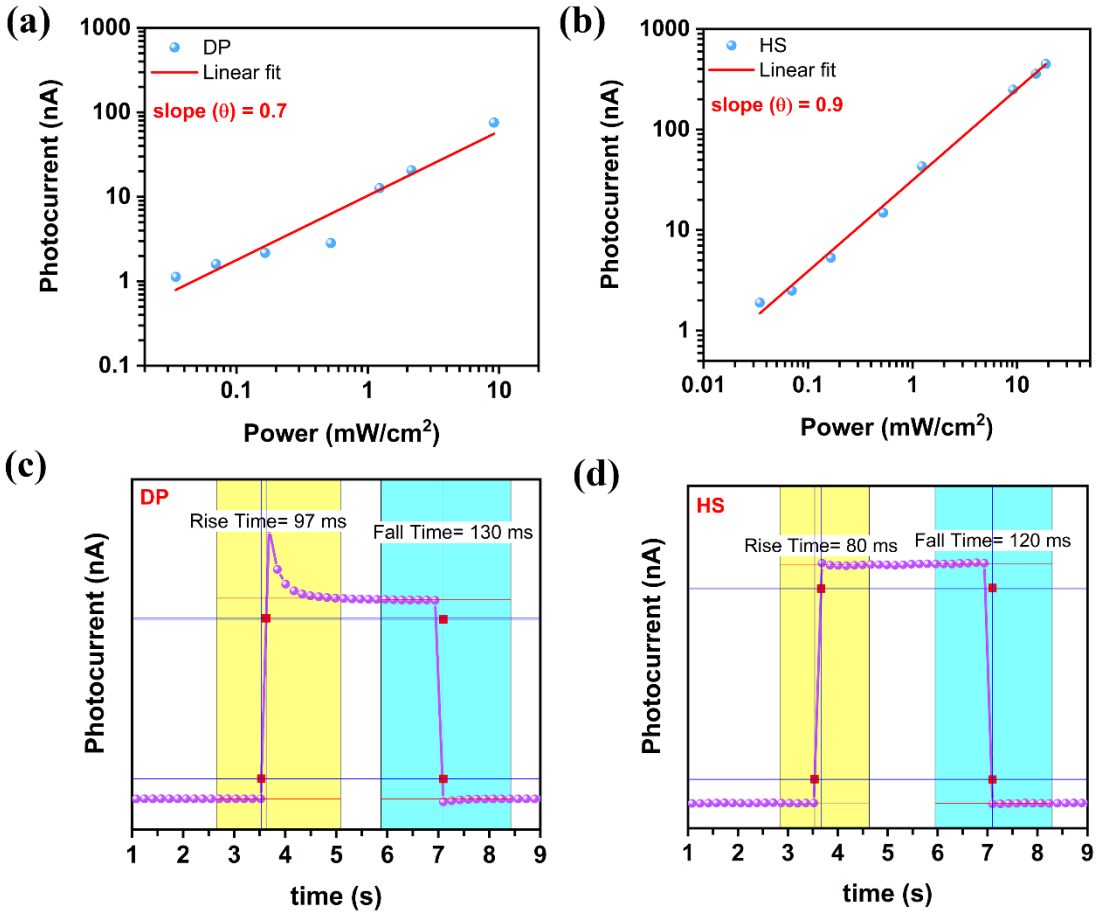

Fig. 3.16: (a, b) Behaviour of photocurrent of $Cs_2AgBiBr_6$ DP and $Cs_2AgBiBr_6/WS_2$ heterostructure under different intensity illumination. The symbols represent the experimental data points, and the solid line displays the linear fitting of the data points. **(c)** Photocurrent rise and fall time profiles of $Cs_2AgBiBr_6$ DP. **(d)** Photocurrent response speed of the $Cs_2AgBiBr_6/WS_2$ heterostructure device.

A desirable characteristic of a photodetector across a wide range of light intensities is consistent responsivity to incident light. This characteristic is referred to as Linear Dynamic Range (LDR). Our device exhibits a high LDR value of 75 dB calculated using the following equation[57]

$$LDR = 20\log\left(\frac{I_{ph}}{I_{dark}}\right) \quad (6)$$

Where I_{ph} and I_{dark} are the current values under light and dark conditions. This high value of LDR can be attributed to the strong light-matter interaction observed in the $Cs_2AgBiBr_6/WS_2$ heterostructure, which is crucial for detecting both strong and weak light in practical applications.[16] Also, the $Cs_2AgBiBr_6/WS_2$ heterostructure exhibits fast photoresponse in comparison to the bare $Cs_2AgBiBr_6$ DP device.

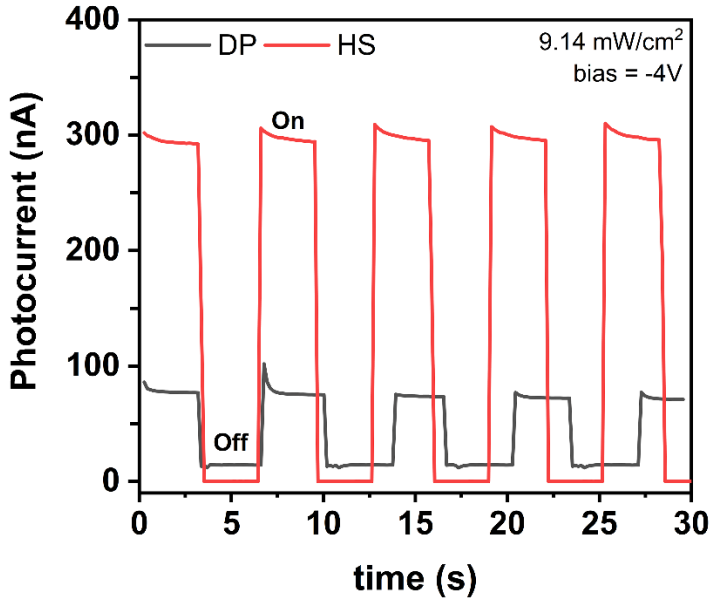

Fig. 3.17: Comparison of photocurrent response of $Cs_2AgBiBr_6$ DP and $Cs_2AgBiBr_6/WS_2$heterostructure under identical conditions.

The rise time and decay time of the $Cs_2AgBiBr_6/WS_2$ heterostructure were measured as 80 ms and 120 ms, respectively, showing a faster response than the bare $Cs_2AgBiBr_6$ DP device (**Fig. 3.16(c, d)**). We have compared the on/off ratio of $Cs_2AgBiBr_6$ DP and $Cs_2AgBiBr_6/WS_2$ heterostructure (**Fig. 3.17**). A significant enhancement (~100 times) in the on/off ratio is observed in the $Cs_2AgBiBr_6/WS_2$ heterostructure. Such a high on/off ratio in $Cs_2AgBiBr_6/WS_2$ heterostructure is attributed to the minimized self-trapped emission, suppressed dark current, and efficient charge transport at the interface, confirmed by the PL quenching and reduced recombination decay time in $Cs_2AgBiBr_6/WS_2$ heterostructure.

3.5 Conclusions

We have effectively showcased a rapid, surfactant/ligand-free, and easily scalable mechanochemical method for synthesizing $Cs_2AgBiBr_6$ DP nanosheets and the in-situ growth of $Cs_2AgBiBr_6/WS_2$ heterostructure. The phase of the $Cs_2AgBiBr_6$ DP and its heterostructure with WS_2 were intact, as confirmed by the XRD measurements. The TEM and SAED analysis

confirmed that the small-sized $Cs_2AgBiBr_6$ DP nanosheets were decorated over larger WS_2 nanosheets. Raman studies display the signature of both $Cs_2AgBiBr_6$ DP and WS_2 in the heterostructure. Raman shifts in the A_{1g} and E_{2g} modes of WS_2 in the heterostructure confirmed the electron transfer into WS_2 and lattice strain due to milling. Significant enhancement in absorption, drastic PL quenching, and reduced carrier decay time are responsible for enhanced charge transport and superior photoresponse by the $Cs_2AgBiBr_6/WS_2$ heterostructure. It was demonstrated that the STE emission is exceptionally reduced in the heterostructure due to the involvement of intermediate energy levels of WS_2 nanosheets. XPS measurements confirmed the highly pure phase growth of $Cs_2AgBiBr_6$ DP and WS_2 nanosheets. XPS analysis showed an increase in electron density in WS_2 after heterojunction formation due to the charge transfer from the DP. A specific planar heterostructure device was fabricated using an e-beam lithography technique with gold electrodes. A significant enhancement in photocurrent is observed in the $Cs_2AgBiBr_6/WS_2$ heterostructure. The dark current in the heterostructure was also suppressed by two orders of magnitude due to the depletion region and Schottky barrier at $Au/Cs_2AgBiBr_6/WS_2$ interface. The $Cs_2AgBiBr_6/WS_2$ heterostructure exhibits significant responsivity of 2.01 A/W, a high detectivity value ~ 3.6×10^{13} Jones, a high light-to-dark current ratio 5.9×10^{3}, and a nearly linear response with incident intensity. The rise and fall time of the device are obtained as 80 ms/120 ms. A high LDR value of 75 dB suggests the capability of the $Cs_2AgBiBr_6/WS_2$ heterostructure device to detect weak and strong light signals for practical use. These findings suggest that incorporating TMDCs with perovskites can effectively broaden their functionality, thereby improving the performance of nano-scale optoelectronic devices utilizing nanomaterials.

References

1 L. Protesescu, S. Yakunin, M. I. Bodnarchuk, F. Krieg, R. Caputo, C. H. Hendon, R. X. Yang, A. Walsh and M. V. Kovalenko, *Nano Lett*, 2015, **15**, 3692–3696.

2 G. R. Yettapu, D. Talukdar, S. Sarkar, A. Swarnkar, A. Nag, P. Ghosh and P. Mandal, *Nano Lett*, 2016, **16**, 4838–4848.

3 G. P. Nagabhushana, R. Shivaramaiah and A. Navrotsky, *Proc Natl Acad Sci U S A*, 2016, **113**, 7717–7721.

4 X. Zhang, Z. Li, E. Hong, M. Deng, L. Su and X. Fang, *Adv Funct Mater*, , DOI:10.1002/adfm.202312293.

5 E. Hong, Z. Li, X. Zhang, X. Fan and X. Fang, *Advanced Materials*, , DOI:10.1002/adma.202400365.

6 T. Yan, Z. Li, L. Su, L. Wu and X. Fang, *Adv Funct Mater*, , DOI:10.1002/adfm.202302746.

7 X. Deng, Z. Li, F. Cao, E. Hong and X. Fang, *Adv Funct Mater*, , DOI:10.1002/adfm.202213334.

8 G. Volonakis, M. R. Filip, A. A. Haghighirad, N. Sakai, B. Wenger, H. J. Snaith and F. Giustino, *Journal of Physical Chemistry Letters*, 2016, **7**, 1254–1259.

9 H. Chen, C. Wu, R. Li and H. Chen, *Crystals (Basel)*, , DOI:10.3390/cryst11091101.

10 Z. Zhang, Y. Liang, H. Huang, X. Liu, Q. Li, L. Chen and D. Xu, *Angewandte Chemie*, 2019, **131**, 7341–7345.

11 H. Li, F. Li, Z. Shen, S. T. Han, J. Chen, C. Dong, C. Chen, Y. Zhou and M. Wang, *Nano Today*, 2021, 37.

12 C. Wu, B. Du, W. Luo, Y. Liu, T. Li, D. Wang, X. Guo, H. Ting, Z. Fang, S. Wang, Z. Chen, Y. Chen and L. Xiao, *Adv Opt Mater*, , DOI:10.1002/adom.201800811.

13 Q. Hu, Z. Deng, M. Hu, A. Zhao, Y. Zhang, Z. Tan, G. Niu, H. Wu and J. Tang, *Sci China Chem*, 2018, **61**, 1581–1586.

14 A. Dey, A. F. Richter, T. Debnath, H. Huang, L. Polavarapu and J. Feldmann, *ACS Nano*, 2020, **14**, 5855–5861.

15 F. Schmitz, N. Lago, L. Fagiolari, J. Burkhart, A. Cester, A. Polo, M. Prato, G. Meneghesso, S. Gross, F. Bella, F. Lamberti and T. Gatti, *ChemSusChem*, , DOI:10.1002/cssc.202201590.

16 F. Fang, Y. Wan, H. Li, S. Fang, F. Huang, B. Zhou, K. Jiang, V. Tung, L. J. Li and Y. Shi, *ACS Nano*, 2022, **16**, 3985–3993.

17 H. Zhang, *ACS Nano*, 2015, **9**, 9451–9469.

18 A. K. Mia, M. Meyyappan and P. K. Giri, *Biosensors (Basel)*, 2023, 13.

19 Q. Li, J. Lu, P. Gupta and M. Qiu, *Adv Opt Mater*, 2019, 7.

20 X. Song, X. Liu, D. Yu, C. Huo, J. Ji, X. Li, S. Zhang, Y. Zou, G. Zhu, Y. Wang, M. Wu, A. Xie and H. Zeng, *ACS Appl Mater Interfaces*, 2018, **10**, 2801–2809.

21 Q. H. Wang, K. Kalantar-Zadeh, A. Kis, J. N. Coleman and M. S. Strano, *Nat Nanotechnol*, 2012, 7, 699–712.

22 Q. Liu, X. Wang, J. Wang and X. Huang, *Wuli Huaxue Xuebao/ Acta Physico - Chimica Sinica*, 2019, 35, 1099–1111.

23 S. Muduli, P. Pandey, G. Devatha, R. Babar, T. M, D. C. Kothari, M. Kabir, P. P. Pillai and S. Ogale, *Angewandte Chemie*, 2018, **130**, 7808–7812.

24 L. Wang, X. Zou, J. Lin, J. Jiang, Y. Liu, X. Liu, X. Zhao, Y. F. Liu, J. C. Ho and L. Liao, *ACS Nano*, 2019, **13**, 4804–4813.

25 Y. Wu, P. Wang, X. Zhu, Q. Zhang, Z. Wang, Y. Liu, G. Zou, Y. Dai, M. H. Whangbo and B. Huang, *Advanced Materials*, , DOI:10.1002/adma.201704342.

26 C. Wu, B. Du, W. Luo, Y. Liu, T. Li, D. Wang, X. Guo, H. Ting, Z. Fang, S. Wang, Z. Chen, Y. Chen and L. Xiao, *Adv Opt Mater*, , DOI:10.1002/adom.201800811.

27 F. Fang, H. Li, S. Fang, B. Zhou, F. Huang, C. Ma, Y. Wan, S. Jiang, Y. Wang, B. Tian and Y. Shi, *Adv Opt Mater*, , DOI:10.1002/adom.202001930.

28 L. Z. Lei, Z. F. Shi, Y. Li, Z. Z. Ma, F. Zhang, T. T. Xu, Y. T. Tian, D. Wu, X. J. Li and G. T. Du, *J Mater Chem C Mater*, 2018, **6**, 7982–7988.

29 J. Song, L. Xu, J. Li, J. Xue, Y. Dong, X. Li and H. Zeng, *Advanced Materials*, 2016, **28**, 4861–4869.

30 Y. Wang, L. Song, Y. Chen and W. Huang, *ACS Photonics*, 2020, **7**, 10–28.

31 C. Fang, H. Wang, Z. Shen, H. Shen, S. Wang, J. Ma, J. Wang, H. Luo and D. Li, *ACS Appl Mater Interfaces*, 2019, **11**, 8419–8427.

32 S. Kumar, I. Hassan, M. Regue, S. Gonzalez-Carrero, E. Rattner, M. A. Isaacs and S. Eslava, *J Mater Chem A Mater*, 2021, **9**, 12179–12187.

33 B. Yang, W. Pan, H. Wu, G. Niu, J. H. Yuan, K. H. Xue, L. Yin, X. Du, X. S. Miao, X. Yang, Q. Xie and J. Tang, *Nat Commun*, , DOI:10.1038/s41467-019-09968-3.

34 A. K. Mia, A. Bora, M. T. Hossain, S. Sinha and P. K. Giri, *J Mater Chem B*, 2023, **11**, 10206–10217.

35 R. Chahal, A. Bora and P. K. Giri, *ACS Appl Energy Mater*, 2023, **6**, 8794–8807.

36 H. Zeng, G. Bin Liu, J. Dai, Y. Yan, B. Zhu, R. He, L. Xie, S. Xu, X. Chen, W. Yao and X. Cui, *Sci Rep*, , DOI:10.1038/srep01608.

37 S. J. Zelewski, J. M. Urban, A. Surrente, D. K. Maude, A. Kuc, L. Schade, R. D. Johnson, M. Dollmann, P. K. Nayak, H. J. Snaith, P. Radaelli, R. Kudrawiec, R. J. Nicholas, P. Plochocka and M. Baranowski, *J Mater Chem C Mater*, 2019, **7**, 8350–8356.

38 C. Lan, C. Li, J. C. Ho and Y. Liu, *Adv Electron Mater*, 2021, 7.

39 P. Hou, W. Yang, N. Wan, Z. Fang, J. Zheng, M. Shang, D. Fu, Z. Yang and W. Yang, *J Mater Chem C Mater*, 2021, **9**, 9659–9669.

40 M. Shi, G. Li, W. Tian, S. Jin, X. Tao, Y. Jiang, E. A. Pidko, R. Li and C. Li, *Advanced Materials*, , DOI:10.1002/adma.202002137.

41 T. Wang, D. Yue, X. Li and Y. Zhao, *Appl Catal B*, , DOI:10.1016/j.apcatb.2019.118399.

42 Z. L. Liu, R. R. Liu, Y. F. Mu, Y. X. Feng, G. X. Dong, M. Zhang and T. B. Lu, *Solar RRL*, , DOI:10.1002/solr.202000691.

43 A. Bora, L. P. L. Mawlong, A. K. Mia and P. K. Giri, *ACS Appl Nano Mater*, , DOI:10.1021/acsanm.3c06043.

44 Y. T. Yeh, Y. Tang, Z. Lin, K. Fujisawa, Y. Lei, Y. Zhou, C. Rotella, A. L. Elías, S. Y. Zheng, Y. Mao, Z. Liu, H. Lu and M. Terrones, *Advanced Materials*, , DOI:10.1002/adma.201703321.

45 B. Wu, W. Ning, Q. Xu, M. Manjappa, M. Feng, S. Ye, J. Fu, S. Lie, T. Yin, F. Wang, T. Wee Goh, P. Cholakkal Harikesh, Y. Kang Eugene Tay, Z. Xiang Shen, F. Huang, R. Singh, G. Zhou, F. Gao and T. Chien Sum, *Strong self-trapping by deformation potential limits photovoltaic performance in bismuth double perovskite*, 2021, vol. 7.

46 Z. Li, H. Li, K. Jiang, D. Ding, J. Li, C. Ma, S. Jiang, Y. Wang, T. D. Anthopoulos and Y. Shi, *ACS Appl Mater Interfaces*, 2019, **11**, 40204–40213.

47 H. Lei, D. Hardy and F. Gao, *Adv Funct Mater*, 2021, 31.

48 F. Ji, J. Klarbring, F. Wang, W. Ning, L. Wang, C. Yin, J. S. M. Figueroa, C. K. Christensen, M. Etter, T. Ederth, L. Sun, S. I. Simak, I. A. Abrikosov and F. Gao, *Angewandte Chemie - International Edition*, 2020, **59**, 15191–15194.

49 H. Lei, D. Hardy and F. Gao, *Adv Funct Mater*, 2021, 31.

50 J. Ghosh, L. P. L. Mawlong, G. B. Manasa, A. J. Pattison, W. Theis, S. Chakraborty and P. K. Giri, *J Mater Chem C Mater*, 2020, **8**, 8917–8934.

51 Z. Zhang, Q. Sun, Y. Lu, F. Lu, X. Mu, S. H. Wei and M. Sui, *Nat Commun*, , DOI:10.1038/s41467-022-31016-w.

52 M. Ghasemi, L. Zhang, J. H. Yun, M. Hao, D. He, P. Chen, Y. Bai, T. Lin, M. Xiao, A. Du, M. Lyu and L. Wang, *Adv Funct Mater*, , DOI:10.1002/adfm.202002342.

53 A. K. Mia, M. Meyyappan and P. K. Giri, *Nanoscale*, 2024, **16**, 8583–8596.

54 J. D. Yao, Z. Q. Zheng, J. M. Shao and G. W. Yang, *Nanoscale*, 2015, **7**, 14974–14981.

55 R. Yang, S. Feng, J. Xiang, Z. Jia, C. Mu, F. Wen and Z. Liu, *ACS Appl Mater Interfaces*, 2017, **9**, 42001–42010.

56 L. Zeng, L. Tao, C. Tang, B. Zhou, H. Long, Y. Chai, S. P. Lau and Y. H. Tsang, *Sci Rep*, , DOI:10.1038/srep20343.

57 J. Ghosh and P. K. Giri, *JPhys Materials*, 2021, 4.

58 L. Yang, Y. Li, W. Zhang, Y. Liu, J. Cao, Y. Cao, J. Bao, Z. Wang, L. Wang and X. Huang, *Chemical Communications*, 2022, **58**, 7765–7768.

59 Q. Wang, Q. Zhang, X. Luo, J. Wang, R. Zhu, Q. Liang, L. Zhang, J. Z. Yong, C. P. Yu Wong, G. Eda, J. H. Smet and A. T. S. Wee, *ACS Appl Mater Interfaces*, 2020, **12**, 45235–45242.

Chapter 4 Lead-free Halide Double Perovskites Nanoflakes as High-Performance SERS Substrates for Detection of Trace Organic Pollutants: Chemical Enhancement versus Field Enhancement Effects

Besides the conventional optoelectronic applications, perovskite semiconductors have been utilized in Surface-enhanced Raman Scattering (SERS) applications. SERS enables ultrasensitive molecular detection, but conventional Pb-based perovskite substrates suffer from toxicity and instability. To address this, we synthesized a lead-free double perovskite $Cs_2AgBiBr_6$ substrate and optimized self-trapped exciton (STE) defects via post-synthesis annealing under an Argon atmosphere to control defect-assisted charge transfer. The optimized substrate achieved remarkable SERS performance, detecting Methylene blue (MB) and Rhodamine 6G (R6G) at 10^{-10} M with enhancement factors of 5.04×10^7 and 1.37×10^7, respectively. Strong amplification was also observed for other cationic dyes, Crystal violet (CV), Rhodamine b (RhB), and Malachite green (MG). Finite element simulations and DFT analysis revealed the different contributions from chemical and electromagnetic enhancement. Notably, the $Cs_2AgBiBr_6$ substrate exhibited long-term stability, maintaining SERS activity after four months in ambient conditions. These results demonstrate the potential of $Cs_2AgBiBr_6$ as a highly efficient, stable, and metal-free SERS platform for advanced sensing and environmental monitoring applications.

4.1 Introduction

Surface-enhanced Raman spectroscopy (SERS) is known for its advantages, such as non-destructive testing, extremely high sensitivity, molecular vibrational fingerprinting, and multiplex detection. It has emerged as a widely utilized spectroscopic technique in chemical and biological sensing and environmental monitoring.[1–5] This enhancement occurs when analytes adsorb onto specific metal nanostructures, like gold and silver nanoparticles.[6–15] Numerous studies employ substrates containing these metallic nanostructures for SERS-based detection. For instance, silver (Ag) nanoparticles are often thermally deposited on glass substrates to create effective SERS platforms.[16,17] Nonetheless, SERS measurements on bare Ag substrates frequently encounter unwanted background noise, which can impede the accurate detection of analytes at low concentrations.[17] Recently, semiconductors or metal-semiconductor hybrid materials, such as Ag-perovskite nanostructures, have been added to the range of SERS-active materials traditionally limited to metals. These materials can serve as

alternatives to, or enhancements for, conventional metallic substrates, providing robust platforms for SERS applications. A key advantage of semiconductors over metals lies in their tunable SERS activity, which can be finely adjusted by manipulating factors like particle size, shape, doping level, defects, band structure, and crystal phase.[18–20]

Perovskite stands out among semiconductors for its unique properties like tunable bandgap, strong light absorption, high carrier mobility, and cost-effectiveness, making it an ideal material for active layers in various optoelectronic applications such as solar cells,[21,22] light-emitting diodes,[23–25] and photodetectors.[26–28] Numerous research teams have successfully developed perovskite- or metal-perovskite-based substrates with effective SERS detection capabilities.[29] The charge transfer enhancement mechanism, driven by chemical interaction between adsorbed molecules and semiconductor substrates at the interface, is considered a key factor in enhancing the SERS signal. Notably, lead-based perovskite materials have shown significant promise as novel SERS substrates in recent developments, which opens new ways in the chemical enhancement of the SERS mechanism. However, the toxicity of lead still hampers the implication of lead-based perovskites in environmental applications. Recently, all inorganic lead-free halide double perovskites have garnered much attention towards optoelectronic applications owing to their low toxicity and high stability, which makes them a better replacement for lead (Pb).[30,31] The chemical formula of the double perovskite is described as $A_2BB'X_6$ where A is a heavy metal cation (Cs^+, MA^+, FA^+, Rb^+), B belongs to the monovalent cation (Na^+, K^+, Ag^+), B' is a trivalent cation (Bi^{3+}, Sb^{3+}, Tb^{3+}, Ce^{3+}, Eu^{3+}), and X belongs to the halogen group (Cl^-, Br^-, I^-). Besides solar cell applications, double perovskites hold great potential for other applications like X-ray detectors,[32] biosensing,[33] neuromorphic computing,[34] etc.

In this study, we have employed $Cs_2AgBiBr_6$ double perovskite (DP) as a SERS substrate for the detection of organic pollutants, such as Methylene blue (MB), Malachite green (MG), Rhodamine 6G (R6G), Crystal violet (CV), and Rhodamine B (RhB). We show that the charge transfer between DP and organic molecules is the main mechanism behind the high SERS enhancement. The interaction between the organic molecules and the DP was studied via photoluminescence (PL) and absorption spectroscopy. Raman, XPS analysis, and ultraviolet photoelectron spectroscopy (UPS) analyzed the charge transfer mechanism. Further, the charge transfer mechanism was confirmed with the help of theoretical simulations, which aligns well with our experimental results. A high enhancement factor of $\sim 5.04 \times 10^7$ and a high sensitivity of 10^{-10} M were measured for the MB molecule. Similarly, the enhancement factor obtained for

other dyes is ≥ 10^5. These findings demonstrate a substantial improvement over lead-based perovskite materials and their plasmonic heterostructures incorporating noble metals. This advancement paves the way for lead-free halide double perovskites, which serve as highly sensitive SERS substrates while exhibiting excellent stability, cost-effectiveness, and non-toxicity.

4.2 Experimental Section

4.2.1 Chemicals

Silver bromide (AgBr, >99.99%, Sigma Aldrich), Bismuth bromide ($BiBr_3$, >99%, Sigma Aldrich), Cesium bromide (CsBr, >99.99%, Sigma Aldrich), Hydrobromic acid (HBr, 47%, >99.9%, Sigma Aldrich). MB, RhB, CV, MG, R6G.

4.2.2 Preparation of $Cs_2AgBiBr_6$ DP SERS substrate

The space-confined method was utilized to synthesize $Cs_2AgBiBr_6$ DP samples.[35] To prepare the precursor solution, CsBr (53 mg), $BiBr_3$ (56 mg), and AgBr (24 mg) were dissolved in 5 mL HBr. After a two-hour reaction at 120 °C, the solution was completely transparent. A bare SiO_2 substrate (1×1 cm^2) was positioned on top of a plasma-treated sapphire substrate (0.8 × 0.8 cm^2) that had been treated at 50 W Ar plasma for 10 minutes. A drop of the precursor solution (40 µL, 0.04 M) was drop-casted on a sapphire substrate, and the SiO_2 substrate was put firmly on top. The entire assembly was then heated for 24 hours at 70 °C on the hot plate. To ensure the optimal contact between the sapphire substrate and DP samples, the temperature was gradually decreased to room temperature over approximately one hour. The two substrates were subsequently separated, resulting in the formation of triangular-shaped DP on the sapphire substrate. During the heating process (24 hours), an external pressure of 20 kPa (achievable through applying appropriate weights) was exerted on the entire assembly (sapphire/precursor/SiO_2) to further constrain the growth environment, facilitating the growth of 2D $Cs_2AgBiBr_6$ flakes. This approach is promising for the advancement of DP semiconductors for SERS applications. The resulting $Cs_2AgBiBr_6$ DP has a lateral size of ~ 10-40 µm, and variable thickness down to 20 nm, obtained by exerting 20 kPa pressure and precursor concentration of 0.04 M. The solution containing different dyes for sensing was prepared by dissolving appropriate amounts of organic dyes into DI water to prepare different molar concentrations. The solution was then drop-casted on the DP substrate and heated at 80 °C for 30 minutes.

4.3 Characterization Tools

The materials' phase and crystal structure were characterized using an X-ray diffractometer (Rigaku RINT 2500 TRAX III) with Cu Kα radiation. The morphology and elemental analysis of the $Cs_2AgBiBr_6$ DP were examined using a JEOL JSM-7610F field emission scanning electron microscope (FESEM). Elemental composition analysis of the $Cs_2AgBiBr_6$ DP was performed with X-ray photoelectron spectroscopy (XPS) (Ulvac-phi, Inc.), employing an Al Kα X-ray beam (1486.6 eV) at 20 kV and 84 W, with high-resolution XPS spectra fitted using XPS Peak Fit 4.1 software. UV-visible diffused reflectance spectroscopy (DRS) spectra were acquired using a PerkinElmer Lambda950 spectrometer. The thickness of the nanoflakes was measured by atomic force microscopy (Cypher, Oxford Instruments). At room temperature, photoluminescence (PL) measurements of the $Cs_2AgBiBr_6$ DP were conducted with a 488 nm laser excitation source using a high-resolution micro-Raman system (LabRam HR800, Jobin Yvon). The laser power used for the PL mapping was 0.124 μW, and the acquisition time was set for 1 second. Raman and SERS investigations were conducted using the same spectrometer (LabRam HR800, Jobin Yvon) with laser excitation sources at 532 nm and 633 nm. All SERS measurements were performed with a 100x objective lens, a 1800 grating per mm, and a laser power of 0.42 mW to prevent laser-induced damage. The acquisition time for all the Raman measurements was set to 5 s.

4.4 Computational Details

The charge transfer characteristics were evaluated through density functional theory (DFT) calculations using plane wave basis sets in Quantum Espresso.[36–38] Core electrons were represented with ultrasoft pseudopotentials (USPP),[39] while the exchange-correlation potential was modeled using the Perdew-Burke-Ernzerhof (PBE)[40] functional within the generalized gradient approximation (GGA). The plane wave cutoff energy was set to 62 Ry, with a force convergence criterion of 0.001 eV/Å, and the energy convergence cutoff was set to 1×10^{-5} for improved accuracy.

To model molecular adsorption on the surface of a DP, a slab geometry was constructed along the (111) direction with a 20 Å vacuum layer added to minimize interactions with neighboring atoms. The choice of (111) direction was dictated by the observed growth orientation of the DP flakes. Charge density difference isosurfaces were visualized in VESTA software, using the formula:

$$\Delta\rho_{cdd} = \rho_{Cs_2AgBiBr_6/MeB} - \rho_{Cs_2AgBiBr_6} - \rho_{MeB}$$

where $\Delta\rho_{cdd}$ represents the charge density difference, $\rho_{Cs_2AgBiBr_6/MeB}$ is the total charge density of the $Cs_2AgBiBr_6$ surface with the adsorbed molecule (MeB), $\rho_{Cs_2AgBiBr_6}$ is the charge density of the $Cs_2AgBiBr_6$ surface alone, and ρ_{MeB} is the charge density of the molecule in isolation.

4.5 FEM Simulations

Finite Element Method (FEM) simulations were performed using the CST Microwave Studio design environment. The dielectric dispersion characteristics of $Cs_2AgBiBr_6$ were imported from the study by Jöbsis et al.[41] A perfectly matched layer (PML) boundary condition was applied along the Z direction, while electric and magnetic field boundary conditions were set along the Y and X directions, respectively. The thickness of the synthesized perovskite structure was determined based on Atomic Force Microscopy (AFM) measurements. To ensure improved accuracy, adaptive tetrahedral meshing was employed in the simulations.

4.6 Results and Discussions

4.6.1 Morphology Analysis

A schematic representation of the space-confined methodology for the synthesis of $Cs_2AgBiBr_6$ DP is presented in **Fig. 4.1(a)**. Details regarding the sample fabrication process can be found in the experimental section. The hexagonal arrangement of sapphire's in-plane lattice characteristics, surface inertness, and atomic flatness render it an ideal van der Waals (vdW) epitaxial substrate for developing 2D materials. The confined space is created using a hydrophilic substrate (plasma-treated sapphire) in conjunction with hydrophobic SiO_2. The wetting properties of hydrobromic acid on sapphire significantly surpass those on SiO_2, leading to the preferential growth of $Cs_2AgBiBr_6$ DP on sapphire. Sapphire has a crystal structure characterized by the space group R-3c (a=4.76 Å, c=12.99 Å), while $Cs_2AgBiBr_6$ DP is indexed to the cubic phase with the space group $fm\bar{3}m$ (a=11.25 Å). The lattice mismatch factor at the interface is reported to be 3.6% between $Cs_2AgBiBr_6$ (111) and sapphire (0001).[35] Therefore, $Cs_2AgBiBr_6$ DP aligns well with the sapphire, making the sapphire an ideal substrate for the epitaxial growth of $Cs_2AgBiBr_6$ DP. The triangular morphology of the as-grown $Cs_2AgBiBr_6$ double perovskite (DP) can be attributed to epitaxial growth, surface energy minimization, and kinetic factors. Triangular structures commonly emerge to minimize the total surface energy during crystal formation. In a system favoring a layer-by-layer (2D) growth mode, the edges of triangular islands correspond to energetically favorable low-energy facets, as reported in

various studies[35]. This indicates that the sapphire substrate orientation plays a crucial role in the formation of triangular 2D $Cs_2AgBiBr_6$ DP.

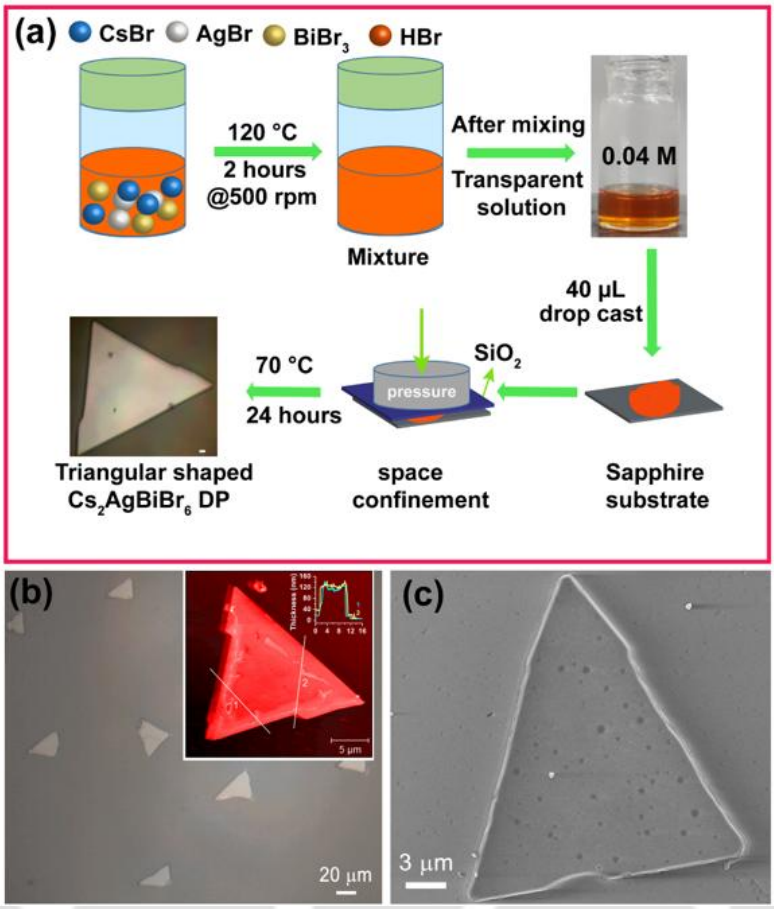

Fig. 4.1: **(a)** Schematic illustration of the space-confinement method for the growth of $Cs_2AgBiBr_6$ DP. **(b)** Optical image of triangular-shaped $Cs_2AgBiBr_6$ DP. The inset shows the AFM image of the DP flakes with the corresponding height profile of the $Cs_2AgBiBr_6$ DP flake. **(c)** The magnified FESEM image of the Cs2AgBiBr6 DP flake.

The concentration of the precursor solution and the pressure applied to the substrates are the primary factors affecting the thickness and size of $Cs_2AgBiBr_6$ DP.[42] **Fig. 4.1(b)** illustrates the optical image of the as-synthesized $Cs_2AgBiBr_6$ DP flakes. To determine the thickness of these flakes, atomic force microscopy (AFM) measurements were performed. The inset presents the AFM image of the $Cs_2AgBiBr_6$ DP, with the thickness of the DP flake estimated to be approximately 100 nm. The corresponding height profile of the scanned area is included. Additionally, field emission scanning electron microscopy (FESEM) was employed to study the morphology of the $Cs_2AgBiBr_6$ DP flakes. **Fig. 4.1(c)** shows the FESEM image of a single large triangular $Cs_2AgBiBr_6$ DP flake. Circular dots are visible on the surface of the larger triangles, likely residues from the HBr solvent used during synthesis. The FESEM image

confirms the formation of triangular-shaped $Cs_2AgBiBr_6$ DP over a large area, as shown in **Fig. 4.2(a).** The lateral size of these triangular flakes ranges from approximately 10 to 40 µm. However, along with the larger triangles, smaller and thinner triangles were also observed, likely due to the non-uniform pressure applied during the substrate preparation process.

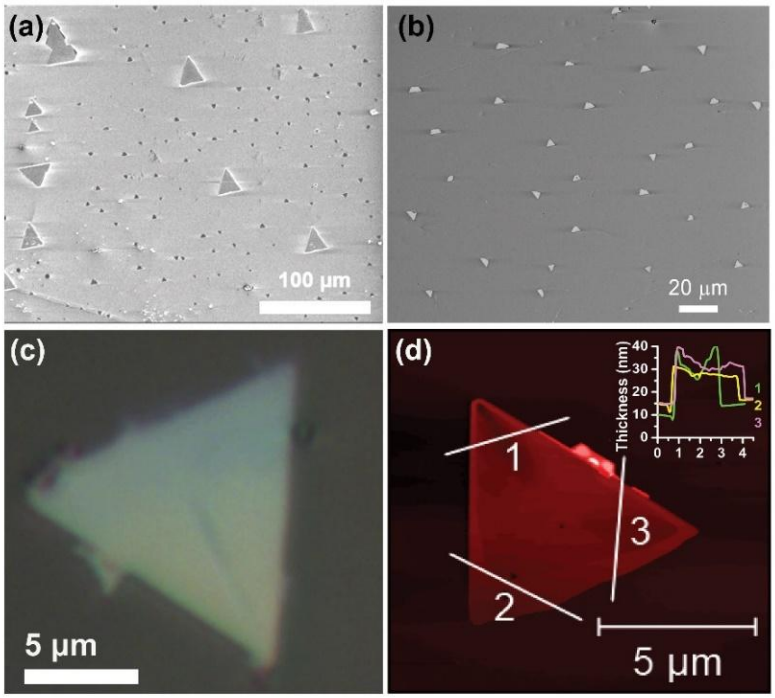

Fig. 4.2: (a) FESEM image of the large area uniform growth of $Cs_2AgBiBr_6$ DP flakes prepared by the space-confinement method. **(b)** shows the magnified FESEM image. **(c)** Optical image of the smaller triangles of $CS_2AgBiBr_6$ DP flakes. **(d)** AFM image of 2D $Cs_2AgBiBr_6$ DP flake. The inset shows the height profile of the corresponding flake.

Fig. 4.2(b) provides an enlarged FESEM image of the thinner triangular flakes, while **Fig. 4.2(c)** depicts an optical image of the smaller triangular $Cs_2AgBiBr_6$ DP flakes. The corresponding AFM image is shown in **Fig. 4.2(d)**, with a height profile indicating a thickness optimization of approximately 20 nm, which is referred to as 2D $Cs_2AgBiBr_6$ DP. The chemical composition of the $Cs_2AgBiBr_6$ DP was analyzed using energy-dispersive X-ray spectroscopy (EDX). The elemental distribution maps for Cs, Ag, Bi, and Br are shown in **Fig. 4.3(a),** revealing a uniform distribution of elements across the $Cs_2AgBiBr_6$ nanoflake, indicative of high purity with no detectable impurities. Furthermore, **Fig. 4.3(b)** presents the FESEM-EDX image of the MB dye adsorbed on the Cs2AgBiBr6 DP flake. Elemental mapping reveals a uniform distribution of the $Cs_2AgBiBr_6$ DP's constituent elements, along with sulfur from the MB analyte, confirming the uniform adsorption of the dye on the flake surface.

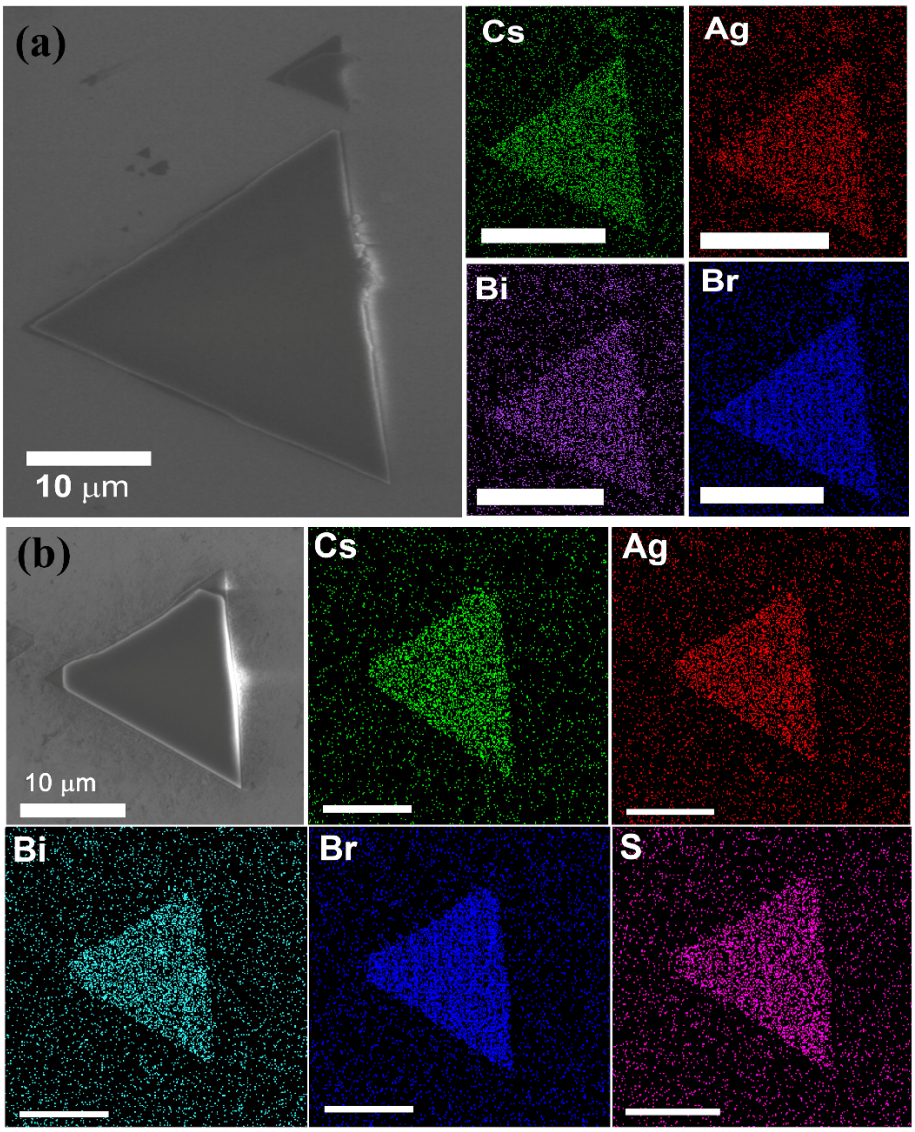

Fig. 4.3: (a) The FESEM-EDX image of the $Cs_2AgBiBr_6$ DP flakes with the elemental mapping of each element of $Cs_2AgBiBr_6$ DP. **(b)** FESEM-EDX elemental mapping of each constituent element of the $Cs_2AgBiBr_6$/MB complex. The scale bar in elemental mapping is 10 μm.

4.6.2 Structural Analysis

The crystal phase of the synthesized $Cs_2AgBiBr_6$ DP was validated through X-ray diffraction analysis. As illustrated in **Fig. 4.4(a)**, the prominent peaks associated with (111), (222), and (333) planes closely match the reported results, confirming the phase purity and (111) orientation of the crystal.[42] The inset shows the magnified view of the (333) crystal plane. **Fig. 4.4(b)** displays the Raman spectra of $Cs_2AgBiBr_6$ DP flakes with varying thickness. The Raman peak around 179 cm^{-1} corresponds to the A_{1g} longitudinal optical (LO) phonon mode, while the two lower frequency peaks, at approximately 135 cm^{-1} and 74 cm^{-1}, are attributed to vibrational

modes with E_{1g} and T_{2g} symmetries, respectively, confirming the successful synthesis of $Cs_2AgBiBr_6$ DP.[43]

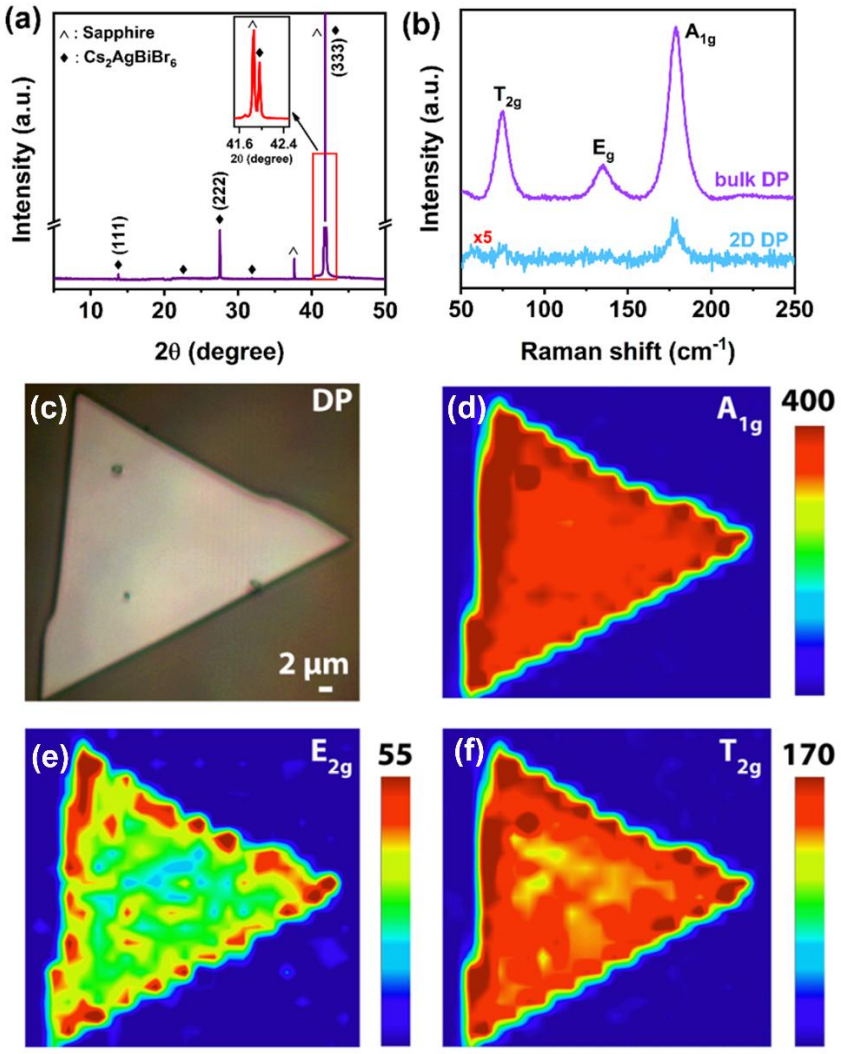

Fig. 4.4: (a) The XRD pattern of as-synthesized $Cs_2AgBiBr_6$ DP flakes. The inset shows a magnified peak indicated by a red box. **(b)** The Raman spectra of $Cs_2AgBiBr_6$ DP flakes for different thicknesses. Bulk spectra correspond to the DP flakes with ~100 nm thickness, and blue spectra correspond to a thickness of ~20 nm. **(c)** Optical image of the $Cs_2AgBiBr_6$ DP flake. **(d-f)** Raman mapping of all three characteristic Raman peaks of $Cs_2AgBiBr_6$ DP flake.

The E_{1g} mode is associated with the asymmetric stretching of Br atoms around Bi, while the T_{2g} mode involves the scissoring motion of Br atoms along with the coordinated motion of Cs atoms. No obvious shift was observed in the peak position of 2D $Cs_2AgBiBr_6$ flakes compared to the bulk counterparts. However, the intensity of 2D $Cs_2AgBiBr_6$ DP significantly reduces due to a reduction in the phonon density. Raman mapping was conducted using an excitation laser source of 532 nm to confirm the uniformity of the sample (**Fig. 4.4(c-f)**). The uniform

distribution of all three characteristic peaks was observed in DP flakes, indicating the high-purity growth of DP. However, we observed high intensity of Raman modes at the edges of the DP flakes, which can be ascribed to the electrostatic potential fluctuations at the edges of DP.[35]

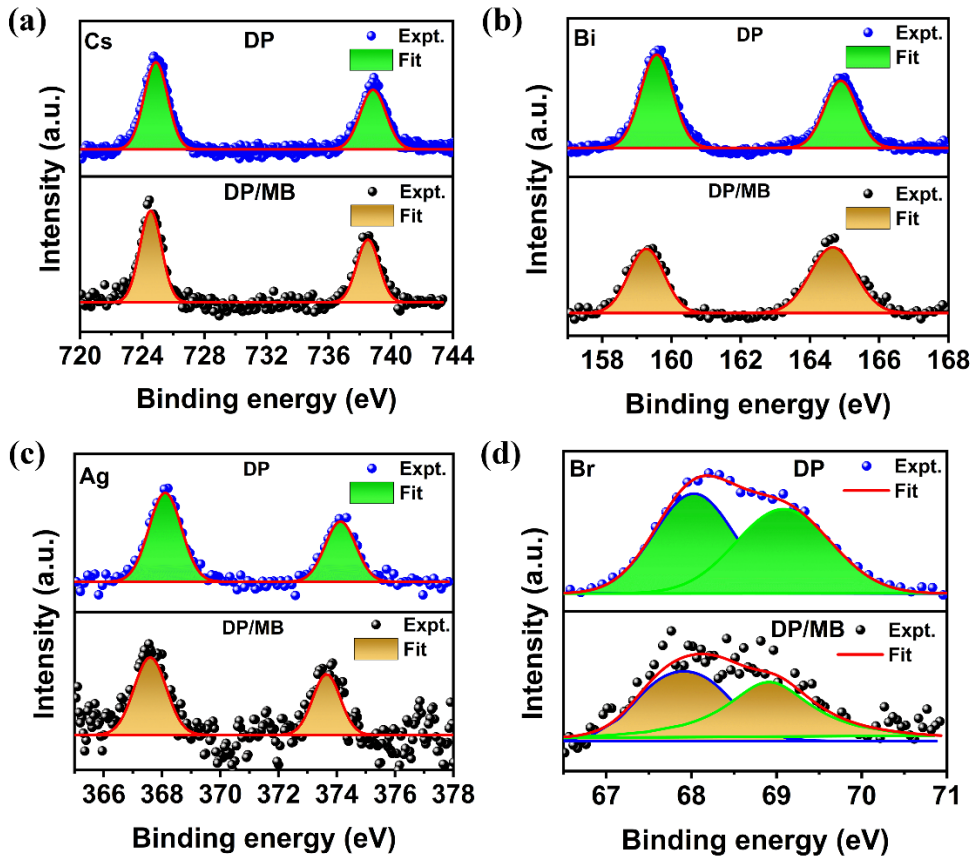

Fig. 4.5: (a-d) The high-resolution XPS spectra of Cs, Bi, Ag, and Br elements, respectively, in $Cs_2AgBiBr_6$ and $Cs_2AgBiBr_6$/MB flakes.

X-ray photoelectron spectroscopy (XPS) measurements were performed to analyze the chemical composition and charge transfer between the DP and the adsorbed analyte. High-resolution XPS spectra of Cs, Ag, Bi, and Br are presented in **Fig. 4.5(a-d),** showing no impurity peaks in the DP sample after absorption of methylene blue (MB) on the DP sample. **Fig. 4.5** illustrates the high-resolution XPS spectra of pristine $Cs_2AgBiBr_6$ DP, indicating the phase-pure growth of $Cs_2AgBiBr_6$ DP.[44] **Table 4.1** summarizes the binding energy peak positions and full width at half maximum (FWHM) values for DP before and after dye adsorption. Notably, there is a shift towards lower binding energy in DP following dye adsorption, indicating a charge transport pathway from the MB analyte to the $Cs_2AgBiBr_6$ DP.[44] Additionally, ultraviolet photoelectron spectroscopy (UPS) was conducted to find the valence

band and conduction band values of the DP, providing insights into its band structure, which will be discussed in later sections.

Table 4.1. Binding energies of $Cs_2AgBiBr_6$ DP sample before and after adsorption of methylene blue analyte obtained from XPS analysis.

Sample / Elements		DP (eV)	FWHM (eV)	DP/MB (eV)	FWHM (eV)	Shift (eV)
Cesium	$3d_{3/2}$	724.87	1.7	724.53	1.6	0.34
	$3d_{5/2}$	738.84	1.9	738.51	1.7	0.33
Silver	$3d_{3/2}$	368.01	1.3	367.59	1.3	0.42
	$3d_{5/2}$	374.12	1.2	373.64	1.1	0.48
Bismuth	$4f_{5/2}$	159.27	1.2	159.14	1.1	0.13
	$4f_{7/2}$	164.65	1.5	164.45	1.1	0.25
Bromine	$3d_{3/2}$	68.09	1.2	68.03	1.1	0.06
	$3d_{5/3}$	69.07	1.3	69.02	1.2	0.05

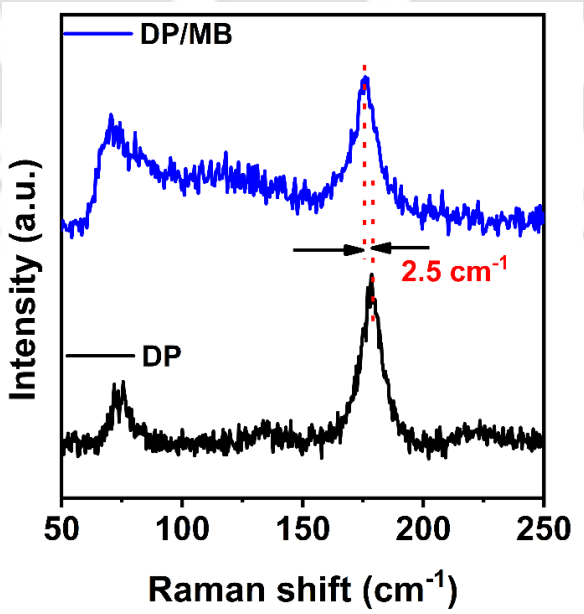

Fig. 4.6: Comparison of Raman spectra of $Cs_2AgBiBr_6$ DP before and after MB adsorption.

Fig. 4.6 represents the Raman spectra of $Cs_2AgBiBr_6$ DP before and after adsorption of the MB analyte. Notably, no obvious change in the Raman spectra was observed before and after dye adsorption, confirming the phase stability of the DP. Furthermore, a significant red shift (~2.5 cm^{-1}) was observed in the A_{1g} mode of DP after MB adsorption, indicating the charge transfer from MB to the DP.[44]

4.6.3 Optical Properties

We further investigated the optical properties of $Cs_2AgBiBr_6$ DP nanoflakes before and after analyte adsorption through UV-visible absorption and PL spectroscopy measurements. **Fig. 4.7(a)** shows the absorption spectra of $Cs_2AgBiBr_6$ DP before and after the adsorption of MB and CV analytes on the surface of DP. We observed a hump near 380 nm in the absorption spectra of DP, which might be due to the presence of 2D $Cs_2AgBiBr_6$ nanoflakes within the sample, as confirmed by the FESEM images.[42]

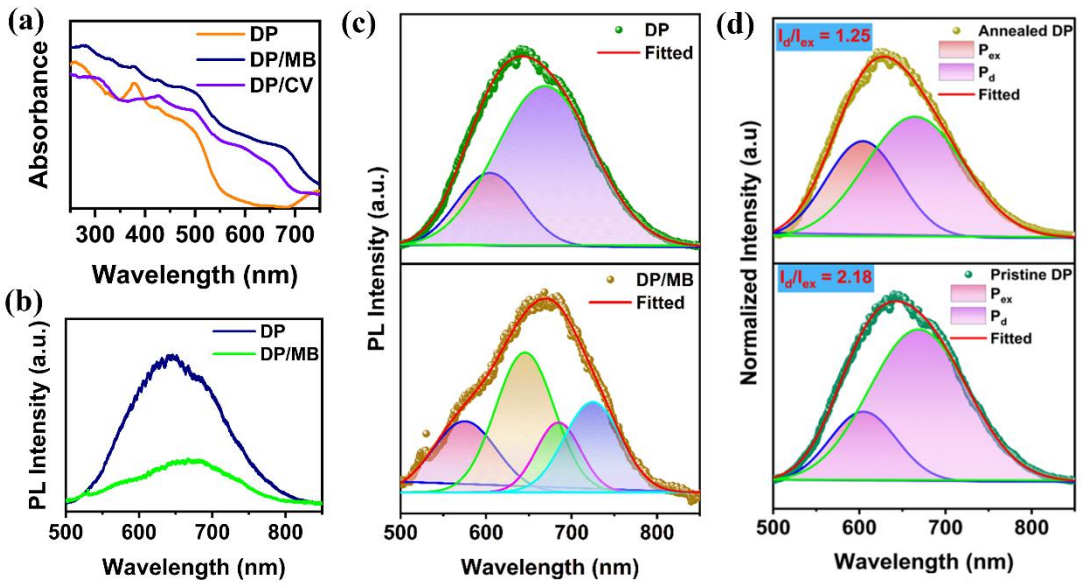

Fig. 4.7: (a) Absorption spectra of pristine $Cs_2AgBiBr_6$ DP and a comparison with different analytes (MB, CV) adsorbed on the DP flakes. **(b)** PL spectra of $Cs_2AgBiBr_6$ DP and $Cs_2AgBiBr_6$ DP/MB complex. **(c)** Depicts the deconvoluted PL spectra of $Cs_2AgBiBr_6$ DP before and after MB adsorption. **(d)** Deconvoluted PL spectra of $Cs_2AgBiBr_6$ DP before and after annealing.

The absorbance of the perovskite after the adsorption of analytes on the flakes was enhanced due to the co-absorption of both materials. However, we see a decreasing trend in the absorption spectra towards higher wavelengths, indicating that the substrate's SERS activity will be low at higher excitation wavelengths. The spectra indicate a clear transition after 500 nm wavelength in the DP/MB and DP/CV samples, similar to the DP sample, confirming the

adsorption of the molecule onto the DP flakes. The bandgap of $Cs_2AgBiBr_6$ DP is obtained as 2.08 eV, consistent with the previous reports.[44] **Fig. 4.7(b)** shows the PL spectra of DP before and after the adsorption of MB. For pristine DP, the PL spectra show a broader and weaker peak distribution, indicating the presence of defects and the indirect bandgap nature of the $Cs_2AgBiBr_6$ DP, respectively. To get more insights into this, we deconvoluted the PL spectra for both pristine and with the MB present at the surface of the sample (**Fig. 4.7(c)**). The PL peaks situated at 604 nm and 668 nm are ascribed to the excitonic and self-trapped exciton emission, respectively, which agrees with the reported literature.[45] The PL of DP quenched significantly after dye adsorption, indicating the charge transfer process between DP and MB analyte. The deconvoluted PL spectra of DP/MB suggested the presence of four peaks, out of which two peaks are associated with the DP's excitonic and self-trapped emission situated at ~645 nm and ~724 nm, respectively. The lower energy peak situated at ~575 nm is associated with the MB emission, which originates from the π-π* transition associated with the resonance of the π electrons present due to sulphur. The higher energy peak at ~ 684 nm is associated with the π-π* transition due to benzene rings.[46] We observed a significant red shift (around ~39 nm) in the PL emission of DP after the adsorption of the analyte, indicating the strong interaction between DP and the adsorbed molecules required for the sensing. The emission from self-trapped excitons (STEs) in the double perovskite (DP) sample can be optimized by reducing the Ag_{Bi} and Bi_{Ag} anti-site defects. To achieve this, the as-grown DP sample was annealed in a chemical vapor deposition (CVD) system under an inert atmosphere. The annealing process was conducted at 120 °C for 80 minutes, with the quartz tube purged with argon gas to minimize contamination by other impurities. PL spectra for both the pristine and annealed samples, recorded under similar conditions, are shown in **Fig. 4.7(d)**. In the spectra, the excitonic emission is denoted as the P_{ex} peak, while the STE emission is labeled as the P_d peak, with corresponding intensities as I_{ex} and I_d, respectively. The ratio of I_d/I_{ex} for the pristine and annealed samples was found to be 2.18 and 1.25, respectively, indicating a reduced contribution of self-trapped states in the annealed DP. The impact of this reduction on the SERS performance of the samples will be discussed in the subsequent sections.

PL mapping of $Cs_2AgBiBr_6$ DP under 488 nm excitation laser reveals location-dependent behavior of the DP flakes as shown in **Fig. 4.8(a)**. PL intensity and peak position vary across the sample, with edges exhibiting stronger PL than the core. This increased PL emission at the edges is attributed to the electrostatic potential fluctuations, consistent with the previous studies showing enhanced geometrical PL at the edges of the perovskite crystals.[35] These potential

fluctuations arise due to structural and charge defects (Ag_{Bi} anti-site vacancies, uncoordinated bonds, structural deformation, etc). The higher PL intensity observed at the edges of the $Cs_2AgBiBr_6$ DP flakes indicates a higher concentration of defects in these regions. **Fig. 4.8(b)** presents the PL mapping of the DP/MB flake. After the adsorption of the analyte, the PL intensity of the DP was significantly quenched, exhibiting consistent behavior across the entire DP flake. Interestingly, the PL mapping reveals a trend of increasing PL intensity moving from the edge toward the center of the flake, which is contrary to the behavior observed in pristine DP flakes. This trend suggests that MB adsorption occurs predominantly at the edges of the flake compared to its core, likely due to the higher defect density at the edges facilitating greater interaction with the analyte.

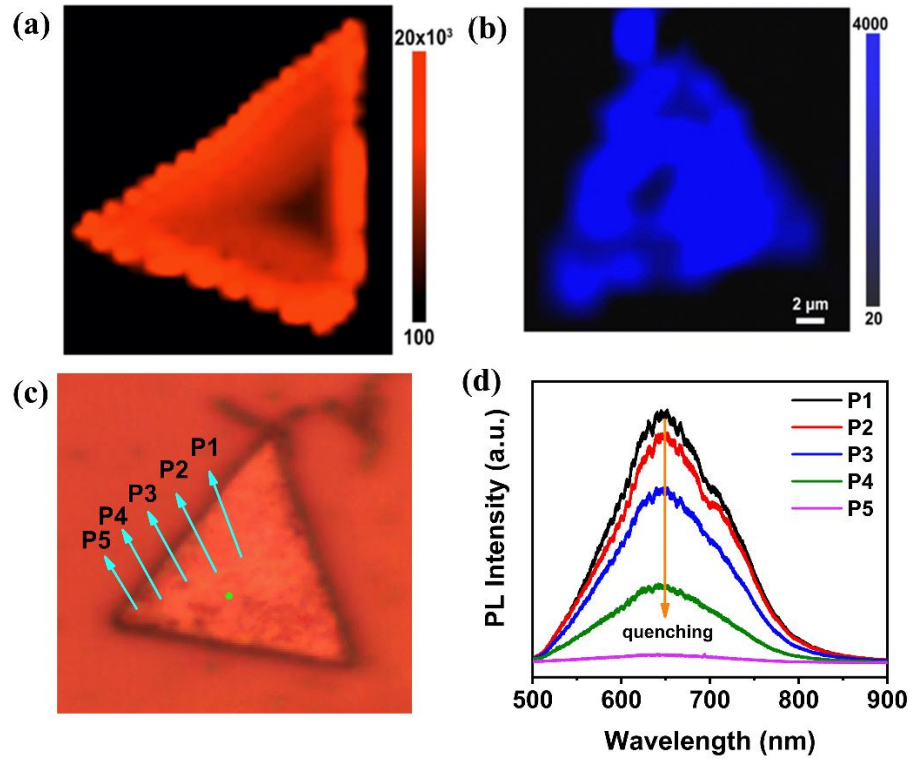

Fig. 4.8: (a) PL mapping of the $Cs_2AgBiBr_6$ DP flake. **(b)** PL mapping of the $Cs_2AgBiBr_6$/MB flake. **(c)** Optical image of the DP/MB flake. Green dots indicate the position of PL spectra obtained at different locations of the flake. **(d)** PL spectra corresponding to the different locations from the centre to the edge of the DP/MB flake, as shown in **Fig. (c)**.

We conducted PL measurements at different positions of the $Cs_2AgBiBr_6$ DP flakes after the adsorption of the analyte onto the sample. **Fig. 4.8(c)** shows the optical image of the $Cs_2AgBiBr_6$ DP flakes with the markings of the PL along different locations. The PL quenching happens when the dye is adsorbed on the DP flake. We observed more quenching of the PL at

the edges of the flake, which suggested that dye adsorption is more prominent at the edges compared to the core, supporting the PL mapping. **Fig. 4.8(d)** represents the PL spectra at the different locations of the flake marked in **Fig. 4.8(c)**. The high quenching at the edges of the flakes indicates that the charge transfer is more at those locations, which concludes that the Raman signal should be stronger at the edges of the flakes compared to the core.

4.6.4 SERS performance of $Cs_2AgBiBr_6$ DP

To evaluate the capability of $Cs_2AgBiBr_6$ DP substrates to detect SERS signals from various chemical species, five samples were randomly selected, containing MB, MG, CV, RhB, and R6G. Each sample produces distinct SERS signals, as shown in **Fig. 4.9**, demonstrating the substrate's versatility in supporting SERS measurements for various chemical species. This highlights the $Cs_2AgBiBr_6$ DP substrate as a stable and reliable platform for SERS applications.

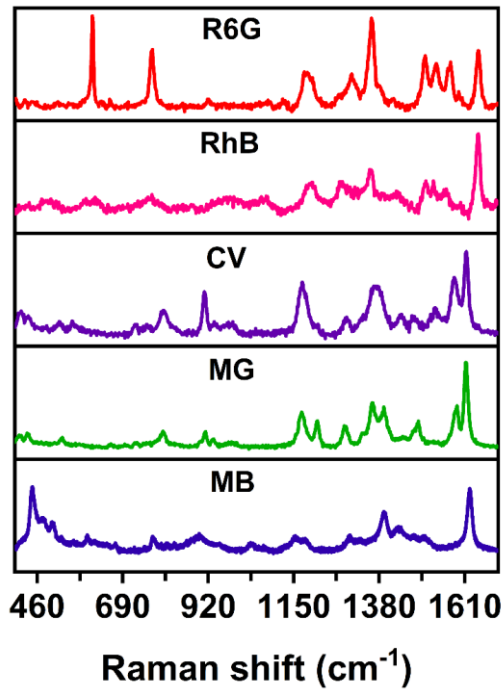

Fig. 4.9: Raman spectra of different analytes adsorbed on the $Cs_2AgBiBr_6$ DP flakes.

Additionally, SERS spectra of 10^{-6} M R6G on $Cs_2AgBiBr_6$ DP substrate with different thicknesses are shown in **Fig. 4.10**. The sample with the higher thickness (~100 nm) is represented as bulk DP/R6G, and the sample with the lower thickness (~20 nm) is described as 2D DP/R6G. Notably, 2D $Cs_2AgBiBr_6$ DP shows clear SERS detection of R6G compared to bulk counterparts, suggesting the high sensitivity of 2D $Cs_2AgBiBr_6$ DP. In addition, SERS spectra of 10^{-4} M MB were collected on different thicknesses (**Fig. 4.11(a)**). We observed no significant change in the intensity of the characteristic peak (1620 cm^{-1}) of MB with

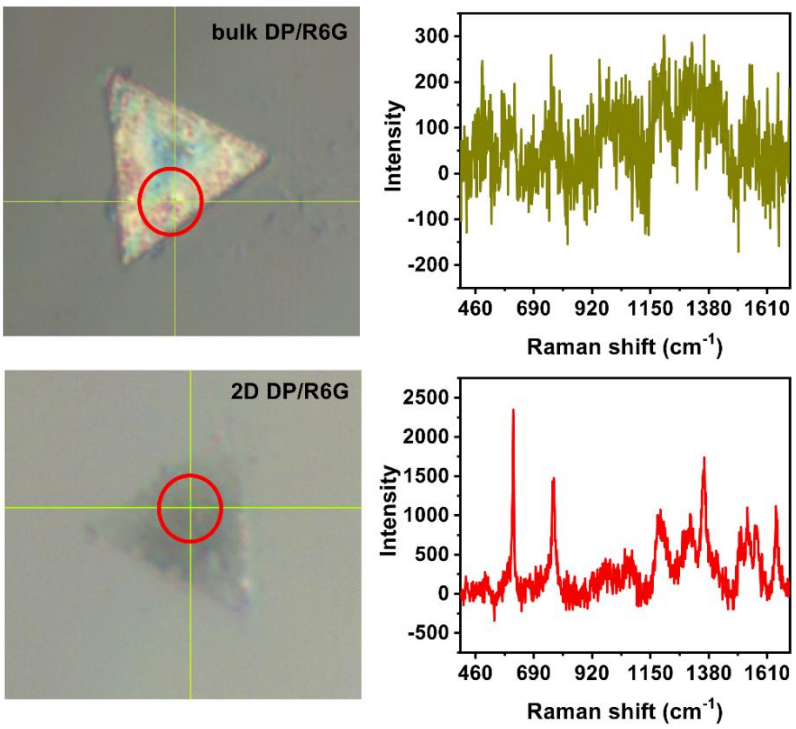

Fig. 4.10: Comparison of the SERS performance of $Cs_2AgBiBr_6$ DP flakes of R6G analyte with varying thicknesses of the DP.

thickness. However, the intensity of the $Cs_2AgBiBr_6$ DP characteristic Raman modes was significantly reduced in the case of lower thickness, suggesting that the SERS signal highly depends upon the nature of the analyte (**Fig. 4.11(b)**).

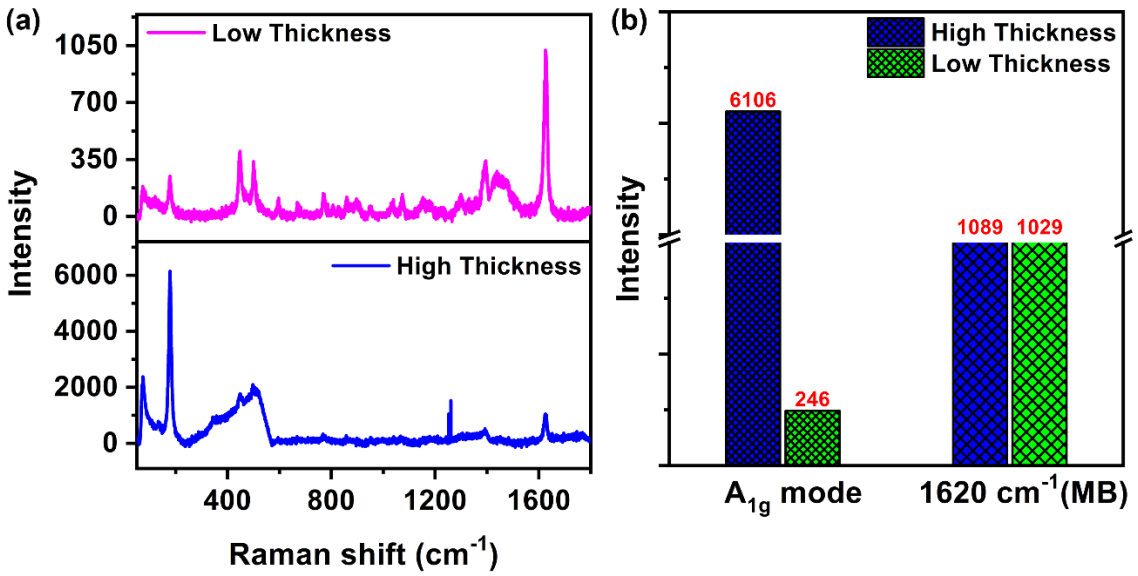

Fig. 4.11: (a) Raman spectra of MB on $Cs_2AgBiBr_6$ DP with varying thicknesses. **(b)** depicts the comparison of the intensities of the A_{1g} mode and the 1620 cm^{-1} mode of MB adsorbed on different thicknesses.

Usually, the SERS performance decreases while the excitation wavelength increases due to the lower absorption intensity of the perovskites at higher wavelengths. Furthermore, we collected the SERS spectra of MB on $Cs_2AgBiBr_6$ DP substrate with different laser excitations like pre-resonance (532 nm), near-resonance (633 nm), and post-resonance (785 nm) (**Fig. 4.12(a)**). The SERS performance of $Cs_2AgBiBr_6$ DP shows high enhancement with 633 nm (1.96 eV) laser excitation due to resonance of the excitation energy with the sub-band gaps of the DP and molecular resonance of the MB molecule (**Fig. 4.12(b)**). However, the 633 nm laser is unable to excite the charge from HOMO to the LUMO of the R6G and RhB analyte.[47] For comparison purposes, all the measurements were conducted using a 532 nm excitation laser source.

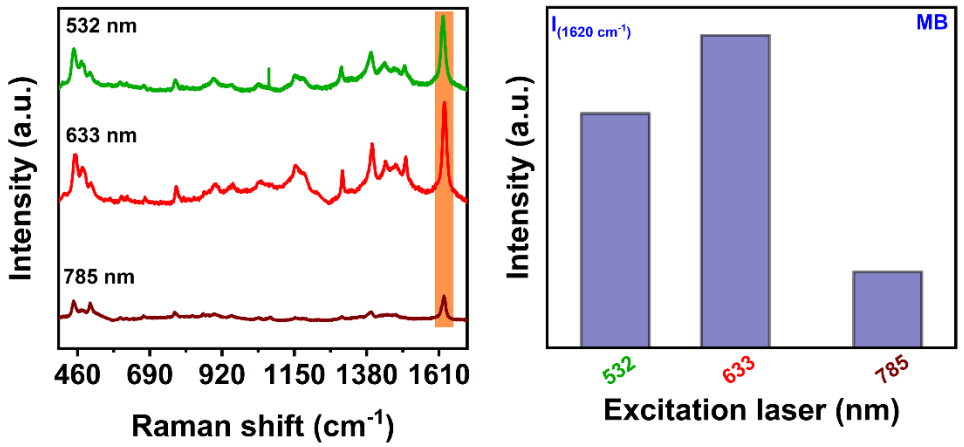

Fig. 4.12: (a) SERS spectra of MB analyte on $Cs_2AgBiBr_6$ DP substrate using different laser excitation sources. **(b)** indicates the intensity of the characteristic mode of the MB analyte with different laser excitation.

The Raman enhancement factor (EF) is the most widely used metric to evaluate the quality of the SERS effect, as it reflects the intensity of an analyte's Raman signal on a SERS substrate. The simplified EF calculation considers factors such as accumulation time, grating, excitation wavelength, and solution concentration, as outlined in prior studies. The EF for $Cs_2AgBiBr_6$ DP flakes can be calculated using the following equation.[48]

$$EF = \frac{I_S}{I_R} \times \frac{C_R}{C_S} \tag{4.1}$$

where I_S represents the intensity (in counts) of the reference Raman peak for the specific dye on the $Cs_2AgBiBr_6$ DP substrate at a particular concentration of C_S; I_R denotes the intensity (in counts) of the reference Raman peak for the dye on the sapphire substrate, and $C_R = 10^{-3}$ M corresponds to the concentration of the dye for measuring I_R. The concentration of the dye for the sapphire substrate is limited by the detection ability of the substrate.

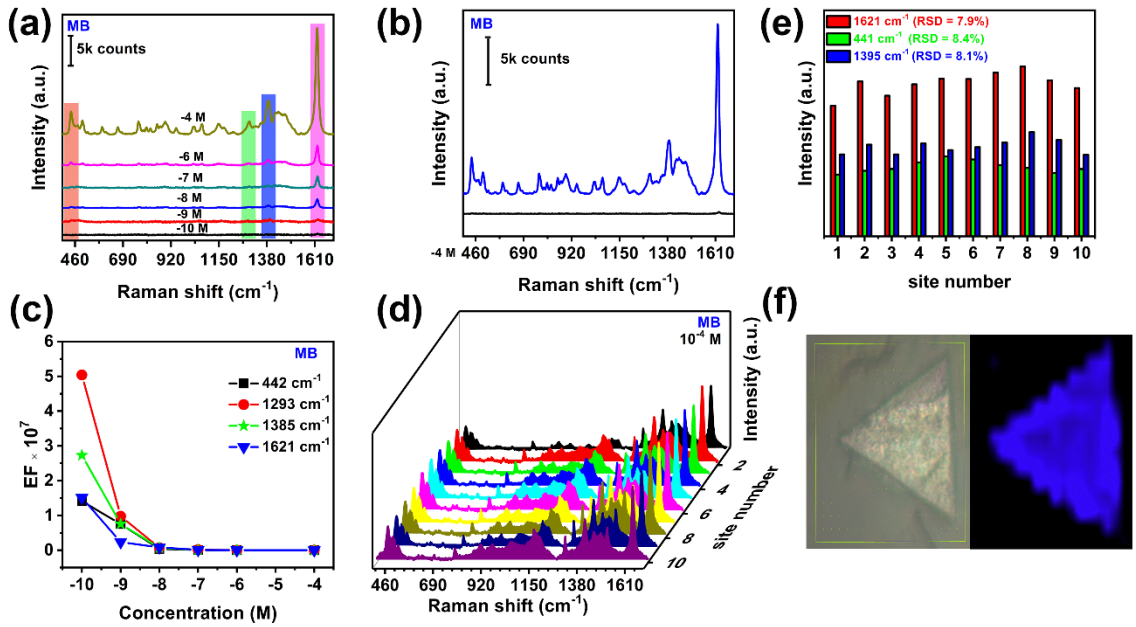

Fig. 4.13: (a) Raman spectra of MB dye at different concentrations on $Cs_2AgBiBr_6$ DP substrate. **(b)** Raman spectra of MB on $Cs_2AgBiBr_6$ DP (10^{-4} M) and Sapphire (10^{-3} M) substrate. **(c)** Comparison of the Enhancement factor for MB at different concentrations for different modes. **(d)** Raman spectra of MB on 10 randomly chosen points on the $Cs_2AgBiBr_6$ DP flake. **(e)** Raman peak intensity fluctuations of the three highest peaks were used to calculate the relative standard deviation. **(f)** Raman mapping of the MB analyte adsorbed on the $Cs_2AgBiBr_6$ DP substrate. The mapping shows the intensity of the characteristic peak of MB (1620 cm^{-1}).

Fig. 4.13(a) shows the Raman spectra of different concentrations of MB on the $Cs_2AgBiBr_6$ DP substrate. Our sample shows outstanding sensitivity of MB up to 10^{-10} molar concentration, making it an ideal substitute for noble metals plasmonic SERS substrates. All the characteristic Raman peaks associated with the MB were present in the spectra, and the modes are listed in **Table 4.2**. **Fig. 4.13(b)** shows the Raman signal of MB on the sapphire substrate (10^{-3} M) and with the DP flakes (10^{-4} M) on the $Cs_2AgBiBr_6$ DP substrate. The bare sapphire substrate alone was able to detect the dye at a concentration of only 10^-3 molar, indicating that the sensitivity of the dye is greatly enhanced by the $Cs_2AgBiBr_6$ DP. **Fig. 4.13(c)** shows the EF of the four characteristic peaks of MB with varying concentrations of the analyte. The EF for the 1293 cm^{-1} peak of the MB (10^{-10} M) dye is the highest among other characteristic peaks, which is approximately 5×10^7. To evaluate the homogeneity and reproducibility of the $Cs_2AgBiBr_6$ DP substrate, Raman signals were monitored at 10 randomly selected active sites after MB adsorption (**Fig. 4.13(d)**). The intensity of Raman spectra at 441 cm^{-1}, 1395 cm^{-1}, and 1620 cm^{-1}, recorded from these 10 locations, is shown in **Fig. 4.13(e)**.

Table 4.2: Comparison of the reported band positions of MB and our SERS spectrum.

Sr. No.	Wavenumber (cm^{-1}) (Reported)	Peak assignment	Obtained SERS spectrum (cm^{-1})
1.	949	C-H in-plane bending	945.6
2.	1067	C-H in-plane bending	1069
3.	1181	C-N stretching	-
4.	1301	β(CH); υ (C-N) $_{Ring}$	1296
5.	1392	C-H in-plane ring deformation	1389
6.	1444	C-N asymmetric stretching	-
7.	1618	C-C ring stretching	1620

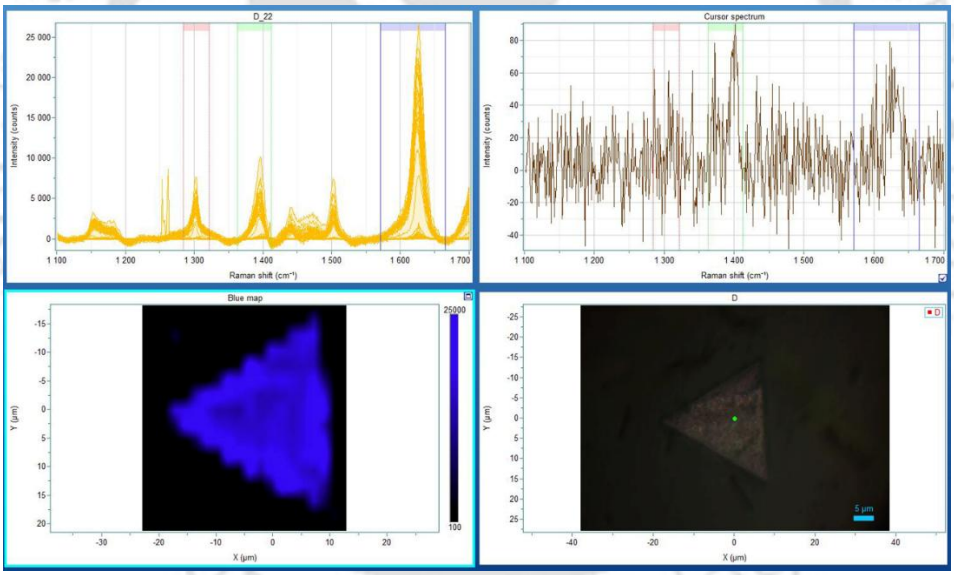

Fig. 4.14: Raw image of the SERS measurement of MB on $Cs_2AgBiBr_6$ DP flake.

The relative standard deviation (RSD) of the SERS signal intensity, representing the ratio of the standard deviation to the mean value, was calculated to quantify signal consistency across the sites, yielding a maximum intensity variation of 8.4% for the 441 cm^{-1} Raman peak. **Fig. 4.13(f)** shows the Raman mapping of the SERS spectra at 1620 cm^{-1}, generated from measurements taken at various locations on the $Cs_2AgBiBr_6$ DP flake. The raw image of the live measurement is shown in **Fig. 4.14**, which indicates a negligible signal from the surrounding region of the DP flakes. Notably, the SERS performance of $Cs_2AgBiBr_6$ DP flakes

shows maximum enhancement at the edges of the flakes compared to their core. This is mainly attributed to the maximum adsorption of the dye on the edges of the flakes, where there are more defects. As discussed earlier, the PL quenching at the edges is more because of the electrostatic potential fluctuations, which act as an active hot spot for the adsorption of the analyte.[49]

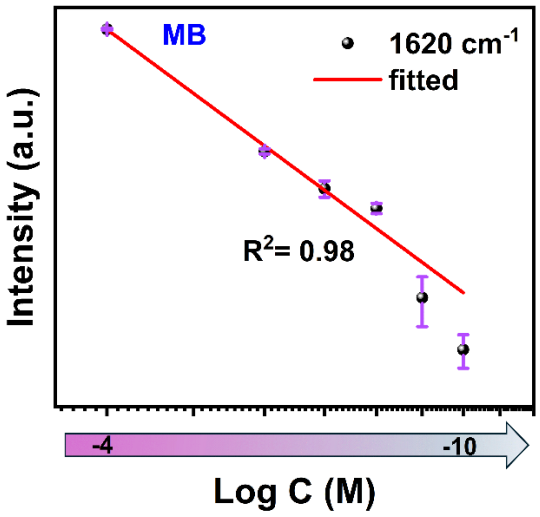

Fig. 4.15: SERS signal intensity of the MB analyte with different molar concentrations.

The SERS performance of $Cs_2AgBiBr_6$ DP was further evaluated to verify the quantitative detection capabilities of the DP. Results indicated a strong linear correlation between the Raman intensity of MB and its logarithmic concentration (log C) with an R^2 value of 0.98 (**Fig. 4.15**). Rhodamine 6G (R6G) was utilized as a probe molecule to evaluate the versatility of the $Cs_2AgBiBr_6$ DP substrate. Raman spectra at various R6G concentrations are displayed in **Fig. 4.16(a)**, with distinctive peaks at 610 cm^{-1} and 770 cm^{-1} detectable even at ultra-low concentrations (10^{-10} M). The substrate's uniformity was confirmed by measuring Raman spectra at 10 randomly chosen active sites (**Fig. 4.16(b)**). Additionally, Raman mapping of the $Cs_2AgBiBr_6$ DP flakes with adsorbed R6G was performed, as shown in **Fig. 4.16(c)**. The Raman mapping revealed high uniformity across the substrate, even at a low concentration of 10^{-6} M, demonstrating the substrate's reproducibility and consistent performance. Interestingly, no SERS signal was detected from the bare sapphire substrate, indicating that molecular adsorption occurred exclusively on the $Cs_2AgBiBr_6$ DP flakes. This selectivity may be attributed to the electrostatic interaction between the DP and the molecule or the moisture-sensitive capability of $Cs_2AgBiBr_6$ DP, which enhances molecule adsorption and SERS signal detection. This property makes $Cs_2AgBiBr_6$ DP a valuable and efficient choice for advanced

SERS applications. The RSD of the SERS signal's intensity for three different peaks is shown in **Fig. 4.16(d)**.

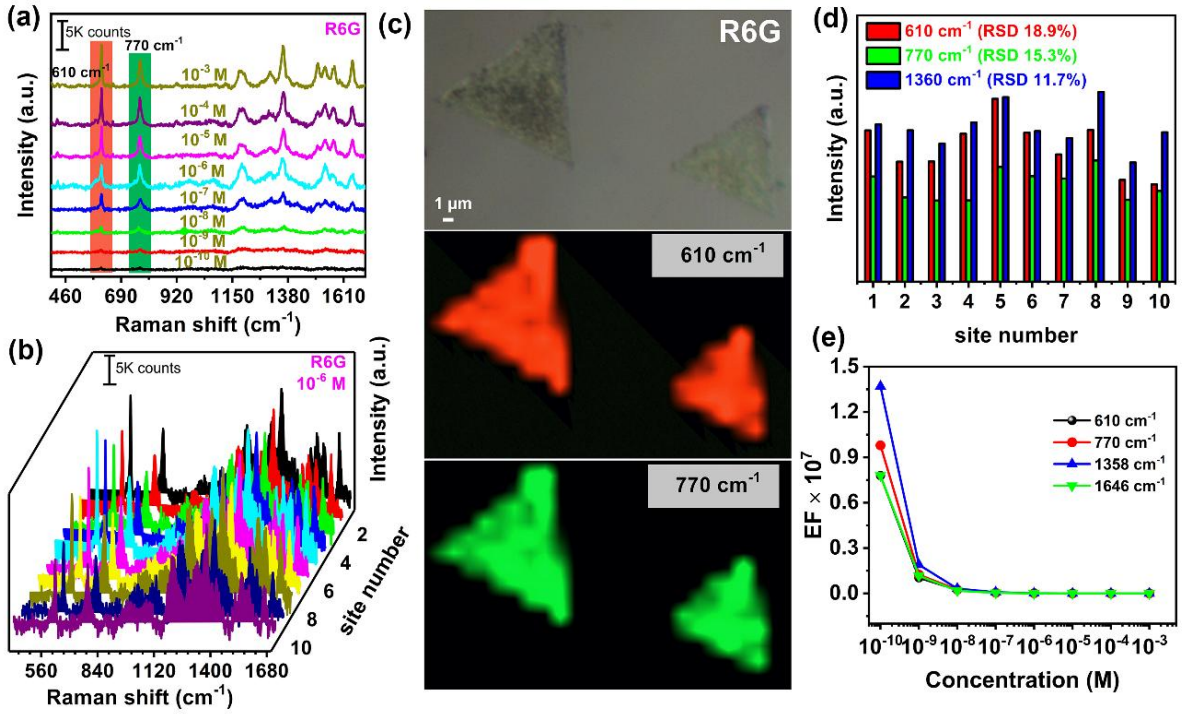

Fig. 4.16: (a) Raman spectra of R6G analyte obtained from different concentrations using $Cs_2AgBiBr_6$ DP. **(b)** Raman spectra taken on 10 different locations on $Cs_2AgBiBr_6$ DP flake with the molar concentration of 10^{-6} M. **(c)** Raman mapping of characteristic modes of R6G analyte (610 cm^{-1}, 770 cm^{-1}) adsorbed on $Cs_2AgBiBr_6$ DP substrate with concentration 10^{-6} M. **(d)** Intensity variation of the highest peaks taken on 10 different locations. **(e)** EF as a function of concentration of the analyte.

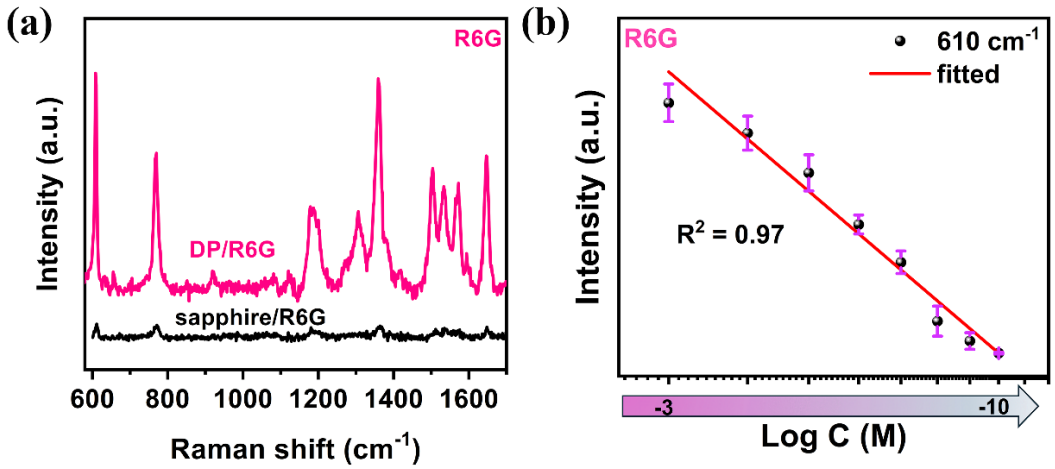

Fig. 4.17: (a) Comparison of the SERS performance of R6G analytes on $Cs_2AgBiBr_6$ DP (10^{-6} M) and sapphire substrates (10^{-3} M). **(b)** Variation of the SERS intensities of the characteristic modes of the R6G molecule with the molar concentrations.

The maximum RSD for the peak at 610 cm^{-1} is calculated as 19.7 % which is marginally higher than the other probe molecule (MB). For the calculation of EF, the Raman spectra were recorded on the bare sapphire substrate and the $Cs_2AgBiBr_6$ DP substrate (**Fig. 4.17(a)**). The EF for the different peaks is shown in **Fig. 4.16(e)**. The highest EF calculated for the peak 1358 cm^{-1} is 1.4 × 10^7, which is significantly higher than the reported perovskite SERS substrates, making $Cs_2AgBiBr_6$ DP a versatile, stable, and highly efficient SERS substrate. As shown in **Fig. 4.17(b)**, the Raman intensity of R6G also exhibits a linear relationship with log C, with an R^2 value of 0.97. The results demonstrate that the synthesized DP substrate exhibits excellent homogeneity, reproducibility, and a low detection limit, even without incorporating any metal nanoparticles, thereby broadening its potential applications as a SERS substrate.

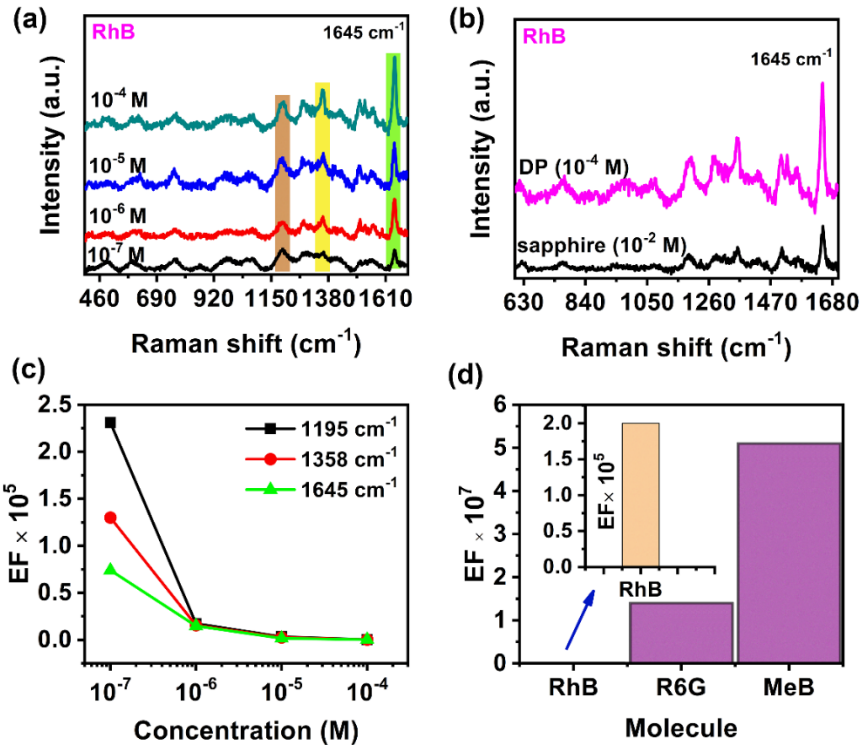

Fig. 4.18: (a) Raman spectra of RhB analyte for different concentrations using $Cs_2AgBiBr_6$ DP substrate. **(b)** Raman spectra of the RhB molecule using $Cs_2AgBiBr_6$ DP substrate and sapphire substrate for 10^{-4} M and 10^{-2} M concentrations, respectively. **(c)** represents the EF for different peak positions of the RhB molecule using the $Cs_2AgBiBr_6$ DP substrate. **(d)** Comparison of the highest EF calculated for different dyes (RhB, R6G, MB).

The sensitivity and EF of the RhB probe molecule still hamper the versatility of many SERS substrates reported earlier. To verify the quantitative SERS performance of $Cs_2AgBiBr_6$ DP, the RhB molecule was studied. The $Cs_2AgBiBr_6$ DP substrate was able to detect the RhB

molecule as low as 10^{-7} M of concentration. **Fig. 4.18(a)** shows the Raman spectra of RhB at different concentrations. The EF was calculated for the different concentrations of the Raman peaks at 1195 cm^{-1}, 1358 cm^{-1}, and 1645 cm^{-1}. **Fig. 4.18(b)** shows the Raman spectra of RhB on a sapphire substrate (10^{-2} M) and $Cs_2AgBiBr_6$ DP substrate (10^{-4} M), indicating the increased SERS performance. The limited sensitivity of RhB might refer to the band alignment of the molecule with the $Cs_2AgBiBr_6$ DP substrate. **Fig. 4.18(c)** shows the EF of the $Cs_2AgBiBr_6$ DP SERS substrate for the RhB molecule for three distinct Raman peaks.

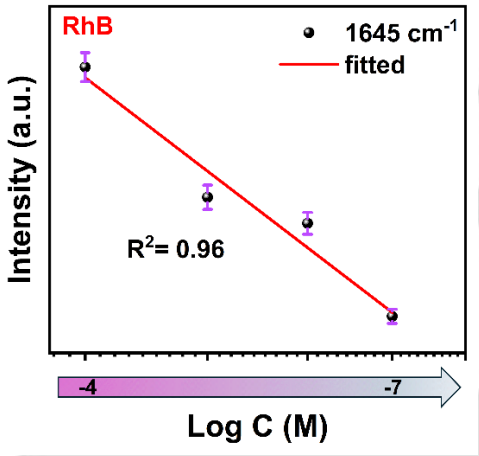

Fig. 4.19: Variation of the SERS signal intensity of the RhB molecule with different molar concentrations.

Table 4.3: Calculation of the EF of different modes of the MB, R6G, and RhB molecules.

Molecules	Peak Position (cm^{-1})	I_S/I_R	C_R/C_S	Enhancement Factor (EF)
MB ($C_S=10^{-10}$ M) ($C_R=10^{-10}$ M)	441	1.41	10^7	1.41×10^7
	1296	5.04	10^7	5.04×10^7
	1386	2.73	10^7	2.73×10^7
	1620	1.15	10^7	1.15×10^7
R6G ($C_S=10^{-10}$ M) ($C_R=10^{-3}$ M)	610	7.8	10^6	7.8×10^6
	766	9.8	10^6	9.8×10^6
	1356	1.37	10^7	1.37×10^7
	1646	7.8	10^6	7.8×10^6
RhB ($C_S=10^{-7}$ M) ($C_R=10^{-2}$ M)	1193	2.31	10^5	2.31×10^5
	1356	1.3	10^5	1.3×10^5
	1645	0.74	10^5	0.74×10^5

Fig. 4.19 indicates the linear relationship between the intensity of the Raman signal and the concentration of the RhB molecule, with an R^2 value of 0.96. Although the sensitivity of RhB is limited, the EF is improved by many folds using the $Cs_2AgBiBr_6$ DP SERS substrate, thereby opening new doors for DPs in sustainable environment materials. **Table 4.3** represents the EF calculations for the different dyes. **Fig. 4.18(d)** shows the comparison of the EF for various molecules. The Raman peaks with the highest EF for the specific peaks are compared, indicating the high SERS performance of $Cs_2AgBiBr_6$ DP for the MB analyte, followed by the R6G and then RhB analytes. Raman mapping of SERS performance of $Cs_2AgBiBr_6$ DP for MG and CV analytes along with the respective optical images is shown in **Fig. 4.20(a-d)**. The mapping shows similar behavior of MG and CV as of other dyes, indicating the uniformity, homogeneity, and versatility of the $Cs_2AgBiBr_6$ DP substrate.

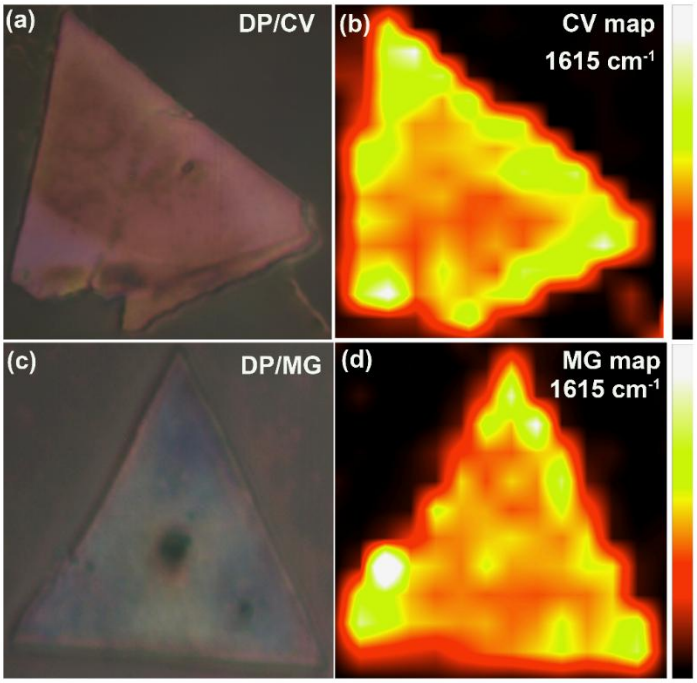

Fig. 4.20: (a, c) shows the $Cs_2AgBiBr_6$ DP flakes with CV and MG adsorbed on the surface, respectively. **(b, d)** shows the Raman mapping of the characteristic modes of CV and MG on the Cs_2AgBiB_6 DP SERS substrate, respectively.

A brief comparison of the performance of perovskite-based SERS substrates is listed in **Table 4.4**. The $Cs_2AgBiBr_6$ DP SERS substrate exhibits the highest enhancement factor (up to 10^7) as compared to the lead-based perovskite substrates and their heterostructures with noble metal plasmonic materials. **Table 4.5** provides a comparison of the SERS performance of $Cs_2AgBiBr_6$ DP with the other non-perovskite-based SERS substrates. These findings provide insightful information that allows lead-free DPs to detect environmental pollutants with

sensitivity comparable to or even higher than some of the most studied materials for SERS applications.

Table 4.4: Comparison of the performance of the reported perovskite-based SERS substrates.

SERS Substrates Type	Substrate Materials	Enhancement Factor	Molecules	References
Perovskite Quantum Dots	$CsPbBr_3$/ZIF-8 composite	1.17×10^5	4-MPY	[55]
Single-Crystalline Perovskite	$MAPBCl_3$	2.6×10^5	4-MPY	[56]
Engineered Perovskite	$CsPb_2Br_5$ Chip (single atom site)	1.08×10^7	R6G	[57]
Perovskite/metal Heterojunction	3D $ZnTiO_3$/Ag nanoparticles	3×10^7	R6G	[58]
	$Au/CsPbBr_3$	5.9×10^6		[59]
Double Perovskites	$Cs_2AgBiBr_6$ DP	5.04×10^7	MB	*This work*
		1.37×10^7	R6G	
		2.31×10^5	RhB	

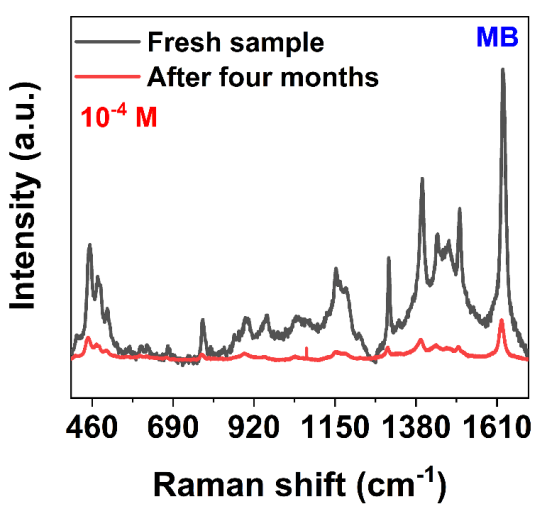

Fig. 4.21: Comparison of the SERS performance of the freshly prepared $Cs_2AgBiBr_6$ DP sample and after storing it for four months in ambient conditions.

The stability of perovskite materials remains a significant challenge for their real-world applications. However, the $Cs_2AgBiBr_6$ DP substrate demonstrated remarkable durability, successfully detecting the MB molecule even after being stored in an ambient environment

with relatively high humidity for four months. **Fig. 4.21** compares the Raman spectra of MB adsorbed on a freshly prepared sample with those obtained from the aged sample. The results indicate that the DP substrate maintains its performance, showcasing superior stability compared to the other perovskite-based SERS substrates. This highlights the potential of $Cs_2AgBiBr_6$ DP for long-term and practical SERS applications.

Table 4.5: Comparison of the SERS performance of $Cs_2AgBiBr_6$ DP with other semiconductor-based SERS substrates.

Substrate material	Molecule	Limit of Detection (LOD) (M)	Enhancement Factor (EFs)	Features	Ref.
$SnSe_2$	R6G	1×10^{-12}	6.33×10^6	Light trapping ability	[60]
1T-WTe_2	R6G	4×10^{-14}	1.8×10^9	Universal capability and stability	[61]
$W_{18}O_{49}$/Monolayer Mos_2	R6G	1×10^{-10}	3.45×10^7	Perfect linear relationship (R^2 = 0.9915)	[62]
Plasma-treated Graphene QDs	RhB	1×10^{-8}	3.67×10^6	Ultra-small size and uniformity	[63]
Defective-Nb_2O_5	MB	1×10^{-8}	5.15×10^7	Plasmon-free and cost-effective	[64]
Oxygen-incorporated MoS_2	R6G	1×10^{-7}	1.4×10^5	Universality and expandability	[65]
2h-WS_2	R6G	1×10^{-7}	NA	Large area	[66]
2D $Cs_2AgBiBr_6$ nanoflakes	MB	1×10^{-10}	5.04×10^7	Uniformity, Large area, cost-effective	*This work*
	R6G	1×10^{-10}	1.37×10^7		
	RhB	1×10^{-7}	2.31×10^5		

4.6.5 SERS Mechanism

The fundamental mechanism of SERS enhancement remains a topic of significant debate. However, chemical enhancement (CM) and electromagnetic enhancement (EM) are two widely recognized mechanisms.[50] EM enhancement primarily arises from the generation of a strong localized electric field around nanostructures when they are activated by an excitation wavelength that matches their resonant plasmon frequency.[51] This effect is particularly prominent in metallic nanostructures due to the presence of abundant conduction electrons, which oscillate coherently with the incident light, amplifying the local electric field. In contrast, CM enhancement is more prevalent in semiconductor-based systems. It is based on the concept

of photo-induced charge transfer resonance, where charge transfer occurs between the energy levels of the molecule and the semiconductor material. This mechanism relies on the alignment of the energy levels between the analyte and the substrate, facilitating resonance interactions that enhance the Raman signal. Raman scattering signals are enhanced due to modifications in electronic states resulting from the interaction between the molecule and the semiconductor.[52] Understanding the precise roles and interplay of the chemical (CM) and electromagnetic (EM) enhancement mechanisms in SERS is still an active area of research. Finite element method (FEM) and DFT simulations were conducted to understand the underlying effect for the high SERS performance of DP.

The defect-related energy levels in the bandgap of the material can significantly affect the SERS performance. In the case of semiconductor-based SERS substrates, it is well known that the SERS performance can be enhanced by many folds through defect engineering in the system.[53] In the present case, to understand the defect-assisted phot-induced charge transfer mechanism, we obtained the SERS spectra of MB on two different samples, as shown in **Fig. 4.22(a, b)**. As explained in the previous sections, the pristine sample contains more STE defects than the annealed sample. Interestingly, the intensity (counts) of the characteristic Raman mode of the MB molecule is reduced significantly from 16k to 4k on the annealed SERS substrate. This huge change in SERS detection confirms that the sample with more defects enhances the SERS activity of the DP substrate. Also, the Raman signal of the molecule is higher at the edges of the DP flakes compared to its core. The defects (in both annealed and pristine samples) are more prominent at the edges of the flakes, which is confirmed by the PL mapping of the DP, due to which the Raman signal at the edges is stronger than that at the core. The relative increment of the Raman signal from center to edge is higher in the defective samples. This establishes the critical role of charge transfer through defects in the enhanced SERS activity of the DP substrate.

Quantifying the STEs and their relation to SERS performance is often difficult in Perovskite materials due to the complex interplay of defects. However, we employed a post-growth annealing process to control the STE concentration and its correlation with SERS performance. We thermally annealed the $Cs_2AgBiBr_6$ DP sample at different temperatures. The samples were annealed at 100, 150, 200, and 250 °C temperature in air for 30 minutes. PL and SERS spectra were collected for all the samples. The overall PL intensity of the DP samples increases with the annealing temperature (**Fig. 4.22(c)**) due to the enhanced crystallinity of the sample, though the relative intensity of the STE peak decreases with respect to the excitonic peak intensity.

Note that for annealing at 250 °C, the overall PL intensity decreased suggesting the thermal degradation of the sample at higher temperatures. We deconvoluted the PL spectra (see **Fig. 4.22(d)**) for each measurement to calculate the relative concentration of STE through the ratio of I_d/I_{ex}, which quantifies the defect concentration in the DP as discussed in the earlier sections.

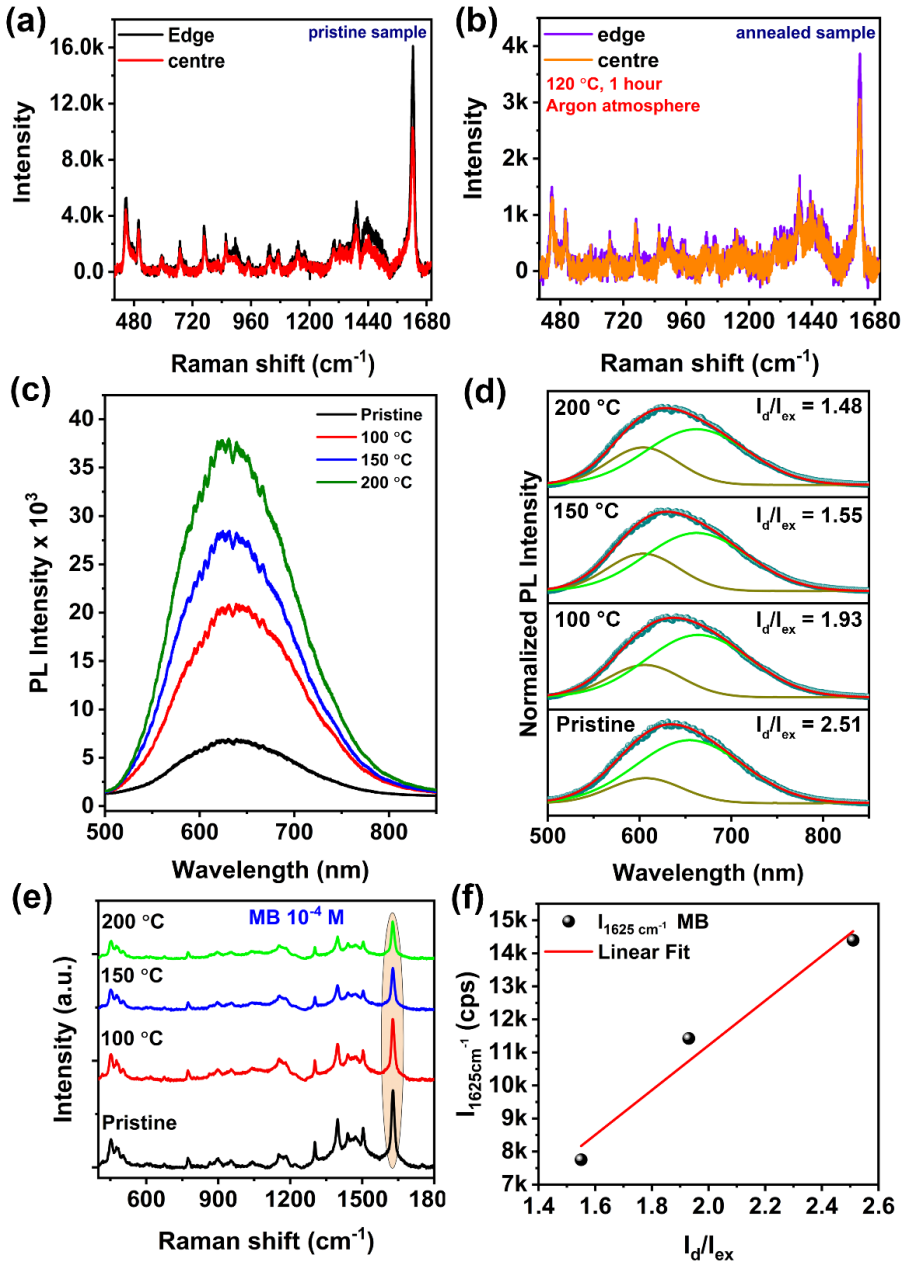

Fig. 4.22: (a) SERS spectra of the MB molecule on the as-grown DP sample in the centre and at the edge. **(b)** The corresponding SERS spectra of the MB molecule on the annealed DP samples. **(c)** PL spectra of $Cs_2AgBiBr_6$ DP after annealing at different temperatures. **(d)** Deconvoluted PL spectra showing the contribution of two peaks and their intensity ratio for different annealing temperatures. **(e)** SERS spectra of MB on $Cs_2AgBiBr_6$ DP substrate annealed at different temperatures. **(f)** Direct correlation between the STE concentration and the SERS intensity of MB on the DP substrate.

The I_d/I_{ex} ratio decreased systematically from 2.51 to 1.48 when annealed from room temperature to 200 °C. SERS spectra for each sample were taken separately for the MB analyte with a concentration of 10^{-4} M (**Fig. 4.22(e)**). The as-grown sample (with the highest defect concentration) showed the highest SERS signal intensity. The SERS intensity systematically decreases with the decrease in the I_d/I_{ex} ratio, confirming that the STEs actively contributed to the charge transfer process. A direct correlation between the defect density and SERS signal intensity of the characteristic peak of MB (~1625 cm^{-1}) is shown in **Fig. 4.22(f)**, which shows a linear behavior, clearly implying that the SERS enhancement is mainly caused by the charge transfer through the defects in the DP flakes.

Furthermore, UPS studies were conducted to investigate the valence band edge position relative to the vacuum level and to understand the charge transfer processes in the $Cs_2AgBiBr_6$ DP/MB complex. The work function was calculated using the formula[52]

$$\phi = h\upsilon - E_{Onset} \quad (2)$$

Where $h\upsilon$ is the photon energy of the He I source (21.2 eV), and E_{Onset} is the secondary electron cut-off energy, determined by extrapolating a tangent to the high binding energy region. To determine the distance between valence band maxima (VBM) and the Fermi level, the linear portion of the spectrum at the low binding energy edge was extrapolated to the energy axis. By analyzing the UPS spectra of $Cs_2AgBiBr_6$ DP, the work function (ϕ) and valence band edge (VB) positions were identified. The conduction band edge (CB) positions were subsequently determined for $Cs_2AgBiBr_6$ DP using the bandgap values obtained from diffuse reflectance spectroscopy (DRS) measurements. For $Cs_2AgBiBr_6$ DP, the VB and CB were located at -6.81 eV and -4.73 eV, respectively, obtained from UPS spectra shown in **Fig. 4.23(a)**. The energy levels of MB were obtained from the reported literature.[54] The highest occupied molecular orbital (HOMO) and lowest unoccupied molecular orbital (LUMO) for MB dye are located at -6.26 eV and -4.55 eV, respectively. The energy band diagram in **Fig. 4.23(b)** reveals multiple thermodynamically viable charge transfer pathways under 532 nm excitation. These pathways include molecular resonance (μ_{mol}) within the MB molecule, exciton resonance (μ_{exc}) of $Cs_2AgBiBr_6$ DP and STEs, photo-induced charge transfer (μ_{PICT}) facilitated by the alignment of energy levels between $Cs_2AgBiBr_6$ DP and the MB molecule. Each of these mechanisms can significantly influence the Raman signal of the molecule. This interplay enhances the Raman signal intensity, contributing to the overall SERS performance. These pathways

highlight the complex interactions between the semiconductor substrate and the analyte that underpin the observed signal enhancement.

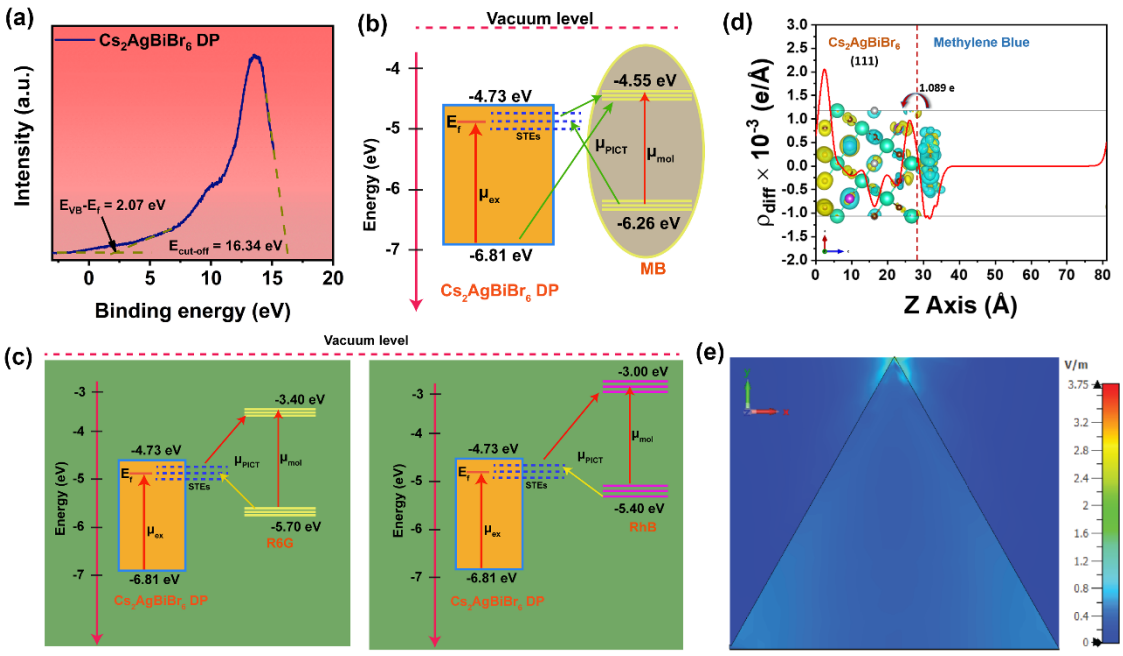

Fig. 4.23: (a) UPS spectra obtained for $Cs_2AgBiBr_6$ DP substrate. **(b)** Schematic of the charge transfer mechanism using band alignment of $Cs_2AgBiBr_6$ DP and MB analyte. **(c)** Schematic of the charge transfer mechanism using band alignment of $Cs_2AgBiBr_6$ DP, R6G, and RhB analyte. **(d)** Computational analysis of charge transfer between $Cs_2AgBiBr_6$ DP and MB molecules using DFT simulations. The blue regions indicate the charge deficiency, while the yellow region shows the charge accumulation after dye adsorption on $Cs_2AgBiBr_6$ DP. **(e)** FEM simulation showing the EM enhancement of triangular $Cs_2AgBiBr_6$ DP.

Fig. 4.23(b) depicts the way the defect states (STEs) in DP facilitate the charge transfer (CT) process. The presence of the trap states in $Cs_2AgBiBr_6$ DP allows electrons from the HOMO level of MB to transfer more efficiently to the $Cs_2AgBiBr_6$ DP due to favorable energy level alignment. The introduction of newly generated defect energy states within the forbidden energy gap provides an efficient charge transfer pathway, which significantly alters the polarizability tensor of the material, leading to enhanced SERS activity of DP. **Fig. 4.23(c)** shows the band alignment of DP with R6G and RhB molecules. The difference between the LUMO levels of MB is less than the R6G and RhB molecules. The energy difference between the VB of DP and the LUMO energy level of the R6G and RhB molecules is higher than the excitation laser source (532 nm). Thus, some of the charge pathways are prohibited in R6G and

RhB molecules. Thus, the MB demonstrates superior enhancement due to its strong charge transfer interactions, efficient adsorption, and favorable molecular orientation.

Fig. 4.23(d) illustrates the charge density difference (CDD) plot for the $Cs_2AgBiBr_6$-MB composite system, derived from DFT calculations. In the plot, yellow regions represent areas of charge accumulation, while blue regions indicate charge depletion. The figure demonstrates that charge transfer occurs from the molecule to the $Cs_2AgBiBr_6$ substrate. Bader charge analysis was conducted to quantify this transfer, revealing a net depletion of 1.089e from the molecule, which is subsequently gained by the semiconductor. This result aligns well with the charge transfer analysis obtained from UPS spectra. Additionally, the excitation energy of the 532 nm laser (2.66 eV) is sufficient to promote ground-state electrons to these higher conducting energy states, thereby increasing the charge carrier population in the conduction states and enhancing the Raman signal.

We utilized finite element method (FEM) simulations to investigate the distinct contributions of various mechanisms involved in SERS amplification. The morphology of DP flakes was analyzed through optical images, as shown in Figure S1(c) (Supplementary Information). The flake size and thickness were accurately reproduced based on the AFM image of the sample surface (inset of Figure S1(d), SI) to ensure that the experimental conditions were faithfully represented in the simulations. The FEM simulation revealed that the maximum field enhancement occurs at the corners of the flakes, as depicted in **Fig. 4.23(e)**. This field enhancement comes from the surface plasmonic effect of the metals present in the DP material, like Ag and Bi. However, the maximum electric field enhancement factor ($|E/E_0|$) was determined to be 1.15 at an excitation wavelength of 532 nm. Using the relation $\sim|E/E_0|^4$, the electromagnetic (EM) enhancement factor was calculated as 1.75, which is negligible compared to the total EF of 5.04×10^7. Note that the contribution of electromagnetic (EM) enhancement in a semiconducting system is predominantly influenced by the inter-structural spacing of the material. A smaller gap generally results in a higher EM enhancement, as reported in the literature[52]. In our study, the separation between the two distinct triangular structures is relatively larger, leading to a significantly reduced EM contribution. Thus, the charge transfer-related CM mechanism contributes a factor of 2.88×10^7, which is remarkably high. These findings demonstrate that the SERS enhancement in DP flakes is mostly arising from the CM enhancement. The CM enhancement comes from the contribution of the photo-induced charge transfer process between the aligned energy levels of DP and molecules, and the additional STE defect states present in the system.

4.7 Conclusion

For the first time, we have utilized the all-inorganic, lead-free double perovskite $Cs_2AgBiBr_6$ for SERS-based detection of organic pollutants. A cost-effective, solvent-based method was employed to fabricate high-quality triangular $Cs_2AgBiBr_6$ flakes, which serve as an efficient SERS substrate. Comprehensive analyses, including Raman spectroscopy, XPS, and XRD measurements, confirmed the phase purity of the $Cs_2AgBiBr_6$ DP. XPS studies further revealed that the DP retained its cubic phase after analyte adsorption, with a noticeable shift toward lower binding energies in the high-resolution XPS peaks of individual elements, indicating charge transfer from the MB molecule to the $Cs_2AgBiBr_6$ DP. Additionally, the observed PL quenching, favorable band alignment, and computational studies confirmed that chemical enhancement underpins the SERS detection mechanism. This is further demonstrated through the control/manipulation of STE defects in DP. Beyond MB, the $Cs_2AgBiBr_6$ DP successfully detected other molecules, including RhB, R6G, CV, and MG, demonstrating its versatility. Remarkably, an enhancement factor of 5.04×10^7 and 1.37×10^7 was achieved for MB and R6G molecules, respectively, with detection sensitivity reaching concentrations as low as 10^{-10} M, surpassing all other perovskite-based SERS substrates. The $Cs_2AgBiBr_6$ DP SERS substrate exhibited excellent environmental stability for up to four months. The $Cs_2AgBiBr_6$ DP not only enhances the sensitivity and accuracy of SERS applications but also establishes itself as a promising platform for detecting low-concentration analytes with high reliability.

References

1 T. tiao Pan, W. Guo, P. Lu and D. Hu, *J Sci Food Agric*, 2021, **101**, 3595–3604.

2 R. Xu, L. Tan, W. Xu, L. Xiao, Y. Zheng, Y. Li and Y. Lou, *Chemical Communications*, 2024, **60**, 12872-12875. DOI:10.1039/d4cc04136d.

3 M. Ye, T. Su, J. Li, X. Chen, D. Ying, S. Wu, Z. Wang and N. Duan, *Nano Res*, 2024, **17**, 9990–9998. DOI:10.1007/s12274-024-6951-4.

4 M. Shao, C. Ji, J. Tan, B. Du, X. Zhao, J. Yu, B. Man, K. Xu, C. Zhang and Z. Li, *Opto-Electronic Advances*, 2023, **6**, 230094. DOI:10.29026/oea.2023.230094.

5 K. Kant, R. Beeram, Y. Cao, P. S. S. dos Santos, L. González-Cabaleiro, D. García-Lojo, H. Guo, Y. Joung, S. Kothadiya, M. Lafuente, Y. X. Leong, Y. Liu, Y. Liu, S. S. B. Moram, S. Mahasivam, S. Maniappan, D. Quesada-González, D. Raj, P. Weerathunge, X. Xia, Q. Yu, S. Abalde-Cela, R. A. Alvarez-Puebla, R. Bardhan, V. Bansal, J. Choo, L. C. C. Coelho, J. M. M. M. de Almeida, S. Gómez-Graña, M. Grzelczak, P. Herves, J. Kumar, T. Lohmueller, A. Merkoçi, J. L. Montaño-Priede, X. Y. Ling, R. Mallada, J. Pérez-Juste, M. P. Pina, S. Singamaneni, V. R. Soma, M. Sun, L. Tian, J. Wang, L. Polavarapu and I. P. Santos, *Royal Society of Chemistry*, 2024, preprint, DOI: 10.1039/d4nh00226a.

6 T. Itoh, Y. S. Yamamoto and Y. Ozaki, *Royal Society of Chemistry*, 2017, **46**, 3904-3921. DOI: 10.1039/c7cs00155j.

7 Z. Li, X. Huang and G. Lu, *Royal Society of Chemistry,* 2020, **8**, 3956-3969, DOI: 10.1039/d0tc00002g.

8 C. Y. Liu, R. Ram, R. B. Kolaru, A. S. Jana, A. S. Sadhu, C. S. Chu, Y. N. Lin, B. N. Pal, S. H. Chang and S. Biring, *Biosensors **2022**, 12(10), 807*. DOI:10.3390/bios12100807.

9 C.-W. Huang, B.-J. Lin, H.-Y. Lin, C.-H. Huang, F.-Y. Shih, W.-H. Wang, C.-Y. Liu and H.-C. Chui, *Surface-enhanced Raman scattering of suspended monolayer graphene*, 2013, **8**, 480.

10 H. Liu, Y. He and K. Cao, *John Wiley and Sons Inc*, 2021, **8**, 2100982. DOI: 10.1002/admi.202100982.

11 J. Zhang, L. L. Wang, M. F. Hou, L. P. Luo, Y. J. Liao, Y. K. Xia, A. Yan, Y. P. Weng, L. P. Zeng and J. H. Chen, *Biosens Bioelectron*, 2018, **118**, 1–8.

12 B. Wrzosek, Y. Kitahama and Y. Ozaki, *Journal of Physical Chemistry C*, 2020, **124**, 20328–20339.

13 C. Y. Liu, R. Ram, R. B. Kolaru, A. S. Jana, A. S. Sadhu, C. S. Chu, Y. N. Lin, B. N. Pal, S. H. Chang and S. Biring, *Biosensors 2022, **12(10)**, 807*. DOI:10.3390/bios12100807.

14 V. Dzhagan, N. Mazur, O. Kapush, M. Skoryk, Y. Pirko, A. Yemets, V. Dzhahan, P. Shepeliavyi, M. Valakh and V. Yukhymchuk, *ACS Omega*, 2024, **9**, 4819–4830.

15 R. Peng, T. Zhang, S. Yan, Y. Song, X. Liu and J. Wang, *Multidisciplinary Digital Publishing Institute (MDPI)*, *Nanomaterials* **2023**, *13*(22), 2968. DOI: 10.3390/nano13222968.

16 Y. Jing, R. Wang, Q. Wang, Z. Xiang, Z. Li, H. Gu and X. Wang, *Springer Science and Business Media B.V.*, 2021, **4**, 885–905. DOI: 10.1007/s42114-021-00330-0.

17 C. Y. Liu, J. Y. Guo, J. Y. Lin, K. Uma and S. W. Liu, *J Mater Chem C Mater*, 2024, **12**, 10172–10180.

18 J. Lu, X. Du, Z. Li, Y. Song, C. Zhang, J. Yu and Q. Peng, *Appl Opt*, 2020, **59**, 5589.

19 N. Pan, J. Tian, Z. Shi, W. Zhang, Y. Gao, T. You and P. Yin, *J Mater Chem C Mater*, 2023, **11**, 13256–13262.

20 J. Wang, C. Qiu, H. Pang, J. Wu, M. Sun and D. Liu, *J Mater Chem C Mater*, 2021, **9**, 9011–9020.

21 A. Chilvery, S. Das, P. Guggilla, C. Brantley and A. Sunda-Meya, *Taylor and Francis Ltd.*, 2016, **17**, 650-658. DOI: 10.1080/14686996.2016.1226120.

22 S. S. Mali, J. V. Patil, J. Y. Shao, Y. W. Zhong, S. R. Rondiya, N. Y. Dzade and C. K. Hong, *Nat Energy*, 2023, **8**, 989–1001.

23 M. Li, Y. Yang, Z. Kuang, C. Hao, S. Wang, F. Lu, Z. Liu, J. Liu, L. Zeng, Y. Cai, Y. Mao, J. Guo, H. Tian, G. Xing, Y. Cao, C. Ma, N. Wang, Q. Peng, L. Zhu, W. Huang and J. Wang, *Nature*, 2024, **630**, 631–635.

24 A. Fakharuddin, M. K. Gangishetty, M. Abdi-Jalebi, S. H. Chin, A. R. bin Mohd Yusoff, D. N. Congreve, W. Tress, F. Deschler, M. Vasilopoulou and H. J. Bolink, *Nature Research*, 2022, preprint, DOI: 10.1038/s41928-022-00745-7.

25 S. Aftab, G. Koyyada, Z. Haider, E. Akman, F. Kabir, M. Aslam, M. K. A. Mohammed, M. A. Assiri and J. H. Kim, *Elsevier Ltd*, 2024, **46**, 101490. DOI: 10.1016/j.mtphys.2024.101490.

26 L. Min, Y. Zhou, H. Sun, L. Guo, M. Wang, F. Cao, W. Tian and L. Li, *Light Sci Appl*, 2024, **13**, 280. DOI:10.1038/s41377-024-01636-6.

27 Y. Tang, P. Jin, Y. Wang, D. Li, Y. Chen, P. Ran, W. Fan, K. Liang, H. Ren, X. Xu, R. Wang, Y. (Michael) Yang and B. Zhu, *Nat Commun*, **14**, 4961 (2023). DOI:10.1038/s41467-023-40711-1.

28 R. Mastria, K. J. Riisnaes, A. Bacon, I. Leontis, H. T. Lam, M. A. S. Alshehri, D. Colridge, T. H. E. Chan, A. De Sanctis, L. De Marco, L. Polimeno, A. Coriolano, A. Moliterni, V. Olieric, C. Giannini, S. Hepplestone, M. F. Craciun and S. Russo, *Adv Funct Mater*, **34**, 2024, 2401903. DOI:10.1002/adfm.202401903.

29 Z. Yin, Y. Li, J. Xu, Z. F. Qian and K. Xiong, *Elsevier Ltd*, 2022, **27**, 100815. DOI: 10.1016/j.mtphys.2022.100815.

30 M. Y. Sofi, M. S. Khan, J. Ali and M. A. Khan, *Sci Rep*, **14**, 5520 (2024). DOI:10.1038/s41598-024-54386-1.

31 S. Ghosh, H. Shankar and P. Kar, *Royal Society of Chemistry*, *Mat Adv*, 2022,**3**, 3742-3765. DOI: 10.1039/d2ma00071g.

32 W. Pan, H. Wu, J. Luo, Z. Deng, C. Ge, C. Chen, X. Jiang, W. J. Yin, G. Niu, L. Zhu, L. Yin, Y. Zhou, Q. Xie, X. Ke, M. Sui and J. Tang, *Nat Photonics*, 2017, **11**, 726–732.

33 S. Chand Yadav, A. Srivastava, V. Manjunath, A. Kanwade, R. S. Devan and P. M. Shirage, *Elsevier Ltd*, 2022, **26**, 2022, 100731. DOI: 10.1016/j.mtphys.2022.100731.

34 J. Lao, W. Xu, C. Jiang, N. Zhong, B. Tian, H. Lin, C. Luo, J. Travas-Sejdic, H. Peng and C. G. Duan, *J Mater Chem C Mater*, 2021, **9**, 5706–5712.

35 F. Fang, H. Li, S. Fang, B. Zhou, F. Huang, C. Ma, Y. Wan, S. Jiang, Y. Wang, B. Tian and Y. Shi, *Adv Opt Mater*, 2021, **9**, 2001930. DOI:10.1002/adom.202001930.

36 G. Kresse and J. Furthmü, *Efficient iterative schemes for ab initio total-energy calculations using a plane-wave basis set*, Phys. Rev. B **54**, 11169 (1996).

37 I. Preface and R. G. Parr, *DENSITY FUNCTIONAL THEORY*, **vol 123**, pp 141-158. DOI.org/10.1007/978-1-4757-0818-9_5

38 P. Giannozzi, S. Baroni, N. Bonini, M. Calandra, R. Car, C. Cavazzoni, D. Ceresoli, G. L. Chiarotti, M. Cococcioni, I. Dabo, A. Dal Corso, S. De Gironcoli, S. Fabris, G. Fratesi, R. Gebauer, U. Gerstmann, C. Gougoussis, A. Kokalj, M. Lazzeri, L. Martin-Samos, N. Marzari, F. Mauri, R. Mazzarello, S. Paolini, A. Pasquarello, L. Paulatto, C. Sbraccia, S. Scandolo, G. Sclauzero, A. P. Seitsonen, A. Smogunov, P. Umari and R. M. Wentzcovitch, *Journal of Physics Condensed Matter*, **21** 395502. DOI:10.1088/0953-8984/21/39/395502.

39 P. J. Hasnip and C. J. Pickard, *Comput Phys Commun*, 2006, **174**, 24–29.

40 J. P. Perdew, K. Burke and M. Ernzerhof, *Generalized Gradient Approximation Made Simple*, Phys. Rev. Lett. **78**, 1396 (1997)

41 H. J. Jöbsis, V. M. Caselli, S. H. C. Askes, E. C. Garnett, T. J. Savenije, F. T. Rabouw and E. M. Hutter, *Appl. Phys. Lett.* **119**, 131908 (2021). DOI:10.1063/5.0061899.

42 F. Fang, Y. Wan, H. Li, S. Fang, F. Huang, B. Zhou, K. Jiang, V. Tung, L. J. Li and Y. Shi, *ACS Nano*, 2022, **16**, 3985–3993.

43 P. Pistor, M. Meyns, M. Guc, H. C. Wang, M. A. L. Marques, X. Alcobé, A. Cabot and V. Izquierdo-Roca, *Scr Mater*, 2020, **184**, 24–29.

44 R. Chahal, A. K. Mia, A. Bora and P. K. Giri, *J Mater Chem C Mater*, 2024, **12**, 12835–12846.

45 R. Chahal, A. Bora and P. K. Giri, *ACS Appl Energy Mater*, 2023, **6**, 8794–8807.

46 A. Fernández-Pérez, T. Valdés-Solís and G. Marbán, *Dyes and Pigments*, 2019, **161**, 448–456.

47 Z. Zhang, Y. Yu and P. Wang, *ACS Appl Mater Interfaces*, 2012, **4**, 990–996.

48 N. S. Singh and P. K. Giri, *ACS Appl Nano Mater*, 2024, **7**, 13579–13589.

49 T. Jena, M. T. Hossain, U. Nath, M. Sarma, H. Sugimoto, M. Fujii and P. K. Giri, *NPJ 2D Mater Appl*, **7**, 8 (2023). DOI:10.1038/s41699-023-00367-3.

50 I. Alessandri and J. R. Lombardi, *American Chemical Society*, 2016, 116, 24, 14921–14981. DOI: 10.1021/acs.chemrev.6b00365.

51 S. Y. Ding, E. M. You, Z. Q. Tian and M. Moskovits, *Royal Society of Chemistry*, *Chem. Soc. Rev.*, 2017,**46**, 4042-4076, DOI: 10.1039/c7cs00238f.

52 S. Ghosal, A. Bora and P. K. Giri, *Nanoscale*, 2023, **16**, 309–321.

53 G. Song, S. Cong and Z. Zhao, *Chem Sci*, 2022, **13**, 1210–1224.

54 Y. Shan, Z. Zheng, J. Liu, Y. Yang, Z. Li, Z. Huang and D. Jiang, *NPJ Comput Mater*, **3**, 11 (2017). DOI:10.1038/s41524-017-0008-0.

55 M. Xin, Y. Fu, Y. Zhou, J. Han, Y. Mao, M. Li, J. Liu and M. Huang, *New Journal of Chemistry*, 2020, **44**, 17570–17576.

56 Z. Yu, W. Yu, J. Xing, R. A. Ganeev, W. Xin, J. Cheng and C. Guo, *ACS Photonics*, 2018, **5**, 1619–1627.

57 R. Feng, Q. Miao, X. Zhang, P. Cui, C. Wang, Y. Feng, L. Gan, J. Fu, S. Wang, Z. Dai, L. Hu, Y. Luo, W. Sun, X. Zhang, J. Xiao, J. Wu, B. Zhou, M. Zou, D. He, X. Zhou and X. Han, *Sci China Mater*, 2022, **65**, 1601–1614.

58 J. Lu, X. Du, Z. Li, Y. Song, C. Zhang, J. Yu and Q. Peng, *Appl Opt*, 2020, **59**, 5589.

59 T. Man, W. Lai, C. Zhu, X. Shen, W. Zhang, Q. Bao, J. Chen, Y. Wan, H. Pei and L. Li, *Adv Funct Mater*, **32**, 32, 2022, 2201799. DOI:10.1002/adfm.202201799.

60 W. Li, L. Xiong, N. Li, S. Pang, G. Xu, C. Yi, Z. Wang, G. Gu, K. Li, W. Li, L. Wei, G. Li, C. Yang and M. Chen, *J Mater Chem C Mater*, 2019, **7**, 10179–10186.

61 L. Tao, K. Chen, Z. Chen, C. Cong, C. Qiu, J. Chen, X. Wang, H. Chen, T. Yu, W. Xie, S. Deng and J. Bin Xu, *J Am Chem Soc*, 2018, **140**, 8696–8704.

62 M. Li, X. Fan, Y. Gao and T. Qiu, *Journal of Physical Chemistry Letters*, 2019, **10**, 4038–4044.

63 N. S. Singh, F. Mayanglambam, H. B. Nemade and P. K. Giri, *ACS Appl Nano Mater*, 2022, **5**, 6352–6364.

64 S. Ghosal, S. Nandi and P. K. Giri, *ACS Appl Nano Mater*, 2024, **7**, 20484–20497.

65 Z. Zheng, S. Cong, W. Gong, J. Xuan, G. Li, W. Lu, F. Geng and Z. Zhao, *Nat Commun*, **8**, 1993 (2017). DOI:10.1038/s41467-017-02166-z.

66 Y. Guan, M. Chen, Y. Ding, Y. Fang, F. Huang, C. Y. Xu, L. Zhen, Y. Li, L. Yang and P. Xu, *ACS Nano*, 2024, **18**, 17339–17348.

Chapter 5 All Inorganic Lead-free $Cs_2AgBiBr_6$ Double Perovskite Single Crystal / $Cs_3Bi_2I_9$ Nanocrystals Heterojunction for High-Performance Photodetector Application

We report the design and characterisation of a heterojunction photodetector based on a $Cs_2AgBiBr_6$ single crystal (SC) and $Cs_3Bi_2I_9$ (CBI) nanocrystals (NCs), demonstrating enhanced charge collection efficiency and significantly reduced dark current due to the built-in electric field at the junction interface. Highly crystalline, cubic-shaped CBI NCs were synthesised via a mechanochemical approach and subsequently deposited onto the double perovskite single crystal through a drop-casting method, forming a $Cs_2AgBiBr_6/Cs_3Bi_2I_9$ perovskite–perovskite heterojunction. The heterojunction device exhibited a marked increase in photocurrent and suppression of dark current, attributed to the enhanced generation of photocarriers and efficient interfacial charge transfer facilitated by the built-in electric potential. Compared to the pristine $Cs_2AgBiBr_6$ SC device, the heterojunction configuration yielded a ~30-fold improvement in the on/off current ratio and an approximate six-fold enhancement in responsivity, reflecting superior photodetection performance. Photophysical analyses, including steady-state photoluminescence (PL), time-resolved PL, and Raman spectroscopy, confirmed effective photoinduced charge transfer from CBI NCs to the $Cs_2AgBiBr_6$ matrix. Ultraviolet photoelectron spectroscopy (UPS) revealed a type-II band alignment at the heterointerface, favouring charge separation and transport across the junction. Complementary density functional theory (DFT) calculations further corroborated significant electron transfer from the CBI NCs to the $Cs_2AgBiBr_6$ SC, in agreement with the observed device characteristics. These findings underscore the potential of all-inorganic, lead-free halide perovskite heterojunctions in advancing high-performance photodetector technologies.

5.1 Introduction

Due to their exceptional optoelectronic properties, lead-based perovskites have been widely utilised in solar cells (SCs), photodetectors (PDs), and various other optoelectronic devices.[1–4] The rapid advancement in this field was initially driven by lead-based perovskite solar cells (PeSCs), which have achieved remarkable power conversion efficiencies exceeding 26% in a relatively short time frame, rivalling those of conventional crystalline silicon SCs. Despite this progress, the inherent toxicity of lead and issues related to the long-term stability of lead-based perovskites present significant challenges.[5] Consequently, the development of lead-free perovskite alternatives has become a critical focus in the field. Various metal cations, including

Sn^{2+}, Zr^{4+}, Ag^{+}, and Bi^{3+}, have been investigated as potential substitutes for Pb^{2+} in perovskite structures for PD applications.[6–10] However, the practical application of Sn-based perovskites in photovoltaics remains limited due to the facile oxidation of Sn^{2+} to Sn^{4+} under ambient conditions. Among various alternatives, bismuth (Bi^{3+}) has emerged as a promising candidate to replace Pb^{2+} due to its nontoxicity and isoelectronic character. However, the inherent charge imbalance and the resultant low-dimensional crystal structures often limit the optoelectronic performance of Bi-based perovskite analogues compared to their lead-based counterparts.[9] Notably, double perovskites, with the general formula $A_2B^{+}B^{3+}X_6$, have gained significant attention as viable lead-free alternatives. In these structures, the divalent Pb^{2+} site is substituted by a combination of monovalent (B^{+}) and trivalent (B^{3+}) metal cations, forming a stable perovskite-like framework. Among them, $Cs_2AgBiBr_6$ has emerged as a leading candidate due to its favourable optoelectronic properties, which are comparable to those of lead-based perovskites, along with its reduced toxicity and enhanced environmental stability.[11]

The solid-state synthesis and crystallographic characterisation of Cs_2AgBiX_6 (X = Cl, Br) have been reported by Woodward et al., who employed powder X-ray diffraction (PXRD) analysis combined with Rietveld refinement techniques to confirm the formation of a cubic crystal structure belonging to the *Fm3m* space group (No. 225).[12] Building upon this foundation, Giustino and co-workers explored both the experimental synthesis and computational design of lead-free halide double perovskites, providing insights into the thermodynamic stability and electronic band structures of Cs_2AgBiX_6 (X = Cl, Br).[13–15] Wei et al. further investigated the electronic structure of $Cs_2AgBiBr_6$ through first-principles calculations, with a particular focus on the order–disorder phase transition and its influence on the material's band structure.[16] Additionally, Schade and colleagues conducted comprehensive structural and optical studies on $Cs_2AgBiBr_6$ powder samples, elucidating its behaviour across the phase transition temperature.[17] Although a single-crystal structure was not reported, the authors provided detailed crystallographic parameters of $Cs_2AgBiBr_6$ at both room and low temperatures based on neutron powder diffraction (NPD) measurements. Zhan et al. investigated the application of $Cs_2AgBiBr_6$ thin films in humidity sensing, demonstrating remarkable environmental stability and exceptionally rapid response and recovery times.[18] In the broader context of optoelectronic applications, double perovskites have been utilised in various device architectures, including solar cells[19,20] and X-ray detectors[21,22], typically in the form of thin films or compressed powder pellets.

Traditionally, $Cs_2AgBiBr_6$-based photodetectors (PDs) have been predominantly fabricated using single-crystal (SC) architectures, which exhibit a high charge transport figure of merit ($\mu\tau \approx 6.3 \times 10^{-3}$ cm^2 V^{-1}) and a low surface trap density of approximately 1.74×10^9 cm^{-3}.[23] Alternatively, oxide films such as TiO_2 and SnO_2 have been employed as functional interfacial layers to form semiconductor–oxide heterojunctions, thereby enhancing charge extraction and device stability. For instance, a SnO_2-based heterojunction has demonstrated a responsivity of 0.11 A W^{-1} at 350 nm, while a TiO_2-based device exhibited a response time of 2 ms and a specific detectivity of 2.1×10^{10} Jones.[24] However, the use of conventional oxide films fabricated via spin-coating techniques often introduces oxygen vacancies and grain boundary defects, which act as non-radiative recombination centres. These defect states lead to enhanced carrier recombination, thereby reducing charge transport efficiency and ultimately causing a decline in overall photodetection performance.[25]

To overcome these challenges, we have fabricated an all-inorganic lead-free heterostructure photodetector using $Cs_2AgBiBr_6$ single crystal and $Cs_3Bi_2I_9$ NCs. To fabricate the heterostructure on the substrate, a high-quality $Cs_2AgBiBr_6$ single crystal (SC) was first synthesized in hydrobromic acid (HBr) via the low-temperature crystallisation (LTC) method. The ball milling method was utilized to synthesize high crystallinity $Cs_3Bi_2I_9$ NCs. Furthermore, CBI NCs were drop-casted on top of the $Cs_2AgBiBr_6$ DP SC to form a uniform NC thin film. This approach facilitates the fabrication of a visually uniform, structurally stable, and low-toxicity photodetector (PD). The resulting planar heterostructure device exhibits higher photocurrent and reduced dark current, thus enhancing the responsivity and detectivity of the device. The on/off ratio increased 30 times compared to the pristine DP SC device due to the reduced carrier recombination and generation of charge carriers at the DPSC/CBI interface. Furthermore, Ultraviolet photoelectron spectroscopy (UPS) and Density Functional Theory (DFT) corroborated the efficient charge transfer from CBI NCs to the $Cs_2AgBiBr_6$ SC. This study lays the groundwork for lead-free inorganic perovskite/perovskite heterostructures, paving the way for future optoelectronic applications.

5.2 Materials and Methods

5.2.1 Materials

Caesium Bromide (Sigma Aldrich, Trace metal basis, >99.9%), Bismuth Bromide (Alfa Asar, Trace metal basis, >99%), Silver Bromide (Sigma Aldrich, Trace metal basis, >98%), Caesium Iodide (Sigma Aldrich, Trace metal basis, >99.9%), Bismuth Iodide (Sigma Aldrich, Trace

metal basis, >99.9%), Hydrobromic Acid (Sigma Aldrich, ACS Reagent 48%), Toluene (Sigma Aldrich, Anhydrous >99.8%), Oleylamine (Sigma Aldrich, >98%). All the chemicals were used without any alteration.

5.2.2 Synthesis of $Cs_2AgBiBr_6$ Single Crystal

The $Cs_2AgBiBr_6$ single crystals (SCs) were grown under ambient air conditions following a procedure similar to that reported previously.[26] In brief, 10 mL of hydrobromic acid (HBr) was used as the solvent, into which 1.0 mmol of $BiBr_3$, 2.0 mmol of CsBr, and 1.0 mmol of AgBr were added to form the precursor mixture. The resulting solution, containing an orange precipitate, was sonicated for 10 minutes to promote dissolution and then heated to 120 °C for 3 hours to obtain a clear, supersaturated solution, suitable for crystal growth. Then the prepared solution was subjected to a controlled cooling protocol to facilitate the gradual crystallization of $Cs_2AgBiBr_6$. The process involved four sequential steps: (i) cooling at a rate of 2 °C per hour from 120 °C to 90 °C, (ii) further cooling at 1 °C per hour down to 60 °C, (iii) maintaining the temperature at 50 °C for 12 hours to promote crystal growth, and (iv) the solution was allowed to cool naturally to the room temperature. In the final stage, well-faceted single crystals with lateral dimensions 3 × 3 × 2 mm were obtained. The as-grown crystals were subsequently washed with isopropanol (HPLC grade, Sigma-Aldrich) to remove residual precursors and then dried at 60 °C to yield high-quality $Cs_2AgBiBr_6$ SCs suitable for further characterization and device fabrication.

5.2.3 Synthesis of $Cs_3Bi_2I_9$ Nanocrystals

The $Cs_3Bi_2I_9$ perovskite nanocrystals (NCs) were synthesized using a two-step surfactant-assisted mechanochemical approach.[27] In the standard procedure, 0.3 mmol of CsBr and 0.2 mmol of BiI_3 were subjected to ball milling in a planetary micro mill (PM100, Retch) at a rotation speed of 450 rpm for 2 hours, resulting in the formation of a fine $Cs_3Bi_2I_9$ powder. To obtain surfactant-capped nanocrystals, a small quantity of oleylamine (0.08 mL) was subsequently introduced into the milling jar, followed by an additional 1 hour of milling. The final product was then dispersed in 10 mL toluene to yield a stable colloidal suspension of $Cs_3Bi_2I_9$ NCs, suitable for further optical and structural characterization.

5.2.4 Device Fabrication

The $Cs_2AgBiBr_6$ SC/CBI NC film heterojunction was fabricated by drop-casting a colloidal dispersion of CBI nanocrystals onto the top surface of the cleaned single crystal. The deposited layer was then annealed at 70 °C on a hot plate, promoting solvent evaporation, film

densification, and enhanced interfacial adhesion between the CBI NCs and the $Cs_2AgBiBr_6$ substrate. This step ensured the formation of a uniform and well-bonded perovskite–perovskite heterojunction interface. For electrical contact formation, gold (Au) electrodes with a thickness of approximately 80 nm were deposited on top of the heterostructure using a vacuum thermal evaporation technique with metal shadow masks. The use of gold electrodes provides excellent electrical conductivity, chemical stability, and ohmic contact with the underlying semiconductor layers. The resulting Au/$Cs_2AgBiBr_6$ SC/CBI NC/Au device structure was thus prepared for subsequent photoelectrical measurements. For comparative analysis, a pristine single-crystal (SC) detector with the configuration Au/$Cs_2AgBiBr_6$ SC/Au was also fabricated under identical conditions. This reference device, lacking the CBI NC film, serves as a control sample to evaluate the influence of the CBI NC layer on the overall photoresponse, charge transport, and photodetection performance of the heterojunction device.

5.2.5 DFT Calculations

First-principles calculations based on density functional theory (DFT) were performed using the Vienna Ab initio Simulation Package (VASP).[28] The exchange-correlation interactions were described within the generalized gradient approximation (GGA) using the Perdew-Burke-Ernzerhof (PBE) functional.[29,30] A plane-wave kinetic energy cutoff of 400 eV was employed for all calculations. Brillouin zone integrations were carried out using a Monkhorst-Pack k-point mesh of 6 × 6 × 6. Electronic structure analyses focused on the charge density distribution and density of states (DOS).[31] Charge transfer characteristics were evaluated via Bader charge analysis, as implemented by Henkelman and co-workers. Charge density visualizations were generated using the VESTA software. The charge density difference (CDD), ρcdd, was computed as:

$$\rho_{cdd} = \rho_{Cs2AgBiBr6/Cs3Bi2I9} - \rho_{Cs2AgBiBr6} - \rho_{Cs3Bi2I9} \quad (5.1)$$

where $\rho_{Cs2AgBiBr6/Cs3Bi2I9}$, $\rho_{Cs2AgBiBr6}$ and $\rho_{Cs3Bi2I9}$ correspond to the charge densities of the heterostructure and the individual pristine constituents, respectively.

5.3 Characterization Techniques

To determine the crystal structure of the $Cs_2AgBiBr_6$ single crystal (SC), Single crystal and Powder X-ray diffraction (XRD) analysis were performed using a Bruker Nonius Smart Apex II X-ray Single crystal diffractometer (CCD) and a Rigaku RINT2500 TTRAX-III diffractometer equipped with Cu Kα radiation, respectively. The Raman spectra of the prepared

samples were collected using high-resolution micro-Raman spectroscopy (LabRam HR800, Jobin Yvon), employing an Ar^+ ion laser with an excitation wavelength (λ_{ex}) of 532 nm. A 100× objective lens was used to focus the laser beam onto a 1 μm spot size, with an excitation power of 140 μW. The scattered Raman signal was collected in backscattering geometry through a multimode fibre grating (1800 grooves mm^{-1}) and detected by a charge-coupled device (CCD). Raman spectra were recorded under a fixed, continuous acquisition time, ensuring high spectral resolution and signal-to-noise ratio. The surface morphology and elemental distribution of the as-grown $Cs_2AgBiBr_6$ SC were investigated using field emission scanning electron microscopy (FESEM, SIGMA 300, Zeiss) operated at an accelerating voltage of 200 kV. The chemical composition and surface electronic states of the $Cs_2AgBiBr_6$ SC and $Cs_2AgBiBr_6$ SC/$Cs_3Bi_2I_9$ nanocrystal (NC) thin film heterostructure were analyzed using X-ray photoelectron spectroscopy (XPS) on a PHI 5000 VersaProbe III spectrometer (ULVAC-PHI, Inc.), employing an Al Kα X-ray source (1486.6 eV) with a beam current of 20 mA. UV–visible absorption spectra were recorded using a PerkinElmer Lambda 950 spectrophotometer, while steady-state photoluminescence (PL) spectra were obtained with a Horiba Jobin Yvon Fluoromax-4 fluorimeter, utilizing a 405 nm excitation laser source at room temperature. Time-resolved photoluminescence (TRPL) measurements were performed at room temperature using a 405 nm pulsed laser excitation source (Lifespec II, Edinburgh Instruments), with an instrument response time below 50 ps. Electrical and photoresponse characteristics of the fabricated devices were measured using a shielded DC probe station equipped with a Keithley 4200 SCS system, and an external laser source connected with a function generator. All measurements were conducted under ambient atmospheric conditions at room temperature, without the use of a glovebox.

5.3 Results and Discussions

5.3.1 Characterization of $Cs_2AgBiBr_6$ SC

Lead-free $Cs_2AgBiBr_6$ single crystals (SCs) with dimensions of approximately 3 mm × 3 mm × 2 mm were synthesized through a controlled slow-cooling method (**Fig. 5.1(a)**). The truncated octahedral morphology of the as-grown SCs is presented in **Fig. 5.1(a)**. To obtain a smooth and reflective surface, the crystals were subsequently cleaned with IPA. The primary objective of the cleaning step was to eliminate residual precursor impurities and surface contaminants.

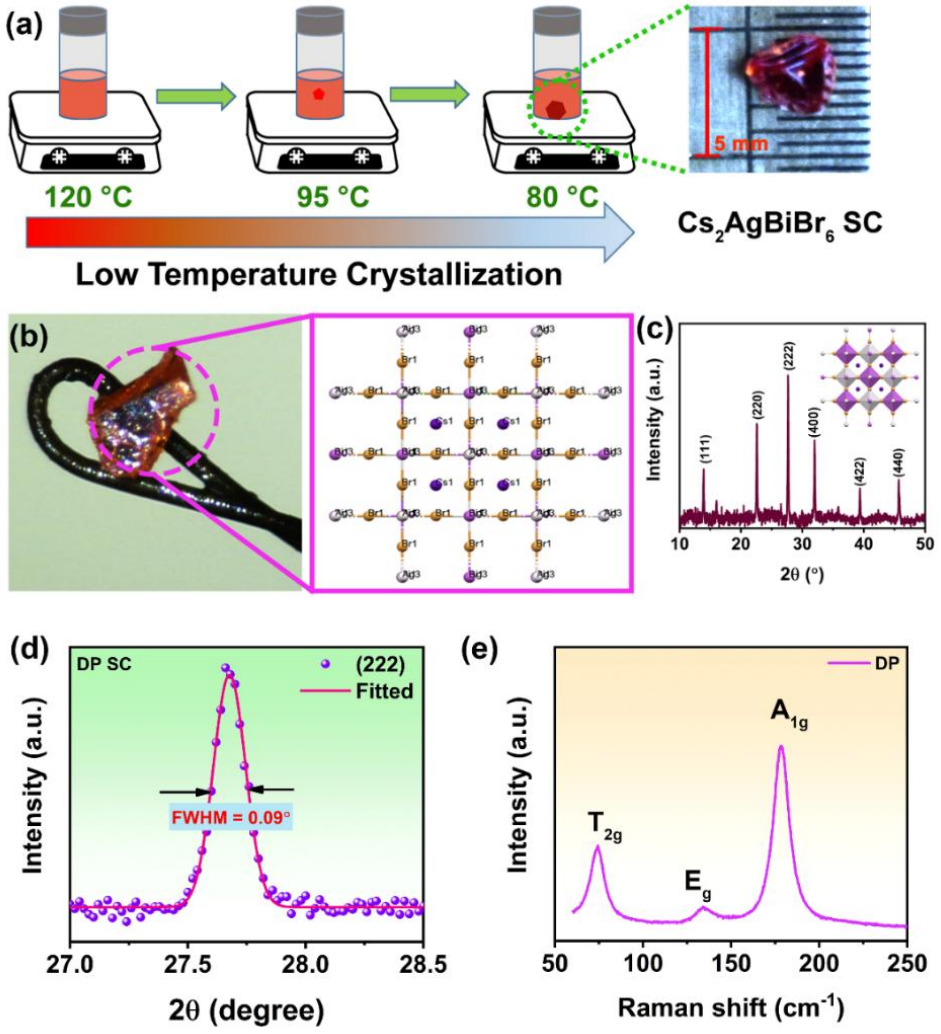

Fig. 5.1: (a) Schematic illustration of the synthesis method of $Cs_2AgBiBr_6$ single crystal. **(b)** Optical image of the small part of the $Cs_2AgBiBr_6$ single crystal mounted in the SCXRD system and the obtained 3D structure of the single crystal. **(c)** Powder XRD pattern of the $Cs_2AgBiBr_6$ single crystal. **(d)** Gaussian fitting of the (222) plane of the $Cs_2AgBiBr_6$ single crystal. **(e)** Raman spectra of the $Cs_2AgBiBr_6$ single crystal.

This treatment enhanced the collection efficiency of photoinduced charge carriers and improved the adhesion of gold (Au) electrodes on the crystal surface. Structurally, the double perovskite $Cs_2AgBiBr_6$ possesses a unit cell twice the size of a conventional 3D lead halide perovskite, owing to the substitution of two Pb^{2+} ions with one monovalent Ag^{+} and one trivalent Bi^{3+} ion. The phase purity and structural quality of the polished $Cs_2AgBiBr_6$ single crystals were verified using single-crystal X-ray diffraction (SCXRD), powder X-ray diffraction (PXRD), and Raman spectroscopy, as shown in **Fig. 5.1 (b, c)**. Single-crystal XRD measurement confirmed the growth of the highly crystalline Cs2AgBiBr6 single crystal.

Table 5.1: The unit cell parameters obtained from SCXRD measurement.

Parameters	Compound name
Formula	$Ag_2Bi_2Br_{12}Cs_4$
Mol.wt.	2124.26
Crystal System	Cubic
Space group	Fm-3m
a (Å)	11.264(6)
b (Å)	11.264(6)
c (Å)	11.264(6)
α (°)	90
β (°)	90
γ (°)	90
V (Å^3)	1429.3(2)
Density, gcm^{-3}	4.936
Abs. coeff., mm^{-1}	35.408
F (000)	1800
Total no. of reflections	110
Reflections, I > 2σ(I)	110
Max. θ/°	25.242
Ranges (h, k, l)	-14 ≤ h ≤ 14 -14 ≤ k ≤ 14 -14 ≤ l ≤ 14
Complete to 2θ (%)	98.9
Data / restraints / parameters	110/0/8
GooF (F^2)	1.265
R indices [I > 2σ(I)]	0.0112
wR$_2$ [I > 2σ(I)]	0.0258
R indices (all data)	0.0112
wR$_2$ (all data)	0.0258

The corresponding 3D structure obtained from SCXRD showed the high-purity arrangement of Ag and Bi atoms. The corresponding structural parameters obtained from SCXRD are listed in **Table 5.1**. Prominent PXRD reflections were observed at 2θ values of 14.06°, 23.42 °, 27.84°, 32.01°, 39.34°, and 45.74°, which correspond to the (111), (220), (222), (400), (422) and (400) crystal planes of $Cs_2AgBiBr_6$, respectively. Furthermore, the narrow full-width at half maximum (FWHM) of 0.09° for the (111) peak indicates an excellent crystalline quality of the $Cs_2AgBiBr_6$ SCs **(Fig. 5.1(d))**.[23] The Raman spectrum of the crystal, presented in **Fig. 5.1(e)**, exhibits distinct vibrational modes at 75 cm^{-1}, 133 cm^{-1} and 178 cm^{-1}, which are in good agreement with previously reported values for $Cs_2AgBiBr_6$.[32] The Raman band at 133 cm^{-1} is attributed to the E_g mode, which arises from the asymmetric stretching vibrations of Br ions surrounding Bi ions. In contrast, the band observed at 178 cm^{-1} corresponds to the A_{1g} mode, associated with the symmetric stretching vibrations of Br atoms around Bi atoms within the [$BiBr_6$] octahedral framework. The T_{2g} Raman mode arises from the oscillations of caesium atoms along with the other atoms.[33]

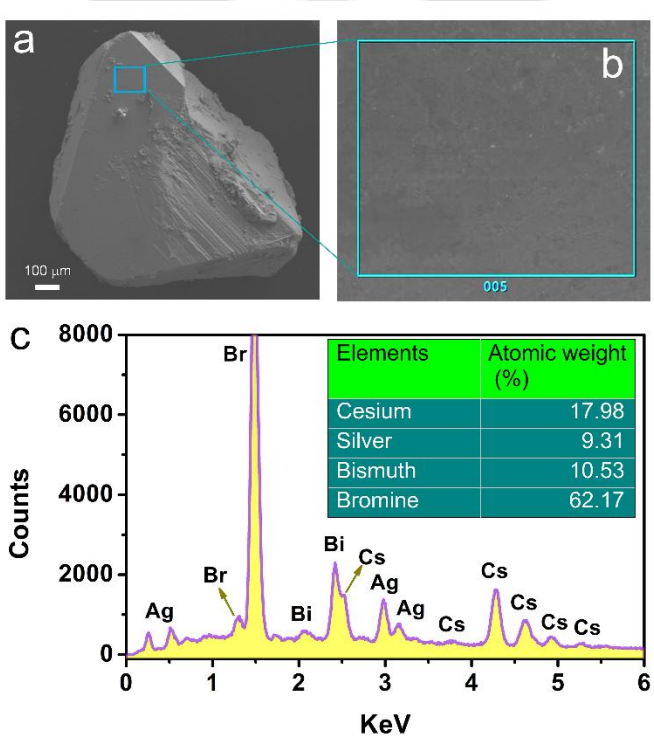

Fig. 5.2: (a) FESEM image of the $Cs_2AgBiBr_6$ single crystal. **(b)** Magnified FESEM image of the marked area of $Cs_2AgBiBr_6$ single crystal. **(c)** Corresponding FESEM-EDX atomic spectra of $Cs_2AgBiBr_6$ single crystal. The inset shows the corresponding atomic percentage of each element.

To further confirm the elemental composition, energy-dispersive X-ray (EDX) measurement was performed on the $Cs_2AgBiBr_6$ single crystals. The scanning electron microscopy (SEM)

image of the crystal is presented in **Fig. 5.2(a, b)**. The corresponding EDX spectrum is shown in **Fig. 5.2(c).** Quantitative EDX analysis confirmed the stoichiometric composition of the crystal, with the atomic percentages of Br, Ag, Cs, and Bi determined to be 62.17%, 9.31%, 17.98%, and 10.53%, respectively. The optical properties of the $Cs_2AgBiBr_6$ double perovskite single crystals were further examined. The absorbance and photoluminescence (PL) emission spectra of the polished $Cs_2AgBiBr_6$ crystal are presented in **Fig. 5.3(a)**. Consistent with previous reports, the absorption spectrum reveals a distinct band edge near 630 nm.[34,35] Considering the indirect nature of the electronic transition, the optical bandgap was estimated to be approximately 1.97 eV, as depicted in **Fig. 5.3(c).** Furthermore, the crystal exhibits a broad PL emission with a Stokes-shifted peak centered at 662 nm, characteristic of indirect bandgap semiconductors. To elucidate the origin of the broad PL spectrum observed in the 600–800 nm range, Gaussian fitting was performed using two distinct PL peaks (**Fig. 5.3(b)**). The first peak (P_{ex}), centered at 633 nm, is attributed to the band-edge emission associated with the indirect bandgap transition. In contrast, the second peak (P_{STE}), located at 700 nm, is assigned to self-trapped excitons (STEs) or defect-related states within the band structure.[33,36,37]

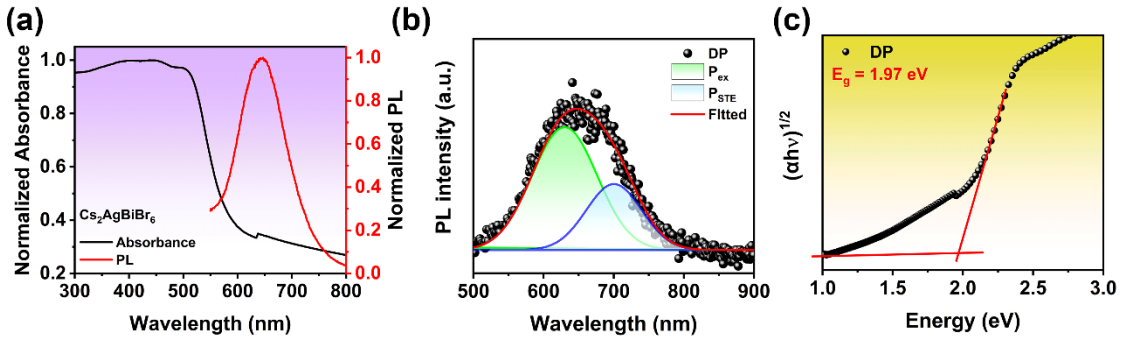

Fig. 5.3: (a) Absorbance and PL spectra of $Cs_2AgBiBr_6$ single crystal. **(b)** Gaussian fitting of the PL spectra of Cs2AgBiBr6 SC. **(c)** Tauc plot of $Cs_2AgBiBr_6$ single crystal.

5.3.2 Characterization of $Cs_3Bi_2I_9$ NCs

Fig. 5.4 illustrates the synthesis route of $Cs_3Bi_2I_9$ nanocrystals by the ball mill method as discussed in the experimental section. Transmission electron microscopy (TEM) was employed to investigate the morphology and structural features of the as-synthesized **$Cs_3Bi_2I_9$** perovskite nanocrystals. The TEM image shown in **Fig. 5.5(a)** reveals uniform cubic-shaped nanocrystals with an average size of ~42 nm. To further evaluate their crystallinity and lattice structure, high-resolution TEM (HRTEM) analysis was performed (**Fig. 5.5(b)**). The observed lattice fringe spacing of 0.27 nm corresponds to the (204) crystallographic plane of CBI, confirming

the high crystalline quality of the NCs.[38] Additionally, the energy-dispersive X-ray (EDX) analysis, presented in **Fig. 5.5(c-f)**, confirms the elemental composition of the nanocrystals, indicating the presence of all expected constituent elements in their appropriate proportions.

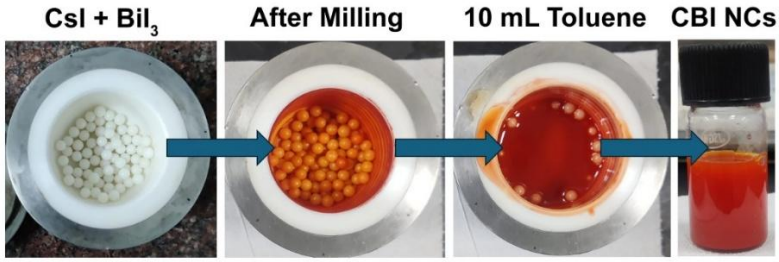

Fig. 5.4: Schematic illustration of the preparation method of $Cs_3Bi_2I_9$ NCs using the ball milling method.

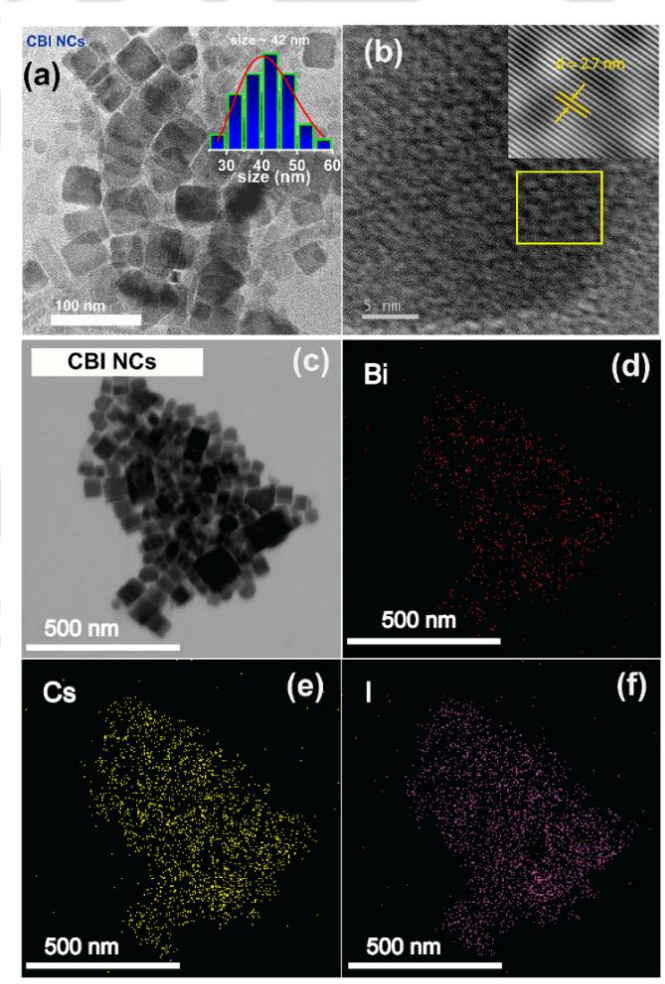

Fig. 5.5: (a) FETEM image of the $Cs_3Bi_2I_9$ NCs. The inset shows the size distribution graph of the NCs. **(b)** High-resolution FETEM image of the $Cs_3Bi_2I_9$ NCs. The inset shows the IFFT image of the yellow-marked area. **(c-e)** FETEM image of the $Cs_3Bi_2I_9$ NCs and corresponding elemental mapping, respectively.

The corresponding EDX spectrum confirmed the phase-pure stoichiometry ratio of the $Cs_3Bi_2I_9$ nanocrystals **(Fig. 5.6)**. The X-ray diffraction (XRD) pattern of the as-synthesised CBI nanocrystals, shown in **Fig. 5.7 (a)**, further confirms the phase purity and successful formation of the CBI perovskite, with no detectable impurity phases. The distinct diffraction peaks observed at 2θ values of 12.8°, 21.1°, 25.84°, 27.65°, 29.86°, and 32.4° correspond to the (101), (110), (202), (203), (204), and (205) crystal planes of CBI, respectively, which are in excellent agreement with previously reported literature values[38] and the JCPDS file data (01-089-1846).

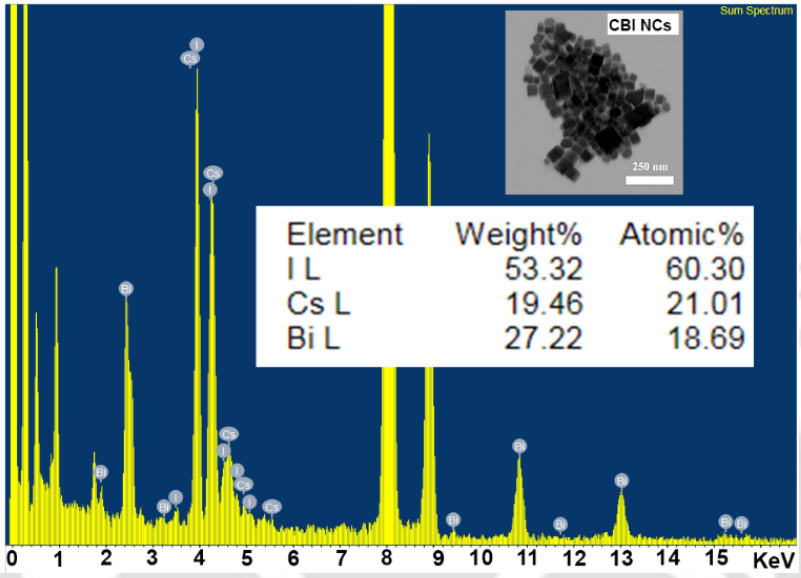

Fig. 5.6: FETEM-EDX spectra of $Cs_3Bi_2I_9$ NCs.

Raman spectra were recorded for the CBI powder and NC thin film as shown in **Fig. 5.7(b).** The Raman spectra of powder CBI showed all characteristic Raman modes, confirming the high-quality synthesis by the ball milling method. However, only the A_{1g} mode is clearly visible in the CBI NC thin film Raman spectra due to the high emissive nature of the nanocrystals. The optical characteristics of the colloidal CBI NCs were further analyzed through absorbance and photoluminescence (PL) spectroscopy, as presented in **Fig. 5.7(c)**. The PL emission peak at **550** nm originates from the band-to-band excitonic recombination of photogenerated charge carriers, which aligns well with the absorption edge.[39,40] The bandgap of the CBI NCs was estimated by Tauc's plot as 2.25 eV, aligning well with the absorption and size of the NCs. Owing to their strong light-harvesting efficiency and high luminescent intensity, CBI NCs are widely utilized in optoelectronic applications, including heterojunction-based photodetectors. The strong absorption peak around 450 nm is due to the highly excitonic nature of the CBI nanocrystals.

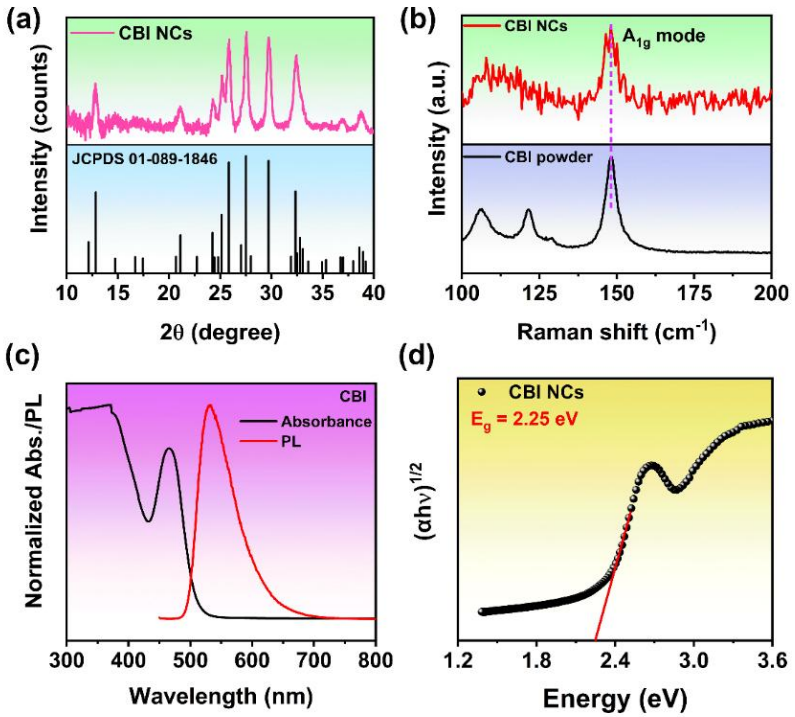

Fig 5.7: (a) XRD pattern of $Cs_3Bi_2I_9$ NC thin film and JCPDS file. **(b)** Raman spectra of $Cs_3Bi_2I_9$ powder and nanocrystal thin film. **(c)** Absorbance and PL spectra of $Cs_3Bi_2I_9$ NCs. **(d)** Corresponding Tauc's plot of $Cs_3Bi_2I_9$ NCs.

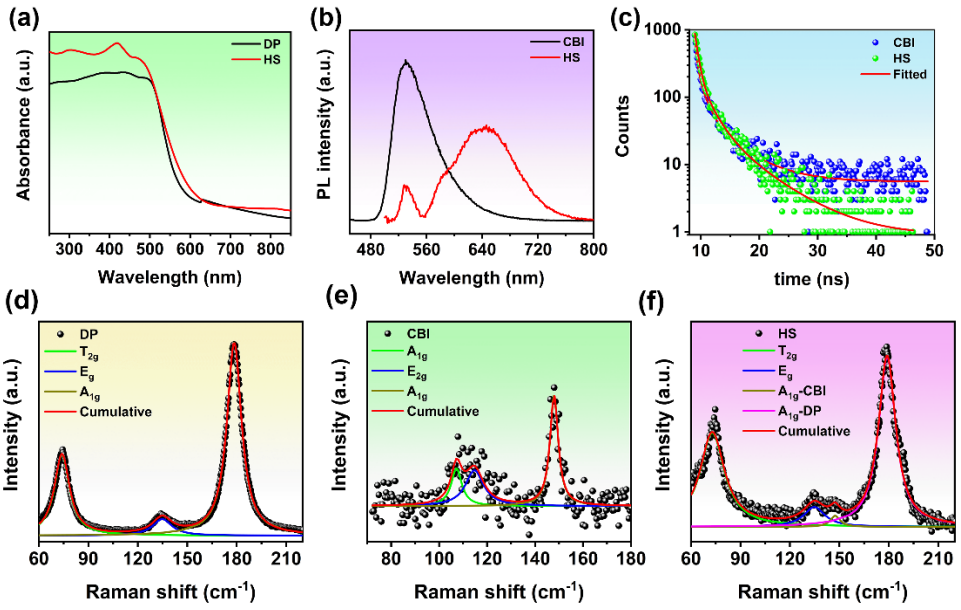

Fig. 5.8: (a) Absorbance spectra of $Cs_2AgBiBr_6$ SC and $Cs_2AgBiBr_6/Cs_3Bi_2I_9$ heterostructure. **(b, c)** Steady-state PL and time-resolved PL spectra of $Cs_3Bi_2I_9$ NC film and $Cs_2AgBiBr_6/Cs_3Bi_2I_9$ heterostructure. **(e-f)** Deconvoluted Raman spectra of $Cs_2AgBiBr_6$ SC, $Cs_3Bi_2I_9$ NC thin film, and $Cs_2AgBiBr_6/Cs_3Bi_2I_9$ heterostructure.

Table 5.2: Peak positions of A_{1g} Raman mode in pristine and the HS materials obtained from the fitted Raman spectra in **Fig. S5**.

Material	A_{1g}-mode (peak position) (cm^{-1})
$Cs_2AgBiBr_6$ (DP)	178.93
$Cs_3Bi_2I_9$ (CBI)	147.44
$Cs_2AgBiBr_6$/$Cs_3Bi_2I_9$ HS	DP (A_{1g}) - 178.45 CBI (A_{1g}) - 147.93

5.3.3 Characterization of the $Cs_2AgBiBr_6$ SC/$Cs_3Bi_2I_9$ NCs Heterostructure

Fig. 5.8 (a) presents a comparison of the absorption spectra of pristine $Cs_2AgBiBr_6$ single crystals (SCs) and the CBI NCs film/$Cs_2AgBiBr_6$ SC heterostructure. An enhanced overall absorption is observed in the CBI NCs/$Cs_2AgBiBr_6$ hybrid structure compared to the pristine $Cs_2AgBiBr_6$ SC, which can be attributed to the co-absorption characteristics of both constituent materials. The heterojunction sample exhibits extended absorption beyond 600 nm, arising from multiple reflections and light-trapping effects at the CBI NC film/$Cs_2AgBiBr_6$ interface.[41,42] Notably, a pronounced enhancement in the 400–550 nm region is observed, primarily due to the combined absorption contributions of CBI NCs and $Cs_2AgBiBr_6$ SCs.[43] The charge transfer dynamics and photogenerated carrier separation within the CBI NCs/$Cs_2AgBiBr_6$ heterojunction were further investigated using steady-state and time-resolved photoluminescence (PL) measurements. **Fig. 5.8(b)** compares the PL spectra of CBI NC films deposited on $Cs_2AgBiBr_6$ single crystals and quartz substrates. Both films exhibit a PL emission peak at 540 nm and 650 nm, corresponding to the band-edge excitonic recombination in CBI and Cs2AgBiBr6 SC, respectively. However, the PL intensity of the CBI NCs on $Cs_2AgBiBr_6$ SC is significantly quenched compared to that on the quartz substrate. This strong PL quenching indicates efficient transfer of photogenerated charge carriers from the CBI NC layer to the $Cs_2AgBiBr_6$ SC across the heterojunction interface, thereby reducing radiative recombination within the CBI NCs.[43] Owing to its efficient photocarrier generation and separation, the $Cs_2AgBiBr_6$ SC/CBI NC film double perovskite/perovskite heterojunction demonstrates significant potential for optoelectronic and photodetection applications. The time-resolved photoluminescence (TRPL) decay profiles of CBI NC films deposited on quartz and $Cs_2AgBiBr_6$ SC substrates are shown in **Fig. 5.8(c)**. A bi-exponential fitting was employed to extract the average PL decay lifetimes, which were found to be 6.65 ns for the CBI NC film and 5.8 ns for the $Cs_2AgBiBr_6$ SC/CBI NC hybrid structure. The notable reduction in the decay

time of the heterojunction film indicates efficient transfer of photogenerated charge carriers from CBI to Cs2AgBiBr6, effectively suppressing radiative recombination.[43] This enhanced charge transfer efficiency directly contributes to the increased photocurrent response observed in the heterojunction-based photodetector. The Raman spectra of $Cs_2AgBiBr_6$ SC, CBI NC thin film, and $Cs_2AgBiBr_6$ SC/CBI NC thin film heterostructure were deconvoluted (**Fig. 5.8(d-f)**). The Raman spectra of the heterostructure illustrate the combination of the two materials, confirming its formation. The corresponding shift in the A_{1g} Raman modes of both materials indicated charge transfer, as shown in **Table 5.2**.

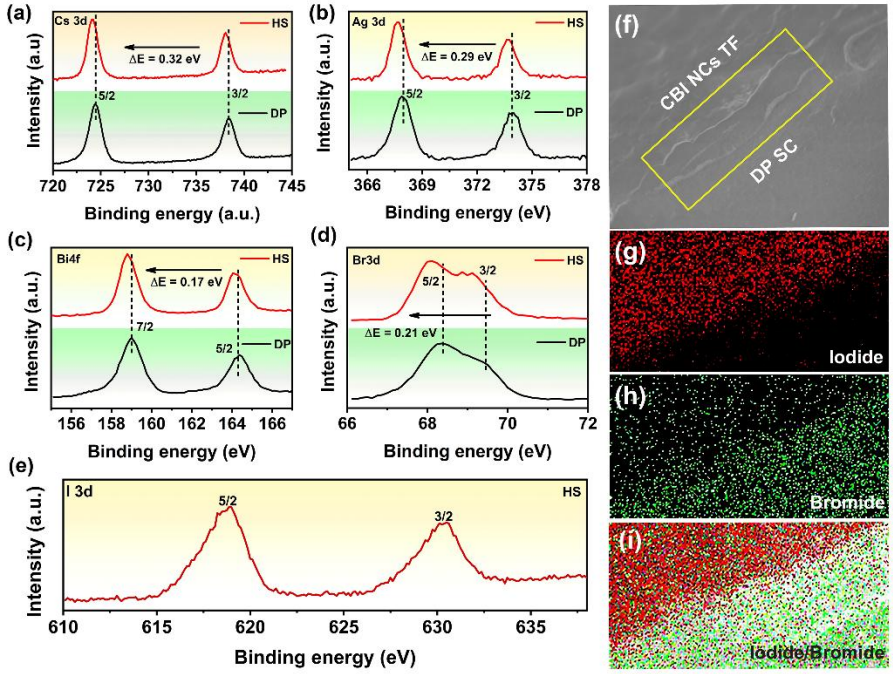

Fig. 5.9: (a-d) Comparison of the XPS spectra of each element of $Cs_2AgBiBr_6/Cs_3Bi_2I_9$ with the elements of pristine Cs2AgBIBr6 SC. **(e)** XPS spectra of iodine element present in $Cs_2AgBiBr_6/Cs_3Bi_2I_9$ heterostructure. **(g-j)** Cross-sectional FESEM image of the HS interface and corresponding elemental mapping of Iodide (from CBI NCs) and bromide (from DP SC).

X-ray photoelectron spectroscopy (XPS) measurements showed distinct peaks for each element in the $Cs_2AgBiBr_6$ SC/CBI heterostructure (**Fig. 5.9(a-e)**). The shift in the binding energies of each element of $Cs_2AgBiBr_6$ SC after heterostructure formation suggested the charge transfer from CBI to $Cs_2AgBiBr_6$ SC.[32] Furthermore, the presence of distinct peaks of iodine confirmed the uniform formation of the heterostructure. The XPS spectra for each element are deconvoluted to understand the elemental composition of each material present in the HS system. The peak area (A) and XPS sensitivity factor (RSF) are listed in **Table 5.3**. XPS analysis of DPSC/CBI HS shows a surface composition of $Cs_{2.67}Ag_{0.82}Bi_1Br_{4.40}I_{0.74}$

(Normalized to Bi=1). Comparison with the ideal phases and theoretical 90:10 mixture indicates that the Ag/Bi ratio matches the expected proportion, confirming ~90% $Cs_2AgBiBr_6$ and ~10% $Cs_3Bi_2I_9$. However, the surface is clearly Cs-rich and Br/I-deficient compared to the ideal stoichiometry (**Table 5.4**). This deviation suggests Cs segregation and partial halide loss, phenomena commonly observed in halide double perovskites under vacuum or X-ray exposure.

Table 5.3: Stoichiometric ratio calculations obtained from deconvoluted XPS spectra of each element.

Element	Peak Area (A)	RSF (S)	Corrected Intensity (A/S)	Atomic %	Stoichiometric Ratio (Bi=1)
Cs	60835.42	7.041	8640.17	27.8	2.67
Ag	15819.38	5.987	2642.29	8.5	0.82
Bi	29549.46	9.140	3232.98	10.4	1.00
Br	14966.11	1.053	14212.83	45.7	4.40
I	14777.52	6.206	2381.17	7.7	0.74

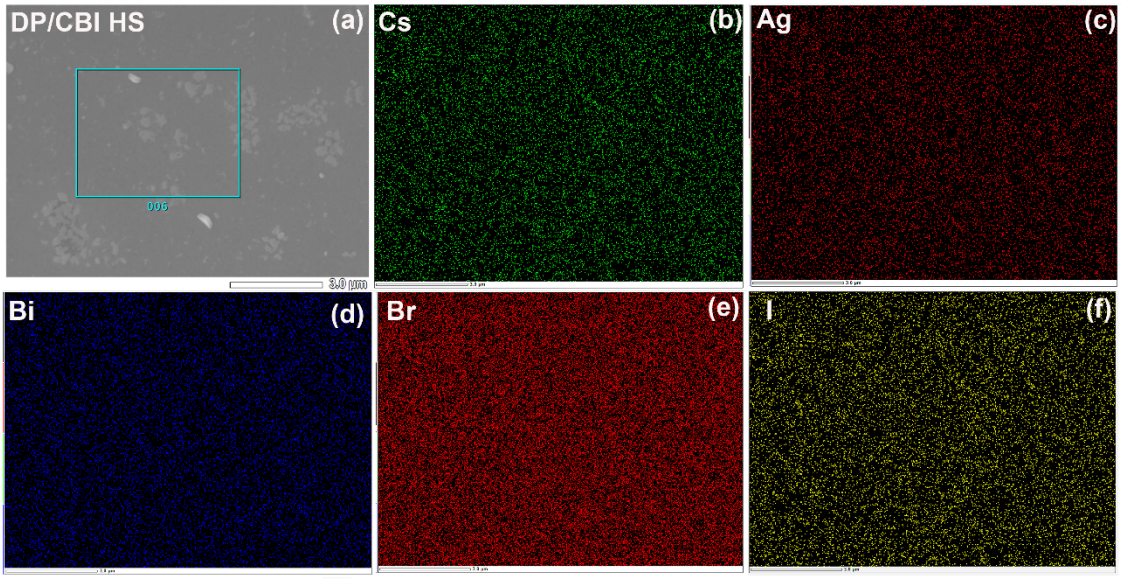

Fig. 5.10: (a) FESEM image of the DP/CBI HS. **(b-f)** FESEM-EDX mapping of all the constituent elements present in the HS.

To further substantiate the interface quality, we analysed the surface and cross-sectional SEM imaging along with corresponding EDX mapping (**Fig. 5.9(f-i)).** The cross-sectional images clearly demonstrate a continuous and well-adhered NC layer on top of the single crystal. Additionally, elemental mapping of iodine (from $Cs_3Bi_2I_9$) and bromine (from $Cs_2AgBiBr_6$)

has been provided to distinctly identify the NC layer and the underlying single crystal, confirming uniform heterointerface formation and consistent film thickness. The FESEM-EDX mapping of all the constituent elements of the HS indicates the uniform formation of the CBI NC thin film on the DP single crystal surface (**Fig. 5.10 (a-f)**).

Table 5.4: Comparison of the theoretical and measured composition of the DPSC/CBI HS from XPS data.

Composition	Cs	Ag	Bi	Br	I	Comment
Ideal $Cs_2AgBiBr_6$	2	1	1	6	0	No Iodide
Ideal $Cs_3Bi_2I_9$	1.50	0	1	0	4.50	No Silver, No Bromide
Theoretical (90:10) ($Cs_2AgBiBr_6$:$Cs_3Bi_2I_9$)	1.91	0.82	1	4.91	0.82	Expected for 90:10 mixture for Bi=1
XPS (Bi=1)	2.67	0.82	1	4.40	0.74	Measured surface composition

5.3.4 Photodetector Performance

A planar heterojunction X-ray detector with the configuration Au/$Cs_2AgBiBr_6$ SC/CBI NC film/Au was fabricated using a $Cs_2AgBiBr_6$ SC. The device architecture of the photodetector is illustrated in the **Fig. 5.12(a)**. For comparison, a control device with the same structure but without the CBI NC film (Au/$Cs_2AgBiBr_6$ SC/Au) was also fabricated to evaluate the influence of the CBI NC layer on the detector's performance. The optical image of the fabricated device is presented in the inset of **Fig. 5.12(a)**, where the active illuminated area was estimated to be approximately 5×10^{-4} cm^2 using ImageJ software. A 450 nm laser was used for the photodetector application due to the maximum absorption of the heterostructure device in the range of 300-600 nm wavelength. The current–voltage (I–V) characteristics of the $Cs_2AgBiBr_6$ SC and $Cs_2AgBiBr_6$ SC/CBI NC device were measured both in the dark and under varying laser power densities, as depicted in **Fig. 5.12(b, c)**, respectively. With increasing laser power density, the photocurrent increased, confirming efficient photoresponse. The $Cs_2AgBiBr_6$/CBI heterostructure demonstrates a significantly enhanced photocurrent and a substantial suppression of dark current, compared to the pristine $Cs_2AgBiBr_6$ double perovskite (DP) device, as shown in **Fig. 5.12(d)**. Multiple devices were fabricated to test the reliability and reproducibility of the HS. The resulting devices exhibited similar I-V characteristics under

identical conditions, with a sample standard deviation of less than 7%, confirming the uniformity and reproducibility of the HS devices (**Fig. 5.11(a)**). To further substantiate our claims, we fabricated a control device by coating the DP single crystal with a Poly(methyl methacrylate) PMMA layer (5 mg dissolved in 5 mL Chlorobenzene) and measured its I-V characteristics under identical conditions (**Fig. 5.11(b)**). The DP-PMMA device showed reduced dark current, proving that PMMA effectively passivates surface defects. However, the photocurrent enhancement was negligible compared to the HS device. Moreover, the dark current of the DP-PMMA device remained higher than that of the HS device.

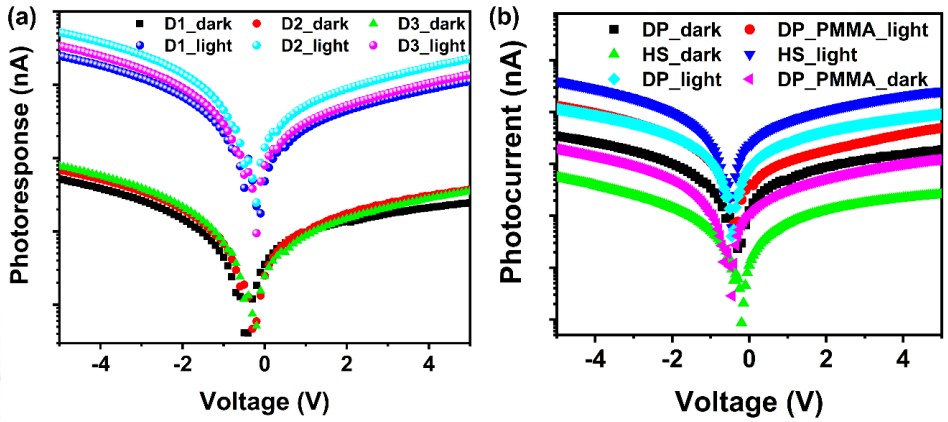

Fig. 5.11: (a) I-V characteristics of the multiple HS devices with the same configuration. **(b)** Comparison of the I-V characteristics of DP, DP-PMMA, and HS devices.

These results clearly indicate that while PMMA passivation reduces surface trap-assisted leakage, it neither generates significant photocurrent nor creates a built-in electric field. Therefore, the superior performance of the HS device arises predominantly from the combined effects of enhanced optical absorption and efficient interfacial charge separation driven by the built-in electric field at the heterojunction interface. The dark current in the heterostructure was suppressed significantly (one order of magnitude). The observed improvement in photocurrent in the heterojunction device can primarily be attributed to the strong light absorption of Cs2AgBiBr6 and the efficient charge transfer at the $Cs_2AgBiBr_6$/CBI interface, which collectively facilitate enhanced photocarrier separation and transport.[44] The current on/off ratios for both devices are compared in **Fig. 5.12(e)**, revealing that the $Cs_2AgBiBr_6$/CBI heterostructure achieves an enhancement of nearly two orders of magnitude (≈30×) over the pristine $Cs_2AgBiBr_6$ SC detector. This substantial improvement can be attributed to efficient interfacial charge transfer, reduced self-trapped exciton emission, and suppressed dark current within the heterostructure. The results are consistent with the photoluminescence (PL)

quenching and shorter carrier recombination lifetimes observed earlier, confirming that the strong interfacial coupling between $Cs_2AgBiBr_6$ and CBI facilitates rapid charge separation and minimizes non-radiative recombination losses. Furthermore, to quantitatively investigate the relationship between photocurrent and illumination power density, the photocurrent response at a bias voltage of -5 V was measured and plotted, as shown in **Fig. 5.12(f, g)**.

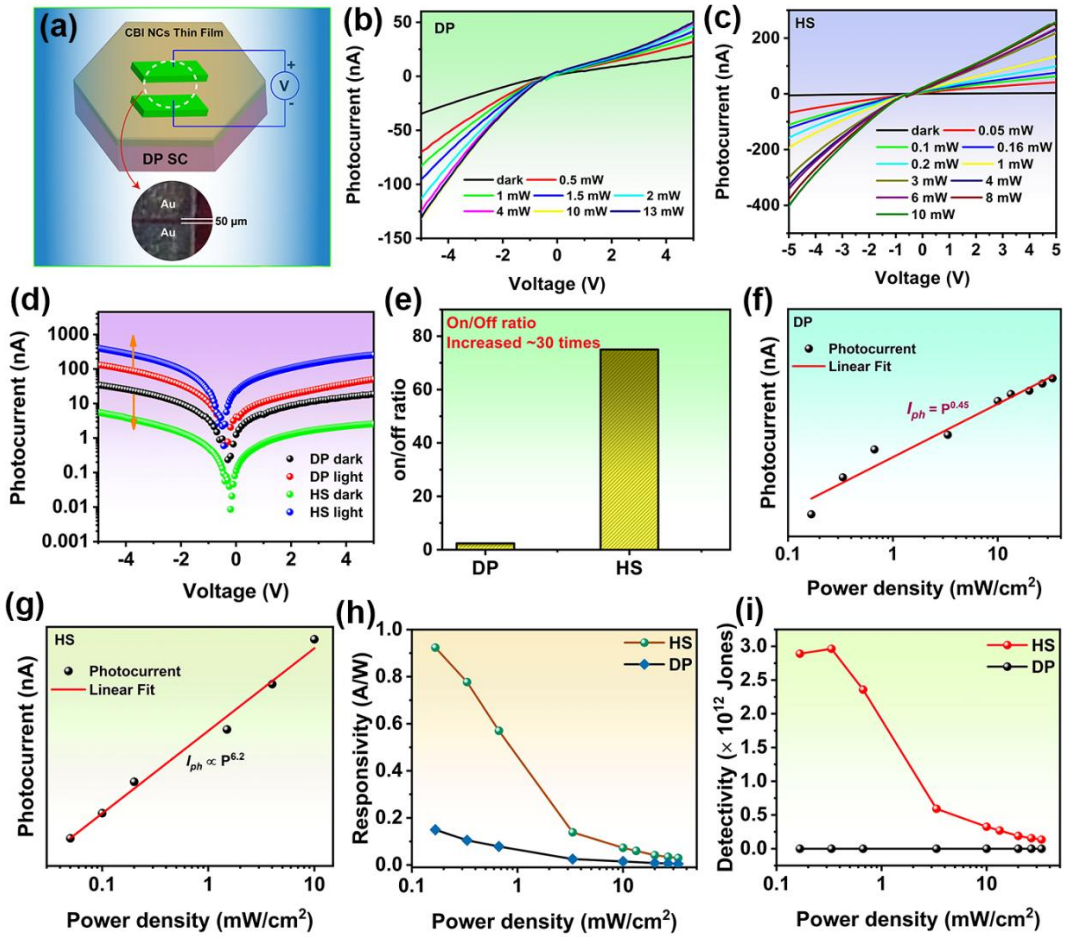

Fig. 5.12: (a) Schematic of the $Cs_2AgBiBr_6/Cs_3Bi_2I_9$ heterostructure device. The inset shows the optical image of the device. **(b, c)** I-V curve of the $Cs_2AgBiBr_6$ Sc and $Cs_2AgBiBr_6/Cs_3Bi_2I_9$ heterostructure device. **(d)** Comparison of the I-V curve of $Cs_2AgBiBr_6$ and $Cs_2AgBiBr_6/Cs_3Bi_2I_9$ heterostructure device. **(e)** Comparison of the on/off ratio of $Cs_2AgBiBr_6$ and $Cs_2AgBiBr_6/Cs_3Bi_2I_9$ device. **(f, g)** Photoresponse vs laser power density of $Cs_2AgBiBr_6$ and $Cs_2AgBiBr_6/Cs_3Bi_2I_9$ heterostructure device. **(h, i)** comparison of the responsivity and specific detectivity of $Cs_2AgBiBr_6$ and $Cs_2AgBiBr_6/Cs_3Bi_2I_9$ heterostructure device, respectively.

The observed dependence further validates the efficient photoresponse behaviour and robust charge separation dynamics in the $Cs_2AgBiBr_6$/CBI heterostructure system. From the power law, the θ value for each case is calculated, and the HS showed improved θ values compared

to the pristine sample, making it more ideal for photodetector applications. Responsivity (R) and specific detectivity (D) are key parameters commonly used to evaluate the performance of photodetectors. The responsivity (R) represents the device's efficiency in converting incident optical power into electrical current, whereas the specific detectivity (D) reflects its ability to distinguish weak optical signals from background noise. The responsivity can be calculated using the relation:[44]

$$R = \frac{I_{light} - I_{dark}}{P_{in} \times A} \tag{5.2}$$

where I_{light} and I_{dark} are the photocurrent and dark current, respectively, P_{in} is the incident light power density, and A is the active illuminated area. The specific detectivity (D*) can be calculated using the equation below:[45]

$$D = \frac{R}{\sqrt{2qI_{dark}}} \tag{5.3}$$

Where R is the responsivity of the device, q is the electronic charge, and I_{dark} is the dark current of the HS device. Remarkably, under a light power density of 0.2 mW cm^{-2}, the $Cs_2AgBiBr_6$/CBI heterostructure photodetector exhibits a high responsivity of 0.92 A W^{-1}, as shown in **Fig. 5.12(h)**, highlighting its excellent photoresponse efficiency under low-light conditions.

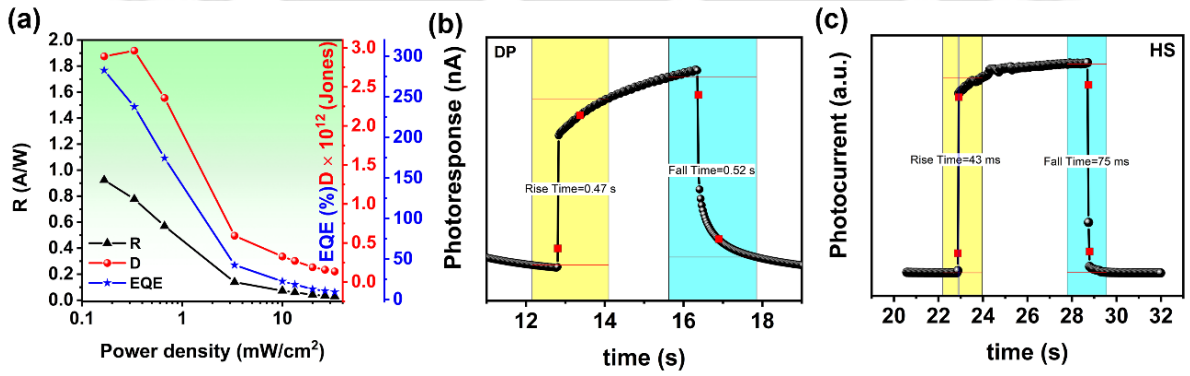

Fig. 5.13: (a) Comparison of responsivity, detectivity and external quantum efficiency of the $Cs_2AgBiBr_6$/$Cs_3Bi_2I_9$ heterostructure device. **(b, c)** rise and fall time of pristine $Cs_2AgBiBr_6$ SC and $Cs_2AgBiBr_6$/$Cs_3Bi_2I_9$ heterostructure device.

As the incident light power density increases, a gradual decrease in responsivity is observed. This reduction can be attributed to the enhanced carrier recombination rate at higher illumination intensities, which limits the number of photogenerated carriers contributing to the

external current. Despite this trend, the $Cs_2AgBiBr_6$/CBI heterostructure photodetector exhibits an exceptionally high specific detectivity (D*) of 2.97×10^{12} Jones at a low power density of 0.2 mW cm^{-2} (**Fig. 5.12(i)**), highlighting its remarkable sensitivity to weak optical signals. These results clearly demonstrate that the present heterostructure device exhibits superior performance, particularly in terms of both detectivity and current on/off ratio.

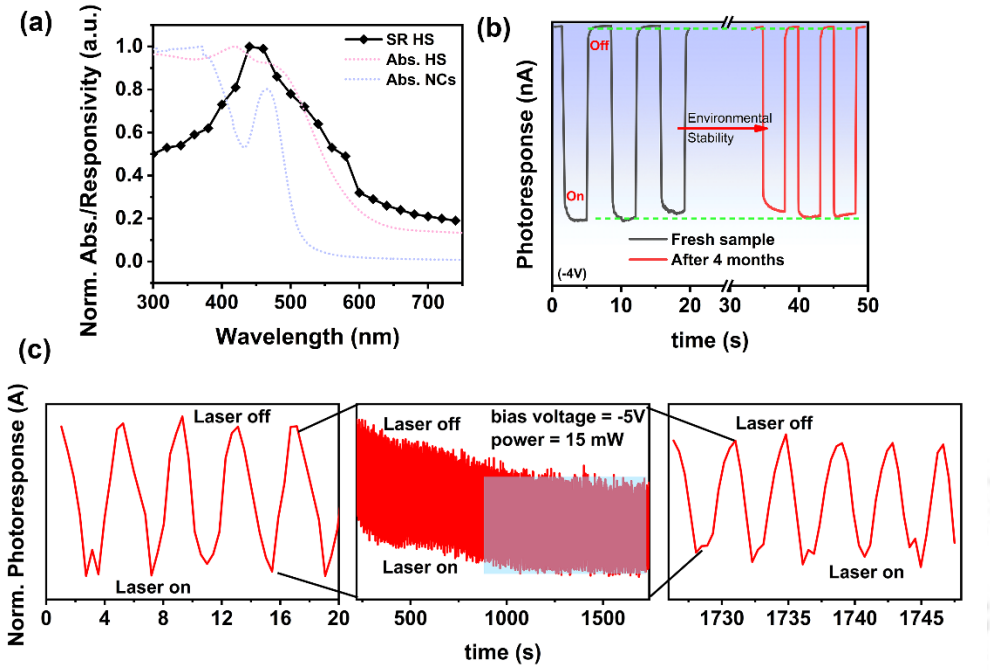

Fig. 5.14: (a) Spectral responsivity of the HS device with reference to the absorbance of HS and CBI NCs. **(b)** Stability performance of the HS device after 4 months of storage under ambient conditions. **(c)** Photoresponse of the HS device under continuous illumination of a 450 nm laser.

The external quantum efficiency of the device was calculated using the relation:[45]

$$EQE = \frac{hcR_\lambda}{e\lambda} \tag{5.4}$$

Where R_λ is the responsivity for a specific wavelength and λ is the wavelength used for the photodetection. The EQE of the $Cs_2AgBiBr_6$ SC/CBI HS improved by ~100× that of the pristine $Cs_2AgBiBr_6$ SC device (**Fig. 5.13(a)**). Furthermore, the rise and fall time of the HS device was reduced significantly (**Fig. 5.13(b, c)**). The spectral responsivity of the HS device was measured over a wavelength range of 300 to 750 nm (**Fig. 5.14 (a)**). The HS device exhibited its highest responsivity between 420 to 480 nm, with a gradual decrease at longer wavelengths consistent with the excitonic absorption peak of CBI NCs. To better understand this behaviour, the spectral responsivity of the HS device was compared with the absorption

spectra of both the heterostructure and the CBI NCs. The spectral response closely follows the HS absorption profile, indicating that the photoresponse is governed by the combined light-harvesting properties of the constituent materials. The high responsivity observed in the 420-480 nm region correlates well with the enhanced excitonic absorption arising primarily from the CBI NCs, while the extended response at longer wavelengths is attributed to the absorption contribution from the DP single crystal. This correspondence confirms that the heterostructure enables broadband photodetection across the entire visible region. These improved characteristics of the HS device proved the significance of perovskite-perovskite heterostructure in advanced optoelectronic applications. There was no reduction in the photoresponse of the HS device after 4 months of storage in ambient conditions (**Fig. 5.14 (b)**), proving the high stability of the lead-free halide perovskite-perovskite heterostructure for advanced optoelectronic applications. Furthermore, operational stability measurements were carried out on HS devices under continuous 450 nm laser illumination. The device was tested at a relatively high bias voltage (-5V) and an elevated laser power (15 mW) to assess its operational robustness under harsh conditions. The photocurrent and dark current were monitored continuously for more than 2000 s and more than 800 cycles (**Fig. 5.14(c)**). An initial gradual increase in both dark current and photocurrent was observed during the first ~1000 s of illumination, after which the device response stabilized.

Table 5.5. Comparison of the photodetection performance of lead-based and lead-free perovskite single crystals.

Device Configuration	**R (A/W)**	**D*(Jones)**	**Rise/fall time**	**references**
Au/$CsPbBr_3$ SC/Au	0.028	---	90.7/57 ms	46
Au/Ti/$MAPbCl_3$ SC/Pt	0.046	1.2×10^{10}	24/62 ms	47
Au/Er-$Cs_2AgBiBr_6$ SC/Au	0.016	2.94×10^{10}	242/342 ms	48
C/$(PA)_2PbBr_4$/C	2.22	2.3×10^{13}	1.59/1.66 ms	49
Ag/Quassi-2D perovskite/Ag	0.016	2.06×10^{12}	220/240 µs	50
Au/$CH_3NH_3PbBr_3$/Au	5600	6.59×10^{11}	3.2/9.2 µs	51
Ag/$(BA)_2CsAgBiBr_7$/C	0.422×10^{-3}	3.86×10^{10}	420/910 µs	52
Au/$Cs_2AgBiBr_6$/$Cs_3Bi_2I_9$/Au	0.98	2.97×10^{12}	43/75 ms	*This work*

This transient behaviour may be attributed to charge accumulation and interfacial capacitance effects, particularly considering the low modulation frequency of the laser pulse (250 mHz), which can influence carrier extraction dynamics and interfacial equilibrium. After this initial equilibration period, the device reached a steady-state operational condition. Importantly, no degradation in either photocurrent or dark current was observed during the 2000s continuous illumination test, confirming the excellent operational stability of the HS device even under prolonged, relatively extreme illumination conditions. **Table 5.5** summarises the comparative metrics of lead-based and lead-free perovskite SC photodetectors, indicating potential application of DPSC/CBI NCs HS for advanced optoelectronic applications.

5.3.5 UPS Study

Ultraviolet photoelectron spectroscopy (UPS) measurements were performed to determine the energy band positions and to gain deeper insight into the carrier transfer kinetics across the $Cs_2AgBiBr_6$/CBI heterojunction. The UPS spectra were utilized to extract both the work function (ϕ) and the valence band maximum (VBM) positions, enabling the construction of the energy band alignment diagram when combined with the optical bandgap values obtained from absorption spectroscopy.

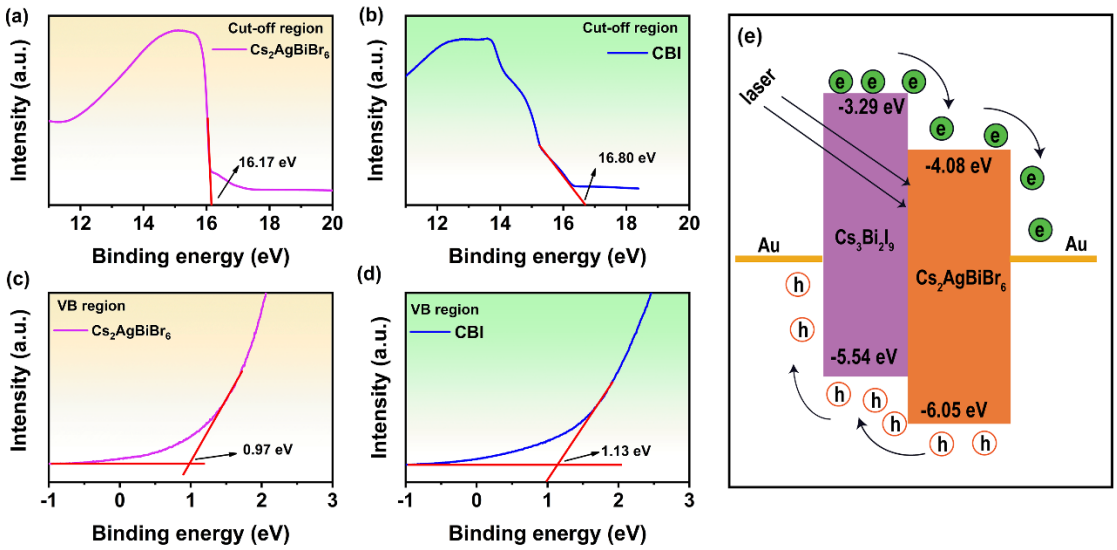

Fig. 5.15: (a, b) UPS cut-off region for $Cs_2AgBiBr_6$ and $Cs_3Bi_2I_9$, respectively. **(c, d)** UPS valence band edge region for $Cs_2AgBiBr_6$ and $Cs_3Bi_2I_9$, respectively. **(e)** Energy-level diagram of Au/$Cs_3Bi_2I_9$/ $Cs_2AgBiBr_6$ /Au heterojunction showing photogenerated charge carrier generation and separation.

The work function (ϕ) was calculated using the relation:[26]

$$\phi = h\nu - E_{\text{cutoff}} \quad (5.5)$$

where $h\nu$ represents the photon energy of the He I source (21.2 eV), and E_{cutoff} corresponds to the secondary electron cut-off energy observed at higher binding energy. The intersection points between the secondary electron cut-off and the baseline provide the value of E_{cutoff}. As illustrated in **Fig. 5.15(a, b)**, the cut-off energies were determined to be 16.17 eV for $Cs_2AgBiBr_6$ and 16.80 eV for CBI, respectively. These values were subsequently used to evaluate the relative work functions and band alignment, which are crucial for understanding charge transport and interfacial carrier dynamics in the heterojunction system. Based on the UPS measurements, the work functions (ϕ) of $Cs_2AgBiBr_6$ and $Cs_3Bi_2I_9$ were determined to be 5.03 eV and 4.4 eV, respectively. The energy difference between the Fermi level (E_n) and the valence band maximum (E_v), denoted as ($E_n - E_v$), was obtained by extrapolating the linear portion of the UPS spectra toward the low-binding energy region. As shown in **Fig. 5.15(c, d)**, these values were found to be 0.97 eV for $Cs_2AgBiBr_6$ and 1.13 eV for $Cs_3Bi_2I_9$, respectively. Using these parameters, the energy band alignment diagram for the $Cs_2AgBiBr_6$/CBI heterojunction was constructed, as illustrated in **Fig. 5.15(e)**. The diagram confirms the formation of a type-II staggered band alignment, which facilitates efficient charge separation across the interface. Due to the difference in work functions between the two materials, electrons flow spontaneously from CBI (lower ϕ) to $Cs_2AgBiBr_6$ (higher ϕ) until Fermi-level equilibrium is achieved. This interfacial charge redistribution leads to the establishment of a built-in electric field at the junction, promoting directional carrier transport and suppressing recombination losses, thereby enhancing photodetector performance. As a consequence of the difference in work functions, an inherent electric field is established at the $Cs_2AgBiBr_6$/CBI heterojunction interface. This built-in field gives rise to a depletion region and an internal potential barrier, which collectively suppress the flow of thermally generated carriers across the junction, thereby reducing the dark current of the device.[26] Under laser irradiation, the junction electric field facilitates the generation and rapid separation of electron–hole pairs, enabling self-biased photodetection even in the absence of an external voltage. When an external bias is applied, the efficient separation and collection of charge carriers by the electrodes further enhances the photoresponse, resulting in a significant increase in detector responsivity. The exceptionally high responsivity and detectivity observed in the heterojunction detector can be attributed to a synergistic combination of effects, including: (i) the optical photon reabsorption due to PL emission of the CBI nanocrystals generating more charge carriers and (ii) the efficient charge transfer and collection induced by band bending at the type-

II heterojunction interface. Together, these mechanisms contribute to enhanced photocarrier extraction efficiency, reduced recombination losses, and ultimately, superior photodetection performance of the $Cs_2AgBiBr_6$/CBI heterostructure device.

5.3.6 DFT Calculations

To gain a deeper understanding of the charge transfer dynamics at the perovskite heterojunction interface and the associated electronic structure, we performed first-principles density functional theory (DFT) calculations. The simulations were conducted using a single cubic unit cell of $Cs_2AgBiBr_6$ and a hexagonal unit cell of $Cs_3Bi_2I_9$, the latter transformed to an orthorhombic configuration to construct a heterostructure model. The optimized atomic structures of $Cs_2AgBiBr_6$, $Cs_3Bi_2I_9$, and their heterointerface are illustrated in **Fig. 5.16(a)**.

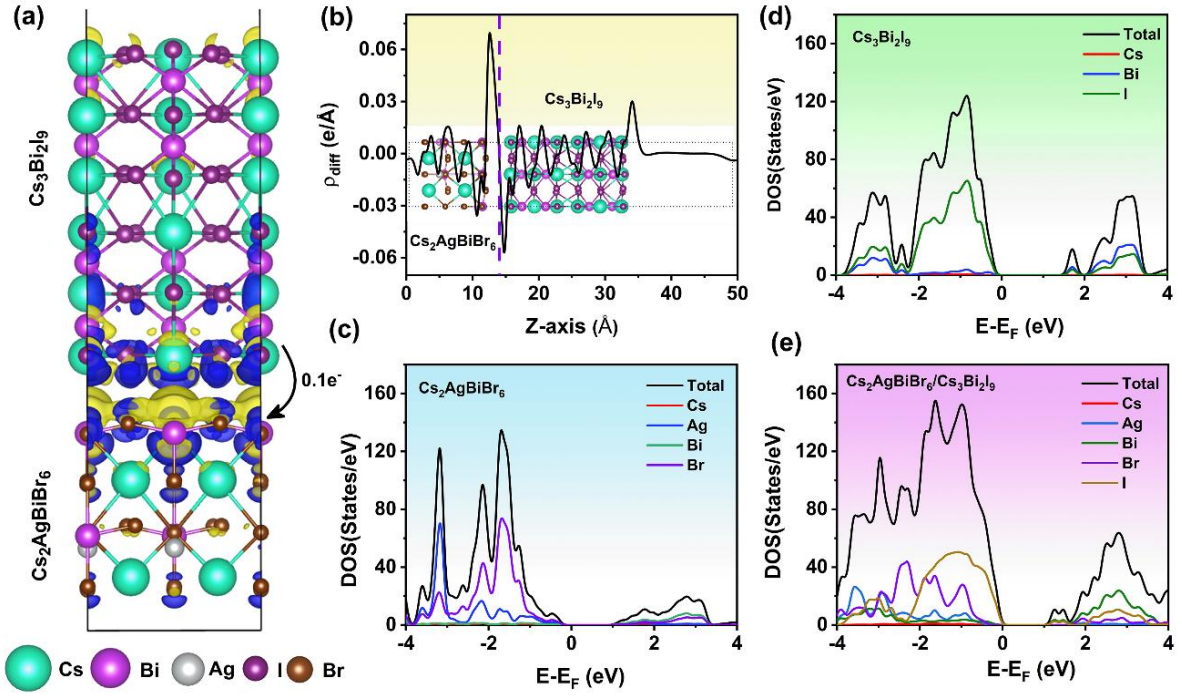

Fig. 5.16: (a) Optimised configuration of $Cs_2AgBiBr_6/Cs_3Bi_2I_9$ heterostructure. **(b)** Charge density difference of $Cs_2AgBiBr_6/Cs_3Bi_2I_9$ heterostructure. Projected density of states of **(c)** $Cs_2AgBiBr_6$, **(d)** $Cs_3Bi_2I_9$, **(e)** $Cs_2AgBiBr_6/Cs_3Bi_2I_9$ heterostructure.

To probe the interfacial charge redistribution and migration behaviour, we performed the charge density difference (CDD) analysis. As shown in **Fig. 5.16(a)**, the yellow and blue isosurfaces represent regions of electron accumulation and depletion, respectively, indicating a net electron transfer from $Cs_3Bi_3I_9$ toward the surface of $Cs_2AgBiBr_6$.[32] This directionality of charge flow is further substantiated by the plane-averaged CDD profile (**Fig. 5.16(b)**), which exhibits prominent positive peaks in the $Cs_2AgBiBr_6$ region and corresponding negative peaks

in the $Cs_3Bi_2I_9$ domain. Bader charge analysis quantifies this transfer, revealing a net charge loss of approximately 0.1e per unit cell from $Cs_3Bi_2I_9$, which is subsequently gained by $Cs_2AgBiBr_6$. These results suggest a lower work function for $Cs_2AgBiBr_6$ compared to $Cs_3Bi_2I_9$, corroborating the observed electron migration direction. As a consequence of this interfacial charge redistribution, $Cs_3Bi_2I_9$ exhibits p-type character, while $Cs_2AgBiBr_6$ becomes increasingly n-type. Such band alignment facilitates favourable band bending under reverse bias, promoting efficient charge separation and thereby enhancing the photocurrent response. To elucidate the impact of heterojunction formation on the electronic structure, we conducted total and projected density of states (TDOS and PDOS) analysis. The computed band gaps for pristine $Cs_3Bi_2I_9$ and $Cs_2AgBiBr_6$ are found to be approximately 1.2 eV and 1.5 eV, respectively (**Fig. 5.16(c, d)**), which are somewhat underestimated due to the well-known limitations of standard DFT in accurately predicting bandgap energies. Nonetheless, our focus is on understanding the relative evolution of the electronic states upon hybridization. Notably, the heterostructure exhibits a reduced bandgap, accompanied by the emergence of additional electronic states near the Fermi level (**Fig. 5.16(e)**) compared to the individual pristine materials. This phenomenon is expected to enhance charge carrier mobility, suppress recombination processes, and improve photodetection efficiency. Furthermore, our DFT calculations confirm the formation of a type-II (staggered) band alignment at the $Cs_2AgBiBr_6/Cs_3Bi_2I_9$ interface, consistent with the results obtained from ultraviolet photoelectron spectroscopy (UPS) measurements.

5.4 Conclusion

In summary, we have demonstrated the potential of a novel $Cs_2AgBiBr_6$ single crystal (SC)/$Cs_3Bi_2I_9$ (CBI) nanocrystal film heterojunction for high-performance photodetection applications. The $Cs_2AgBiBr_6$ single crystals were synthesized via a conventional slow-cooling crystallization method, while the CBI nanocrystals were prepared using a surfactant-assisted mechanochemical route to obtain a stable colloidal dispersion in toluene. The heterojunction architecture was constructed by depositing the CBI NC film onto the $Cs_2AgBiBr_6$ SC surface, forming a well-defined perovskite–perovskite interface. Comprehensive photoluminescence (PL) and time-resolved photoluminescence (TRPL) analyses confirmed the efficient transfer of photogenerated charge carriers from the CBI NC film to the $Cs_2AgBiBr_6$ SC, indicating strong interfacial coupling and effective charge separation. These observations highlight the favourable band alignment and reduced carrier recombination within the heterostructure, underscoring its promise for advanced optoelectronic applications. Compared with the pristine

$Cs_2AgBiBr_6$ single-crystal device, the fabricated Au/$Cs_2AgBiBr_6$ SC/CBI NC film/Au heterojunction detector exhibited a higher photocurrent response and a significantly lower dark current, confirming its superior photoresponse efficiency and enhanced photodetection capability. The observed enhancement in photocurrent can be attributed to effective carrier generation and separation, facilitated by the favourable band bending at the type-II $Cs_2AgBiBr_6$/CBI heterojunction interface. The built-in electric field established across the heterojunction enables efficient drift-assisted charge separation, thereby minimizing carrier recombination losses. As a result, the device exhibited a remarkable responsivity of 0.98 AW^{-1} under -5V external bias, confirming the presence of a strong potential capable of driving charge transport. The device exhibited a high specific detectivity of 2.97×10^{12} Jones, which is exceptionally high compared to the pristine $Cs_2AgBiBr_6$ SC device. The results showed a higher on/off ratio and fast rise and fall time compared to the pristine $Cs_2AgBiBr_6$ SC device. Moreover, density functional theory (DFT) electronic structure calculations revealed a clear electron transfer from CBI to $Cs_2AgBiBr_6$, consistent with the experimentally observed type-II band alignment and the enhanced charge separation efficiency. Collectively, these findings confirm that the $Cs_2AgBiBr_6$/$Cs_3Bi_2I_9$ heterojunction exhibits a synergistic combination of higher absorption and efficient interfacial charge transfer, positioning it as a promising candidate for next-generation high-performance photodetectors and broad-spectrum optoelectronic devices.

References

1 S. Wang, Y. Jiang, E. J. Juarez-Perez, L. K. Ono and Y. Qi, *Nat Energy*, DOI:10.1038/nenergy.2016.195.

2 Z. Chen, Q. Dong, Y. Liu, C. Bao, Y. Fang, Y. Lin, S. Tang, Q. Wang, X. Xiao, Y. Bai, Y. Deng and J. Huang, *Nat Commun*, DOI:10.1038/s41467-017-02039-5.

3 G. Tong, L. K. Ono and Y. Qi, *Wiley-VCH Verlag*, 2020, preprint, DOI: 10.1002/ente.201900961.

4 A. Kojima, K. Teshima, Y. Shirai and T. Miyasaka, *J Am Chem Soc*, 2009, 131, 6050–6051.

5 C. N. Savory, A. Walsh and D. O. Scanlon, *ACS Energy Lett*, 2016, 1, 949–955.

6 T. Leijtens, G. E. Eperon, N. K. Noel, S. N. Habisreutinger, A. Petrozza and H. J. Snaith, *Adv Energy Mater*, DOI:10.1002/aenm.201500963.

7 H. Cho, Y. H. Kim, C. Wolf, H. D. Lee and T. W. Lee, *Wiley-VCH Verlag*, 2018, preprint, DOI: 10.1002/adma.201704587.

8 Z. Zhu, Q. Sun, Z. Zhang, J. Dai, G. Xing, S. Li, X. Huang and W. Huang, *Royal Society of Chemistry*, 2018, preprint, DOI: 10.1039/C8TC03164A.

9 M. Lyu, J. H. Yun, P. Chen, M. Hao and L. Wang, *Wiley-VCH Verlag*, 2017, preprint, DOI: 10.1002/aenm.201602512.

10 A. Babayigit, A. Ethirajan, M. Muller and B. Conings, *Nature Publishing Group*, 2016, preprint, DOI: 10.1038/nmat4572.

11 X. Li, J. Shi, J. Chen, Z. Tan and H. Lei, *MDPI*, 2023, preprint, DOI: 10.3390/ma16124490.

12 E. T. McClure, M. R. Ball, W. Windl and P. M. Woodward, *Chemistry of Materials*, 2016, 28, 1348–1354.

13 M. R. Filip, S. Hillman, A. A. Haghighirad, H. J. Snaith and F. Giustino, *Journal of Physical Chemistry Letters*, 2016, 7, 2579–2585.

14 M. R. Filip, X. Liu, A. Miglio, G. Hautier and F. Giustino, *Journal of Physical Chemistry C*, 2018, 122, 158–170.

15 G. Volonakis, M. R. Filip, A. A. Haghighirad, N. Sakai, B. Wenger, H. J. Snaith and F. Giustino, *Journal of Physical Chemistry Letters*, 2016, 7, 1254–1259.

16 J. Yang, P. Zhang and S. H. Wei, *Journal of Physical Chemistry Letters*, 2018, 9, 31–35.

17 L. Schade, A. D. Wright, R. D. Johnson, M. Dollmann, B. Wenger, P. K. Nayak, D. Prabhakaran, L. M. Herz, R. Nicholas, H. J. Snaith and P. G. Radaelli, *ACS Energy Lett*, 2019, 4, 299–305.

18 Z. Weng, J. Qin, A. A. Umar, J. Wang, X. Zhang, H. Wang, X. Cui, X. Li, L. Zheng and Y. Zhan, *Adv Funct Mater*, DOI:10.1002/adfm.201902234.

19 E. Greul, M. L. Petrus, A. Binek, P. Docampo and T. Bein, *J Mater Chem A Mater*, 2017, 5, 19972–19981.

20 C. Wu, Q. Zhang, Y. Liu, W. Luo, X. Guo, Z. Huang, H. Ting, W. Sun, X. Zhong, S. Wei, S. Wang, Z. Chen and L. Xiao, *Advanced Science*, DOI:10.1002/advs.201700759.

21 L. Yin, H. Wu, W. Pan, B. Yang, P. Li, J. Luo, G. Niu and J. Tang, *Adv Opt Mater*, DOI:10.1002/adom.201900491.

22 B. Yang, W. Pan, H. Wu, G. Niu, J. H. Yuan, K. H. Xue, L. Yin, X. Du, X. S. Miao, X. Yang, Q. Xie and J. Tang, *Nat Commun*, DOI:10.1038/s41467-019-09968-3.

23 Q. Hu, Z. Deng, M. Hu, A. Zhao, Y. Zhang, Z. Tan, G. Niu, H. Wu and J. Tang, *Sci China Chem*, 2018, 61, 1581–1586.

24 W. Shen, U. Jung, Z. Xian, B. Jung and J. Park, *J Alloys Compd*, DOI:10.1016/j.jallcom.2022.167329.

25 J. A. Steele, W. Pan, C. Martin, M. Keshavarz, E. Debroye, H. Yuan, S. Banerjee, E. Fron, D. Jonckheere, C. W. Kim, W. Baekelant, G. Niu, J. Tang, J. Vanacken, M. Van der Auweraer, J. Hofkens and M. B. J. Roeffaers, *Advanced Materials*, DOI:10.1002/adma.201804450.

26 J. Ghosh, N. K. Tailor, K. Ghosh, J. Jayarathne, S. Choudhary, C. Crean, P. K. Giri, S. Satapathi and P. Sellin, *Adv Opt Mater*, DOI:10.1002/adom.202402497.

27 J. Ghosh, J. O'Neill, M. G. Masteghin, I. Braddock, C. Crean, R. Dorey, H. Salway, M. Anaya, J. Reiss, D. Wolfe and P. Sellin, *ACS Appl Nano Mater*, 2023, 6, 14980–14990.

28 G. Sun, J. Kürti, P. Rajczy, M. Kertesz, J. Hafner and G. Kresse, *Performance of the Vienna ab initio simulation package (VASP) in chemical applications q*, .

29 P. J. Hasnip and C. J. Pickard, *Comput Phys Commun*, 2006, 174, 24–29.

30 J. P. Perdew, K. Burke and M. Ernzerhof, *Generalized Gradient Approximation Made Simple*, 1996.

31 G. Kresse and J. Furthmü, *Efficient iterative schemes for ab initio total-energy calculations using a plane-wave basis set*, 1996.

32 R. Chahal, S. Ghosal, J. Ghosh and P. K. Giri, *Nanoscale*, 2025, 17, 9401–9417.

33 R. Chahal, A. Bora and P. K. Giri, *ACS Appl Energy Mater*, 2023, 6, 8794–8807.

34 K. Du, W. Meng, X. Wang, Y. Yan and D. B. Mitzi, *Angewandte Chemie*, 2017, 129, 8270–8274.

35 F. Ji, J. Klarbring, F. Wang, W. Ning, L. Wang, C. Yin, J. S. M. Figueroa, C. K. Christensen, M. Etter, T. Ederth, L. Sun, S. I. Simak, I. A. Abrikosov and F. Gao, *Angewandte Chemie - International Edition*, 2020, 59, 15191–15194.

36 H. Lei, D. Hardy and F. Gao, *John Wiley and Sons Inc*, 2021, preprint, DOI: 10.1002/adfm.202105898.

37 W. Yuan, G. Niu, Y. Xian, H. Wu, H. Wang, H. Yin, P. Liu, W. Li and J. Fan, *Adv Funct Mater*, DOI:10.1002/adfm.201900234.

38 J. Wang, Y. Li, L. Ma, G. Shen and Q. Yang, *Adv Funct Mater*, DOI:10.1002/adfm.202203072.

39 W. G. Li, X. D. Wang, J. F. Liao, Y. Jiang and D. Bin Kuang, *Adv Funct Mater*, DOI:10.1002/adfm.201909701.

40 B. Ghosh, B. Wu, H. K. Mulmudi, C. Guet, K. Weber, T. C. Sum, S. Mhaisalkar and N. Mathews, *ACS Appl Mater Interfaces*, 2018, 10, 35000–35007.

41 X. Song, X. Liu, D. Yu, C. Huo, J. Ji, X. Li, S. Zhang, Y. Zou, G. Zhu, Y. Wang, M. Wu, A. Xie and H. Zeng, *ACS Appl Mater Interfaces*, 2018, 10, 2801–2809.

42 Y. H. Zhou, Z. Bin Zhang, P. Xu, H. Zhang and B. Wang, *Nanoscale Res Lett*, DOI:10.1186/s11671-019-3183-8.

43 R. Chahal, A. K. Mia, A. Bora and P. K. Giri, *J Mater Chem C Mater*, 2024, 12, 12835–12846.

44 F. Fang, Y. Wan, H. Li, S. Fang, F. Huang, B. Zhou, K. Jiang, V. Tung, L. J. Li and Y. Shi, *ACS Nano*, 2022, 16, 3985–3993.

45 J. Ghosh, L. P. L. Mawlong, G. B. Manasa, A. J. Pattison, W. Theis, S. Chakraborty and P. K. Giri, *J Mater Chem C Mater*, 2020, 8, 8917–8934.

46 J. Ding, S. Du, Z. Zuo, Y. Zhao, H. Cui and X. Zhan, *Journal of Physical Chemistry C*, 2017, **121**, 4917–4923.

47 G. Maculan, A. D. Sheikh, A. L. Abdelhady, M. I. Saidaminov, M. A. Haque, B. Murali, E. Alarousu, O. F. Mohammed, T. Wu and O. M. Bakr, *Journal of Physical Chemistry Letters*, 2015, **6**, 3781–3786.

48 H. Wang, H. Hu, K. Homewood and Y. Gao, *Opt. Mater. (Amst).*, DOI:10.1016/j.optmat.2024.115327.

49 K. Dong, H. Zhou, Z. Gao, M. Xu, L. Zhang, S. Zhou, H. Cui, S. Wang, C. Tao, W. Ke, F. Yao and G. Fang, *Adv. Funct. Mater.*, DOI:10.1002/adfm.202306941.

50 L. Liang, X. Niu, X. Zhang, Z. Wang, J. Wu and J. Luo, *Adv. Opt. Mater.*, DOI:10.1002/adom.202201342.

51 H. Jing, R. Peng, R. M. Ma, J. He, Y. Zhou, Z. Yang, C. Y. Li, Y. Liu, X. Guo, Y. Zhu, D. Wang, J. Su, C. Sun, W. Bao and M. Wang, *Nano Lett.*, 2020, **20**, 7144–7151.

52 Q. Yin, J. Wu, H. Ye, H. Li, Z. K. Zhu, C. Zhang, L. Xu, Z. Han and J. Luo, *Adv. Opt. Mater.*, DOI:10.1002/adom.202403183.

Chapter 6 Summary and Outlooks

This chapter summarizes the highlights and major contributions of the thesis. New findings on the controlled growth of different morphologies (Single Crystal, Thin Film, Nanosheets, Nanoflakes) of the $Cs_2AgBiBr_6$ double perovskites and their heterostructures with TMDs and other perovskites are summarized. New findings on the heterostructure of $Cs_2AgBiBr_6$ with other materials for improved optoelectronic and sensing applications are summarized.

The scope of the future work is discussed at the end of this chapter.

6.1 Highlights and summary of the Thesis contributions

This thesis presents a comprehensive investigation into the controlled growth, structural engineering, and optoelectronic properties of bulk and nanostructured Cs2AgBiBr6 double perovskites (DPs). The research encompasses the design and fabrication of type-II heterojunctions incorporating few-layer WS_2 for enhanced photoconductive performance, as well as the chemical vapor deposition (CVD) synthesis of $Cs_2AgBiBr_6$ thin films on various substrates. Furthermore, by employing $Cs_2AgBiBr_6$ as a substrate, the work explores self-trapped exciton (STE)-assisted charge transfer mechanisms and their role in achieving enhanced surface-enhanced Raman scattering (SERS) responses. Furthermore, we have explored the all-inorganic lead-free perovskite-perovskite heterojunction with improved photodetection capabilities. Collectively, these studies provide critical insights into the photo-physics and fundamental processes governing light absorption, charge transfer, and interfacial dynamics in double perovskite systems. They also lay an important foundation for developing sustainable, lead-free, and multifunctional optoelectronic devices tailored for modern energy and photonic applications.

The overall contributions of this thesis are outlined below:

A. Controlled Growth and Characterization of $Cs_2AgBiBr_6$ Double Perovskite by a CVD Method

In this work, we have successfully demonstrated, for the first time, a chemical vapor deposition (CVD)-based growth of $Cs_2AgBiBr_6$ double perovskite (DP) thin films. Using a $BiBr_3$ seed layer, we achieved the formation of highly crystalline and uniform $Cs_2AgBiBr_6$ thin films on a variety of substrates. The substrate temperature was found to play a critical role in determining the phase purity and film quality, serving as the primary parameter for process optimization. Raman spectroscopy and XRD analyses confirmed that a pure $Cs_2AgBiBr_6$ phase is obtained

at an optimal substrate temperature of 130 °C. However, at higher substrate temperatures, both techniques revealed a phase transition from $Cs_2AgBiBr_6$ to $Cs_3Bi_2Br_9$, indicating the thermal instability of the double perovskite phase under such conditions. Controlled experiments on intermediate products provided valuable insights into the film growth mechanism, elucidating the sequential formation and transformation steps occurring during the CVD process. It is noteworthy that grain aggregation at elevated substrate temperatures results in a deterioration of film quality, characterised by increased surface roughness and reduced uniformity. To further examine the strain-induced effects and optimize the film morphology, we carried out growth studies on different substrates. The optimized $Cs_2AgBiBr_6$ thin film deposited on a SiO_2 substrate exhibited excellent crystallinity, reduced pinhole defects, enhanced surface homogeneity, and low roughness, confirming the effectiveness of the growth parameters. Furthermore, Raman thermometry measurements were performed to investigate the thermal transport properties of the $Cs_2AgBiBr_6$ thin films, focusing on both suspended and supported configurations. The extracted thermal conductivity values were approximately 1.97 ± 0.48 W m^{-1} K^{-1} for the suspended $Cs_2AgBiBr_6$ film and 16.14 ± 1.58 W m^{-1} K^{-1} for the supported film, which are in close agreement with theoretical predictions. The notable difference between the two configurations arises from enhanced heat dissipation to the substrate in the supported films, leading to higher apparent thermal conductivity. Overall, this study establishes a reliable CVD-based synthesis route for high-quality lead-free double perovskite thin films, while providing critical understanding of the temperature-dependent growth mechanism, strain effects, and thermal transport behaviour - all of which are essential for advancing the integration of $Cs_2AgBiBr_6$ in energy-efficient and optoelectronic device applications. Our investigations revealed that the $Cs_2AgBiBr_6$ thin film exhibits excellent thermal and environmental stability. The material retains its structural integrity and phase purity up to a temperature of 220 °C, as confirmed by temperature-dependent analyses. Moreover, the as-grown $Cs_2AgBiBr_6$ DP maintained its crystalline phase and optical characteristics for over three months under high-humidity ambient conditions, underscoring its remarkable resistance to environmental degradation—a crucial attribute for long-term device operation. A planar photodetector device fabricated from the $Cs_2AgBiBr_6$ thin film demonstrated excellent optoelectronic performance, producing a strong photocurrent of 10.1 μA at a modest bias voltage of 2 V. The device also exhibited a high current on/off ratio of approximately 44, along with rapid photoresponse dynamics, characterized by rise and fall times of 170 μs and 177 μs, respectively. Notably, the photodetector displayed self-powered operation, indicating efficient charge separation driven by the intrinsic built-in electric field. This study represents the first systematic report on the

CVD-grown $Cs_2AgBiBr_6$ thin film and its photoelectronic behaviour, providing a strong foundation for the future integration of lead-free double perovskites into a wide range of stable, high-performance optoelectronic and photodetection devices. "*This work has been published in ACS Applied Energy Materials 6 (17), 8794-8807 (2023).*"

B. Facile In-situ Growth of $Cs_2AgBiBr_6/WS_2$ heterostructure for enhanced ultraviolet Photodetection

In this study, we successfully demonstrated the synthesis of $Cs_2AgBiBr_6$ DP nanosheets and the in-situ formation of $Cs_2AgBiBr_6/WS_2$ heterostructures via a rapid, surfactant- and ligand-free mechanochemical process. This method offers several advantages, including simplicity, scalability, and environmental friendliness, making it highly suitable for large-scale fabrication of lead-free perovskite-based heterostructures. XRD analysis confirmed the phase purity and structural integrity of both the individual $Cs_2AgBiBr_6$ nanosheets and the resulting $Cs_2AgBiBr_6/WS_2$ heterostructure, indicating that the mechanochemical synthesis did not alter their crystalline phases. TEM and SAED analyses further revealed that small $Cs_2AgBiBr_6$ nanosheets were uniformly distributed and anchored onto the surfaces of larger WS_2 nanosheets, forming a well-defined heterointerface. The presence of characteristic vibrational modes corresponding to both $Cs_2AgBiBr_6$ and WS_2 was confirmed through Raman spectroscopy, validating successful heterostructure formation. Notably, the Raman shifts observed in the A_{1g} and E_{2g} modes of WS_2 within the heterostructure indicate electron transfer from $Cs_2AgBiBr_6$ to WS_2 and the presence of lattice strain induced during the milling process. Optoelectronic characterization revealed that the $Cs_2AgBiBr_6/WS_2$ heterostructure exhibits a significantly enhanced photoresponse compared to pristine $Cs_2AgBiBr_6$, attributed to its improved light absorption, strong PL quenching, and reduced carrier recombination lifetime. These findings collectively confirm that efficient interfacial charge transfer and coupling between the two materials lead to superior photoconductive performance, underscoring the promise of $Cs_2AgBiBr_6/WS_2$ heterostructures for next-generation optoelectronic and photodetection applications. It was observed that the incorporation of WS_2 nanosheets within the $Cs_2AgBiBr6/WS_2$ heterostructure led to a significant suppression of self-trapped exciton (STE) emission, attributed to the participation of intermediate electronic energy states introduced by WS_2. These intermediate states facilitate efficient carrier transfer and relaxation pathways, thereby reducing radiative recombination via STE processes. The formation of high-purity crystalline phases of both $Cs_2AgBiBr_6$ DP and WS_2 nanosheets was confirmed through XPS analysis. Following the creation of the heterojunction, XPS spectral shifts revealed an

increase in electron density within WS_2, consistent with charge (electron) transfer from $Cs_2AgBiBr_6$ to WS_2, further corroborating the existence of strong electronic coupling at the interface. To evaluate the device performance, a planar heterostructure photodetector was fabricated using gold (Au) electrodes, patterned via electron-beam lithography for precise contact definition. The resulting $Cs_2AgBiBr_6/WS_2$ heterostructure device exhibited a substantial enhancement in photocurrent, demonstrating its superior photoresponse efficiency compared to the pristine counterparts. Additionally, the formation of a depletion region and a Schottky barrier at the Au/$Cs_2AgBiBr_6/WS_2$ interface contributed to a two-order-of-magnitude reduction in dark current, highlighting the heterostructure's excellent carrier selectivity and low noise characteristics. These findings collectively underscore the critical role of interfacial charge transfer and built-in electric fields in enhancing the photoconductive performance of the $Cs_2AgBiBr_6/WS_2$ heterostructure, positioning it as a promising platform for high-sensitivity, low-noise optoelectronic devices. The $Cs_2AgBiBr_6/WS_2$ heterostructure photodetector exhibited excellent optoelectronic performance, characterized by a high specific detectivity (D*) of approximately 3.6×10^{13} Jones and an almost linear photocurrent response with respect to the incident light intensity. The device demonstrated a notably high photo-responsivity of 2.01 A W^{-1}, along with a large light-to-dark current ratio (I_{light}/I_{dark}) of 5.9×10^3, confirming its strong sensitivity and low noise behavior. Furthermore, the transient photoresponse measurements revealed rapid rise and decay times of 80 ms and 120 ms, respectively, highlighting the device's ability to achieve swift carrier dynamics under illumination. In addition, the high linear dynamic range (LDR) of 75 dB indicates the heterostructure's capability to efficiently detect both weak and intense optical signals, making it suitable for a wide range of practical photodetection applications. These findings collectively demonstrate that the integration of TMDCs such as WS_2 with lead-free double perovskites effectively broadens their functionality, resulting in enhanced charge transport, improved carrier separation, and superior optoelectronic performance. This work thus establishes a promising route for the development of next-generation nanoscale photodetectors and multifunctional optoelectronic devices based on hybrid perovskite–TMDC heterostructures. *"This work has been published in Journal of Materials Chemistry C 12 (33), 12835-12846 (2024)."*

C. Space Confined Growth of Cs2AgBiBr6 Nanoflakes for High Performance SERS Substrate

In this study, we have, for the first time, demonstrated the application of a lead-free, all-inorganic double perovskite (DP), $Cs_2AgBiBr_6$, as an efficient surface-enhanced Raman scattering (SERS) substrate for the detection of organic pollutants. High-quality triangular $Cs_2AgBiBr_6$ nanoflakes were synthesized using an economical, solution-based growth technique, yielding well-defined crystalline facets ideal for SERS activity. Comprehensive structural and compositional analyses—including XPS, XRD, and Raman spectroscopy—confirmed the phase purity and structural stability of the $Cs_2AgBiBr_6$ double perovskite. Importantly, XPS measurements indicated that the material retained its cubic phase even after analyte adsorption, verifying its chemical robustness under experimental conditions. The high-resolution XPS spectra of the individual elements exhibited a systematic shift toward lower binding energies, suggesting charge transfer from the adsorbed MB molecules to the $Cs_2AgBiBr_6$ surface. This interfacial charge transfer was further supported by PL quenching experiments, theoretical simulations, and favourable band alignment analyses, collectively confirming that the SERS enhancement mechanism in $Cs_2AgBiBr_6$ is predominantly governed by chemical enhancement, rather than electromagnetic effects. The manipulation and control of self-trapped exciton (STE) states within the $Cs_2AgBiBr_6$ DP further substantiated the proposed chemical enhancement mechanism in the SERS process. We provided a direct correlation between defect density and the SERS peak intensity. The versatility of the $Cs_2AgBiBr_6$ DP as a SERS-active platform was demonstrated through its effective detection of multiple organic dye molecules, including MB, rhodamine B (RhB), rhodamine 6G (R6G), crystal violet (CV), and malachite green (MG). Remarkably, the $Cs_2AgBiBr_6$ DP exhibited exceptionally high enhancement factors (EFs) of 5.04×10^7 for MB and 1.37×10^7 for R6G, surpassing all previously reported perovskite-based SERS substrates. The substrate demonstrated ultrahigh sensitivity, capable of detecting analyte concentrations as low as 10^{-10} M, highlighting its superior charge-transfer efficiency and surface reactivity. Furthermore, the $Cs_2AgBiBr_6$ DP SERS substrate exhibited outstanding environmental stability, retaining its SERS activity and structural integrity for up to four months under ambient conditions. This prolonged operational stability, coupled with its high sensitivity and reproducibility, underscores the potential of $Cs_2AgBiBr_6$ double perovskite as a reliable and durable platform for low-concentration molecular sensing and practical SERS-based analytical applications. *"This work has been published in Nanoscale 17(15), 9401-9417 (2025)."*

D. All Inorganic Lead-free $Cs_2AgBiBr_6$ single Crystal/$Cs_3Bi_2I_9$ NC heterostructure for Photodetection Applications

In this work, we have demonstrated the development of a novel $Cs_2AgBiBr_6$ single crystal /$Cs_3Bi_2I_9$ nanocrystal film heterojunction, exhibiting significant potential for high-performance photodetection applications. The $Cs_3Bi_2I_9$ (CBI) nanocrystals (NC) were synthesized using a surfactant-assisted mechanochemical method, yielding a stable colloidal dispersion in toluene with excellent optical and structural uniformity. Meanwhile, high-quality $Cs_2AgBiBr_6$ single crystals were grown via a conventional slow-cooling crystallization technique, ensuring large crystal domains and minimal defect density. The heterojunction architecture was fabricated by depositing the CBI NC film onto the polished surface of the $Cs_2AgBiBr_6$ SC, forming a well-defined perovskite–perovskite interface. This configuration effectively combines the broad optical absorption of the CBI nanocrystals with the high carrier mobility and low trap density of the $Cs_2AgBiBr_6$ single crystal. Comprehensive steady-state PL and TRPL analyses confirmed the efficient transfer of photogenerated carriers from the CBI NC film to the $Cs_2AgBiBr_6$ SC, indicative of strong interfacial electronic coupling and highly efficient charge separation dynamics. These findings underscore the potential of the $Cs_2AgBiBr_6$/$Cs_3Bi_2I_9$ heterojunction as a promising lead-free hybrid platform for next-generation optoelectronic and photodetection devices. The fabricated Au/$Cs_2AgBiBr_6$/$Cs_3Bi_2I_9$/Au heterojunction photodetector exhibited a remarkably enhanced photocurrent response and a significantly reduced dark current compared to the pristine $Cs_2AgBiBr_6$ SC device. These improvements clearly demonstrate the superior photoresponse efficiency and enhanced photodetection capability of the heterojunction architecture. The observed increase in photocurrent is primarily attributed to the favourable band alignment and band bending at the type-II $Cs_2AgBiBr_6$/$Cs_3Bi_2I_9$ heterointerface, which promotes efficient carrier generation and spatial separation. The presence of a built-in electric field across the junction enables drift-assisted charge separation, effectively suppressing carrier recombination losses and enhancing charge extraction efficiency. As a result of this optimized charge transport mechanism, the heterojunction device displayed an impressive responsivity of 0.98 A W^{-1} under an external bias of −5 V, confirming the presence of a strong internal potential gradient capable of efficiently driving charge carriers across the interface. These findings highlight the synergistic interaction between the double perovskite and bismuth halide nanocrystal components, establishing the $Cs_2AgBiBr_6$/$Cs_3Bi_2I_9$ heterojunction as a promising platform for high-sensitivity, lead-free photodetection applications. The $Cs_2AgBiBr_6$/$Cs_3Bi_2I_9$ heterojunction photodetector exhibited a remarkably high specific detectivity (D*) of 2.97×10^{12} Jones,

significantly surpassing that of the pristine $Cs_2AgBiBr_6$ single-crystal-based device. In addition to its enhanced sensitivity, the heterojunction device demonstrated a faster temporal response, characterized by shorter rise and decay times, along with a substantially higher current on/off ratio, indicative of superior charge transport dynamics and reduced recombination losses. The underlying mechanism for this improved performance was further elucidated through density functional theory (DFT) electronic structure calculations, which revealed a distinct electron transfer pathway from $Cs_3Bi_2I_9$ to $Cs_2AgBiBr_6$. This theoretical insight aligns well with the experimentally observed type-II band alignment, confirming that the staggered energy-level configuration facilitates efficient carrier separation and interfacial charge transfer. Collectively, these findings establish the $Cs_2AgBiBr_6/Cs_3Bi_2I_9$ heterojunction as a promising candidate for next-generation, high-performance, and lead-free photodetectors. The device's synergistic combination of enhanced optical absorption, efficient carrier extraction, and strong interfacial coupling underscores its potential for broad-spectrum optoelectronic applications, paving the way for environmentally sustainable perovskite-based photonic technologies. *"This work is under preparation for a manuscript and will be communicated soon".*

6.2 Scope of the Future Work

This thesis has primarily focused on the development and exploration of lead-free double perovskite materials, emphasizing the synthesis of different morphologies of $Cs_2AgBiBr_6$ DP and the design of novel methodologies for advanced optoelectronic and sensing applications. The systematic studies presented herein have advanced the understanding of structure–property relationships, charge transfer mechanisms, and interfacial phenomena in double perovskite systems.

Given the promising results and fundamental insights obtained in this work, the current research can be further extended toward a broader range of technological applications, as outlined below:

1. Continued efforts toward the partial or complete substitution of toxic lead with environmentally benign metal cations in halide perovskites will be crucial for the development of sustainable, non-toxic materials for a wide range of optoelectronic and energy-related applications.
2. The combination of perovskite nanocrystals or thin films with various two-dimensional (2D) materials such as MoS_2, WSe_2, $MoSe_2$, Bi_2O_2Se, and MXenes can be explored to

develop high-performance heterojunction photodetectors exhibiting ultrafast photoresponse, superior charge mobility, and enhanced environmental stability.

3. A detailed study of the transient absorption, carrier trapping mechanisms, interfacial charge transfer kinetics, and recombination dynamics in perovskite/2D material heterostructures is essential for optimizing their optical and electrical properties. Such insights will be instrumental in designing next-generation high-sensitivity optoelectronic devices.
4. The fabrication of transport-layer-free perovskite photodetectors with self-powered operation, low cost, and high performance represents a key step toward the realization of energy-efficient photodetection systems suitable for real-world applications. The addition of suitable transport layers can be studied for improved device performance.
5. Advanced interface engineering strategies can be employed to fabricate high-performance plasmonic–perovskite solar cells, leveraging localized surface plasmon resonances (LSPRs) to improve light harvesting, charge separation, and device efficiency, thereby moving toward commercial viability.
6. Further improvement in the efficiency and operational stability of large-area perovskite solar cells/photodetectors deposited via vapor–solution hybrid techniques can be achieved by optimizing interfacial layers, modifying energy band alignment, and implementing passivation strategies, ultimately facilitating commercial-scale device integration.
7. The controlled incorporation of main-group, transition-metal, and rare-earth metal cations into double perovskite nanocrystals through pressure-mediated solid-state synthesis offers a promising pathway for tuning their structural, optical, and electronic properties. A systematic investigation of the resulting dopant-induced modifications in photophysical behaviour—such as bandgap modulation, defect passivation, and exciton dynamics—could lead to the development of tailor-made perovskite materials for specialized light-emitting, photodetection, and energy-harvesting applications.